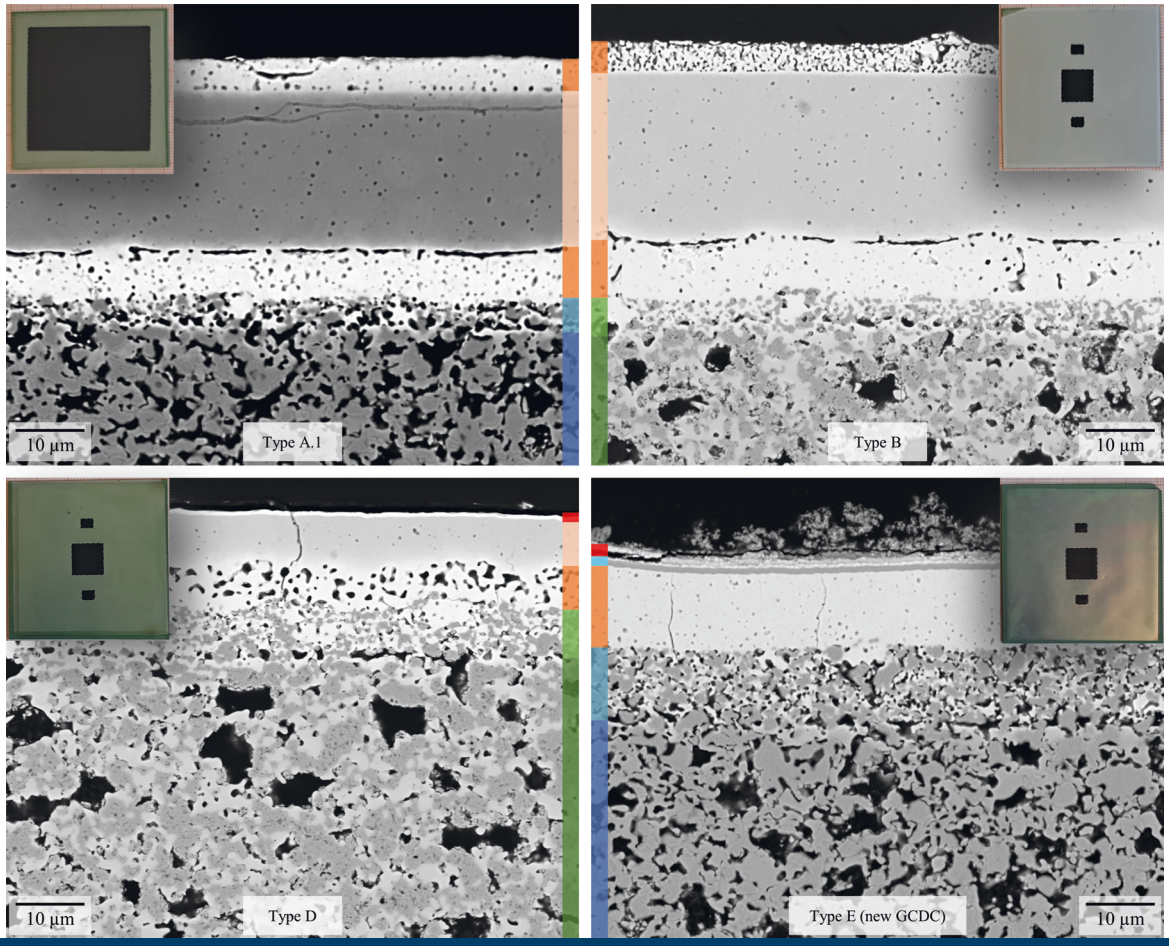


# Development of an oxygen ion conducting solid oxide electrolysis cell based on gadolinium-doped cerium oxide as fuel electrode and electrolyte material

Denise Josefine Ramler

Energie & Umwelt / Energy & Environment
Band / Volume 689
ISBN 978-3-95806-879-7

Mitglied der Helmholtz-Gemeinschaft

JÜLICH
Forschungszentrum

Schriften des Forschungszentrums Jülich
Reihe Energie & Umwelt / Energy & Environment Band / Volume 689

Forschungszentrum Jülich GmbH
Institute of Energy Materials and Devices (IMD)
Werkstoffsynthese und Herstellungsverfahren (IMD-2)

# Development of an oxygen ion conducting solid oxide electrolysis cell based on gadolinium-doped cerium oxide as fuel electrode and electrolyte material

Denise Josefine Ramler

Schriften des Forschungszentrums Jülich
Reihe Energie & Umwelt / Energy & Environment Band / Volume 689

ISSN 1866-1793 ISBN 978-3-95806-879-7

Bibliografische Information der Deutschen Nationalbibliothek.
Die Deutsche Nationalbibliothek verzeichnet diese Publikation in der
Deutschen Nationalbibliografie; detaillierte Bibliografische Daten
sind im Internet über http://dnb.d-nb.de abrufbar.

| | |
|---|---|
| Herausgeber und Vertrieb: | Forschungszentrum Jülich GmbH<br>Zentralbibliothek, Verlag<br>52425 Jülich<br>Tel.: +49 2461 61-5368<br>Fax: +49 2461 61-6103<br>zb-publikation@fz-juelich.de<br>www.fz-juelich.de/zb |
| Umschlaggestaltung: | Grafische Medien, Forschungszentrum Jülich GmbH |
| Druck: | Grafische Medien, Forschungszentrum Jülich GmbH |
| Copyright: | Forschungszentrum Jülich 2026 |

Schriften des Forschungszentrums Jülich
Reihe Energie & Umwelt / Energy & Environment, Band / Volume 689

ISSN 1866-1793
ISBN 978-3-95806-879-7

Vollständig frei verfügbar über das Publikationsportal des Forschungszentrums Jülich (JuSER)
unter www.fz-juelich.de/zb/openaccess.

**Abstract**

The global transition toward $CO_2$-neutral energy systems requires a significant expansion of hydrogen technologies, with solid oxide electrolysis cells (SOECs) offering a highly efficient route for hydrogen production via high-temperature electrolysis. However, despite their superior efficiency, SOECs remain technologically less mature than low-temperature alternatives such as alkaline or proton exchange membrane electrolyzers. Advancing SOEC development therefore demands innovation in both cell design and manufacturing strategies to achieve high performance, mechanical stability, and cost-efficiency.

This dissertation focuses on the development and investigation of fully screen-printed, fuel electrode-supported solid oxide cells featuring a co-sintered tri-layer electrolyte architecture. The work was conducted within the framework of the ElChFest project, which aims to model the electro-chemo-mechanical behavior of gadolinium-doped ceria based solid oxide cells and understand crack formation phenomena in the electrolyte during operation. A key objective was to fabricate mechanically robust and electrochemically efficient cells by optimizing the interplay between powder properties, paste formulation, sintering behavior, and final microstructure. Particular attention was paid to residual stresses induced during manufacturing.

The fabrication strategy centered around screen printing as a scalable and cost-effective deposition method. The project included the transition of previously sputtered barrier layers to screen-printed alternatives. A comprehensive study of powder processing (encompassing pre-calcination and milling) was carried out to tailor the sintering behavior and enable co-sintering of the multi-layer cell. Rheological characterization of screen-printing pastes revealed strong correlations between print quality and parameters such as damping factor, yield point, and particle distribution asymmetry. These findings highlighted the critical role of paste rheology in achieving defect-free and reproducible ceramic layers.

The sintering behavior of gadolinium-doped ceria (GDC) and yttria-stabilized zirconia (YSZ) powders was evaluated using both bulk pellets and screen-printed layers. Gadolinium-doped ceria exhibited an earlier onset of sintering and higher shrinkage than yttria-stabilized zirconia. While co-doping and pre-calcination effectively modified sintering kinetics, translating these findings to printed layers required further adaptation due to the mechanical constraints induced by the support. Co-sintering trials showed that substrate shrinkage behavior had a significant influence on electrolyte densification. Pre-calcined NiO-8YSZ substrates often inhibited proper densification, leading to increased porosity and cell warping.

The development of the tri-layer electrolyte revealed additional microstructural challenges. Interfacial porosity driven by interdiffusion and Kirkendall effects was observed at the GDC/YSZ interfaces, when screen printing was used. This porosity was not present in cells with sputtered barrier layers. Consequently, optimizing the sintering temperature became a balancing act between achieving sufficient densification and suppressing interdiffusion-related degradation.

Electrochemical characterization confirmed that cells with Ni-GDC fuel electrodes outperformed conventional Ni-YSZ cells in terms of stability, validating the choice of doped ceria. While the best electrochemical performance was achieved in cells with sputtered barrier layers, the fully screen-printed cells showed competitive initial current densities and area-specific resistances comparable to the state-of-the-art Jülich Type III reference design. These results underscore the viability of screen printing for fabricating high-performance SOECs, provided that careful attention is paid to interfacial engineering and sintering conditions.

In summary, this work demonstrates that fully screen-printed, fuel electrode-supported SOECs with tri-layer electrolytes can be fabricated with high quality and performance but require tightly controlled processing conditions. The findings emphasize the need for compatible sintering behaviors, advanced paste rheology control, and substrate design tailored for co-sintering. Future work should focus on developing novel, shrinkage-matched substrates to reduce sintering temperatures without compromising densification. Additional research into long-term stability under realistic electrolysis conditions, reversible operation, and varying steam concentrations is also essential to enable the broader deployment of this technology in hydrogen production and energy conversion.

**Kurzfassung**

Der weltweite Übergang zu $CO_2$-neutralen Energiesystemen erfordert einen erheblichen Ausbau der Wasserstofftechnologien, wobei Festoxid-Elektrolysezellen (SOECs) einen hocheffizienten Weg zur Wasserstofferzeugung durch Hochtemperatur-Elektrolyse bieten. Trotz ihrer überlegenen Effizienz sind SOECs jedoch technologisch noch weniger ausgereift als Niedertemperatur-Alternativen wie alkalische oder Protonenaustauschmembran-Elektrolyseure. Die Weiterentwicklung von SOECs erfordert daher Innovationen sowohl im Zelldesign als auch in den Fertigungsstrategien, um eine hohe Leistung, mechanische Stabilität und Kosteneffizienz zu erreichen.

Die vorliegende Dissertation konzentriert sich auf die Entwicklung und Untersuchung von vollständig siebgedruckten, brennstoffelektrodengestützten Festoxidzellen mit einer ko-gesinterten dreischichtigen Elektrolytarchitektur. Die Arbeit wurde im Rahmen des ElChFest-Projekts durchgeführt, dessen Ziel es ist, das elektrochemisch-mechanische Verhalten von gadoliniumdotierten Ceroxid-basierten Festoxidzellen zu modellieren und die Rissbildungsphänomene im Elektrolyten während des Betriebs zu verstehen. Ein wichtiges Ziel war die Herstellung mechanisch robuster und elektrochemisch effizienter Zellen durch Optimierung des Zusammenspiels zwischen Pulvereigenschaften, Pastenformulierung, Sinterverhalten und endgültiger Mikrostruktur. Besonderes Augenmerk wurde auf die während der Herstellung induzierten Restspannungen gelegt.

Die Fertigungsstrategie konzentrierte sich auf den Siebdruck als skalierbares und kostengünstiges Beschichtungsverfahren. Das Projekt umfasste den Übergang von zuvor gesputterten Barriereschichten zu siebgedruckten Alternativen. Es wurde eine umfassende Studie zur Pulververarbeitung (einschließlich Vorkalzinierung und Mahlung) durchgeführt, um das Sinterverhalten anzupassen und das gemeinsame Sintern der Mehrschichtzelle zu ermöglichen. Die rheologische Charakterisierung von Siebdruckpasten ergab starke Korrelationen zwischen der Druckqualität und Parametern wie Dämpfungsfaktor, Fließgrenze und Asymmetrie der Partikelverteilung. Diese Ergebnisse unterstrichen die entscheidende Rolle der Pastenrheologie für die Herstellung fehlerfreier und reproduzierbarer Keramikschichten.

Das Sinterverhalten von gadoliniumdotiertem Ceroxid (GDC) und yttriumstabilisiertem Zirkoniumoxid (YSZ) wurde sowohl an Presstabletten als auch an siebgedruckten Schichten untersucht. Gadoliniumdotiertes Ceroxid zeigte einen früheren Sinterbeginn und eine höhere Schrumpfung als yttriumstabilisiertes Zirkoniumoxid. Während Ko-Dotierung und Vorkalzinierung die Sinterkinetik wirksam modifizierten, erforderte die Übertragung dieser Ergebnisse auf gedruckte Schichten aufgrund der durch den Träger verursachten mechanischen Einschränkungen weitere Anpassungen. Ko-Sinterversuche zeigten, dass das Schrumpfungsverhalten des Substrats einen signifikanten Einfluss auf

die Verdichtung des Elektrolyten hatte. Vorkalzinierte NiO-8YSZ-Substrate verhinderten häufig eine hinreichende Verdichtung, was zu einer erhöhten Porosität und Verformung der Zellen führte.

Die Entwicklung des dreischichtigen Elektrolyten brachte zusätzliche mikrostrukturelle Herausforderungen mit sich. Bei Verwendung des Siebdruckverfahrens wurde an den GDC/YSZ-Grenzflächen eine durch Interdiffusion und Kirkendall-Effekte verursachte Grenzflächenporosität beobachtet. Diese Porosität trat bei Zellen mit gesputterten Barriereschichten nicht auf. Folglich wurde die Optimierung der Sintertemperatur zu einem Kompromiss zwischen der Erzielung einer ausreichenden Verdichtung und der Unterdrückung der durch Interdiffusion verursachten Degradation.

Die elektrochemische Charakterisierung bestätigte, dass Zellen mit Ni-GDC-Brennstoffelektroden herkömmliche Ni-YSZ-Zellen in Bezug auf die Stabilität übertrafen, was die Wahl von dotiertem Ceroxid bestätigte. Während die beste elektrochemische Leistung in Zellen mit gesputterten Barriereschichten erzielt wurde, zeigten die vollständig im Siebdruckverfahren hergestellten Zellen wettbewerbsfähige Anfangsstromdichten und flächenspezifische Widerstände, die mit dem Referenzdesign vom Typ III aus Jülich vergleichbar waren. Diese Ergebnisse unterstreichen die Eignung des Siebdrucks für die Herstellung von hochleistungsfähigen Festoxid-Elektrolysezellen (SOECs), vorausgesetzt, dass den Grenzflächen und den Sinterbedingungen besondere Aufmerksamkeit geschenkt wird.

Zusammenfassend zeigt diese Arbeit, dass vollständig im Siebdruckverfahren hergestellte, brennstoffelektrodengestützte SOECs mit dreischichtigen Elektrolyten mit hoher Qualität und Leistung hergestellt werden können, jedoch streng kontrollierte Verarbeitungsbedingungen erfordern. Die Ergebnisse unterstreichen die Notwendigkeit kompatibler Sinterverhalten, einer verbesserten Kontrolle der Pastenrheologie und eines für das Ko-Sintern maßgeschneiderten Substratdesigns. Zukünftige Arbeiten sollten sich auf die Entwicklung neuartiger, schrumpfungsangepasster Substrate konzentrieren, um die Sintertemperaturen ohne Beeinträchtigung der Verdichtung zu senken. Weitere Forschungen zur Langzeitstabilität unter realistischen Elektrolysebedingungen, zum reversiblen Betrieb und zu unterschiedlichen Dampfkonzentrationen sind ebenfalls unerlässlich, um einen breiteren Einsatz dieser Technologie in der Wasserstofferzeugung und Energieumwandlung zu ermöglichen.

**Table of contents**

**Index of abbreviations**

| | |
|---|---|
| 10GDC | 10 mol% gadolinium-doped ceria |
| 8YSZ | 8 mol% yttria-stabilized zirconia |
| AE | Air electrode |
| AEL | Alkaline-electrolzyer |
| AESC | Air electrode-supported cell |
| ALD | Atomic layer deposition |
| ASR | Area specific resistance |
| BET | Brunauer, Emmet and Teller Method |
| BSE | Backscattered electrons |
| CTE | Coefficient of thermal expansion |
| DPB | Double-phase-boundary |
| DTU | Technical University of Denmark |
| EB-PVD | Electron-beam physical vapor deposition |
| EDS/EDX | Energy dispersive X-ray spectroscopy |
| EIS | Electrochemical impedance spectroscopy |
| ElChFest | Elektro-chemo-mechanische Modellierung von Ceroxid-basierten Festoxidelektrolysezellen |
| ESC | Electrolyte-supported cell |
| FCC | Face-centered cubic |
| FE | Fuel electrode |
| FESC | Fuel electrode-supported cell |
| FTI | Flow transition index |
| FZJ | Forschungszentrum Jülich GmbH |
| GCDC | 0.5 mol% cobalt oxide in gadolinium-doped ceria |
| GDC | Gadolinium-doped ceria |
| GNDC | 0.5 mol% nickel oxide in gadolinium-doped ceria |
| HKA, IDM | Hochschule Karlsruhe – Institute of Digital Materials Science |
| IAM-ET, KIT | Institute for Applied Materials – Electrochemical Technologies, Karlsruher Institute of Technology |
| ICP-OES | Inductively coupled plasma optical emission spectrometry |
| ICSD | Inorganic Crystal Structure Database |

| | |
|---|---|
| IEA | International Energy Agency |
| IMD-1 | Institute of Energy Materials and Devices – Structure and Function of Materials |
| IMD-2 | Institute of Energy Materials and Devices – Material Synthesis and Processing |
| ISC | Inert-supported cell |
| LSC | Lanthanum-strontium-cobaltite |
| LSCF | Lanthanum-strontium-cobalt-ferrite |
| MSC | Metal-supported cell |
| OCV | Open circuit voltage |
| PEM | Proton-exchange-membrane electrolyzer |
| PLD | Pulsed laser deposition |
| PM-MPS | Planetary Mirco Mill – Multistep Pre-Suspension |
| PSD | Particle size distribution |
| PVD | Physical Vapor Deposition |
| ScYSZ | Scandia-yttria-stabilized zirconia |
| SE | Secondary electrons |
| SEM | Scanning electron microscopy |
| SOC | Solid oxide cell |
| SOEC | Solid oxide electrolysis cell |
| SOFC | Solod oxide fuel cell |
| SSA | Specific surface area |
| SSC-GDC | $Sr_{0.5}Sm_{0.5}CoO_{3-\delta}$ – $Ce_{0.9}Gd_{0.1}O_{2-\delta}$ |
| STI | Shear thinning index |
| TM-DPS | Tumbling Mixer – Direct Pre-Suspension |
| TPB | Triple-phase boundary |
| TRL | Technological Readiness Level |
| XRD | X-ray diffraction |
| YSZ | Yttria-stabilized zirconia |

# 1 Introduction

The transition to a $CO_2$-neutral global, european or national economy requires the large-scale deployment of hydrogen technologies, with water electrolysis being predicted to play a central role [1, 2]. According to a recent study by the international Energy Agency (IEA), a significant expansion of water electrolysis capacities will therefore be necessary by 2070 to meet global decarbonization goals [3]. Among the various electrolysis technologies currently being developed, high-temperature electrolysis using solid oxide cells (SOCs) offer superior electrical efficiency [4]. However, its technological maturity still lags behind that of low-temperature alternatives. While technologies such as alkaline-electrolyzers (AELs) and proton-exchange-membrane-electrolyzers (PEMs) have already reached advanced levels of technological maturity (Technological Readiness Level (TRL) 8 - 9 out of a total of 9), solid oxide electrolyzer cells (SOECs) are currently only at a TRL of 6 – 7 [5 - 7].
In SOC development, fuel electrode-supported cells (FESCs) present a promising architecture due to their potential for reduced electrolyte thickness, improved performance and lower hydrogen production cost. While doped ceria ($CeO_2$) is already widely applied as fuel electrode materials in electrolyte-supported (ESC) and metal-supported cells (MSCs), its integration in FESC configurations remains underexplored [8 - 10]. A novel FESC prototype developed at IMD-2, which utilizes a gadolinium-doped ceria (GDC) electrolyte combined with a Ni-GDC fuel electrode, demonstrated a threefold increase in hydrogen output compared to conventional ESCs at equal cell efficiency [11]. These findings facilitated further research into the potential of GDC-based FESCs as high-performance cells for high-temperature electrolysis.

This dissertation was carried out within the framework of the ElChFest project (Elektro-chemo-mechanische Modellierung von Ceroxid-basierten Festoxidelektrolysezellen) funded by the German Federal Ministry of Research, Technology and Space, which aimed to develop a three-dimensional electro-chemo-mechanical model of GDC-based FESCs. The overarching goal was to describe the interplay between microstructures, electrochemical operation parameters and the onset of mechanical degradation, particularly crack formation that was observed within the electrolyte in the prototype cell [12]. Modeling internal stress distributions as a function of current density is intended to enable the identification of safe operation windows and informed knowledge-based optimization strategies for improved cell performance and long-term stability.
As part of the ElChFest project, IMD-2 (Institute of Energy Materials and Devices - Materials Synthesis and Processing) was responsible for the fabrication of complete and functional SOCs for subsequent mechanical and electrochemical characterization carried out by the project partners IMD-1 (Institute of Energy Materials and Devices – Structure and Function of Materials), IAM-ET, KIT (Institute for Applied Materials – Electrochemical Technologies, Karlsruher Institute of Technology) and HKA, IDM (Hochschule Karlsruhe – Institute of Digital Material Science). Additionally, a key focus lay in the

investigation of chemical expansion phenomena in the cerium oxide-based electrolyte and fuel electrode under electrolysis conditions. Based on these investigations, this thesis aimed to optimize the microstructure of the GDC-based FESC to enhance both its mechanical robustness and electrochemical performance in long-term operation.

As mentioned before, a critical challenge for these cells is the formation of cracks in the electrolyte during electrolysis operation, particularly at elevated current densities. This failure mode is primarily attributed to the chemical expansion of ceria, resulting from an electrochemical reduction at the fuel electrode – electrolyte interface [13]. While operation close to the thermoneutral voltage (approximately 1.3 V) is thermodynamically favorable and typically yield high current densities, it also exacerbates mechanical stress within the cell. Thus, improving the mechanical integrity of the electrolyte is essential to allow efficient and safe operation.

Residual stresses introduced during cell manufacturing can potentially play a major role in the mechanical stability of the electrolyte. These stresses arise from mismatches in thermal expansion coefficients and sintering behavior between the individual layers within the multi-layer ceramic system [14 - 17]. The thermal processing parameters, such as the co-sintering temperature of the half-cell (1400 °C) and sintering kinetics, are therefore critical. Strategies such as lowering the sintering temperature or duration can help mitigate residual stress, but often at the cost of reduced electrolyte densification, which is crucial for cell functionality. To address this trade-off, the use of finer, more reactive starting powders was considered, necessitation adjustments not only to the sintering process but also to the powder preparation route. However, modifying the starting powders and their processing methods directly impacts the resulting microstructure and by extension also the electrochemical performance of the cell. Key microstructural features such as grain size, porosity, layer thicknesses and the continuity of the nickel network in the fuel electrode all influence performance. The triple-phase boundaries (TPB) are of particular importance since the electrochemical reactions are confined to this area [18 - 21]. To support data-driven optimization and robust modelling, it was intended to develop a broad range of microstructural variants for characterization within the project. Achieving such variability requires control over powder processing and paste formulation. Adjustments include calcination, milling and reformulation of screen-printing pastes used to deposit the various layers, as screen-printing was the main technique used for fabrication. Paste formulation must be tailored to the properties of each powder system, requiring appropriate selection and concentration of additives to ensure printability. Rheological characterization provides critical insight into paste quality and is a key factor in achieving reproducible and defect-free screen-printed layers [22].

Consequently, this thesis not only explores the impact of powder and paste processing on layer microstructure but also seeks to establish correlations between paste rheology, sintering behavior, microstructural development and final cell performance. Additionally, it is intended that the insights acquired within this thesis facilitate the development of printable pastes for the fabrication of high-quality layers suitable for SOC applications, even beyond the scope of this work. Furthermore, it is

aimed to fabricate the two barrier layers of the tri-layer electrolyte structure via screen-printing, which were previously produced via more expensive physical vapor deposition (PVD) techniques in the prototype cell. Transitioning to screen printing for these layers offers a pathway to further reduce manufacturing costs, thereby contributing to the overall economic viability of green hydrogen production.

# 2 Fundamental Background

## 2.1 Solid oxide cells

### 2.1.1 Operation principle

Solid oxide cells (SOCs) are high temperature electrochemical devices that enable the direct conversion between chemical and electrical energy with high efficiencies, making them highly relevant for a future hydrogen economy. They can be operated in two modes, as solid oxide fuel cells (SOFCs) for electricity generation and as solid oxide electrolysis cells (SOECs) for hydrogen or syngas production through water electrolysis or water and $CO_2$ co-electrolysis respectively. Typical operation temperatures for oxygen ion-conducting SOC systems range between 600 °C and 850 °C [23].

To facilitate these electrochemical reactions, SOCs are typically constructed with a dense electrolyte layer which is positioned between two porous electrodes. The electrode in contact with the fuel gas is referred to as the fuel electrode (FE), while the electrode exposed to air or oxygen containing atmosphere is the air electrode (AE). This layered design allows for the spatial separation of oxidation and reduction reactions while enabling only selective ion transport through the dense electrolyte, which composes the fundamental working principle of SOCs. For example, in fuel cell mode, according to Equation (*2.1*), oxygen molecules are reduced at the air electrode to oxygen ions, which travel through the electrolyte toward the fuel electrode. Here, these oxygen ions react with hydrogen, forming water and releasing the electrons into an external circuit where this electricity can be harvested (Equation (*2.2*)). In electrolysis mode, the reverse reactions take place, leading to the splitting of water molecules under the formation of hydrogen which is showcased in the net reaction in Equation (*2.3*) [24].

$$\frac{1}{2}\,O_2 + 2e^- \rightleftarrows O^{2-} \tag{2.1}$$

$$H_2 + O^{2-} \rightleftarrows H_2O + 2e^- \tag{2.2}$$

$$H_2 + \frac{1}{2}\,O_2 \rightleftarrows H_2O \tag{2.3}$$

Therefore, in SOFC operation, this process generates an electric current, while in SOEC operation, the reactions are driven in reverse direction by supplying electrical energy, leading to water electrolysis and hydrogen production. An illustration of these working principles is showcased in Figure 2.1.

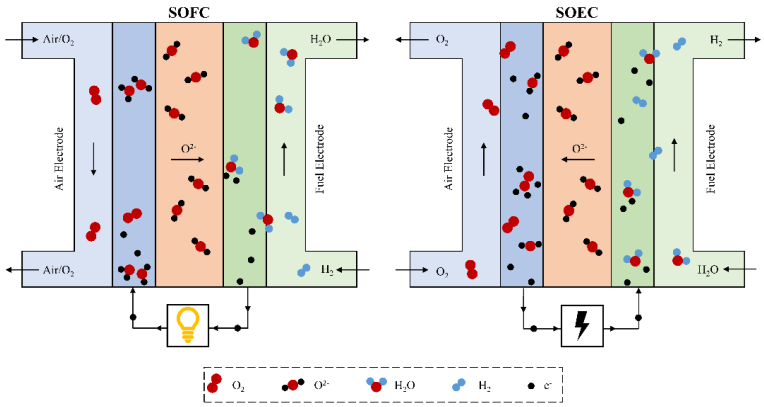


**Figure 2.1:** Schematic illustration of the two operation modes of SOCs. Fuel cell mode as a solid oxide fuel cell (SOFC) to generate electricity as shown on the left and electrolysis mode as a solid oxide electrolysis cell (SOEC) for fuel gas production as shown on the right side of the illustration. Figure adapted from [25].

However, these electrochemical reactions do not occur uniformly across the electrodes but are instead confined to specific regions known as triple-phase boundaries (TPBs). These are sites where the ion conductor, electron conductor and gas phase are in direct contact. In electrodes where a ceramic pure ionic conductor is combined with a metallic electron conductor, TPBs are essential to enable charge transfer and electrochemical activity. These cermet composites, typically composed of a ceramic like yttria-stabilized zirconia (YSZ) with metallic nickel, get specifically designed to provide a large amount of TPBs. Here, the ceramic phase ensures ionic conductivity and compatibility with the electrolyte, while the metal provides electronic conductivity and catalytic activity for hydrogen oxidation or steam electrolysis. Therefore, the efficiency of SOCs with such electrodes is closely linked to the effective TPB length, as longer TPBs increase the number of active sites available for electrochemical reactions, thereby enhancing overall performance [25]. However, not all electrode configurations rely on TPBs in the same way. For instance, in systems using both Ni and gadolinium-doped ceria (GDC), under reducing conditions the GDC phase itself is able to conduct electrons, meaning that the electrochemical reactions are also occurring along this double-phase boundary (DPB). Similarly, in air electrodes made from perovskites such as lanthanum-strontium-cobaltite (LSC) or lanthanum-strontium-cobalt-ferrite (LSCF), no additional phase is needed, as these materials already offer ionic and electronic conductivity, as well as catalytic functionality. In electrode configurations that purely rely on DPBs, microstructure becomes an increasingly important factor compared to cermet electrodes, where composition and ratios additionally influence TPB length [26].

The driving force for SOC operation is the difference in chemical potential between the fuel side and the air side, fundamentally being the oxygen ion activity at the local interfaces of electrolyte and electrodes, which generates a voltage across the cell. This cell voltage is influenced by various factors. Among other things, it is mainly influenced by gas compositions at the electrodes, temperature, the

materials used for electrolyte and electrodes, the electrical load and the subsequent internal resistance of the cell. Here, a distinction can be made between the theoretical cell voltage ($E_{\mathrm{th}}$), the open circuit voltage (OCV) which is measured between the electrodes when no electrical load is applied and the working voltage, measured at defined operating points.

The theoretical cell voltage of a solid oxide cell is determined by the Nernst equation, which expresses the equilibrium potential difference generated by the redox reactions occurring at the electrodes, based on the chemical potentials of the reacting species. For the earlier example of hydrogen-fueled SOC operating with hydrogen and water vapor at the fuel electrode and pure oxygen at the air electrode, the theoretical cell voltage $E_{\mathrm{th}}$ can be expressed by the following variation of the Nernst equation [27 - 29]:

$$E_{\mathrm{th}} = E^{\circ} + \frac{RT}{z_{\mathrm{e}} F} \ln\left(\frac{p_{\mathrm{H_2}} \cdot p_{\mathrm{O_2}}^{1/2}}{p_{\mathrm{H_2O}}}\right) \tag{2.4}$$

Here, $E^{\circ}$ is the standard electrode potential, $R$ is the universal gas constant, $T$ the absolute temperature, $F$ the Faraday constant, $z_e$ the number of transferred electrons (in this case 2) and $p$ denotes the partial pressures of the gaseous species, which is equivalent to their chemical activity. This voltage represents the maximum reversible voltage of the cell, assuming ideal behavior and no losses. However, in real systems, the aforementioned open circuit voltage is often lower than the theoretical value. There are several factors that can contribute to this discrepancy, not including measurement or setup errors such as insufficient contacting or gas diffusion issues [30]:

- Gas leakage or cross-diffusion through seals or defective electrolytes can allow partial mixing of reactants, leading to direct reaction between fuel and oxidizing agents which changes the concentration of said reactants and products.
- Electronic conductivity in the electrolyte, especially in materials like ceria as a mixed ionic-electronic conductor under reducing conditions, can lead to internal short-circuiting and parasitic currents.

Therefore, OCV values are a valuable diagnostic tool as they can serve as an indicator of the quality and integrity of a cell. A measured OCV close to the theoretical value generally implies good sealing and dense electrolyte microstructure, proper electrode functionality and minimal electronic leakage through the electrolyte. Conversely, significantly lower OCV values may point to issues such as gas leakage, internal parasitic currents or electrode dysfunction.

When the cell is operated under load, specifically when current flows either to generate electricity in fuel cell mode or to drive electrolysis in SOEC mode, the operating cell voltage deviates further from the OCV due to internal resistance and kinetic losses. These losses are commonly categorized as [31]:

- Ohmic losses: Voltage drops due to resistance to ionic transport in the electrolyte and electronic resistance in electrodes or interconnects on the stack level.
- Activation and polarization losses: Associated with the energy that must be overcome for electrochemical reactions to proceed at the electrode surfaces. They are heavily dependent on electrode material selection and microstructure (TPB activity).
- Mass transport losses: They occur when reactants are not supplied or reaction products are not removed fast enough at the electrode surfaces, leading to reduced effective reaction rates.

The direction and magnitude of these losses differ depending on whether the cell is operated in fuel cell or electrolysis mode. In SOFC mode, the cell produces electrical energy and the voltage drops below the OCV as current increases. In SOEC mode, the cell consumes electrical energy and the applied voltage must exceed OCV to overcome the losses and drive reactions. Here, the required input voltage increases with increasing current density. This behavior is typically visualized in I-V curves, which illustrate the relationship between current density and cell voltage for both operating modes. The efficiency of SOC operation depends critically on minimizing these losses through careful materials selection, microstructural optimization and thermal management [32, 33].

### 2.1.2 Solid oxide cell designs

Solid oxide cell layers are typically manufactured to be very thin, often only a few micrometers thick, to minimize ohmic resistance and maximize cell efficiency. However, such thin layers have low mechanical stability which is crucial for handling during manufacturing, stack assembly and operation. To address this, at least one layer within the SOC is made significantly thicker to serve as the mechanically supporting component. Depending on which layer provides mechanical support, SOCs can be categorized into five different cell types [26, 34]. A visual overview is presented in Figure 2.2.

If the electrolyte serves as the supporting layer, the cell is referred to as an electrolyte-supported cell (ESC). In this configuration, electrolyte thicknesses range between 50 and 250 µm, compared to 2 – 20 µm when used as a non-supporting layer. ESCs offer the advantage of lower leakage rates, which can lead to higher cell efficiencies and purer reaction products. However, increasing the electrolyte thickness also increases ohmic resistance by increasing the oxygen ion transport pathway. Therefore, ESCs typically require operating temperatures above 800 °C to ensure sufficient reaction kinetics and ionic conductivity. A key advantage in ESCs is their straightforward manufacturing process. Cell manufacturing typically starts with the load bearing layer. For ESCs this means that the electrolyte can be densified completely at higher temperatures, before any other layer is deposited. To achieve such a dense electrolyte layer, usually high sintering temperatures of approximately 1300 °C to 1500 °C are

needed. Since the electrolyte is sintered before electrode deposition, the properties of the electrodes, such as microstructure and material composition, can be chosen more freely and adjusted more easily. Additionally, the risk of mixed-phase formation is reduced, as the sintering of subsequently deposited electrodes typically occurs at lower temperatures [35, 36].

The electrode layers can also function as the mechanically supporting structure. In this case, a distinction is made between the functional layer at the electrolyte interface and a thicker substrate layer at the current collector interface. For example, in a fuel electrode-supported cell (FESC), the load bearing layer is not the thin functional fuel electrode layer directly adjacent to the electrolyte, but a thicker substrate typically made of the same material, usually made with a coarser microstructure. Here, electrochemical reactions can technically still occur within the support, albeit to a lesser extent. The functional layer in state-of-the-art FESCs typically ranges from 5 to 20 µm in thickness, while the supporting substrate can reach up to 1000 µm. A key advantage of FESCs is the ability to use very thin electrolyte layers ranging between 2 to 20 µm, which significantly reduces ohmic resistance. This also allows FESCs to operate at lower temperatures while achieving efficiencies comparable to those of ESCs. However, FESCs generally have higher manufacturing costs due to additional sintering steps when co-sintering is not feasible. The thick support can also introduce polarization stemming from gas-diffusion issues, which can negatively impact cell performance. Additionally, there are material constraints associated with the fuel electrode in FESCs. During manufacturing, the fuel electrode material must withstand high sintering temperatures which are necessary for producing dense electrolyte layers as they are only deposited after fuel electrode sintering. Although co-sintering can reduce the number of sintering steps, the requirement for high-temperature stability of the fuel electrode remains. This presents challenges in developing new fuel electrode materials, as both the material and its microstructure must remain stable under these processing conditions. Selected materials must therefore be resistant to diffusion, phase transformation, cracking, delamination, or severe microstructural changes such as extensive grain coarsening during manufacturing [26, 37].

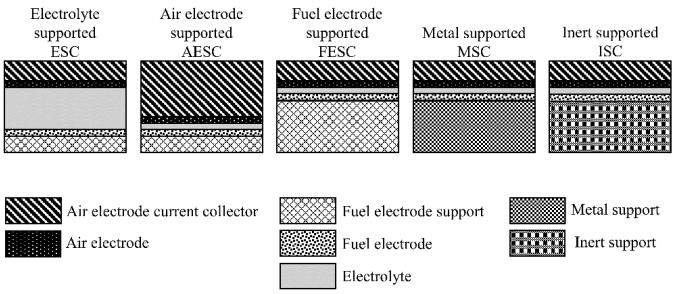


**Figure 2.2:** Schematic illustration of the five main solid oxide cell design types categorized by their mechanically supporting layer. Electrolyte-supported cells (ESCs), air electrode supported-cells (AESCs), fuel electrode-supported cells (FESCs), metal supported cells (MSCs) and inert-supported cells (ISCs) Figure adapted from [26]. Illustration is not true to scale.

Air electrode-supported cells (AESCs), another type of electrode-supported architecture, share similar advantages and disadvantages with FESCs. The principle of mechanical stabilization through a thick and porous substrate made of the same material applies to AESCs as well. Here, the functional layer ranges between 15 and 80 µm in thickness, whereas the supporting layer is typically approximately 1 mm thick. Since this work focuses on the development of FESCs, AESCs are not discussed in detail [26].

The remaining two cell types, metal-supported cells (MSCs) and inert-supported cells (ISCs), differ in that their supporting structures do not participate in electrochemical reactions. In MSCs, the metal supports aids in distributing electrons across the cell surface but does not contribute to catalytic activity. In ISC, the least common cell architecture, the supporting substrate solely provides mechanical stability [9, 10, 38]. As neither of these cell types are directly comparable in nature to the cells discussed in this work, they are not discussed further.

### 2.1.3 Manufacturing methods

**Screen Printing**

Screen printing is a straightforward and cost-effective manufacturing process suitable for high-volume production. It is a well-established fabrication method in the electronics industry, with applications in sensors, circuit boards, antennas and photovoltaic cells [39 - 43]. In these cases, screen printing is used to apply functional inks or pastes to a variety of substrates during manufacturing. Solid oxide cells also typically contain one or more functional layers applied by screen printing. As screen printing is the predominant fabrication method in this thesis and the influence of paste rheology on print quality was explicitly investigated, it will be discussed in greater detail below.

In screen printing, a paste consisting of ceramic particles, solvent, binder and dispersant is typically applied in direct contact with the substrate through a screen. Here, the screen consists of a partially covered mesh, where the uncovered area represents the desired print image. Important characteristics of a screen are the mesh count number, the mesh material and the open area. The open area has a significant effect on the resolution of the printed image and is calculated from the mesh count number and the thread thickness, both of which are affected by the thread material. Polyester and stainless-steel threads are most prominently used. The main difference between these two materials is the range of available thread thicknesses and the geometry of the weave. Stainless-steel threads are typically thinner with pointier junctions, whereas polyester threads tend to have larger thicknesses and more elongated, oval-shaped crossing points. Therefore, in principle, the utilization of stainless-steel meshes typically yields thinner layers that exhibit superior surface quality and print resolution in comparison to meshes composed of polyester, as the open area is greater [44].

In the process of off-contact screen printing, the initial step involves the use of a squeegee to apply paste to the screen, thereby filling these open areas of the mesh. This process is referred to as flooding. It is

only during the second step, the print run, that the screen is pressed onto the substrate below by the print squeegee. Contrary to common belief, the paste is not pressed through the mesh of the screen by the squeegee. Instead, the transfer of paste onto the substrate is primarily driven by adhesive forces between paste and substrate being greater than those between paste and mesh. The final step in the screen-printing process entails the separation of the screen from the substrate. During this step, as the screen is lifted off, the paste can form bridges due to cohesion and adhesion effects. These bridges eventually break and the paste levels out as shown in the overview of the screen-printing process described by Messerschmitt in Figure 2.3 [39, 45].

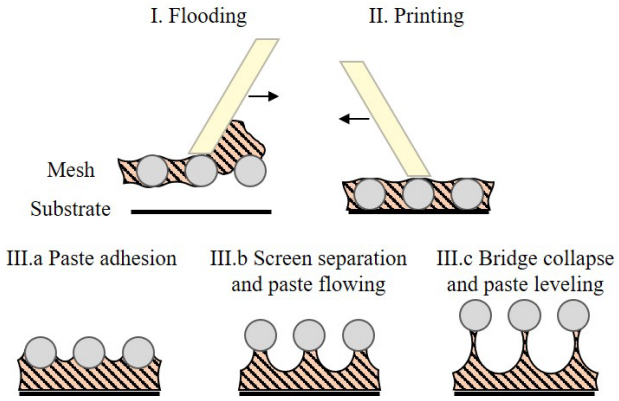


**Figure 2.3:** Overview of the three stages of paste transfer during screen printing as identified by Messerschmitt. I. Flooding, distribution of paste. II. Printing, pressing filled screen onto substrate. III.a Paste adhesion onto the substrate. III.b Screen separation and paste flowing. III.c Bridge collapse and paste leveling. Figure adapted from [45].

Other key factors that influence the print outcome include the printer settings, which are displayed in the print setup schematic in Figure 2.4 [46]. The initial distance between the substrate and the screen is referred to as the snap-off distance. This, in conjunction with the mesh tension and the separation speed, also affects the thickness of the deposited layers. Additionally, the squeegee speed determines the load that causes a desired deformation of the internal paste network during the printing process, thereby enabling the printing process itself. The squeegees are mounted with an inclination of 45° and are typically made out of rubber, with varying degrees of hardness available to suit different applications.

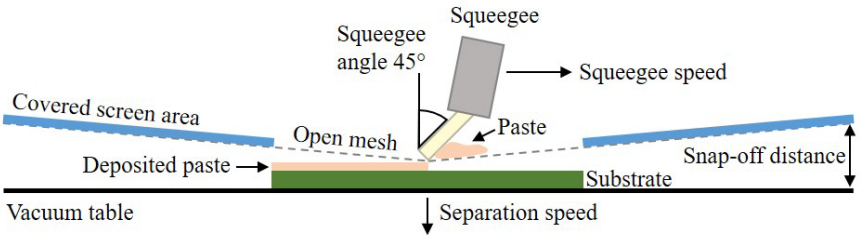


**Figure 2.4:** Schematic representation of the screen-printing process and the relevant printer settings like snap-off distance, separation speed and squeegee speed. Figure adapted from [46].

Despite the simplicity of this process, there is a lack of comprehensive mathematical or physical models that adequately describe its mechanisms. The hypothesis that hydrostatic pressure is the sole reason for the paste transfer through the screen openings has been refuted. Instead, there is a consensus that the printability and print quality are predominantly influenced by the above-mentioned characteristics of the screen, the printer settings and the rheological properties of the pastes, as they primarily determine the leveling behavior of the paste after screen removal and separation of screen and paste.

**Tape casting**

Tape casting is a widely used manufacturing method for producing thin, planar substrates for solid oxide cells. One key advantage of this method is that it allows for the efficient manufacturing of large quantities of thin ceramic sheets. In this process, a ceramic slurry is cast into thin layers using a doctor blade on a moving carrier film. The obtained tape is then dried and cut before thermal treatment steps and further layer deposition [47 - 50].

In 2010, Wolfgang Schafbauer developed the substrate used for the Jülich Type III cells. They are the successor to substrates previously produced by warm pressing in IMD-2. Among other things, this innovation enabled substantial material savings, as the substrate thickness could be reduced from several millimeters before, to only a few hundred micrometers in their current state. As this type of substrate was also utilized for production of the cells investigated in this thesis, their manufacturing method will be briefly discussed in the following. A more detailed investigation and overview of the substrate manufacturing can be found in Schafbauer's dissertation [51]. The substrates are based on a composite of nickel oxide (NiO) and 8 mol% yttria-stabilized zirconia in a ratio of 60:40. For tape casting, the ceramic powders must first be transferred into a flowable suspension. In addition to an organic solvent, in this case a mixture of ethanol and methyl ketone, further additives are required for slurry preparation. Similar to screen-printing pastes, dispersing agents are used to prevent agglomeration of the particles. Additionally, binders are used to adjust the structural strength and viscosity of the slurry, as well as plasticizers to increase the stability of the green tape. All components are mixed together in several homogenization steps for several hours, typically using a roller bench with additional milling balls.

Before the slurry gets poured, it undergoes a vacuum treatment for evacuating any air from the slurry so that no air bubbles impair the structure in the cast substrate.

The prepared slurry is then deposited onto a carrier film and leveled using a doctor blade to produce a thin and uniform green tape. The doctor blade height (also referred to as the blade gap) and casting speed, alongside of slurry viscosity, are critical parameters influencing the final tape thickness and quality. In general, the blade gap primarily determines the wet tape thickness. A larger gap results in a thicker tape, while a smaller gap produces thinner layers. After drying the green tape thickness is further reduced due to solvent evaporation. Furthermore, the speed at which the carrier film is pulled under the blade induces shear forces within the slurry which in turn also influence the thickness and uniformity. Higher casting speeds generally lead to thinner tapes due to shear thinning behavior of the slurry, while lower speeds yield thicker tapes. Typical casting speeds range between 0.5 – 2 cm/s. Therefore, slurries used for tape casting must exhibit pseudoplastic behavior to facilitate homogenous flow while maintaining shape after casting. Here, viscosity must be sufficiently low under an applied load to enable defect free casting.

After drying the tape can be cut into the desired shape to produce flat substrates for solid oxide cell manufacturing. Typically, before other layers are deposited onto this supporting substrate, a thermal treatment is applied to increase mechanical stability. For standard manufacturing of 50 mm × 50 mm Jülich Type III cells, the tapes are cut into 60 mm × 60 mm substrates and are subsequently pre-sintered at 1230 °C for 3 h.

**Sintering**

Sintering is a critical step in the fabrication of solid oxide cells, as it determines the microstructure, mechanical stability and electrochemical performance of the final device. The process involves the densification of ceramic layers through diffusion mechanisms activated at elevated temperature in the range of 1100 °C to 1500 °C, depending on the material system. In SOCs, sintering is not only essential for achieving mechanical integrity, but also for establishing electronic and ionic connectivity across the entire cell structure [52 - 55]. As mentioned before, they are generally fabricated as multilayer ceramic structures, where a dense electrolyte layer is sandwiched between porous electrodes. Among the most common configurations are fuel electrode-supported cells, in which a porous substrate, typically NiO-YSZ, serves as the mechanical support offering stability and the advantage of thinner electrolytes to reduce ohmic resistance. However, the sintering of such a multilayer ceramic component presents several challenges, particularly during the co-sintering process of fabricating the half-cell. Each layer within this multilayer assembly often exhibits naturally different shrinkage behaviors, sintering kinetics and thermal expansion coefficients, leading to mechanical stresses during sintering and thermal cycling in operation. These fundamental differences can result in defects such as bending and subsequent cracking and delamination of layers. Cell bending during co-sintering is a well-documented issue in fuel electrode supported cells [56 - 58]. But also in electrolyte-supported or proton conducting cells, cell

bending is still one of the main challenges to overcome to achieve reliable technology scalability. In FESCs bending typically arises from the differential shrinkage between the electrolyte and the porous fuel electrode support.

Generally, in symmetrical multi-layer systems composed of two types of layers with different sintering behavior, equi-biaxial stresses arise within these layers upon co-sintering according to Equation (*2.5*), where the indices refer to either layer 1 or 2, $t$ is the layer thickness, $\Delta\dot{\varepsilon}$ the strain rate mismatch between the layers and $E'_{\mathrm{p}} = E_{\mathrm{p}}/(1-\nu_{\mathrm{p}})$ with $\nu_{\mathrm{p}}$ being the viscous Poisson's ratio and $E_{\mathrm{p}}$ being the uniaxial viscosity [59, 60].

$$\sigma_1 = \frac{1}{1+mn} E'_{\mathrm{p1}}\, \Delta\dot{\varepsilon} \qquad (2.5)$$

$$\text{with} \quad m = \frac{t_1}{t_2} \quad \text{and} \quad n = \frac{E'_{\mathrm{p1}}}{E'_{\mathrm{p2}}}$$

In asymmetric multi-layer structures, like bi-layers, some of these stresses and tensions are relaxed by bending where the degree of curvature $k$ can be predicted using Equation (*2.6*) where $r$ is the radius of curvature.

$$k = \frac{t_1 + t_2}{r} = \frac{6(m+1)^2 mn}{m^4 n^2 + 2mn(2m^2+3m+2)+1} \cdot \Delta\dot{\varepsilon} \qquad (2.6)$$

Since the dense electrolyte generally tries to shrink more extensively and at a different rate compared to the porous support and this system can be regarded as a bi-layer ceramic structure, curvature can develop in the cell during sintering according to these equations. Additionally, it was found that the extent of this bending not only depends on factors such as the relative layer thicknesses, but also on particle sizes, initial green density and the specific sintering profile applied [61 - 64]. To mitigate cell bending and relate defects, optimization of particle size distributions to align sintering rates of each layer while simultaneously tailoring the sintering profile with controlled heating ramps and dwell times, is vital. However, achieving a flat and defect-free cell after co-sintering still remains a considerable challenge in the field of SOC production.

Furthermore, a fundamental consideration in SOC sintering is balancing the need for densification with the requirement for controlled porosity within the different layers. For example, the electrolyte requires high density, typically exceeding 95 % of theoretical density to ensure gas-tightness and optimal ionic conductivity. The electrodes on the other hand must retain sufficient porosity of approximately 30 to 40 %, to enable effective gas distribution and high amounts of triple-phase boundary sites for electrochemical reactions. Achieving this balance in microstructures is particularly challenging during co-sintering of half-cells, where densification of the electrolyte must occur without excessively densifying the electrodes. Microstructural control during sintering is equally important, as the

temperature and dwell time influence the grain growth within the electrolyte and electrode layers. Excessive grain growth or agglomeration can reduce the active surface area for electrochemical reactions in the electrodes and additionally reduce mechanical strength. Insufficient grain growth may leave residual porosity in the electrolyte, equally limiting structural strength and compromising gas-tightness. The microstructure might also affect the area-specific resistance of cells, making precise control of the sintering essential for optimizing performance [18, 20, 65].
Another critical factor during sintering is the chemical compatibility of the materials in each layer. High-temperature sintering can lead to interdiffusion or reactions between layers, forming undesirable secondary phases that inhibit ionic conductivity. A prominent example of this is the formation of $SrZrO_3$ formation at the interface of strontium-containing air electrodes, such as LSC or LSCF, and the YSZ electrolyte. Therefore, incorporation of barrier layers like gadolinium-doped ceria and careful control of the sintering profile are employed to prevent such reactions during manufacturing and also long-term operation [66 - 68]. However, at high sintering temperatures, both gadolinium and cerium can diffuse into the YSZ layer and vice versa, leading to a compositionally graded region, altering ionic conductivity of these phases. This phenomenon of YSZ and GDC interdiffusion will be investigated in more detail in Chapter 2.2.3.

The choice between co-sintering and sequential sintering also impacts the sintering strategy for SOCs. Co-sintering offers the advantage of reduced processing steps, streamlining the manufacturing process and reducing energy costs. However, precise control of shrinkage behavior in co-sintering is essential. Alternatively, sequential sintering where the electrode support is pre-sintered before the electrolyte is deposited and sintered, can alleviate some of these challenges but introduces additional fabrication steps and may lead to less dense electrolyte microstructures.
Other advanced sintering techniques, including flash sintering, microwave sintering, laser sintering and spark plasma sintering are gaining more attention in SOC research. These methods offer the potential for rapid densification at lower temperatures, reduced energy consumption, significantly shorter dwell times and improved microstructural control. Although promising, their scalability and compatibility with SOC structures and materials continue to be subjects of intensive investigations [69 - 76].
Through careful control of material selection, layer architecture and sintering profiles, it is possible to address many of the challenges associated with the sintering of solid oxide cells. However, the complexity of multilayer ceramic systems and the necessity to simultaneously meet mechanical, microstructural and electrochemical requirements ensure that processing and sintering remain a critical aspect in the development of high-performance and reliable SOCs.

## 2.2 Tri-layer electrolyte prototype cell at IMD-2

The cell design serving as the basis for this thesis was originally developed by Jun Zhang in a previous thesis at IMD-2 and evolved from the standard Jülich Type III FESC design. Like the standard design, it utilizes a NiO-8YSZ fuel electrode support, followed by a NiO-GDC functional fuel electrode layer with a thickness of 7 µm. The defining feature of this cell is its tri-layer electrolyte structure. Directly in contact with the NiO-GDC fuel electrode is a 3.5 µm GDC electrolyte layer, followed by a 0.6 µm YSZ electron-blocking layer and finally a 0.5 µm GDC barrier layer. For the air electrode, both lanthanum-strontium-cobalt-ferrite (LSCF) and lanthanum-strontium-cobaltite (LSC) are viable, but for optimal performance, LSC electrodes with a thickness of 20 µm were used. All stated thicknesses refer to the cell after sintering and a schematic of the cell structure is provided in Figure 2.5 [77].

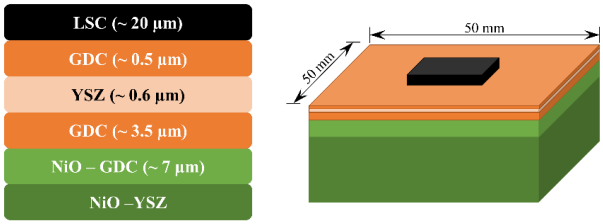


**Figure 2.5:** Schematic illustration of the ceria-based tri-layer electrolyte SOC developed by Jun Zhang and functioning as a basis for this thesis. The indicated thicknesses refer to the state of the cell after sintering at 1400 °C. Figure adapted from [71].

The manufacturing process of this cell proceeds as follows and a visual representation is provided in Figure 2.6. First, the standard Type III NiO-8YSZ support is tape cast and pre-sintered at 1230 °C for 3 h. The NiO-GDC functional fuel electrode layer is then deposited by screen printing onto the substrate and calcined at 1000 °C for 1 h. Subsequently, the GDC electrolyte layer is screen printed on the fuel electrode and the entire half-cell at this point is co-sintered at 1400 °C for 5 h. With this sintering step, the cell reaches its final dimensions of 50 mm × 50 mm. The thin YSZ electron-blocking layer is then applied via electron-beam physical vapor deposition (EB-PVD) to ensure electronic insulation followed by the deposition of a thin GDC barrier layer using bias-assisted magnetron sputtering to prevent strontium zirconate formation during electrode sintering and operation. Finally, the LSC air electrode is deposited again via screen printing onto the GDC PVD layer and sintered at 850 °C for 3 h.

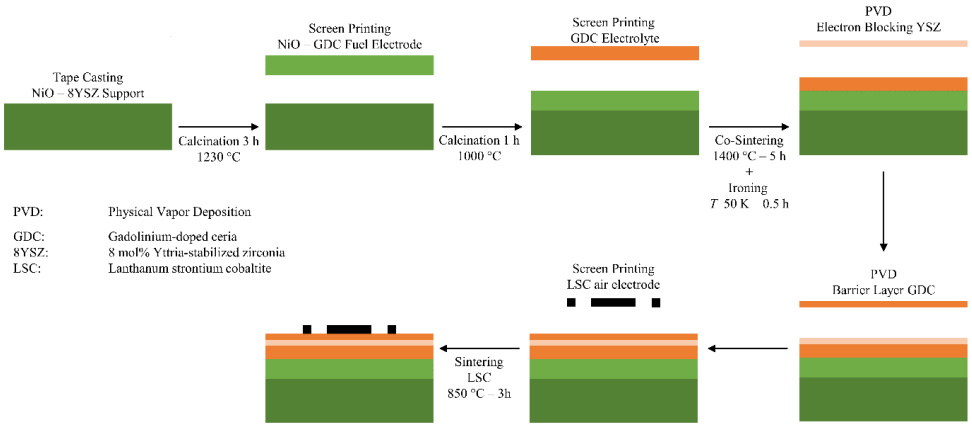


**Figure 2.6:** Schematic overview of the manufacturing route of the prototype tri-layer electrolyte cell developed by Jun Zhang. Figure adapted from [71].

Cells manufactured using this route demonstrate acceptable air leakage rates compared to the standard YSZ-based FESC and exhibit high performance in single cell tests as reported in Zhang's thesis. They achieved an OCV of 1.06 V and a voltage of 0.77 V at a current density of 2 $Acm^{-2}$ at 700 °C under air and $H_2$ + 10 % $H_2O$ atmospheres. The lower-than-expected OCV suggests potential gas leakage through the electrolyte, which is consistent with observed defects in the screen-printed GDC layer that are not able to be fully compensated by the overlaying PVD layers. Electrochemical impedance spectroscopy (EIS) performed on these cells showed low ohmic resistance for the GDC-based cell architecture. Specifically, the GDC cell exhibited an area specific ohmic resistance of 56.1 $m\Omega \cdot cm^2$ at 550 °C [78]. Further electrochemical characterization of this cell architecture in both SOFC and SOEC mode (air and 56 % $H_2O$ / 44 % $H_2$), conducted and published by Lenser, revealed excellent cell performance. At 800 °C, the cell delivers 1.96 $Acm^{-2}$ at 800 mV with a voltage efficiency of 86.3 % in SOFC mode and 1.94 $Acm^{-2}$ at 1100 mV during electrolysis operation [12]. At 700 °C with 12 % relative humidity in the fuel gas, the cell achieves 1.9 $Acm^{-2}$ at 800 mV. From I-V curves at 800 °C and 750 °C no clear degradation was observable. However, post SOEC operation at 750 °C, OCV measurements at 700 °C were much lower than expected, indicated potential increased leakage in the electrolyte. This leakage appeared to be substantial as OCV values continued to decrease at lower temperatures contrary to thermodynamic expectations, further indicating electrolyte degradation. This degradation phenomenon has been proven to be reproducible with multiple cells. Interestingly, cells only tested in SOFC mode showed no sign of this damage. Post-mortem cross-sectional imaging revealed large cracks in the electrolyte, aligned parallel to the oxygen chemical potential gradient, offering the most likely explanation for the observed reduction in OCV. All of these observations combined lead to the hypothesis that ceria-based cells suffer catastrophic damage during high current density SOEC operation, most likely due to electro-chemo-mechanical stresses. Modelling these stresses revealed that tensile stresses in the electrolyte increase with increasing current density during electrolysis. However,

the competing influence of ceria reducibility and fuel electrode polarization is suspected to lead to an inconsistent temperature dependence of these stresses. Therefore, among other necessary investigations and optimization, Zhang suggested that optimization of the microstructure for a reduction in fuel electrode overpotential and a refinement of the manufacturing process could help to mitigate the issue of electrolyte degradation in SOEC mode. It is hypothesized that optimizing the manufacturing process could help with adjusting residual stresses sufficiently within the cells to compensate for the additional stress from chemical expansion, thereby enhancing the mechanical stability of the cell during operation.

### 2.2.1 Ni-GDC based fuel electrode-supported cells

Nickel-gadolinium-doped ceria (Ni-GDC) composites offer several distinct advantages over the conventional nickel-yttria-stabilized zirconia (Ni-YSZ) systems traditionally employed as fuel electrodes in solid oxide cells (SOCs). These advantages pertain not only to initial electrochemical performance but also to long-term stability and degradation behavior, making Ni-GDC particularly attractive for advanced cell architectures [79, 80].

One of the primary benefits of Ni-GDC lies in its enhanced electrochemical activity, especially at intermediate operating temperatures in the range of 600 – 800 °C. This improvement is largely attributed to the increased ionic conductivity at lower temperatures and the mixed ionic and electronic conductivity (MIEC) of GDC. Unlike YSZ, which only conducts oxygen ions, GDC provides both electronic and ionic pathways [81 - 86]. Under reducing conditions at the fuel electrode, this property of GDC extends the electrochemically active area beyond the conventional triple-phase boundary (TPB), allowing for more reaction sites across the fuel electrode. As a result, Ni-GDC fuel electrodes can lead to higher power densities at lower temperatures [87]. In addition to improved electrochemical performance, Ni-GDC electrodes exhibit significantly better tolerance to common fuel impurities such as sulfides [88]. Ni-YSZ electrodes on the other hand tend to degrade rapidly when exposed to even minor amounts of sulfur as it poisons active sites for fuel oxidation [89, 90]. An additional and important advantage of Ni-GDC fuel electrodes lies in their structural and microstructural stability over long-term operation. In Ni-YSZ systems, nickel migration and coarsening are prevalent degradation mechanisms. Although the mechanisms are not fully understood yet, over extended periods of time, Ni is observed to agglomerate and migrate away from the active reaction zone in Ni-YSZ electrodes. This disrupts the percolating Ni networks required for electronic conduction, leading to increased ohmic resistance and a decline in performance [91 - 95]. In Ni-GDC electrodes, while some degree of Ni coarsening can still occur, the presence of GDC as a MIEC phase partially compensates for the loss of metallic connectivity. The GDC matrix supports a portion of the electronic current through its own electronic conductivity, thereby mitigating the impact of local Ni depletion. However, the mechanism of Ni migration and agglomeration in Ni-GDC electrodes was found to be different compared to Ni-YSZ electrodes, where the magnitude seems to be much less pronounced. Nevertheless, the adverse effects of Ni redistribution on cell

resistance are less severe in Ni-GDC systems compared to Ni-YSZ. This property becomes particularly valuable under conditions of long-term operation or thermal cycling, where Ni mobility is accentuated [96 - 99].

For these reasons, considerable attempts have been made by research groups to incorporate Ni-GDC fuel electrodes into their cell architectures. Although most efforts have focused on electrolyte-supported cells (ESC), only a few groups have investigated the viability of fuel electrode-supported (FESC) structures. One such example is the fuel electrode-supported cell developed by the research group around Eric Wachsman at the Maryland Energy Innovation Institute (University of Maryland, USA). Their design consists of a ~ 500 µm Ni-GDC support with a 15 µm Ni-GDC functional layer and a ~ 20 µm thick pure GDC electrolyte. All layers are tape-cast, laminated and finally co-sintered at 1450 °C for 4 h. A composite air electrode consisting of $Sr_{0.5}Sm_{0.5}CoO_{3-\delta}$ – $Ce_{0.9}Gd_{0.1}O_{2-\delta}$ (SSC-GDC) is applied via screen printing and subsequently sintered at 950 °C for 2 h. When adding a porous GDC interlayer between the dense GDC electrolyte and SSC-GDC air electrode, this architecture demonstrated good performance in low-temperature SOFC mode, achieving power densities exceeding 0.55 W/cm² at 500 °C and over 2000 hours of stable operation with negligible degradation. Here, the total area-specific resistance (ASR) remains around 0.4 Ω·cm² when operating at 550 °C and 0.2 $Acm^{-2}$ using air and humidified hydrogen. However, despite its strong SOFC performance, this configuration is not ideally suited for SOEC operation. Under electrolysis condition, the low oxygen partial pressure and high electrochemical driving forces at the fuel electrode promote partial reduction of the GDC electrolyte, resulting in electronic leakage and reduced faradaic efficiency. This is already hinted towards by the relatively low OCV values of below 1 V. Additionally, it is hypothesized that the SSC-GDC air electrode is prone to degradation under the high anodic polarization and oxygen activity in SOEC mode. These factors limit the long-term electrochemical stability and efficiency of this cell design during electrolysis [100 - 101].

Another prominent competitor for Ni-GDC based SOC developments is the Department of Energy Conversion and Storage at the Technical University of Denmark (DTU). Other than the tri-layer electrolyte prototype developed in Jülich, their cell architecture features a bi-layer electrolyte composed of a scandia-yttria-stabilized zirconia (ScYSZ) electrolyte layer and a GDC barrier layer. Because of this configuration, the Ni-GDC fuel electrode is in direct contact with the ScYSZ electrolyte layer, which is particularly important for cell processing and subsequent cell performance. For cell fabrication, support, fuel electrode, electrolyte and barrier layers are tape cast and laminated at 120 °C to form an entire green half-cell. This half-cell is then co-sintered at substantially lower temperatures (1250 °C – 12 h) than the Jülich prototype half-cell (1400 °C – 5 h). According to their evaluation of the microstructure, two distinctive concerning features were observable in pristine cells. One was intense GDC agglomeration and non-uniform GDC distribution present within the fuel electrode, which was attributed to insufficient particle stabilization within the tape slurry. The other key feature was an extensive porosity at the interface between Ni-GDC fuel electrode and ScYSZ electrolyte. Quantitative

analysis revealed that the local fraction of porosity reached up to 50 % and the GDC fraction in contact with the electrolyte was only 5 %. They argue that this is most likely going to limit cell performance as both areas for ionic conduction and electrode activity are diminished and longer pathways between contact points are limiting the utilized fraction of the active surface area. Furthermore, interdiffusion during co-sintering led to a mixed phase forming at the GDC/ScYSZ interface, potentially further impeding ionic conduction pathways. The negative impact of all these factors was evident in the subsequent electrochemical characterization of the cell. Here, the total area specific resistance (ASR) was found to be approximately double the amount compared to state-of-the-art Ni-YSZ based FESCs, with 0.6 Ω·cm² at 778 °C 50/50 steam/hydrogen and air. Despite these results, they conclude that these negative microstructural phenomena do not stem from unavoidable effects caused by the material combination, but that they are processing related issues that can be resolved by optimized processing strategies [102, 103].

These assessments underscore that while Ni-GDC offers clear advantages in electrochemical activity and degradation tolerance, its adoption in fuel electrode-supported cells remains limited. A major reason for this is that GDC is not an optimal choice as a standalone electrolyte due to its partial electronic conductivity under reducing condition, which can lead to parasitic currents within the electrolyte and thus performance loss. As a result, high-performance SOCs still rely on YSZ or ScYSZ as the primary electrolyte material. However, simultaneous integration of GDC and YSZ-based materials introduces significant processing challenges, especially in regard to interfaces. The formation of mixed or interdiffused phases during co-sintering can severely degrade the electrochemical performance by impeding ionic conductivity and creating resistive barriers (see Chapter 2.2.3). Managing these interfacial reactions therefore requires precise control over processing conditions, such as sintering temperature and dwell time. In principle, advanced deposition techniques such as pulsed laser deposition (PLD), sputtering, or atomic layer deposition (ALD) could be employed to fabricate well-controlled interfaces and minimize phase interactions. However, these methods significantly increase manufacturing complexity and cost, counteracting one of the key objectives in SOC development, which is to reduce cost for large-scale implementation.

### 2.2.2 Chemical expansion of ceria

Chemical expansion in cerium oxide is a complex phenomenon involving multiple interrelated factors. However, in this thesis, only the aspects most relevant to solid oxide cells will be briefly discussed in the following. In general terms, chemical expansion refers to changes in the length or volume of a material due to variations in its defect chemistry, in particular, the concentration of point defects such as oxygen vacancies. In ceria-based materials, the dominant mechanism for chemical expansion is the reduction of $Ce^{4+}$ to $Ce^{3+}$ under reducing conditions. This redox reaction introduces oxygen vacancies and leads to a change in stoichiometry, effectively forming a nonstoichiometric solid solution of $CeO_2$

and $Ce_2O_3$. The process of oxygen vacancy formation can be described by the following Equation (*2.7*) using the Kröger-Vink notation [104].

$$2\,CeO_2 \rightarrow 3\,O_O^x + {}^1/_2\,O_{2(g)} + V_O^{\bullet\bullet} + 2\,Ce'_{Ce} \tag{2.7}$$

Although oxygen vacancies are smaller than oxygen ions, the larger ionic radius of $Ce^{3+}$ compared to $Ce^{4+}$ causes an overall expansion of the crystal lattice. Thus, chemical expansion in ceria is a competition between the lattice contraction from oxygen vacancy formation and the expansion due to Ce reduction, with the latter effect dominating. Oxygen vacancies can also be introduced by doping ceria with lower-valent cations (e.g., $Gd^{3+}$), and as such, the total oxygen vacancy concentration depends on both the oxygen partial pressure ($pO_2$) and the dopant concentration. This dependence directly influences the lattice parameter and, therefore, the degree of chemical expansion.

Under solid oxide electrolysis cell (SOEC) operation, significant oxygen partial pressure gradients form across the electrolyte due to high current densities and electrode overpotentials. The lowest $pO_2$ values typically occur near the fuel electrode/electrolyte interface. These gradients result in spatially varying chemical expansion across the electrolyte thickness, which in turn induces mechanical stress within the cell. The effects of such gradients are particularly pronounced in ceria-based electrolytes, where the reduction of $Ce^{4+}$ becomes substantial under low $pO_2$. Because these conditions are difficult to replicate chemically in laboratory settings, data for chemical expansion at very low oxygen partial pressures are often based on interpolation or computational models [105, 106].

In the case of the fuel electrode-supported cells investigated in this work, the tri-layer electrolyte includes both Gd-doped ceria (GDC) and yttria-stabilized zirconia (YSZ). While both materials exhibit oxygen vacancy-driven conductivity, their chemical expansion behavior under reducing conditions is markedly different. YSZ is chemically much more stable than ceria and shows negligible reduction even under low $pO_2$. As a result, its chemical expansion is minimal compared to ceria, which undergoes significant lattice expansion when reduced. This mismatch in chemical expansion between YSZ and GDC can result in local strain concentrations, especially at the interfaces and may contribute to delamination, microcracking, or stress-assisted diffusion phenomena during SOEC operation [12].

Another important consideration is the reversibility of chemical expansion. Unlike thermal expansion, which is fully reversible, chemical expansion is potentially only partially reversible and may exhibit hysteresis depending on the extent and rate of redox cycling. Reoxidation of $Ce^{3+}$ to $Ce^{4+}$ typically reduces the lattice parameter, but some residual strain or microstructural damage may remain after repeated redox cycles. The microstructural consequences of chemical expansion are particularly relevant in multilayer electrolyte architectures. Expansion mismatches can lead to tensile stresses exceeding the fracture strength of the ceramic layers, particularly at interfaces or defect-rich regions. This highlights the importance of accurately characterizing both the magnitude and spatial distribution of chemical expansion when operating ceria based solid oxide cells.

### 2.2.3 Interdiffusion between YSZ and GDC

At elevated temperatures, as encountered during sintering in ceramic processing, interdiffusion between adjacent materials or layers can occur. Generally, the rate of atomic transport is largely influenced by temperature. One essential parameter in quantifying this mass transport using Fick's laws is the diffusion coefficient *D*. This diffusion coefficient can be understood as the magnitude of molar flux through a surface divided by the concentration gradient. In gaseous species *D* generally obeys the relation to temperature and pressure as described in Equation (*2.8*) meaning that diffusion is faster if temperatures *T* are higher and concentrations *p* (partial pressure) are lower [107].

$$D \propto \frac{T^{3/2}}{p} \tag{2.8}$$

In solids, however, diffusion coefficients are much smaller when compared to diffusion coefficients in gases or liquids. This is due to diffusion in solids being mainly driven by thermally activated mechanisms, typically governed by vacancy or interstitial migration. Here, additional energy barriers (activation energies) $E_A$ need to be overcome which is facilitated at higher temperatures as expressed in Equation (*2.9*) [108].

$$D = D_0 \exp\left(-\frac{E_A}{RT}\right) \tag{2.9}$$

Where *R* is the gas constant, *T* the absolute temperature and $D_0$ a pre-exponential factor. Although diffusion coefficients in solids are smaller, because of the exponential dependence, even small increases in processing temperature can result in substantial increases in diffusion rates. Therefore, at sintering temperatures commonly used for SOC fabrication (1200 °C – 1400 °C) cation diffusion across interfaces becomes increasingly relevant. Specifically, chemically distinct (inducing concentration gradient) but structurally similar oxides such as yttria-stabilized zirconia (YSZ) and gadolinium-doped ceria (GDC) can form intermixed interfacial regions.

Both YSZ and GDC adopt the fluorite crystal structure, characterized by a face-centered cubic (FCC) arrangement of cations with oxygen ions occupying all tetrahedral interstitial positions [109]. Doping with aliovalent cations ($Y^{3+}$ in YSZ and $Gd^{3+}$ in GDC) introduces charge-compensating oxygen vacancies that are essential for oxide ion conductivity. In YSZ, typically doped with 8 – 10 mol% $Y_2O_3$, the additional doping not only introduces oxygen vacancies, but simultaneously also stabilizes the high temperature cubic phase that supports high-temperature ionic conduction [110, 111]. Similarly, GDC consists of $CeO_2$ doped with varying amounts of $Gd^{3+}$ and is known for its high oxygen ion conductivity at intermediate temperatures (600 – 800 °C), due in part to the higher polarizability of Ce – O bonds and a larger lattice parameter that facilitates vacancy mobility [112 - 114].

Due to their structural compatibility and similar lattice symmetry, YSZ and GDC are partially or fully miscible at high temperatures. The undoped $CeO_2$ – $ZrO_2$ binary system exhibits wide mutual solubility above ~ 1200 °C, forming a continuous fluorite solid solution over much of the composition range. The presence of dopants like $Y^{3+}$ and $Gd^{3+}$ does not eliminate miscibility, although it can influence phase stability and defect chemistry [115]. During high-temperature sintering, mutual solubility enables the formation of a compositionally graded interfacial region between YSZ and GDC, where $Zr^{4+}$ and $Y^{3+}$ diffuse into GDC and $Ce^{4+}$ and $Gd^{3+}$ into YSZ. This interdiffused zone maintains the fluorite structure but exhibits distinctly different physical and electrochemical behavior compared to the parent phases [116]. The kinetics of this interdiffusion depend on the relative diffusivities of the involved cations. Experimental studies and diffusion modeling have shown that $Zr^{4+}$ typically diffuses faster into ceria-based materials than $Ce^{4+}$ does into zirconia. The net result is an asymmetric diffusion profile, with the interface shifting over time and leading to compositional gradients. For sintering durations on the order of several hours at 1300 °C, diffusion lengths on the order of 1 – 5 µm are realistic. These values are close to the thickness of thin electrolyte layers or interlayers in SOCs, indicating that a significant fraction of the structure may be affected [117 - 118].

A direct consequence of unequal diffusion rates is the formation of Kirkendall porosity at the interface. This phenomenon occurs when the faster-diffusing species leaves behind a net excess of lattice vacancies on one side of the interface. As these vacancies coalesce, they can nucleate pores, leading to mechanical discontinuities and potential leakage paths in the electrolyte. In the YSZ–GDC system, this is especially problematic because the faster ingress of $Zr^{4+}$ into GDC can generate porosity near or within the electrolyte–barrier interface, weakening mechanical integrity and disrupting ionic conduction [119, 120]. Beyond structural considerations, interdiffusion also alters the ionic conductivity of the affected region. GDC, in its pristine form, exhibits higher ionic conductivity than YSZ due to its higher oxygen vacancy concentration and lower vacancy migration barrier. However, as $Zr^{4+}$ and $Y^{3+}$ diffuse into GDC, they modify the defect landscape in several ways. First, $Zr^{4+}$ is less polarizable than $Ce^{4+}$ and its presence tends to increase the binding energy between dopant cations and oxygen vacancies, reducing vacancy mobility. Second, the lattice strain introduced by smaller $Zr^{4+}$ cations disrupts the uniformity of migration pathways. Finally, local clustering of dopants or strain fields may further impede ion transport. As a result, the ionic conductivity of the interdiffused mixed phase tends to be lower than that of pure GDC, particularly in the temperature range where GDC is most advantageous. This leads to an increase in ohmic resistance. Equally significant is the effect of interdiffusion on electronic conductivity, particularly from the perspective of YSZ. Pure YSZ is considered a purely ionic conductor, with negligible electronic transport even under strongly reducing conditions. Its role as an electronically insulating layer is essential in SOCs, especially when it is used to suppress electronic leakage from adjacent mixed conductors like GDC. However, when $Ce^{4+}$ diffuses into YSZ during sintering, it substitutes for $Zr^{4+}$ and introduces redox-active centers into the lattice. Under the low oxygen partial pressures found on the fuel side of the cell, $Ce^{4+}$ can be partially reduced to $Ce^{3+}$. This reduction potential

enables small polaron hopping between $Ce^{3+}$ and $Ce^{4+}$, introducing n-type electronic conduction pathways into the otherwise insulating YSZ matrix. Even modest concentrations of Ce in YSZ have been shown to result in measurable electronic conductivity under reducing conditions. This undermines the function of YSZ as an electronic barrier, allowing a portion of the applied current to be carried by electrons rather than oxygen ions and thus reducing the faradaic efficiency of the cell. It also may lead to internal short-circuiting, especially in thin electrolyte configurations where the entire thickness may be affected by interdiffusion [121 - 123].

To summarize, the interdiffusion between GDC and YSZ during high-temperature processing is thermodynamically possible and kinetically accessible, leading to the formation of a fluorite-structured mixed phase with distinct properties. While structurally coherent with the parent materials, this interdiffused region typically exhibits reduced ionic conductivity, increased electronic conductivity (from the YSZ perspective), and the potential formation of Kirkendall porosity. These can degrade the overall performance and durability of SOCs. Effective mitigation strategies include minimizing co-sintering temperatures and dwell times, controlling layer thicknesses, and employing chemically compatible diffusion barrier layers to preserve the desired electrochemical properties of each functional layer.

# 3 Experimental methods

## 3.1 Synthesis and manufacturing methods

### 3.1.1 Sintering aids for GDC

In the processing of ceramics, the utilization of sintering aids is a common practice. They serve to modify or enhance the densification of the microstructure during the sintering process by increasing the grain boundary mobility and thus promoting grain growth. Furthermore, they allow sintering at lower temperatures leading to a potential reduction in production costs [124 - 130]. This is particularly relevant for GDC, which requires high sintering temperatures (1300 °C – 1500 °C) to ensure sufficient densification for its role as an electrolyte in solid oxide cells. In this thesis, sintering aids were utilized to enhance the densification of the GDC layers within the tri-layer electrolyte, with the potential to reduce the co-sintering temperatures to mitigate detrimental thermally induced interdiffusion effects between YSZ and GDC.

There exist multiple techniques for incorporating additional oxides or ions into a ceramic powder. In this thesis, sintering aids were introduced to the powder after the initial calcination and milling steps which resulted in the desired particle size distributions. Therefore, it is assumed that the doping procedure itself is not significantly altering the particle sizes or surface area of the powder. Nickel and cobalt were selected as sintering aids due to their demonstrated effectiveness in other studies, but also because these elements are already components of the solid oxide cell. Bismuth, a prominent sintering aid for ceria, is not a standard material in these cells and was therefore not considered.

Sintering aids were added to the powder as nitrates, following a similar procedure analogous as that outlined in [131]. For this, 20 g of powder were dispersed in approximately 200 ml of deionized water using a magnetic stirrer. Following the homogenization of the dispersion, 0.1681 g of the respective nitrate, cobalt (II) nitrate hexahydrate ($Co(NO_3)_2 \cdot 6\ H_2O$) or nickel (II) nitrate hexahydrate ($Ni(NO_3)_2 \cdot 6\ H_2O$) was added to the suspension. This is equivalent to 0.5 mol% of the final oxide. Under continuous stirring, the mixture was heated to 150 °C for several hours, until the suspension decomposed into a highly viscous slurry. This was then completely dried at 120 °C in a drying furnace. The resulting powder was ground with mortar to break loose agglomerates before calcination at 400 °C for 2 h This process is intended to transform the nitrates into oxides, which are expected to be homogeneously distributed within the powder or thinly coated around the GDC grains. It is hypothesized that the resulting oxides do not dissolve into the GDC lattice at this point. Studies suggest that this solid solution only occurs at temperatures above 1000 °C, although a comprehensive understanding of the underlying mechanisms remains to be established. Therefore, XRD analyses were carried out in the calcinated and sintered state of the powder to investigate the change in GDC lattice parameter resulting from the incorporation of additional oxides or ions into the lattice.

In addition, studies have examined how the additional doping affects the ion conductivity of GDC. For instance, according to Kleinlogel and Gauckler no change in conductivity was observed in 20 GDC when additional cobalt ions were introduced in a concentration range from 0.1 mol% up to 5 mol% [132]. However, they argued that at high $Co_2O_3$ concentrations (5 mol%), depending on the sintering temperature and dwelling time, there is a possibility for a thin oxide layer to form at the GDC grain boundaries, that is able to get reduced to metallic cobalt during electrochemical measurements when $P_{O_2}$ decreases to lower values than $10^{-22}$ atm. This, in turn, is hypothesized to result in an enhancement of electronic conductivity, which subsequently diminished after additional heat treatments, presumably due to the dissolution of Co from the grain boundaries into the lattice. For GDC with lower concentrations of gadolinium like 10GDC, studies have demonstrated that the incorporation of Co increases the lattice conductivity at temperatures below 500 °C in comparison to cobalt-free 10GDC samples. In the studies by Lewis et al., a maximum conductivity was already reached at a concentration of 2 cation%, with both the lattice conductivity and the grain boundary conductivity increasing [133]. Interestingly, a reduction in lattice parameter was observed for the co-doped samples when sintered at temperatures between 800 °C and 1000 °C, compared to undoped samples. This phenomenon is hypothesized to occur due to the substitution of larger $Ce^{4+}$ ions ($r_{Ce^{4+}}$ = 101 pm) for smaller $Co^{3+}$ ions ($r_{Co^{3+}}$ = 68.5 pm). However, this would also indicate that the reduction of lattice parameter caused by the substitution outweighs the potential increase caused by additional oxygen vacancies. While the lattice parameter of Co-doped GDC remains smaller than that of pure 10GDC, it exhibited an increase within the same temperature range, reaching a plateau at 1000 °C. This behavior mirrors that observed in the undoped samples, suggesting either a solubility limit smaller than 2 cation% or $Co^{3+}$ ions entering the lattice interstitially. A solubility limit being reached is substantiated by the observation that the majority of the cobalt is still found at the grain boundary.

### 3.1.2 Screen printing

All layers produced and evaluated in this work were printed using the EKRA E2 semi-automatic screen printer (EKRA Automatisierungssysteme GmbH, Germany). During the course of this work, the parameters used for printing changed substantially. For example, the setup was adjusted to align with conditions typically used for ‘true’ screen printing. According to the screen printer manual, the method previously used in IMD-2 more closely resembles the technique of stencil printing, in which both squeegees make contact with the screen using the same pressure. Therefore, here printing is carried out by both squeegees (print-print setup, *Druckvariante 3*). In contrast, real screen printing is typically performed using only one squeegee for printing, while the other squeegee floods the screen and fills the mesh openings with paste. To implement this, the print-flood-print-flood setup, available as *Druckvariante 2* in the printer software, was used. In this configuration, the back squeegee serves as the printing squeegee, while the front squeegee is designated as the flooding squeegee. This setup requires

different pressure adjustments for each squeegee. For adjusting the printing squeegee, the squeegee is positioned above the center of the sample which is fixed on the vacuum table. Then, the squeegee is lowered until it presses the screen slightly onto the sample underneath. In contrast, the flood squeegee is adjusted by lowering it until a regular sheet of paper can just be pulled out from between squeegee and screen, after which the squeegee is lowered by an additional full turn of the screw, as instructed by the manual. Since these adjustments are highly dependent on the tension of the mounted screen and the condition of the squeegees, they have to be checked and readjusted each time before starting a new printing experiment. A list of all screens used in this work is presented in Table 3.1.

**Table 3.1:** Overview of all screens used in this thesis. Numbers in brackets indicate changes made during the work, listing the initially used screen (1) followed by the current screen (2).

| Layer | Type | Thread Ø [µm] | Mesh Opening [µm] | Screen Opening [mm²] | Screen Indicator |
|---|---|---|---|---|---|
| YSZ Electrolyte (Standard) | Polyester | 55 | 151 | 56 ×56 | POL48/55/22.5° |
| GDC/YSZ Barrier Layer | Polyester | 27 | 36 | 42 ×42 | POL150/27/22.5° |
| GDC Electrolyte (1) | Polyester | 55 | 151 | 56 ×56 | POL48/55/22.5° |
| GDC Electrolyte (2) | Metal | 18 | 45 | 56 ×56 | VA400/18/22.5° |
| NiO-GDC fuel electrode (1) | Polyester | 48 | 77 | 56 ×56 | POL77/48/22.5° |
| NiO-GDC fuel electrode (2) | Metal | 30 | 98 | 56 ×56 | V-Screen 98/30/22.5° |

It should be noted that the laboratory in which screen printing was performed is not air-conditioned, which is a limitation as paste rheology is strongly influenced by ambient temperature and humidity. Additionally, the vacuum table of the printer does not provide sufficient suction to hold the samples in place during printing. To address this, masks made from < 0.5 mm plastic foils, with a cut-out the size of the sample, are used. The samples are then fixed with help of the mask by applying an adhesive tape across the top left corner of the sample and onto the mask. The mask itself is also secured to the vacuum table with an adhesive tape.

Prior to printing, the cell surface is cleaned using canned compressed air to remove dust particles. After printing, the cells are dried in a drying cabinet at 60 °C for several hours before being submitted for calcination or sintering.

### 3.1.3 Screen-printing paste preparation

For screen-printing paste preparation of NiO-GDC fuel electrode and GDC electrolyte pastes, two significantly different approaches were used in this work that shall be introduced in the following. The YSZ electrolyte paste and the two air electrode pastes made from LSC or LSCF were not manufactured explicitly for this work. These pastes are used in the IMD-2 standardized SOC manufacturing. Therefore, the preparation of these pastes will not be described in this thesis. Detailed information about the materials and chemicals used for the preparation of each developed paste are provided in the respective subsections within this chapter. First, the general outlines of the two preparation methods shall be discussed.

The first preparation route that was used in the initial phases of this work is based on the information provided by the dissertation of Jun Zhang that dealt with the development of the prototype tri-layer electrolyte cell. This processing sequence will be referred to as TM-DPS (**T**umbling **M**ixer – **D**irect **P**re-**S**uspension) as it utilizes a tumbling mixer to directly prepare a ceramic pre-suspension. Figure 3.1 provides an illustration for this processing route, depicting the important steps. Here, solvent, dispersant, ceramic powder and YSZ milling balls are added to a PE-bottle and homogenized using a tumbling mixer (Turbula T2F, Willy A. Bachofen AG**,** Switzerland) at 72 rpm. For fuel electrode paste preparation, NiO and GDC pre-suspensions were prepared separately and mixed subsequently in a ratio of 50 : 50 wt%. Afterwards, the milling balls are removed from the pre-suspension using a sieve. That way, some of the pre-suspension is lost as it adheres to the milling balls. After adding the transport suspension, composed of solvent and binder, final homogenization for both fuel electrode and electrolyte paste takes place in a planetary vacuum mixer (ARV-310, THINKY corporation, Japan) at 1400 rpm for 2 min. This method is characterized by its simplicity and the comparatively short time requirement of approximately 2 days. Furthermore, due to the small number of processing steps, there are only a few possibilities for errors. For more details regarding this processing procedure, please refer to the thesis of Jun Zhang [77].

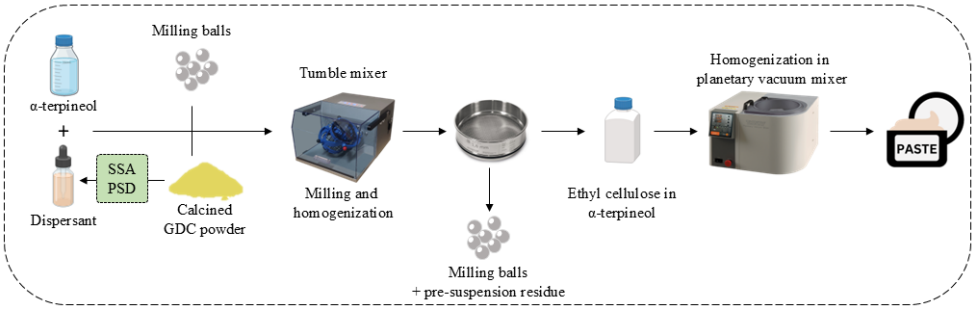


**Figure 3.1:** Illustration of the TM-DPS paste preparation route. The individual process steps are shown using a GDC electrolyte paste as an example.

The disadvantages of this method, however, are the limited control over the resulting particle size distribution and the associated deviations and uncertainty in the subsequent final paste composition, which impedes reproducibility. Since the influence of the particle size distribution on the rheological properties was part of the investigations in this work and its significance was able to be contextualized and highlighted, this method of paste preparation was further evolved for improved process and powder control. This new method will be referred to as PM-MPS (**P**lanetary Micro **M**ill – **M**ultistep **P**re-**S**uspension) and is illustrated in Figure 3.2. Here, the calcined ceramic powder is first subjected to high-intensity ball milling using a planetary micro mill with YSZ lined steel containers (Pulverisette 7 premium line, FRITSCH GmbH, Germany) operated at 500 rpm. The powder is milled using YSZ grinding balls and ethanol. After this milling step, the milling balls are removed by a sieve. As the powder is milled beforehand and therefore separate from the actual paste preparation or formulation, the milling balls can be rinsed completely clean with ethanol, resulting in the entirety of the powder being able to be processed further without any major losses. The ethanol / powder mixture is then dried in a drying furnace, and the resulting calcined and milled powder can be analyzed for its particle size distribution and specific surface area. Depending on these analyses, the exact amount of dispersant required can then be determined, as dispersant concentration should always be based on the available ceramic surface. In addition, an initial quality control of the particle size distribution is automatically carried out at this stage and the powder can be further adjusted if necessary. After pre-mixing solvent and dispersant, the pre-treated powder is added to the mixture which is then homogenized using an ultrasonic bath. Finally, the transport suspension is added to this pre-suspension. A three-roll mill (Exakt 80 E, EXAKT Advanced Technologies GmbH, Germany) is used in the last step for homogenization of transport suspension and pre-suspension to achieve the final screen-printing paste.

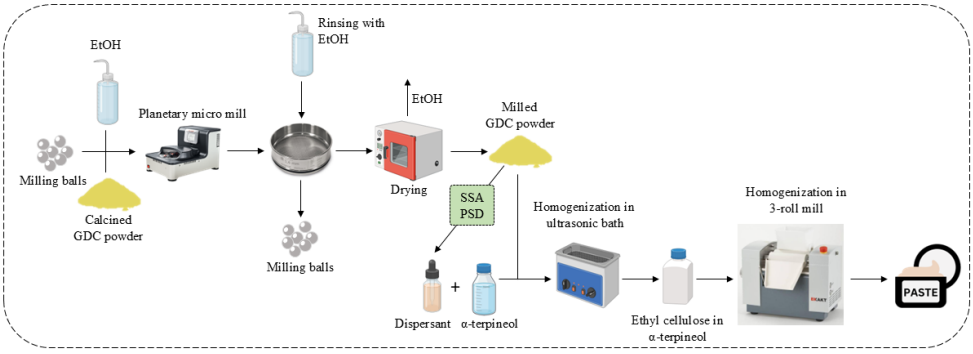


**Figure 3.2:** Illustration of the PM-MPS paste preparation route. The individual processing steps are shown using a GDC electrolyte paste as an example. Here, the powder is milled first, before preparation of the pre-suspension.

The clear advantages of the PM-MPS route are the superior control over the particle size distribution of the powder, which ensures higher reproducibility. In addition, the high-intensity ball milling generally

results in more uniform particle size distributions. Furthermore, none of the powder is lost during the process. By using a three-roll mill, any agglomerates that may form can also be broken up again, leading to better paste stability. Disadvantages are the higher complexity due to the separate grinding of the powder and the associated time requirement of up to 5 days due to the drying phase. However, if the powder has already been prepared, for example by milling larger batches, the paste can be prepared in roughly an hour.

**GDC electrolyte paste**

Table 3.2 lists the materials and chemicals used to produce the GDC electrolyte pastes for this work. The dispersants used at the beginning which were replaced during the course of this work are also listed. However, the following description will only refer to one GDC paste, which showed the best processability and produced the highest layer quality. This description is based on results obtained through investigations carried out as part of this thesis, which will be reported in more detail later.

**Table 3.2:** Overview of materials and chemicals used for the GDC electrolyte paste. Including the formerly used and then exchanged dispersants.

| Material / Chemical | Purpose | Manufacturer | Comment |
|---|---|---|---|
| 10GDC-M | Eectrolyte | Fuelcellmaterials | Calcined and milled |
| α-terpineol $C_{10}H_{18}O$ | Solvent | Sigma-Aldrich | - |
| Nuosperse FX9086 | Dispersant | Elementis Global | 1st dispersant, contains phosphor |
| BYK-P104 | Dispersant | BYK-Chemie | 2nd dispersant, contains silicon |
| Hypermer KD2 | Dispersant | Croda International | Final dispersant |
| Ethyl cellulose | Binder | Sigma-Aldrich | - |

For GDC electrolyte paste preparation, first the 10GDC-M powder is calcined at 1230 °C for 3 h in a closed alumina crucible. This is done to reduce the as-delivered surface area of 39 m²/g and to simultaneously increase the initial primary particle size of approximately 70 nm. Subsequent high-energy milling of the calcined powder in the aforementioned planetary ball mill (YSZ lined steel container, 15 cycles of 5 min milling + 25 min pause, 500 rpm in EtOH with < 1 mm YSZ grinding balls) adjusts the primary particle sizes and $d_{50}$ values to about 0.1 µm ± 0.03 µm. For preparing the pre-suspension, the specific surface area of the calcined and milled powder has to be analyzed. When fixing the amount of GDC powder to 75 wt% for the pre-suspension, the amount of dispersant Hypermer KD2 can be calculated using the powders specific surface area (SSA) and the fixed dispersant concentration of 0.013 g/m². The optimal concentration was determined via zero shear viscosity experiments (see Chapter 3.2.8). Figure 3.3 provides an overview of the recommended paste composition which includes the necessary calculations for dispersant and solvent content. The remainder of the 25 wt% will be composed of the solvent α-terpineol. Solvent, dispersant and GDC are homogenized using an ultrasonic bath for 30 min to form the pre-suspension. Afterwards, this suspension is mixed with the transport

suspension in a ratio of 87 : 13 wt%. The transport suspension itself consists of α-terpineol and ethyl cellulose 45 cp in a ratio of 85 : 15 wt%, which is prepared using a rotor-stator dispersing tool. After pre-mixing by hand, final paste homogenization was achieved by a three-roll mill utilizing the settings displayed in Table 3.3.

**Table 3.3:** Parameters for paste homogenization using a three-roll mill. Pastes are subjected to each setting for at least three passes.

| # | 1. Gap [µm] | 2. Gap [µm] | Line pressure [N/mm] | Speed [rpm] |
|---|---|---|---|---|
| 1 | 60 | 20 | - | 90 |
| 2 | 30 | 10 | - | 90 |
| 3 | 10 | 5 | - | 90 |
| 4 | 5 | - | 3.5 | 70 |

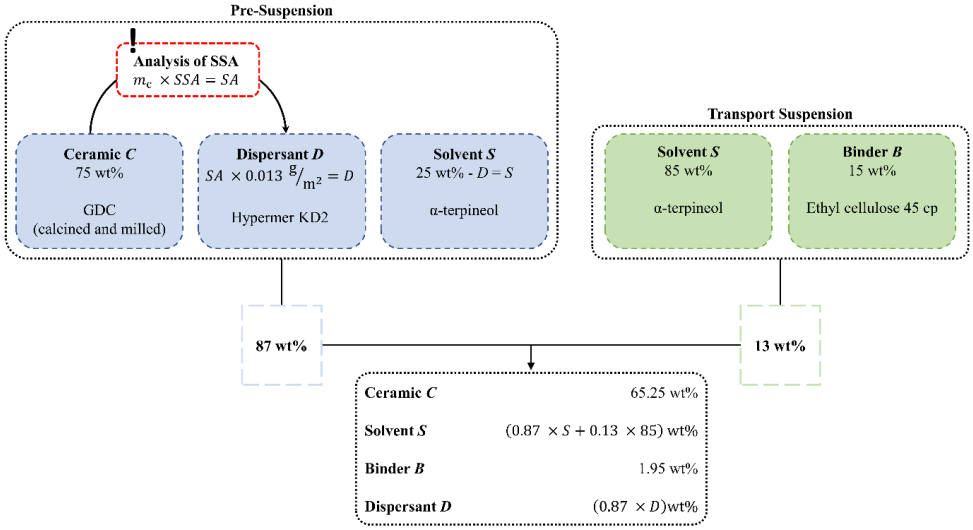


**Figure 3.3:** Overview of the recommended electrolyte paste composition made from 10GDC-M powder (Fuelcellmaterials), calcined at 1230 °C for 3 h and subsequently milled to a monomodal particle size distribution. No fixed values can be given for dispersant and solvent, as these components are dependent on the available ceramic surface area within the paste.

### NiO-GDC fuel electrode paste

The preparation of the NiO-GDC fuel electrode paste is similar to that of the GDC electrolyte paste. Here, GDC pre-suspension and NiO pre-suspensions are prepared separately. The composition of the GDC pre-suspension for the fuel electrode is identical to that of the electrolyte. The NiO pre-suspension is prepared using the same dispersant to mitigate the risk of unwanted effects on the GDC suspension. For this, NiO, α-terpineol and Hypermer KD2 are mixed in a ratio of 72 : 22.25 : 2.75 wt% respectively. GDC and NiO pre-suspensions are combined in a ratio of 55 : 45 wt% and homogenized using the planetary vacuum mixer at 1500 rpm for 1 min. Afterwards, a transport suspension containing 80 wt%

α-terpineol and 20 wt% ethyl cellulose 45 cp is added to the NiO-GDC pre-suspension in a ratio of 85 : 15 wt% (GDC-NiO : transport suspension). The paste is homogenized in the three-roll mill using the settings displayed in Table 3.3. Figure 3.4 provides an overview of the NiO-GDC fuel electrode paste composition. The resulting volume ratio of NiO to GDC is 45 : 55 %.

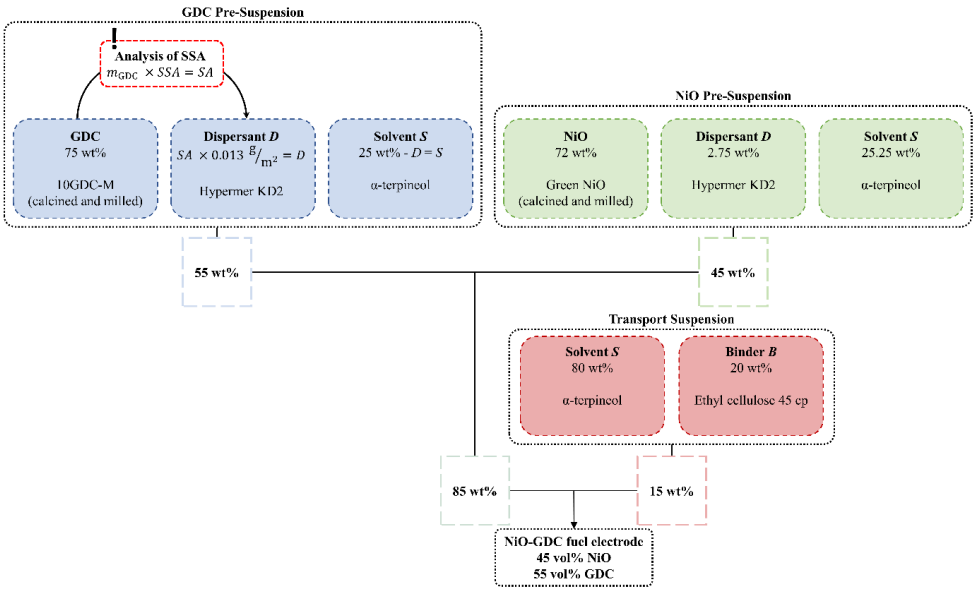


**Figure 3.4:** Overview of the fuel electrode paste composition made from 10GDC-M powder (Fuelcellmaterials), calcined at 1230 °C for 3 h and subsequently milled to a monomodal particle size distribution and untreated NiO (Vogler) powder. No fixed values can be given for dispersant and solvent for the GDC pre-suspension, as these components are dependent on the available ceramic surface area within the paste.

### 3.1.4 Physical vapor deposition (PVD) - Reactive magnetron sputtering

Reactive magnetron sputtering is a physical vapor deposition process used to produce thin films of compounds, such as oxides or nitrides. In this process, a solid target is bombarded with ions from a plasma. Typically, argon ions are used in sputter processes. The atoms or molecules knocked out of the target are then deposited as a thin film on a substrate, positioned opposite to the target. Unlike conventional sputtering, reactive magnetron sputtering involves feeding an additional reactive gas, like oxygen or nitrogen, into the process. This reactive gas then reacts with the sputtered material, either in the gas phase or on the substrate surface. A central element of this process is the magnetron, which is a magnetic field system located behind the target. Here, the permanent or electro-magnets generate a transverse magnetic field parallel to the target surface. This magnetic field forces electrons into spiral-like paths, extending their time near the target surface. As this increases the probability of impact ionization, the formation of a denser plasma in the vicinity of the target is promoted. This allows for a higher sputter rate at lower working pressures compared to other sputtering methods. For magnetron

sputtering, vacuum chambers are usually operated at pressures of below $10^{-2}$ mbar (100 Pa). A high vacuum is necessary to minimize contamination and ensure stable plasma conditions. Furthermore, it allows the sputtered particles to move in a direct manner, which positively influences the homogeneity of the deposited layers. Usually, magnetron sputtering is a line-of-sight based deposition process. Due to their kinetic energy, the sputtering particles mostly follow straight paths. However, scattering by residual gas atoms, especially at higher pressure, can be significant enough for particles to be able to reach deeper substrate areas. Another critical aspect of reactive sputtering is target poisoning, wherein an unwanted reaction layer forms on the target surface. This alters the conductivity and sputtering properties of the target, which can negatively affect process stability and reproducibility. Therefore, precise control of the gas flows and suitable process control are crucial for the quality of the resulting layers [134]. In this work, GDC and YSZ layers for the 3-layer electrolyte were produced from metallic targets using reactive magnetron sputtering (CS400ES cluster system, Von Ardenne Anlagentechnik GmbH, Germany). Prior to each sputtering process, the cells were cleaned with ethanol and subjected to an etching process to remove unwanted species from the surface. The main differences between the coating parameters for these two materials lie in the oxygen flow rates and the DC bias. An $O_2$-flow rate of 4 sccm was used to produce YSZ layers with the correct crystal structure. For the GDC layer, a flow rate twice as high was used. While no additional DC bias was applied to the substrate during the production of the GDC layer, the DC bias during sputtering of the YSZ layer was set to 150 W. The substrate temperature for both processes was 800 °C. A detailed list of the relevant process parameters is shown in Table 3.4.

**Table 3.4:** Overview of the process parameters used for the production of YSZ and GDC layers using reactive magnetron sputtering.

| | YSZ | GDC |
|---|---|---|
| Base pressure (mbar) | $5.3 \times 10^{-8}$ | $5.3 \times 10^{-8}$ |
| Process pressure (mbar) | $6.0 \times 10^{-3}$ | $6.0 \times 10^{-3}$ |
| Ar flow rate (sccm) | 30 | 30 |
| $O_2$ flow rate (sccm) | 4 | 8 |
| Process energy (Wh) | 750 | 700 |
| Power (W) | 250 | 500 |
| DC bias (W) | 150 | - |
| Temperature (°C) | 800 | 800 |

### 3.1.5 Dry pressing

Dry pressing is a straightforward method of forming simple and compact green bodies from ceramic powders. In axial pressing, a dry powder is placed in a die and compressed with a force applied by two

punches. In uniaxial pressing, the movement is restricted to the upper punch, while in biaxial pressing, both the upper and lower punch are utilized for compaction. The achievable density of the green body depends on factors such as particle size distribution and morphology, the bulk or tapped density, the applied force, the duration of action and the type of pressing process that is used. Typically, green densities of up to approximately 60 % of the theoretical density can be achieved through axial pressing. However, depending on the method, density gradients can also occur within the green body, which sometimes still remain after sintering. In principle, isostatic pressing is the only dry pressing method that can produce ceramic bodies without density gradients. In this process, pre-compacted pellets are hermetically sealed within flexible membranes and placed in a chamber filled with hydraulic fluid. In this pressure chamber, a force or pressure is transferred onto the sample simultaneously from all directions by the fluid, resulting in a homogeneous density distribution. Because of this, densities of isostatically pressed bodies typically exceed the densities of axially pressed pellets. If there is no additional heat applied to the sample during the pressing process, this method can also be referred to cold-isostatic pressing [135 - 136]. Figure 3.5 illustrates the different pressing methods and the resulting density distributions.

In this work, dry pressing was used to prepare both 8YSZ and 10GDC samples for various analysis techniques. Uniaxial pressing of 8 mm pellets was used for dilatometric measurements. Unfortunately, due to the small sample diameter, subsequent cold-isostatic pressing of these samples was not possible. For mechanical testing at IMD-1, 20 mm and 40 mm pellets were prepared, depending on the subsequent measurement technique. Here, both uniaxial and isostatic pressing were utilized to investigate the influence of residual porosity. For powder x-ray diffraction, pellets of different sizes were uniaxially pressed to enable sintering. To increase the surface quality, 0.5 % stearic acid was used as a lubricant. Glycerin was only used as a binder for YSZ pellets with a diameter of 40 mm, to facilitate demolding and subsequent handling. However, isostatic pressing of these samples always resulted in a warpage. Therefore, 40 mm YSZ pellets for impulse excitation testing are only available as uniaxially pressed samples. In each uniaxial pressing process, the powder is first subjected to a lower force for one minute to pre-compact it. After the force is removed and potentially entrapped air has been released from the die and sample, the pellet is again subjected to the intended maximum force for two minutes. After the pressing process the force should be reduced gradually over an extended period of time to minimize elastic recovery effects that could lead to cracking of the sample. For clarification, an overview of the pressing parameters for the different sample types are listed in Table 3.5.

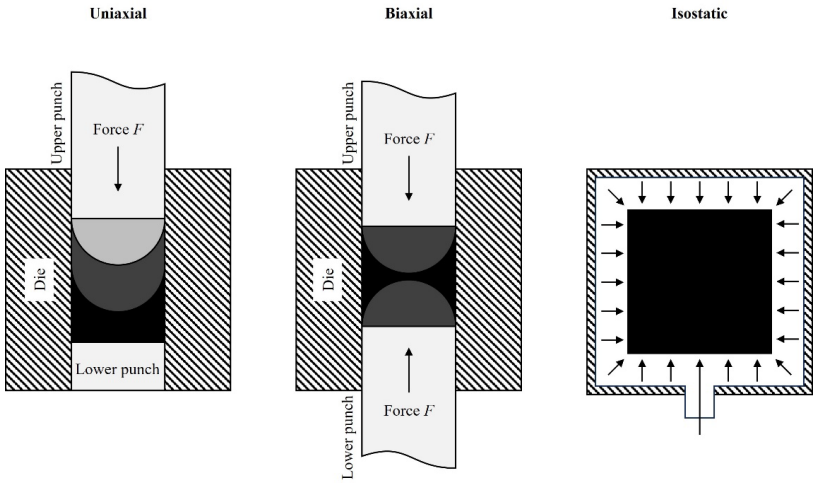


**Figure 3.5:** Schematic representation of uniaxial, biaxial and isostatic pressing. Density gradients are indicated by grayscale differences.

**Table 3.5:** Overview of pellet production parameters for various analysis methods at IMD-1 and IMD-2.

| Analysis Method | Die Ø [mm] | Force 1 [kN] | Force 2 [kN] | Cold-isostatic pressing | | Weight [g] |
|---|---|---|---|---|---|---|
| | | | | Pressure [MPa] | Time [min] | |
| Dilatometry | 8 | 5 | 7 | - | - | ~ 1 |
| XRD | 16 | 10 | 13 | - | - | ~ 2 |
| Vickers, Instrumented Indentation Testing | 20 | 15 | 25 | 300 | 2 | ~ 3 |
| Impulse Excitation | 40 | 30 | 45 | 300 | 2 | ~ 15 |

Instrumented indentation testing at IMD-1 was used to determine the Young's modulus of 10GDC and 8YSZ pellets after exposure to reducing ($10^{-22.5}$ bar < $p_{O2}$ < $10^{-19}$ bar) or oxidizing (air) heat treatments at 700 °C for 2 h. Additionally, the fracture toughness of these materials was determined using Vickers and, in some cases, micropillar indentation testing. To determine the Young's modulus at temperatures up to 800°C under oxidizing and reducing conditions, impulse excitation was used. For this, the samples had to be of a certain weight, which necessitated the use of 15 g of powder.

### 3.1.6 Calcination and sintering

Every ceramic manufacturing process necessarily includes sintering as a consolidation step. Sintering is a thermal process in which pre-compacted powders, formed into green bodies, are converted into more or less dense, mechanically stable ceramic bodies. The driving force behind sintering is the reduction of the total free energy of the system. This primarily includes the minimization of the surface area of particles and the minimization of the interfacial energy between individual particles as well as particles and pores. To achieve this, material diffusion occurs at or through interfaces to reduce the size of pores and to allow particles to grow together and subsequently increase their grain size. In principle, these mechanisms take place in three differentiable phases during solid-state sintering. In the initial phase, sintering necks are formed between neighboring particles to minimize the differences in surface curvature between particles. This does not result in significant volume shrinkage and typically only increases the body's relative density by 5 %. Material transport happens via surface diffusion, volume diffusion and evaporation-condensation reactions. In the second phase or intermediate stage, the microstructure initially contains a connected pore network that is typically located at the grain boundaries. These begin to shrink by means of material transport to these grain boundaries, which facilitates the highest amount of densification during the entire sintering process. Here, pores are assumed to reduce their diameter until they pinch off and become isolated. At the end of this intermediate stage, the ceramic body has already reached approximately 90 % of its theoretical density. In the final stage of sintering, most of the pores are closed and located either at grain boundaries or grain triple points. The further increase in density now occurs mainly through material transport along the grain boundaries, whereby the remaining pores are reduced in size or eliminated. At the same time, grain growth now begins to dominate the process as the main mechanism. Here, the reduction of grain boundary energy is the driving force. In what is known as Ostwald ripening, matter diffuses across the grain boundaries from smaller grains to larger grains. Accordingly, larger grains grow in favor of smaller grains. A central challenge of this stage is that, in principle, grain growth acts opposite to densification. If grains start to grow too quickly, pores can become entrapped within them. Such isolated pores cannot shrink any further as they lack contact with the grain boundary and the diffusion path required for material transport is therefore interrupted. In addition, abnormal grain growth can occur during this final stage if the process is not well controlled. This leads to a heterogenous microstructure, where few grains grow significantly faster than others. This results in a reduced mechanical stability and lower conductivity of the sintered body. Targeted process control is therefore essential to achieve a high final density with low residual porosity and controlled grain sizes. For example, strategies to prevent incomplete densification or abnormal grain growth include a reduction in sintering temperature with longer holding times and the use of sintering aids that control diffusion paths or restrict grain growth. Another procedure that can drastically alter the sintering process is the calcination of the ceramic powder, prior to the manufacturing and subsequent sintering. As calcination usually leads to a reduction in the specific surface area and to a certain degree of grain growth, the sintering reactivity is reduced.

The advantage of this is that the subsequent sintering of the green body happens more slowly and more controlled, which can prevent abnormal grain growth or early pore inclusion. Coarsening and homogenization of particle sizes can also facilitate shaping processes and increase reproducibility. Additionally, in layered systems, such as investigated in this work, it is essential to align the sintering behavior of the individual layers to one another to minimize effects of differential sintering. Differential sintering is another critical challenge during the sintering process of multilayer ceramics, which is caused by incompatible sintering kinetics between layers. It can lead to bending, residual stresses, delamination or cracking [137, 138].
In this work, the GDC starting powder for the electrolyte and fuel electrode was therefore pre-calcined at different temperatures. Calcination and sintering were carried out using conventional electric furnaces equipped with $MoSi_2$ heating elements.

## 3.2 Characterization methods

### 3.2.1 Particle size distribution analysis

In ceramic processing, regardless of the employed fabrication technique, the particle size of a ceramic powder significantly influences its processability, microstructure after sintering, the material's properties and the overall quality of the final product. A comprehensive understanding and control over the particle size distribution (PSD) cannot only ensure higher reproducibility but also facilitate optimized sintering, enhanced processing and potentially superior properties. Therefore, the particle size distributions of all powders used in this thesis were analyzed by means of static light scattering. This analysis technique uses intensity patterns produced by a monochromatic laser passing through a particle dispersion. In general, there are two different methods for analyzing data. The Fraunhofer method proposes that the angle of the laser beam is inversely proportional to the particle size, while the intensity of the scattered light is directly proportional. Only diffraction occurring at the edges of a particle is considered. Consequently, this method should only be applied to samples where the particle diameter is expected to be significantly larger than the laser wavelength. This limitation does not apply to Mie theory analysis. The reason is that this method considers not only diffraction, but also reflection, absorption and refraction of the electromagnetic wave. Therefore, to analyze the data using Mie theory, the complex refractive index of the material must be known. This can be a disadvantage when analyzing powder mixtures of different materials [139, 140]. Since the expected particle sizes of the powders used in this thesis are in the submicron range (~ 100 nm), all powders were analyzed using the Mie theory. PSDs were measured with the Horiba LA 950 (HORIBA Europe GmbH, Germany) particle size measuring instrument. All powders are being dispersed in ethanol and sonicated for at least 3 minutes before each measurement to break loose agglomerates. With this device, particle sizes from single digit nanometers up to 3 mm can be measured with an accuracy of 0.6 %.

Typically, PSDs are presented using $d_{10}$, $d_{50}$ and $d_{90}$ values of the distribution. These values refer to the particle diameters that fall below the 10$^{th}$, 50$^{th}$ and 90$^{th}$ percentile of the distribution, respectively. However, while these metrics are useful for summarizing the range of particle sizes, they offer limited insight into the overall shape of the distribution. This lack of detail poses challenges when trying to investigate and quantify the influence of the PSD on the aforementioned aspects of ceramic processing. Therefore, in this thesis, Sarle's bimodality coefficient $\varphi$ according to Equation (*3.1*) was additionally calculated from the distributions of each powder [141].

$$\varphi = \frac{\gamma_1^2 + 1}{\gamma_2 + \frac{3(n-1)^2}{(n-2)(n-3)}} \tag{3.1}$$

This coefficient considers skewness $\gamma_1$ according to Equation (*3.2*) and excess kurtosis $\gamma_2$ of a distribution according to Equation (*3.3*).

$$\gamma_1 = \frac{n}{(n-1)(n-2)} \sum_{i=1}^{n} \left( \frac{x_i - \bar{x}}{s} \right)^3 \tag{3.2}$$

$$\gamma_2 = \frac{n(n+1)}{(n-1)(n-2)(n-3)} \sum_{i=1}^{n} \left( \frac{x_i - \bar{x}}{s} \right)^4 - \frac{3(n-1)^2}{(n-2)(n-3)} \tag{3.3}$$

Where $x_i$ is the observed value and $\bar{x}$ the arithmetic mean, $s$ is the standard deviation and $n$ is the sample size. In order to better estimate the kurtosis of the distribution, the excess is considered here, which compares the kurtosis of the distribution with the kurtosis of the normal distribution, expressed by the subtraction of the last term. Values of $\varphi$ range between 0 and 1, whereby a monomodal distribution can be assumed up to a value of approximately 0.55. Values above 0.55 indicate a bimodal distribution. As visualized in Figure 3.6, positive values for skewness indicate a right-skewed (or left-leaning distribution), which would likely occur with powders milled from larger particle sizes (top-down

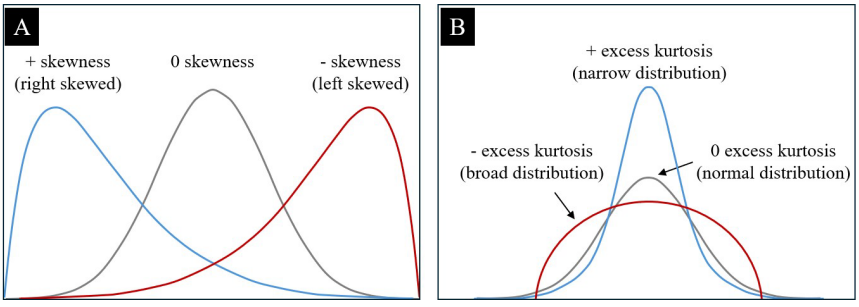


**Figure 3.6:** Schematic illustration of positive and negative skewness in comparison to a normal distribution (**A**) and positive and negative excess kurtosis in reference to a normal distribution (**B**).

processing). Similarly, positive values for excess kurtosis indicate narrow distributions with long tails to both sides, whereas negative values hint toward broad distributions with short tails. Another visual illustration showing the range of values that these parameters can take is included in the appendix.

### 3.2.2 Specific surface area analysis

Similar to the particle size distribution, the specific surface area (SSA) is a vital powder characteristic, one that must be considered when using powders in suspension-based manufacturing processes. In this thesis, the specific surface area was determined using a gas adsorption technique. The specific method employed here, the BET (Brunauer, Emmett and Teller) method, is based on the phenomenon of physisorption of an inert gas on a material's surface. It is based on quantifying the adsorption of gas molecules as a function of partial pressure. First, a monolayer is adsorbed, followed by multilayer adsorption processes as the partial pressure increases. The relevant evaluation range is typically between 0.05 and 0.35 relative pressure, for which the BET equation describes a linear relationship. Using this equation, the volume of the monolayer can be determined. Then, knowing the size of the adsorbed molecule, the specific surface area of the material can be calculated. The amount of gas adsorbed is usually determined volumetrically by measuring the pressure in a closed system. The pressure difference before and after adsorption is then converted into a gas volume using the ideal gas law. Alternatively, a gravimetric measurement can be performed by measuring the sample's weight gain [142].
The device used in this study (Area Meter II, Juwe Laborgeräte, Germany) uses nitrogen at a temperature of 77 K for the measurement. Prior to each measurement other species already present on the material surface are desorbed by applying a vacuum at elevated temperatures.

### 3.2.3 Dilatometric measurements

Two different types of dilatometric measurements were carried out in this thesis to gain further understanding of the sintering behavior of the investigated materials on their own and the influence of interactions between these materials during half-cell co-sintering. In the following, both techniques will be explained briefly.
Dilatometric measurements of pure materials were carried out using a NETZSCH DIL 402 Expedis Classic dilatometer (Erich Netzsch B.V. & Co. Holding KG, Germany). Here, the change in height of a sample gets recorded dependent on given temperature profiles. Generally, samples were analyzed using the standard sintering profile for the half-cell co-sintering. This temperature profile entails a heating rate of 3 K/min up to 1400 °C. After a dwelling time of 5 h, samples were cooled down with a controlled rate of 5 K/min. Additionally, samples were also analyzed utilizing a continuous heating profile. Here, samples were submitted to a heating rate of 5 K/min until a certain dilatation threshold of the device settings was reached, with no set temperature limit. Reaching this threshold could indicate that the material began to soften, to melt or to decompose in a way, that the transmission rods lost sufficient

contact to the specimen. This procedure provides more broad information about sintering behavior [143, 144].

### 3.2.4 X-ray diffraction and residual stress measurements

X-ray diffraction (XRD) is an analytical method used to determine various crystallographic properties of solid materials. For example, information about the general crystallographic structure, lattice parameters, phase identity and phase purity can be obtained. XRD is based on the interaction of X-rays with the periodically arranged atoms of a crystalline material. Monochromatic X-rays are diffracted at these atomic lattice planes and under certain geometric conditions, this diffraction leads to interference phenomena. Constructive interference occurs when the wavefronts reflected by neighboring lattice planes are in phase. This occurs when the phase difference corresponds to an integer multiple $n$ of the radiation wavelength. Mathematically, this principle is described by Bragg's law according to Equation (*3.4)*:

$$n\lambda = 2d \cdot \sin\theta \tag{3.4}$$

Here, $\lambda$ denotes the wavelength of the incident X-rays, $d$ denotes the distance between two neighboring lattice planes and $\theta$ denotes the angle of incidence of the X-rays relative to the lattice plane. When this equation is satisfied, the reflected rays superimpose constructively, resulting in diffraction maximums. Combining all diffraction maximums generates a characteristic diffraction pattern of the crystalline structure. The positions and intensities of the maxima allow conclusions to be drawn about the lattice structure and potential lattice distortions. Since lattice parameters are characteristic of a given crystalline phase, X-ray diffraction enables reliable identification and quantification of crystal phases, for example, in multi-component systems within a detection limit of approximately 1 wt%.

Furthermore, residual stresses in a material can be determined using X-ray diffractometry. Residual stresses in materials cause the lattice spacing $d$ of the material to change, shifting the measured diffraction angle. By comparing this to the stress-free lattice spacing, the direction-dependent strain can be determined. Stress values can be calculated from this strain using the E-modulus of the material. In principle, the $\sin^2\Psi$ method or the omega-stress method can be used to analyze residual stresses, both of which were used in this work. The $\sin^2\Psi$ method is more traditional. Here, the sample is systematically tilted by an angle $\Psi$ which is relative to the normal of the sample surface. For each tilt, the diffraction angle $2\theta$ is measured. The strain calculated from the angle displacement is plotted against the value of $\sin^2\Psi$. In a stress-free state, the diffraction angle would remain constant regardless of the tilt angle $\Psi$ while a linear dependence of the lattice strain on $\sin^2\Psi$ would indicate residual stress. The slope of the resulting straight line is directly proportional to the normal stress in the investigated direction. This method is particularly well-suited for flat, planar samples with an isotropic or non-textured structure. However, only stresses very close to the surface can be investigated here. The omega-

stress method, on the other hand, is advantageous for investigating curved or very sensitive samples as it does not require any tilting of the sample, which in turn also reduces geometrically induced errors. With this method, rather than tilting the sample, the angle of incidence $\omega$ of the X-rays is varied. As the diffraction conditions change with the angle of incidence, the effective measurement depth varies as well. This makes it possible to detect stress gradients close to the surface.
Depending on the analysis method used, different measurement geometries are employed. For investigations using the $\sin^2\Psi$ method, the Bragg-Brentano geometry is typically used. In this geometry the sample is fixed in the center of a focusing circle. The X-ray source and the detector move symmetrically around the sample along this circle, with the angle of incidence $\theta$ and the detector angle $2\theta$ set. However, this geometry is sensitive to height errors and as previously mentioned requires flat samples with smooth surfaces. In contrast, the parallel beam geometry uses optics to generate an almost parallel X-ray beam that is collimated to very small angles. This geometry is less susceptible to surface irregularities or height errors, allowing precise measurements on curved samples with rough surfaces. In combination with the omega-stress method, the parallel beam geometry has clear advantages, particularly when measuring small sample areas or investigating stress gradients. However, with this geometry, beam intensities tend to be lower and complex optic setups are necessary for collimating the beam [145 - 147].

For general phase analysis and determination of lattice constants, the D4 Endeavor diffractometer (Bruker AXS GmbH, Germany) equipped with a Cu-K$\alpha$ radiation source was used. The measurements were carried out in the Bragg-Brentano geometry at room temperature. Residual stress measurements in Bragg-Brentano geometry using $\sin^2\Psi$ method were conducted by Dr. Yoo Jung Sohn (IMD-2) on the Empyrean diffractometer (Malvern Panalytical Ltd., Great Britain). Similarly, residual stress measurements in parallel beam geometry using omega-stress method were carried out by Mirko Ziegner (IMD-1) at the Empyrean diffractometer located in IMD-1. Both diffractometers were equipped with a Cu anode X-ray tube, operated at 45 kV / 40 mA ($\sin^2\Psi$ method) and 45 kV / 45 mA (omega-stress method). For the parallel beam configuration, a parallel plate collimator of 0.18° was used.
For data analysis, the HighScore Software (Malvern Panalytical B.V., the Netherlands) was employed using the Inorganic Crystal Structure Database (ICSD) from FIZ Karlsruhe – Leibniz Institute for Information Infrastructure and Rietveld refinement and residual stress analysis was done using the TOPAS V 4.2 software (Bruker AXS GmbH, Germany).

### 3.2.5 Scanning electron microscopy and energy dispersive X-ray spectroscopy

Scanning electron microscopy (SEM) is an imaging technique, predominantly used for microstructural examination and characterization of solid materials. Depending on the available detectors, qualitative information about the chemical composition of the material can additionally be obtained. In this type of

microscopy, electrons instead of light are used to generate the image. Here, electrons are emitted from an electron source in a high vacuum and accelerated by an electric field, with acceleration voltages usually ranging between 5 kV and 30 kV. The resulting electron beam is then focused using various magnetic lenses and optical components and subsequently used to scan the sample surface. Upon hitting the sample surface, these electrons begin to interact with the sample and different signals are generated. For example, weakly bound electrons can be knocked out of the outer shells of the sample's atoms. These are then referred to as secondary electrons (SE) with a low energy of only about 50 eV. Because of this, only secondary electrons emitted from close to the sample surface can reach the detector. Accordingly, information about the surface structure and topography of the sample are obtained. Furthermore, the primary electrons of the electron beam can also be scattered at the atomic nuclei within the sample. As a result, these electrons retain most of their energy. These so-called backscattered electrons (BSE) usually originate from deeper areas of the sample. The number of backscattered electrons depends on the weight, i.e. the atomic number, of the element. The higher atomic number, the more electrons are scattered. Detection of these signals generates images with a high material contrast in which heavier elements appear brighter, providing initial information about the chemical composition of the sample. More detailed information about the chemical composition and precise identification of the chemical elements present can be obtained by detecting characteristic X-rays. This radiation is emitted from the sample when an electron gets knocked out of one of the inner atomic shells and is replaced by an electron from one of the outer shells. The change in energy level of the second electron causes the emission of a discrete energy amount that is characteristic of each element. This type of analysis is called energy dispersive X-ray spectroscopy (EDS or EDX). Although this allows the respective element to be identified, no conclusions can be drawn about the state of oxidation or potential bonding with neighboring atoms. The energy of this radiation is in the kV range and can be detected from a depth of several µm within the sample [148, 149]. Figure 3.7 schematically summarizes the relevant types of radiation that are emitted during scanning electron microscopy, which were analyzed in this work. Additionally, the respective interaction volume within the sample is indicated.

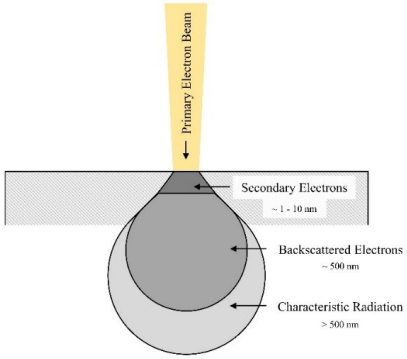


**Figure 3.7:** Illustration of the relevant types of radiation emitted during scanning electron microscopy with their respective interaction volume indicated.

In this work, powders, fractured cross-sections, polished cross-sections and surfaces of half and full cells were analyzed by scanning electron microscopy. Own analyses were performed using the tabletop devices TM3000 (Hitachi High-Technologies Corporation, Japan) equipped with a BSE and EDS detector and the EM-30N (COXEM CO., LTD, South Korea) equipped with SE and BSE detectors. In addition, high resolution micrographs were taken by Dr. Doris Sebold (IMD-2) with the Zeiss Ultra 44 Gemini 450 (Carl Zeiss AG, Germany). The analyses were carried out using SE, BSE, EDS and InLens detectors. Since InLens detectors, unlike SE detectors, are not located laterally below the objective but inside the electron column directly above the sample, it is possible to generate even higher resolution images of the surface properties of a sample, especially of powders when using lower acceleration voltages. Furthermore, within the scope of the project, Luzie Wehner (IMD-1) generated 3D-reconstructions of full cells. For this, roughly 200 to 300 images were taken of each cell using a BSE detector. The cells were cut by a Focused Ion Beam (FIB) (Helios 5 CXe, Thermo Fischer Scientific, USA) at a beam current of 1 nA and an acceleration voltage of 30 kV. The SEM examination was performed on a ZEISS Merlin (Carl Zeiss GmbH, Germany) and an Apreo 2 C (Thermo Fischer Scientific, USA). The Avizo software version 2023.1.1 (Thermo Fischer Scientific, USA) was used for the reconstruction of the structure. For more detailed information on the process of cutting and segmentation, please refer to the dissertation of Luzie Wehner.

### 3.2.6 Laser microscopy

In this work, laser microscopy was used to examine the surface properties of produced solid oxide cell layers. Defects and grain sizes were analyzed. The confocal laser microscope Keyence Color 3D Laser Scanning Microscope VK-9710 (Keyence Corporation, Japan) used for this purpose also allows the

investigation of surface topographies and surface roughness. For this, the laser microscope is equipped with a white light source and a laser source, the latter being used to gather height information. When measuring the surface texture, the sample is scanned along the three spatial directions. The intensity of the reflected light is measured by a detector. Since this is a confocal laser microscope, only the light that is reflected from the current focal point reaches the detector, providing height and depth information.

### 3.2.7 Surface topography, cell and layer dimensions

In this work, the CT 300T optical inspection system (cyberTECHNOLOGIES GmbH, Germany), equipped with various chromatic white light sensors was used to evaluate surface topography and curvature of sintered half-cells. Furthermore, layer thickness and dimensions of dried screen-printed layers were measured. This optical inspection system is a white light interference profilometer, which can perform high resolution 3D surface measurements without touching the sample surface. In this analysis technique, an interferometer is used to split broadband white light into two partial beams. One of which hits a reference surface, while the other scans the sample surface. After these beams are reflected back to the detector, both beams are recombined and superimposed. Due to the short coherence length of white light, interference can only occur if the height of the sample surface corresponds exactly to that of the reference surface. In order to determine the exact height value for each point on the surface, the sensor system is moved along the vertical axis. During this movement, the system records the point maximum interference intensity for each position on the sample surface. This then corresponds to the height of the section examined at that moment.

Depending on the extent of curvature, either a DHS 10000, DHS 3000 or DHS 1000 sensor is used to measure the camber of sintered half-cells. For this, a predefined measurement program, which is also used in the standard production of SOCs in IMD-2 is used.

To obtain information about the height and area of printed and dried layers, a differential scanning method was used that was firstly introduced in a publication by Mücke et al. For this, the DRS-500 triangulation laser sensor with a 125 nm vertical resolution and a spot size of 16 to 23 µm was used. First, layers were printed on 50 x 50 x 1.5 mm stainless steel substrates and scanned using the optical inspection system. Afterwards, the substrates were cleaned, dried and measured again. The measurement data of the clean substrates is then subtracted from their corresponding layer measurement to obtain the differential data set of the isolated layer. With this, potential error sources like substrate unevenness or scratches are accounted for [150]. Two parameters are introduced in order to evaluate the printed layers. These parameters are the layer thickness of the dried layer $d_{dry}$ and the fidelity factor $F_{PE}$, which quantifies the accuracy of the printed image. According to Equation (*3.5)* and Figure 3.8 the fidelity factor is calculated from the ratio of the screen opening edge length $X$s to the edge length of the print image $X_P$. Here, a higher value would indicate higher dimensional accuracy.

$$F_{PE} = \frac{X_S}{X_P} \times 100 \tag{3.5}$$

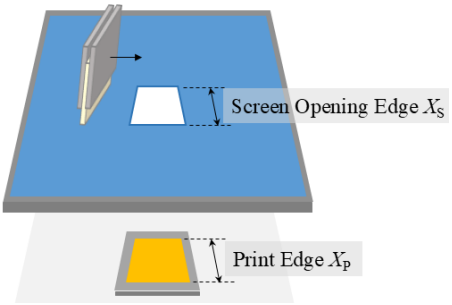


**Figure 3.8:** Graphical representation of the parameters for calculating the fidelity factor $F_{PE}$. Screen with screen opening at the top and a substrate with a printed image below.

### 3.2.8 Rheological characterization methods

**Fundamentals & methodology**

Rheology is the scientific discipline that examines the flow and deformation behavior of materials under the influence of external forces. This science field encompasses the examination of how a substance or body responds to a specific load and how to describe, quantify and elucidate its response. It uses theories of continuum mechanics and derives the laws needed for this from the molecular structure as well as the micro- and nanostructure of different materials, especially in multi-phase systems. As an interdisciplinary science, rheology is closely related to physics, physical chemistry and materials science. Within the framework of rheology, a range of models has been developed to elucidate the behavior of diverse material classes [151]. In the following, some of these concepts will be explained that will later enable the interpretation of the paste behavior and its potential consequences.

To understand the basics of rheology, the fundamental concept of viscosity $\eta$ is crucial. In essence, viscosity quantifies the resistance of a substance to flow. In purely mathematical terms, viscosity can be described using the two-plate model which is displayed in Figure 3.9. Here, a fluid is placed in-between two perfectly parallel plates [152].

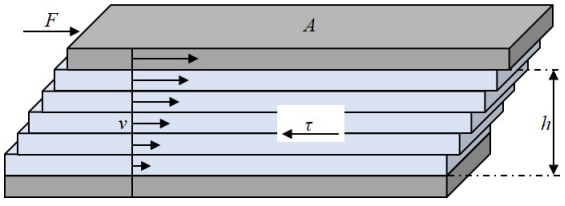


**Figure 3.9:** Two-plate model describing shear experiments in rheology. Figure adapted from [157].

As a force *F* is moving the upper plate to the side, the fluid underneath is subjected to a stress parallel to its surface. This shear stress $\tau$ acts within the fluid and is calculated according to Equation (*3.6)* by dividing the applied force by the area of the moving plate.

$$\tau = \frac{F}{A} \qquad \left[\mathrm{Pa} = \frac{\mathrm{N}}{\mathrm{m}^2}\right] \tag{3.6}$$

For this to hold true, however, the fluid and the plate need to be in firm contact and no slipping of the fluid at the plate interface occurs. Similarly, the induced flow of the fluid needs to be laminar without the presence of turbulences. This laminar flow can be described as infinitesimally thin layers of the fluid which are moving quasi-independently at different speeds. The observed spatial change in flow velocity can be expressed by the shear rate $\dot{\gamma}$ and is calculated by dividing the velocity *v* of the upper plate by the distance *h* between the two plates (see Equation (*3.7)*).

$$\dot{\gamma} = \frac{dv}{dh} \qquad \left[\mathrm{s}^{-1} = \frac{\mathrm{m/s}}{\mathrm{m}}\right] \tag{3.7}$$

Using these two parameters, shear stress and shear rate, the viscosity can be calculated according to Equation (*3.8)*. This relationship applies only to ideally viscous fluids, also known as Newtonian fluids. Here the viscosity is independent of the applied force and does not change with shear rate.

$$\eta = \frac{\tau}{\dot{\gamma}} \qquad \left[\mathrm{Pas} = \frac{\mathrm{Pa}}{\mathrm{s}^{-1}}\right] \tag{3.8}$$

However, many technically relevant fluids, like screen-printing pastes, are non-Newtonian. This means that the viscosity depends on the shear rate applied to the fluid but also on time. Examples of non-Newtonian behavior include pseudoplasticity, dilatancy, thixotropy and rheopexy. Pseudoplasticity, also known as shear thinning, means that the viscosity of a fluid decreases as the shear rate increases. Dilatancy, on the other hand, is characterized by an increase in viscosity as the shear rate increases. The time-dependent behavior of fluids with respect to the duration of the applied load is characterized as thixotropy or rheopexy. Screen-printing pastes exhibit thixotropic behavior, meaning that under prolonged and constant shear, the viscosity decreases with time. In contrast, rheopexy, a less common phenomenon, manifests as an increase in viscosity over time in response to constant shear [153 - 155]. Although viscosity is fundamentally determined by the internal structure of a material, it is not a material-specific property. Even for Newtonian fluids, viscosity is always dependent on ambient parameters such as temperature and pressure. The viscosity of non-Newtonian fluids is also influenced by the applied load, as previously mentioned. This includes the duration of the applied load, its magnitude and the general nature of the load. Typically, viscosity and viscosity curves are used to

evaluate screen printing pastes. However, due to the limitations described above and the complexity of the screen-printing process as described in Chapter 2.1.3, viscosity has only a very limited significance. In general, they can be used to characterize the simplified flow behavior of pastes, even though the results are difficult to transfer to the screen-printing process. Furthermore, within certain limitations, qualitative and comparative statements can be drawn regarding dispersion quality. This is particularly beneficial for suspensions made with non-polar solvents, as conventional methods like zeta potential (ζ-potential) measurements for the assessment are not accessible in these cases. The theory behind this is that a well-dispersed particle suspension exhibits a lower viscosity at very low shear rates than a poorly dispersed suspension. Here it is assumed, that agglomeration of particles entraps free solvent, thus reducing the flowability of the suspension and increasing the internal resistance to flow, i.e., the viscosity. Therefore, for this particular experimental configuration, it is essential to employ low shear rates during the excitation process. This is due to the fact that high shear rates may potentially cause agglomerates to break down, thereby interfering with the dispersion state of the suspension and obscuring the desired information. However, despite its justified field of application, previous studies have already shown that viscosity on its own is not sufficient to adequately describe the behavior and quality of pastes for screen printing. Instead, it was established that their viscoelastic properties have a much more significant influence on the printing result [156].

To obtain information about the viscoelasticity of a material, testing using harmonic oscillation can be carried out. This method enables the distinction between the viscous and elastic material behavior. For this, the sample is excited with a harmonic oscillation or sinusoidal strain as expressed in Equation (*3.9)* [157].

$$\gamma(t) = \hat{\gamma}\cos(\omega t) \tag{3.9}$$

Here, $\hat{\gamma}$ is the strain amplitude and $\omega$ the angular frequency of the oscillation. If the material exhibits purely elastic behavior, the stress response of the sample is instantaneous and follows the same phase.

$$\tau(t) = G\hat{\gamma}\cos(\omega t)$$

or as expressed in its equivalent exponential form:

$$\tau(t) = G\hat{\gamma}e^{i\omega t} \tag{3.10}$$

Here, $G$ is the shear modulus or modulus of rigidity and denotes the relationship between shear stress and shear strain. For a Hookean elastic solid where stress is directly proportional to strain, this modulus is constant. This indicates that energy applied by an external force is stored entirely within the material. Conversely, a purely viscous material demonstrates a response wherein the stress is directly proportional

to the strain rate (shear rate), as opposed to the deformation, as previously outlined in Equation (*3.6)*. For harmonic oscillations, this results in a shear rate function according to Equation (*3.11)* as the derivative of Equation (*3.9)*.

$$\dot{\gamma}(t) = -\hat{\gamma}\omega \sin(\omega t)$$

or as expressed in its equivalent exponential form:

$$\dot{\gamma}(t) = i\omega\hat{\gamma}e^{i\omega t} \tag{3.11}$$

When substituting the shear rate in the stress equation with the shear rate of a harmonic oscillation the following term is obtained.

$$\tau = \eta\, i\omega\hat{\gamma}e^{i\omega t} \tag{3.12}$$

This indicates that for purely viscous materials stress is 90° out of phase from strain, meaning that energy dissipates completely within the material. However, in viscoelastic materials such as screen-printing pastes, viscous and elastic behavior is combined. In such cases, the phase lag or phase shift is typically denoted by $\delta$. The relationship between stress and strain in these material categories is expressed in Figure 3.10. The excitation response of a viscoelastic material can be divided into these two components due to the clearly distinguishable response of viscous and elastic parts. These disparate responses are represented within the storage modulus $G'$ for elastic behavior and the loss modulus $G''$ for viscous behavior according to Equation (*3.13)*.

$$\tau(t) = G'\hat{\gamma}\cos(\omega t) + G''\hat{\gamma}\sin(\omega t)$$

with storage modulus $G'$

$$G' = \frac{\hat{\tau}}{\hat{\gamma}}\cos\delta$$

and loss modulus $G''$

$$G'' = \frac{\hat{\tau}}{\hat{\gamma}}\sin\delta$$

if

$$\tau(t) = \hat{\tau}\cos(\omega t + \delta) \tag{3.13}$$

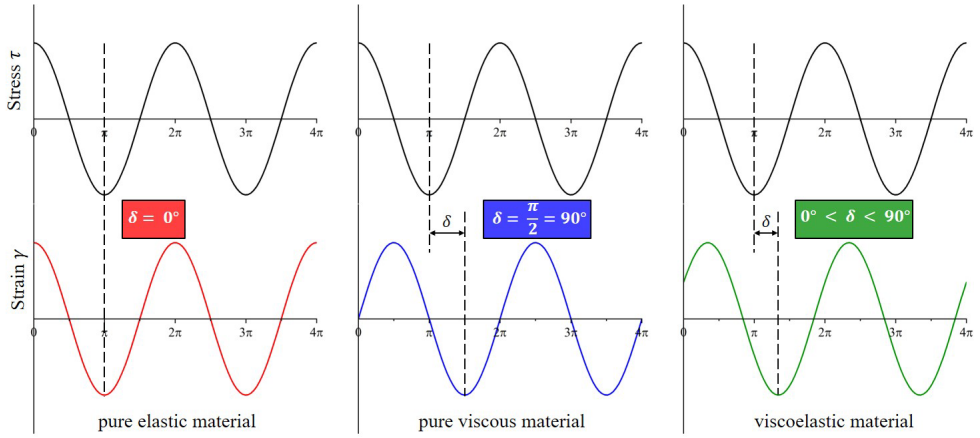


**Figure 3.10:** Stress and deformation behavior in oscillatory amplitude tests of a pure elastic, a pure viscous and a viscoelastic material.

Viscoelastic materials exhibit a load range in which this viscoelasticity is independent of stress or strain. Within this range, structural changes are almost completely reversible. Therefore, this area is referred to as the linear viscoelastic region (LVR) [158]. The ratio of loss modulus $G''$ to storage modulus $G'$ within the LVR provides information about the general behavior of material and is defined as the loss factor or damping factor $tan\delta$ (see Equation (*3.14)*). This factor can be utilized to evaluate whether a viscoelastic body manifests predominantly elastic ($tan\delta < 1$) or predominantly viscous ($tan\delta > 1$) properties.

$$tan\delta = \frac{G''}{G'} \tag{3.14}$$

Furthermore, the end of the LVR is defined as the yield point ($\gamma_y$ strain-based yield point, $\tau_y$ stress-based yield point). Beyond this point, deformation is associated with an irreversible or only partially reversible change in the material's internal structure. In the context of ceramic screen-printing pastes, the yield point is widely regarded as a metric for the strength of the three-dimensional ceramic-binder network. Studies have already shown that this network strength is largely dependent on the solid- and binder content of a paste. In principle, an increase in solids or binder content results in a shift of the yield point towards higher shear stresses or strains, indicating higher network strength. However, it is important to note that the ratio of these two components also influences network strength, such that exceeding extreme ratios can result in a weakening of the network. Furthermore, the value of the yield point is also sensitive to the method of analysis. Experiments with controlled shear stress often lead to less frequency-dependent yield points than strain-based experiments. For instance, in a strain amplitude sweep conducted at a fixed frequency, the strain amplitude is gradually increased and the material's stress response is used to calculate storage and loss modulus. Conducting the same strain amplitude

sweep at a higher frequency typically results in the material behaving “stiffer”, meaning that a given strain amplitude now imposes a higher stress. Consequently, the material is subjected to a greater internal force at the same level of strain, leading to earlier structural breakdown. This results in a yield point appearing at lower strain amplitudes if higher frequencies are used. In contrast, stress amplitude sweeps apply a controlled increase in stress while the resulting strain/deformation is measured. When a higher frequency is used, the material still becomes stiffer, but since the stress is fixed, the induced strain is smaller. As a result, the structure is less likely to yield prematurely at these higher frequencies. This renders yield point analyses via presetting the shear stress more consistent across frequencies than strain-controlled tests. However, it should be noted that both control modes have their own advantages. Stress-controlled tests are most relevant for force-limited operations such as pumping or gravity-driven flow, where it is essential to understand the critical stress needed to initiate movement. Conversely, strain-controlled tests are more suitable for displacement-driven processes such as printing or spreading, where the material is subjected to a prescribed deformation path. Strain-controlled tests also offer enhanced sensitivity to microstructural changes and are safer for fragile materials or materials with unknown yielding behavior, as they prevent uncontrolled overloading. While stress-controlled measurements may appear to offer more direct access to yielding thresholds, strain-controlled tests provide greater resolution of the deformation pathway and the progressive breakdown of structure. Therefore, strain-based measurements are usually considered advantageous for thixotropic materials, as they enable more precise observation of the structural rebuilding process. Furthermore, there exist several calculation methods for the yield point. In this thesis, the offset method was applied for the calculation using amplitude sweep results. The yield point is determined as the point at which the measurement curve deviates from the tangent of the $G'$ curve in the LVR by 3 % was determined as the yield point, as illustrated in Figure 3.11.

However, the point of irreversible deformation can also be marked by a maximum of the $G''$ curve. In an oscillatory amplitude sweep test, a significant increase in the loss modulus indicates that the network structure does not collapse abruptly in the entire shear gap. Instead, initially only micro cracks appear, which eventually cut through the entire sample volume when the maximum is passed and the loss modulus decreases normally.

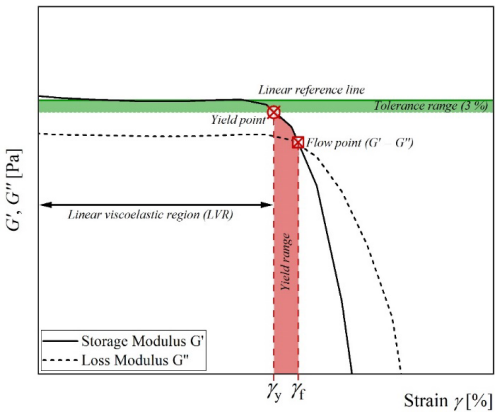


**Figure 3.11:** $G'$ and $G''$ of a paste during strain-based oscillatory amplitude sweep test. Yield point $\gamma_y$ determination via offset method, flow point $\gamma_f$, linear viscoelastic region (LVR) and yield range are indicated.

Additionally, materials that initially exhibit dominant elastic behavior within the LVR possess the ability to transition into dominant viscous behavior or flow. The point at which the transition occurs is defined as the flow point ($\gamma_\mathrm{f}$ strain-based flow point, $\tau_\mathrm{f}$ stress-based flow point). It is the cross-over point of storage and loss modulus ($G' = G''$) in an amplitude sweep test. The area between the yield point and the flow point can be described as the yield range. As suggested and reported on in more detail by Wei et al., the transition behavior can be quantified with the Flow Transition Index (FTI) according to Equation (*3.15)*. *FTI* values close to 1 would indicate abrupt yielding of a brittle material, whereas *FTI* >> 1 is describing a more flexible material and gradual yielding [159]. Since strain responses show a certain dependence on the frequency as already mentioned above, it is advisable to also calculate *FTI* values using shear stresses, even if the difference is found to be minimal [160].

$$FTI = \frac{\gamma_\mathrm{f}}{\gamma_\mathrm{y}} \quad ,regarding\ strain.$$

$$FTI = \frac{\tau_\mathrm{f}}{\tau_\mathrm{y}} \quad ,regarding\ stress. \tag{3.15}$$

With access to the quantifiable elastic (solid-like) and viscous (liquid-like) behavior of screen-printing pastes through storage and loss modulus, their rheological behavior as responses to various load scenarios can be easily and thoroughly characterized.

In the following, dedicated rheological measurement methods are presented that enable a detailed and meaningful characterization of screen-printing pastes. All rheological measurements were carried out using the modular compound rheometer Physica MCR 301 (Anton Paar Germany GmbH, Germany), which was later upgraded to the Physica MCR 302e. All rheological data were collected using serrated parallel plates with a plate diameter of 25 mm. This configuration was chosen to increase the contact between plate and sample and to minimize wall-slip effects, which would lead to the viscosity appearing lower than it actually is. Additionally, with this configuration it is possible to use larger shear gaps when compared to the more commonly used cone-plate geometry. With the cone-plate geometry, depending on the cone angle $\alpha$, the measuring gap is fixed and cannot be adjusted. For example, for $\alpha = 2°$ the gap is fixed to 70 µm. In principle, however, the measuring gap should be at least 10 times larger than the maximum particle size within the sample. Therefore, in this thesis the adjustable gap spacing of the plate-plate geometry was set to 0.5 mm to accommodate potentially occurring agglomeration. One advantage of the cone-plate geometry, however, is that the shear rate remains constant across the entire measuring gap, whereas with the plate-plate geometry it decreases from the inside to the outside towards larger radii. In this case, the software automatically applies correction factors when calculating rheological parameters. Figure 3.12 shows a schematic comparison of these two geometries.

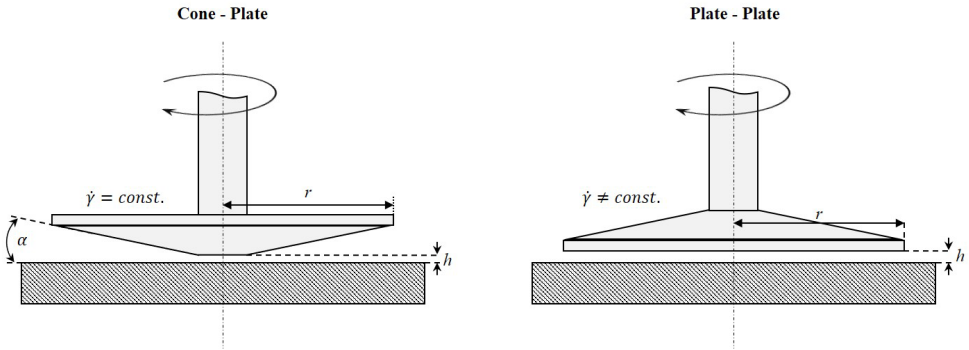


**Figure 3.12:** Schematic representation of the cone-plate and plate-plate measuring systems. Cone-plate geometry with radius *r*, cone angle $\alpha$, minimum measuring gap *h* and constant shear rate $\dot{\gamma}$. Plate-plate geometry with radius *r*, constant shear gap *h* and non-constant shear rate $\dot{\gamma}$. Figure adapted from [157].

Each measurement was performed at temperature of 20 °C, maintained via a temperature control unit (Julabo F25-EH, JULABO GmbH, Germany). Prior to each measurement, a pre-shearing step was conducted at a shear rate of 1 $s^{-1}$ for a duration of 60 s. This was followed by a resting period for the same duration, during which no shear was applied. This was done to pre-condition every sample equally and to nullify potential stresses within the paste that may occur as a result of placing and compressing the sample in between the parallel plates.

A visual illustration showing the range of values that the damping factor $tan\delta$, the phase angle $\delta$ and the flow transition index *FTI* can take is included in the appendix.

**Zero shear viscosity**

In paste preparation it is crucial to ensure that the ceramic powder is finely dispersed prior to the incorporation of the binder component. This is due to the potential of binders to possess stabilizing capabilities. If agglomerates are already present when the binder is added, they are typically unable to be removed again and remain within the paste structure, affecting its rheological behavior and negatively impacting further processing. Therefore, to ensure high dispersion quality of the pre-suspensions, viscosity measurements at very low shear rates were conducted to assess the effectiveness of dispersing agents and their required concentrations. These pre-suspensions comprise only the ceramic powder, dispersed within a pre-solved dispersant-solvent mixture. The measurements were conducted by applying a shear rate $\dot{\gamma}$ of 0.1 $s^{-1}$ to the pre-suspensions for a duration of 50 s with viscosity being recorded at intervals of 10 s. Since ceramic suspensions tend to show thixotropic characteristics and a decrease of viscosity over time is to be expected, the first value is discarded and an arithmetic mean of the remaining four values is calculated and used for evaluation. Here, a lower viscosity value would indicate a higher dispersion quality.

**Viscosity curves**

Typically, screen-printing pastes exhibit shear-thinning behavior, also referred to as pseudoplasticity, which is defined as a decrease in viscosity with an increase in applied shear stress. To assess this property, viscosity curve measurements were performed at shear rates ranging from 0.1 $s^{-1}$ to 1000 $s^{-1}$ with a logarithmic increase of 22 points per decade in rotational mode. In these measurements, the acquisition time was reduced from an initial 10 s to 1 s, following a logarithmic slope. This configuration was used to ensure the acquisition of reliable data at low shear rates, while maintaining a high level of resolution. To further quantify the extent of shear-thinning behavior, a shear-thinning index (*STI*) was calculated. This index, represented by Equation (*3.16)*, quantifies the ratio of viscosity at low shear rates to the viscosity at high shear rates, thereby providing a comprehensive assessment of pseudoplastic behavior. A high *STI* indicates extensive shear-thinning behavior.

$$STI = \frac{\eta_{0.1}}{\eta_{1000}} \tag{3.16}$$

**Oscillation amplitude sweep test**

Amplitude sweep tests were conducted in a strain range of 0.1 – 1000 %, with a logarithmic increase of 6 points per decade at an oscillation frequency $\omega$ of 10 rad/s. In addition to strain $\gamma$, shear stress $\tau$ and temperature $T$, the storage modulus $G'$, loss modulus $G''$ and the phase angle $\delta$ were recorded to assess the viscoelastic properties of each paste. To gain further understanding about the yielding behavior of the pastes, yield and flow points were calculated from these measurements using the built-in RheoCompass software of the rheometer device.

**3-intveral-thixotropy test (3ITT)**

Pastes that exhibit a transition from solid- to liquid-like behavior were analyzed using the 3-interval-thixotropy test to quantify their thixotropic properties. The recovery of the internal paste structure is imperative during the final phase of the screen-printing process, when the screen is separated from the coated substrate and paste leveling occurs (see Chapter 2.1.3). This test for thixotropic behavior is comprised of three intervals. During the initial interval, the resting behavior of the pastes is established as a baseline and the sample is subjected to minimal shear stresses or deformations. For this, load settings are selected from within the linear viscoelastic region, as determined by the amplitude sweep test and in this case were set to a strain $\gamma$ of 1 % at an angular frequency $\omega$ of 10 rad/s. This procedure is essential in ensuring that during this measurement interval the internal structure does not undergo any structural changes and that the viscoelastic properties remain independent from the applied load. In the subsequent interval, the screen-printing process is simulated, with the sample undergoing high shear in a rotational mode. This results in a partial or complete alteration of the paste network structure. Shear rates exceeding 1000 $s^{-1}$ commonly occur during screen printing but are highly dependent on the printing configurations and the characteristics of the screen. According to Equation (*3.17)*, rough estimates regarding shear rates during screen printing can be made and rates of approximately 3000 $s^{-1}$ were calculated from the parameters predominantly used for the coatings investigated in this thesis. This shear rate was applied for a duration of 5 s, which is analogous to the duration of the printing process.

$$\dot{\gamma} = \frac{squeegee\ speed}{screen\ mesh\ opening} \tag{3.17}$$

In the third and final interval, the same load settings are applied as in the first interval to again simulate rest conditions after the printing process. This approach enables the measurement of a quasi-undisturbed rebuilding of the structure as a response of a sample, which can then be analyzed. With this test procedure, a few characteristics can be used to evaluate the thixotropic capabilities of a paste. One significant aspect to consider is the duration required for structural recovery. This is indicated as the time within the third interval until the storage modulus once again reaches higher values than the loss modulus and solid-like behavior becomes dominant. Another commonly used evaluation criterium is the maximum value of the storage modulus that is reached in the third interval upon structure rebuilding and its deviation from the initial state in interval I. The discrepancy between these two values offers insight into the irreversible degradation of the paste network that occurs during the printing process. A complete overview of measurement settings for all intervals is listed in Table 3.6.

**Table 3.6:** Measurement parameters for each interval of the 3-interval-thixotropy test (3ITT). Intervals I and III were measured in oscillation mode. Interval II was measured in rotational mode. Serrated parallel plates with a diameter of 25 mm and a shear gap of 0.5 mm were used.

| Interval | I | II | III |
|---|---|---|---|
| Angular frequency ω | 10 rad/s | - | 10 rad/s |
| Strain γ | 1 % | - | 1 % |
| Shear rate $\dot{\gamma}$ | - | 3000 $s^{-1}$ | - |
| Meas. pt. duration | 5.0 s | 0.5 s | 5.0 s |
| Amount of meas. pts. | 10 | 10 | until equilibrium |
| Temperature *T* | 20 °C | 20 °C | 20 °C |

### 3.2.9 Thermo-optical analysis

In this thesis, the TOMMIplus thermo-optical measurement system was utilized to analyze the bending and shrinkage behavior of half cells during the co-sintering step. A comparison of co-sintering measurements with substrate reference measurements enables the formulation of conclusions regarding the sintering onset of the electrolyte layers and the support, respectively. Additionally, other phenomena, such as the spalling of layers, can be documented and the temperatures at which this spalling occurs can be ascertained. The measuring setup consists of a specialized high-temperature furnace coupled with a CMOS camera (complementary metal-oxide semiconductor) and a light source so that the lateral sample silhouette can be recorded during the sintering process.

### 3.2.10 Air leakage rate

Given that gas tightness of the electrolyte is a critical property that directly correlates with cell performance, the gas leakage of the electrolytes manufactured for this thesis was examined in a series of half cells. The cells were evaluated using the HTL 260 air leak testing device (Pfeiffer Vakuum GmbH, Germany). During testing, the half cells are positioned with the electrolyte facing downwards on the device's intake manifold. Sealing is achieved by silicon gaskets on both sides of the cell. During the measurement process, a vacuum is created on the electrolyte side. In the event of a leak within the cell, air is able to diffuse from the support side through the electrolyte into the vacuum area, subsequently increasing the pressure on the electrolyte side. This pressure change over a defined period of time yields the specific leak rate which is additionally normalized to a defined area. Leakage rates are expressed in the unit $hPa \cdot dm^3 \cdot s^{-1} \cdot cm^{-2}$. Internal standards of the Jülich Type III cell and Zhang's predecessor cell for both oxidized and reduced states are shown in Table 3.7. Although the GDC based cell by Zhang contains a 3-layer electrolyte, the values presented in this table are referring to a single layer screen-printed GDC electrolyte.

**Table 3.7:** Internal air leakage rate values for the Jülich Type III cell and the GDC based cell developed by Jun Zhang *[77]*.

| | Jülich Type III [hPa·dm³·s$^{-1}$·cm$^{-2}$] | Cell developed by Zhang [hPa·dm³·s$^{-1}$·cm$^{-2}$] |
|---|---|---|
| Oxidized | $8.00 \times 10^{-6}$ | $3.54 \times 10^{-6}$ |
| Reduced | $2.00 \times 10^{-5}$ | $3.54 \times 10^{-5}$ |

### 3.2.11 Electrochemical characterization

Electrochemical characterization of the cells investigated in this thesis were mainly carried out by Dr Iurii Kogut at the Karlsruhe Institute of Technology (KIT IAM-ET). The general measurement setup and test bench configuration used for the electrochemical characterization are described in detail in [161] and only essential details relevant for this thesis are summarized here for clarity.

Measurements were conducted with the cells placed in a horizontal configuration. For sealing, gold gaskets were used on the air side to ensure gas tightness during operation. The air electrode was contacted using a 1 cm² gold mesh placed on the electrode surface, while gold point contacts were used for the air-side reference electrodes. For the fuel electrode, a 1 cm² nickel mesh served as the current collector, complemented by smaller nickel meshes to serve as fuel-side reference electrodes. An overview of the contacting geometry and gasket positioning is provided in Figure 3.13.

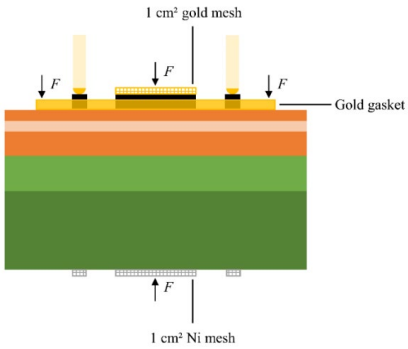


**Figure 3.13:** Schematic of the cell clamping and contacting configuration used for electrochemical measurements at KIT IAM-ET.

In this setup, clamping forces are applied on the rim of the gold gasket and the center of the air electrode. On the fuel side, the clamping force is applied only to the center of the cell area. This clamping configuration results in an unfavorable und non-uniform load distribution across the cell area, which is particularly relevant for solid oxide cells containing ceria-based layers, as these can exhibit special mechanical sensitivity under localized stresses and reducing conditions.

Prior to electrochemical measurements, the cells were subjected to a standard reduction protocol to ensure full reduction of the fuel electrode under controlled conditions. First, the cells were heated to 900 °C at 3 K/min with 0.1 L/min air on the electrode side and 0.1 L/min $N_2$ on the fuel electrode side.

At 900 °C, the cells dwelled for 2 hours to ensure sufficient sealing by the gold gasket on the air side. After cooling down to 800 °C at 3 K/min the cells dwelled again for 2 hours. Afterwards, 100 % $H_2$ was gradually introduced on the fuel side while increasing both gas flows on air and fuel side to 0.25 L/min. Before any measurement, the cell was kept in this state for 1 hour to ensure sufficient reduction of the cell. Table 3.8 provides the detailed reduction steps and gas flow ramping conditions.

**Table 3.8:** Standard reduction protocol for electrochemical characterization conducted by Dr Iurii Kogut at KIT IAM-ET.

| Step | Air Flow Rate [ml/min] (Air Electrode) | $H_2$ Flow Rate [ml/min] (Fuel Electrode) | $N_2$ Flow Rate [ml/min] (Fuel Electrode) | Duration [min] |
|---|---|---|---|---|
| 1 | 125 | 0 | 150 | 10 |
| 2 | 145 | 20 | 150 | 30 |
| 3 | 165 | 40 | 150 | 25 |
| 4 | 205 | 80 | 150 | 20 |
| 5 | 250 | 160 | 90 | 15 |
| 6 | 250 | 250 | 0 | 60+ |

Typically, the following tests were conducted after the reduction protocol to establish a baseline electrochemical behavior for each cell. First, an initial I-V curve measurement was performed in SOFC mode, sweeping from 0 to + 2 $Acm^{-2}$ and back down to 0 $Acm^{-2}$ in steps of 0.02 $Acm^{-2}$ with a hold time of 20 seconds per step. This measurement had a total duration of 4000 seconds (1 hour, 6 minutes, 40 seconds), resulting in a total hold under 100 % $H_2$ at 800 °C for at least 3.5 hours during initial stabilization. After this, the sample often remained under these conditions for an extended period before the first electrochemical impedance spectroscopy (EIS) measurement and a second I–V curve were recorded. Typically, 5.5 % humidity was then applied to the fuel electrode side, followed by a conditioning step in SOFC mode at 1 $Acm^{-2}$ for 24 hours to further stabilize the cell.

I–V and OCV measurements were typically conducted across a temperature range of 650 – 800 °C with varying $H_2O$ content in the fuel gas. The humidity levels investigated included 78.4 %, 60 %, 50 %, 40 %, 20 %, 10 % and 5.5 % $H_2O$ to systematically study the impact of fuel gas composition on cell performance and open-circuit voltage.

# 4 Development of screen-printed gadolinium-doped ceria electrolyte layers

## 4.1 Motivation

The following chapter discusses the development of a screen-printed layer of gadolinium-doped cerium oxide (GDC). Within the ElChFest project, it was intended to build on the findings of the dissertation by Jun Zhang, which deals with the initial development of these layers at IMD-2. However, at the beginning of this work, it became apparent that these previously reported results could not be reproduced. A change in the powder manufacturer was identified as the decisive difference. Initially, it was unclear to what extent this change caused the observed deviations because the relationships between powder properties, screen-printing paste rheology, paste composition and resulting layer properties had not been sufficiently investigated. Additionally, GDC is a relatively difficult material to process, making production of dense layers more challenging. Defects such as agglomerates, holes and the formation of undesirable secondary phases frequently occurred in the preliminary work, which significantly impaired the structural integrity and reproducibility of the manufactured layers [77]. This became evident in stack tests, that revealed significant gas leakage and reoxidation of the cells during testing. Comprehensive investigations carried out as part of this work identified unsuitable dispersing agents as one of the main causes of secondary phase formation. Another central challenge was the difficulty of reliably adapting findings from literature in order to optimize the new paste formulation. Only the analyses carried out here revealed that conventional characterization approaches, such as specifying viscosities at a seemingly arbitrary shear rate value (e.g. $100^{-1}$), are insufficient for adequately describing the complex flow behavior of screen-printing pastes. Similarly, common specifications of paste compositions in weight or volume percent (e.g., solid, binder and dispersant content) have proven to be incomplete as they do not account for critical parameters such as particle size distribution, specific surface area and agglomeration tendency of the used powder [150, 162 - 169]

Based on these findings, particular attention was paid to the selection and adjustment of the paste composition and optimization of the screen-printing process to significantly improve the layer quality.

The developments and results presented in the following are based on these considerations and aim to improve the fundamental understanding of the relationship between material properties, formulation parameters and the structure of screen-printed layers.

Most of the following information have already been communicated in the full-length research article “Influence of powder characteristics on the rheology of ceria-based screen-printing pastes for solid oxide cell applications” published in the Journal of the European Ceramic Society, Volume 45, Issue 15, pp. 117570, 2025, licensed under CC BY 4.0. Specifically, the contents of Chapter 4.3.1, Chapter 4.4, Chapter 4.5 and Chapter 4.7 represent the findings published in the research article mentioned [170].

## 4.2 Powder characterization

### 4.2.1 Influence of the milling technique on PSD and SSA

As already prefaced in Chapter 3.2.1, the particle size distribution plays an important role in the processing and later properties of ceramic materials. It is not only affecting paste rheology, as will be explained in Chapter 4.5.1, it is also influencing microstructure development during sintering (see Chapter 4.2.2), layer uniformity and general processability. Milling the powder is therefore an important step in production of ceramics, as it is here where the median particle size and distribution width is adjusted according to subsequent requirements.

In this work, pastes were prepared in two different ways, which differ significantly in the technique used for powder milling. In the TM-DPS route, low-intensity milling is carried out using PE-bottles in a tumbling mixer. The PM-MPS route utilizes high-energy ball milling with YSZ lined steel containers in a planetary ball mill. More information about the milling procedures are presented in Chapter 3.1.3.

Figure 4.1 A displays the as-received PSD of the commercially available 10GDC-M powder by Fuelcellmaterials, which is the only GDC powder used in this work. Although the PSD shows a median particle size of ~ 0.1 µm when analyzed via static light scattering, SEM analysis revealed that the primary grain size is roughly 0.07 µm (70 nm), which also explains the relatively high specific surface area (SSA) of 39 m²/g. Therefore, to adjust the SSA and primary grain size the powder was subjected to calcination prior to being processed into a paste. Figure 4.1 B shows the PSD of the powder after being calcined at either 1130 °C, 1230 °C or 1340 °C for 3 h each. Generally, higher calcination temperatures also lead to larger grain sizes, now showing very broad left-skewed distributions with particle sizes ranging between 0.3 µm and 800 µm. Subsequent milling of the calcined powders resulted in distinct PSDs, depending on the applied milling technique. Figure 4.1 C presents the PSDs of powders processed with the tumbling mixer, while Figure 4.1 D shows those obtained via planetary ball milling. Milling with the tumbling mixer (TM-DPS route) consistently resulted in bimodal distributions with a primary peak at approximately 0.1 µm and a smaller secondary peak around 1 µm. In contrast, planetary ball milling (PM-MPS route) proved more effective in reducing particle size and narrowing the PSD. Here, the PSDs appear monomodal, showing only one distinctive peak at 0.1 µm. Additionally, a temperature-dependent trend can be observed. Powders calcined at higher temperatures generally resulted in more right skewed and broader distributions after milling, while powders calcined at lower temperatures appear narrower, regardless of the milling technique used.

For reference, Figure 4.2 compares an SEM image of the as-received powder in A with one of the powders calcined at 1230 °C in B and subsequently milled using the tumbling mixer in C. On average, the initial primary particle size of 0.07 µm increased to approximately 0.1 – 0.2 µm as a result of the pre-treatments. Simultaneously, nitrogen adsorption measurements showed a reduction in specific surface are from the original 39 m²/g to 7 m²/g for this powder and to values between 6 m²/g and 16 m²/g

for the others, depending on the pre-calcination temperature and milling method. Table 4.1 summarizes the key characteristics of all powders discussed.

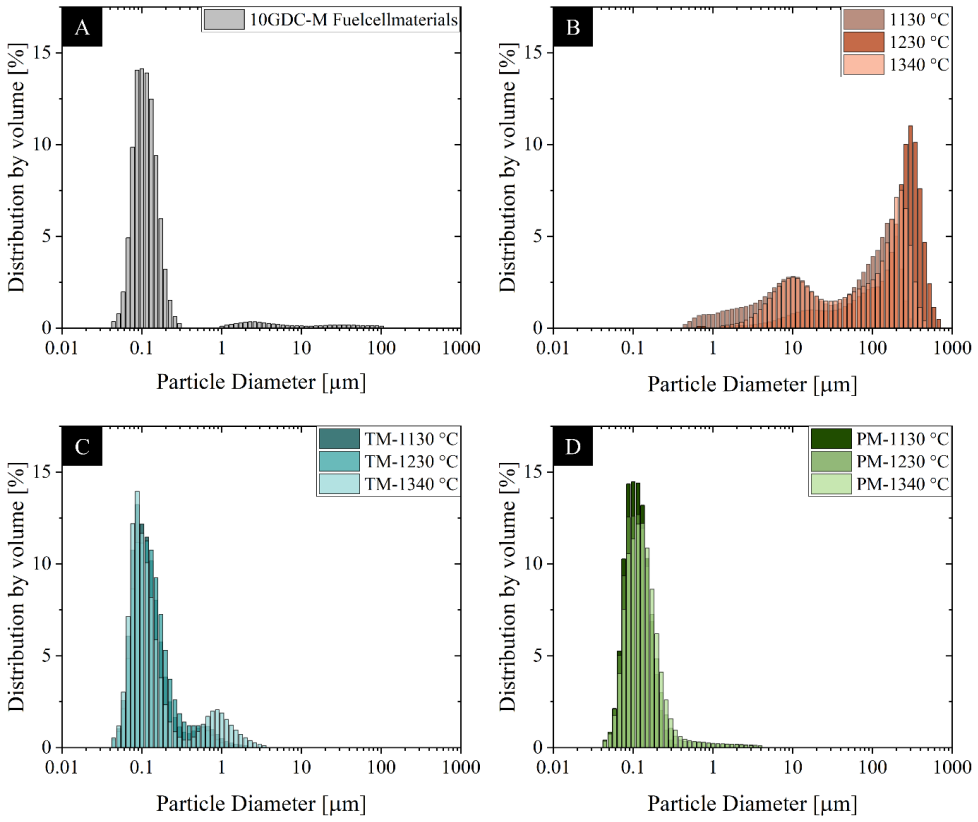


**Figure 4.1: A** Particle size distribution (PSD) of the as-recieved 10GDC-M powder. **B** PSDs of the powder after calcination at 1130 °C, 1230 °C and 1340 °C for 3h, showing temperature-dependent coarsening. **C** PSDs of the calcined powders after milling with a tumbling mixer, resulting bimodal distributions. **D** PSDs of the calcined powders after planetary ball milling, showing narrower, monomodal distributions.

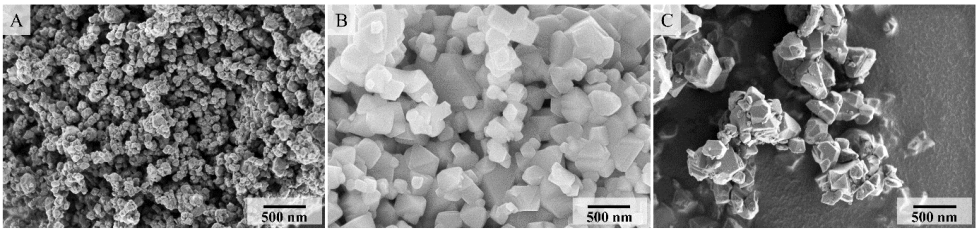


**Figure 4.2:** Scanning electron micrographs taken with an InLens detector. **A** Commercially available powder 10GDC-M (Fuelcellmaterials) with a primary grain size of approximately 0.07 µm. **B** Powder calcined at 1230 °C for 3 h. **C** Powder calcined at 1230 °C for 3 h and subsequently milled in a tumbling mixer, resulting in a primary grain size of roughly 0.1 – 0.2 µm, aggregated into larger agglomerates.

**Table 4.1:** Overview of key characteristics of all powders discussed, including traditional $d_{10}$ / $d_{50}$ / $d_{90}$ values, as well as specific surface area (SSA) and bimodality coefficient $\varphi$, skewness $\gamma_1$ and excess kurtosis $\gamma_2$ of the particle size distribution (PSD).

| Powder | $d_{10}$ / $d_{50}$ /$d_{90}$ [µm] | Bimodality coefficient $\varphi$ | Skewness $\gamma_1$ | Excess Kurtosis $\gamma_2$ | SSA [m²/g] |
|---|---|---|---|---|---|
| 10GDC-M | 0.07 / 0.11 / 0.18 | 0.89 | 2.50 | 5.01 | 39.19 |
| GDC-1130 | 2.24 / 38.59 / 175.74 | 0.58 | 1.22 | 1.09 | 1.93 |
| GDC-1230 | 19.78 / 219.30 / 385. 31 | 0.77 | 1.59 | 1.27 | 0.63 |
| GDC-1340 | 6.26 / 86.62 / 254.67 | 0.59 | 1.70 | 1.72 | 0.27 |
| TM-1130 | 0.07 / 0.10 / 0.27 | 0.76 | 1.28 | 0.14 | 6.60 |
| TM-1230 | 0.07 / 0.11 / 0.27 | 0.71 | 0.92 | -0.78 | 9.34 |
| TM-1340 | 0.06 / 0.10 / 0.76 | 0.77 | 1.70 | 1.72 | 3.65 |
| PM-1130 | 0.07 / 0.10 / 0.16 | 0.56 | 0.42 | -1.60 | 15.67 |
| PM-1230 | 0.07 / 0.11 / 0.20 | 0.53 | 0.39 | -1.60 | 7.50 |
| PM-1340 | 0.07 / 0.12 / 0.22 | 0.78 | 1.24 | -0.05 | 7.31 |

While metrics such as $d_{10}$, $d_{50}$ and $d_{90}$ values are commonly used to quantify particle size distributions, they often fail to capture the full complexity of a distribution's shape. Especially bimodality or asymmetry are not quantifiable when solely relying on percentile values. This limitation becomes evident when comparing PSDs that exhibit similar percentile values but differ in their overall distribution profile. To address this, the bimodality coefficient $\varphi$ was introduced (see Chapter 3.2.1) as a more detailed descriptor, incorporating both skewness and excess kurtosis to better characterize the shape and modality of a distribution. Figure 4.3 illustrates this by comparing two PSDs with comparable $d_{10}$, $d_{50}$ and $d_{90}$ values, yet noticeably different modality.

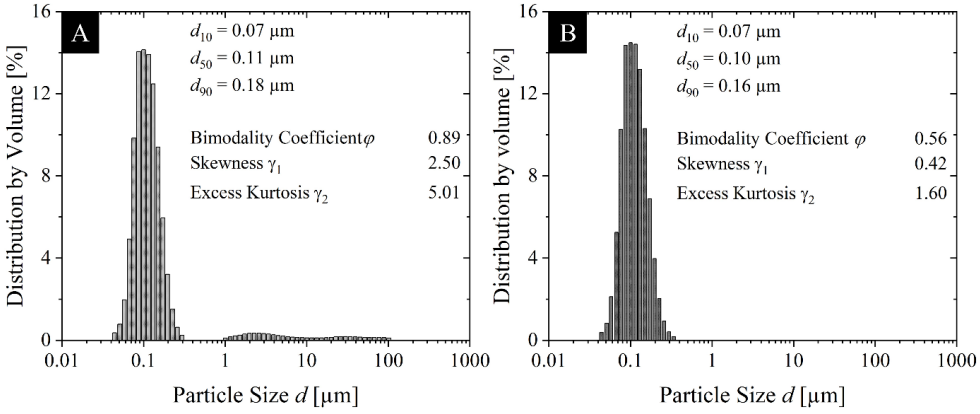


**Figure 4.3:** Comparison of two particle size distributions. Although $d_{10}$, $d_{50}$ and $d_{90}$ values are very similar, the distributions differ in shape. This difference is more accurately described using other distribution descriptors such as the bimodality coefficient $\varphi$, skewness $\gamma_1$ and excess kurtosis $\gamma_2$. **A** Distribution with a $\varphi$ = 0.89 exhibits a clearly bimodal profile. **B** Distribution with a $\varphi$ = 0.56 is quantified as monomodal.

This highlights the added value of the bimodality coefficient in distinguishing between seemingly similar, but ultimately different distributions and provides a new metric for potential correlation with rheological properties of screen-printing pastes.

### 4.2.2 Sintering behavior of GDC and co-doped GDC

In this chapter, the sintering behavior of different GDC powders, intended for use as the electrolyte layer, is systematically examined and compared to that of the YSZ powder used in the standard electrolyte for Type III Jülich cells. To control and align the sintering kinetics and behavior of GDC with those of YSZ, various processing routes were explored. These included calcination of the as-received 10GDC-M powder (Fuelcellmaterials, a Nexceris company, USA) at different temperatures (1130 °C, 1230 °C, 1340 °C), followed by subsequent milling to modify particle sizes and specific surface areas. Additionally, as described in Chapter 3.1.1, co-doping strategies were employed by introducing 0.5 mol% of either $Co_2O_3$ or NiO to the pre-treated GDC powders to influence densification behavior and grain growth. The impact of these modifications was evaluated through dilatometric analysis, focusing on key parameters such as the onset of shrinkage, total shrinkage, maximum shrinkage rate and the temperature at which this maximum rate occurs. These insights are essential for understanding and tailoring the electrolyte microstructure to achieve sufficiently dense layers during co-sintering of half-cells.

Figure 4.4 A presents the sintering onset temperatures of all investigated powders in order from lowest sintering onset to highest sintering onset temperature. Figure 4.4 B showcases the shrinkage rate profiles of the same powders. Values for sintering onset, maximum shrinkage, maximum shrinkage rate and temperature of maximum shrinkage rate are summarized in Table 4.2.

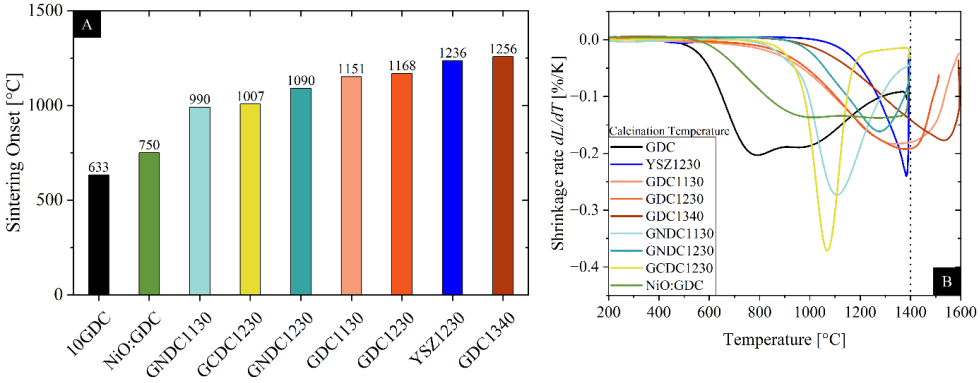


**Figure 4.4: A** Sintering onset temperature of all investigated powders in order from lowest sintering onset to highest sintering onset temperature. **B** Shrinkage rate profiles of the identical investigated powders. Half-cell co-sintering temperature is indicated by the dotted line.

The as-received 10GDC powder exhibited the lowest sintering onset temperature, initiating shrinkage at approximately 633 °C with a relatively high total shrinkage of -27.99 %. However, this early onset was accompanied by a broad and less defined shrinkage rate profile, indicating a wider distribution of particle sizes or a high degree of agglomeration, both of which are typical for as-synthesized powders. Calcination followed by milling significantly altered the sintering behavior.

**Table 4.2:** Summary of dilatometric analysis parameters for the investigated GDC and YSZ powders, including sintering onset temperature, maximum shrinkage, maximum shrinkage rate and the temperature of the maximum shrinkage rate. Included are values for as-received GDC (10GDC), GDC powders calcined at various different temperatures (GDC1130, GDC1230, GDC1340) and co-doped powders with 0.5 mol% $Co_2O_3$ (GCDC1230) and 0.5 mol% NiO (GNDC1130 and GNDC 1230). For reference, the standard YSZ powder used for Type III Jülich cells is also included.

| Powder | Sintering Onset Temperature [°C] | Maximum Shrinkage [%] | Maximum Shrinkage Rate [%/K] | T. at Maximum Shrinkage Rate [°C] |
|---|---|---|---|---|
| 10GDC | 633 | -27.99 | -0.20 | 790 |
| GDC1130 | 1151 | -19.99 | -0.18 | 1345 |
| GDC1230 | 1168 | -21.86 | -0,19 | 1383 |
| GDC1340 | 1256 | -15.23 | -0.18 | 1533 |
| GNDC1130 | 990 | -25.64 | -0.27 | 1107 |
| GNDC1230 | 1090 | -15.17 | -0.16 | 1276 |
| GCDC1230 | 1007 | -19.10 | -0.37 | 1070 |
| YSZ1230 | 1236 | -20.67 | -0.24 | 1384 |
| NiO:GDC (45:55) | 750 | -21.20 | -0.14 | 1002 |

With increasing calcination temperatures, the sintering onset shifted to higher temperatures. This trend can be attributed to increased grain growth and reduction of surface area during calcination, resulting in a more thermally stable powder that requires higher temperatures to initiate densification. However, the difference between GDC powders calcined at 1130 °C and 1230 °C appears to be minor. This indicates that the subsequent milling step after calcination helped to recover some sintering activity by reducing agglomerates, grain sizes and narrowing PSDs. Though the effect of equalization was less pronounced at the highest calcination temperature (1340 °C), where grain growth may have become significant enough to retard densification. Interestingly, the maximum shrinkage rate is very similar across the calcined powders, ranging from – 0.18 %/K to – 0.19 %/K. However, the temperature at which this maximum rate occurred increased significantly, particularly for powder calcined at 1340 °C, which reached its peak shrinkage rate at 1533 °C. This is above the typically employed co-sintering temperature of 1400 °C used for half-cell fabrication. Furthermore, the calcination and milling process led to a narrowing of the shrinkage rate profile, concentration densification over a smaller temperature range. The total shrinkage of the calcined powders however decreased with increasing calcination temperature, with powders calcined at 1130 °C and 1230 °C maintaining shrinkages of around – 20 %,

while the 1340 °C powder showed a significantly reduced shrinkage of approximately – 15 %. This reduction in total shrinkage, combined with the elevated peak shrinkage temperature above the co-sintering temperature, limits the suitability of this powder for the intended application as a powder for electrolyte production.

Among the calcined and milled GDC variants, the powder calcined at 1230 °C demonstrated the most comparable densification behavior to the standard YSZ powder. The maximum shrinkage for GDC1230 reached – 21.86 %, closely matching the – 20.67 % observed for YSZ. Moreover, the temperature at which the maximum shrinkage rate occurred was virtually identical between the powders with 1383 °C for GDC1230 and 1384 °C for YSZ, suggesting favorable alignment in peak densification kinetics. However, notable differences remain. The maximum shrinkage rate of YSZ was slightly higher (- 0.24 %/K) compared to GDC1230 (- 0.18 %/K), indicating a more rapid densification process for YSZ once sintering is initiated. Additionally, YSZ exhibited a higher sintering onset temperature of 1236 °C, whereas GDC1230 began shrinking at a significantly lower temperature of 1168 °C. This earlier onset in GDC could lead to mismatched shrinkage stresses or undesirable porosity gradients evolving during co-sintering, especially in tightly bonded multilayer structures.

Co-doping strategies employing 0.5 mol% of either $Co_2O_3$ or NiO introduced further modifications to the sintering behavior of GDC powders, demonstrating clear differences compared to the solely calcined and milled GDC variants. As previously described in Chapter 3.1.1, these co-dopants are intended to enhance sintering activity by promoting mass transport and facilitating densification at lower temperatures. The impact of co-doping on sintering onset was particularly pronounced. The GDC powder calcined at 1230 °C and co-doped with $Co_2O_3$ (GCDC1230) exhibited a significantly reduced sintering onset of approximately 1007 °C, marking a reduction of over 160 °C compared to the undoped GDC1230. This effect was also evident, though to a lesser extent, in the NiO co-doped powders, where GNDC1230 shows a sintering onset at 1090 °C. However, GNDC1130 shows also a reduction in sintering onset of approximately 160 °C when compared to the undoped counterpart GDC1130. These reductions in sintering onset indicate that both co-dopants effectively lower the activation energy required for densification, with $Co_2O_3$ showing a presumably stronger influence. In addition to lowering the sintering onset, co-doping led to a further narrowing of the shrinkage rate profiles, concentrating densification over a smaller temperature window. Notably, the maximum shrinkage rates achieved during sintering were also influenced by co-doping. The $Co_2O_3$ co-doped GCDC1230 demonstrated the highest maximum shrinkage rate with -0.37 %/K among the investigated powders. NiO co-doping similarly enhanced the maximum shrinkage rates compared to undoped powders, although the extent was less pronounced than with the $Co_2O_3$. Interestingly, GNDC1230 exhibited a slightly lower maximum shrinkage rate than its undoped GDC1230 counterpart, despite the co-doping.

However, the temperatures at which the maximum shrinkage rate occurred were consistently reduced in the co-doped samples compared to undoped GDC. GCDC1230 reached its peak shrinkage rate at 1070 °C, followed by GNDC1130 at 1107 °C and GNDC1230 at 1276 °C. These temperatures are below

the typical co-sintering temperature of 1400 °C, indicating that effective densification of the electrolyte layer can potentially be achieved even at reduced sintering temperatures when utilizing co-doped GDC powders.

While the enhanced sintering kinetics and lower onset temperatures observed for the co-doped GDC powders may be beneficial for aligning sintering behavior, it is important to consider potential challenges associated with accelerated densification at temperatures significantly below the intended sintering temperature. Rapid grain boundary movement and densification starting at lower temperatures can reduce the available time for pore elimination, leading to the potential entrapment of residual porosity within grains. This risk is particularly pronounced when the temperature of the maximum shrinkage rate is far below the co-sintering temperature, as the driving force for further densification diminishes once the system passes beyond that temperature. Consequently, grain growth may proceed without sufficient pore mobility, resulting in closed and entrapped pores that limit the achievable final density. Therefore, careful optimization of the heating profile, dwell times and overall sintering temperature might be needed to prevent premature grain growth that could hinder complete densification during co-sintering of an SOC half-cell.

To further understand the microstructural evolution during sintering and its correlation with the observed dilatometry results, the sintered pellets used for the dilatometry measurements were polished and thermally etched to reveal their grain structures. Representative micrographs of the YSZ reference, as-received GDC, the calcined and milled powders (GDC1130, GDC1230, GDC1340), as well as the co-doped powders GCDC1230 and GNDC1230 are shown in Figure 4.5.

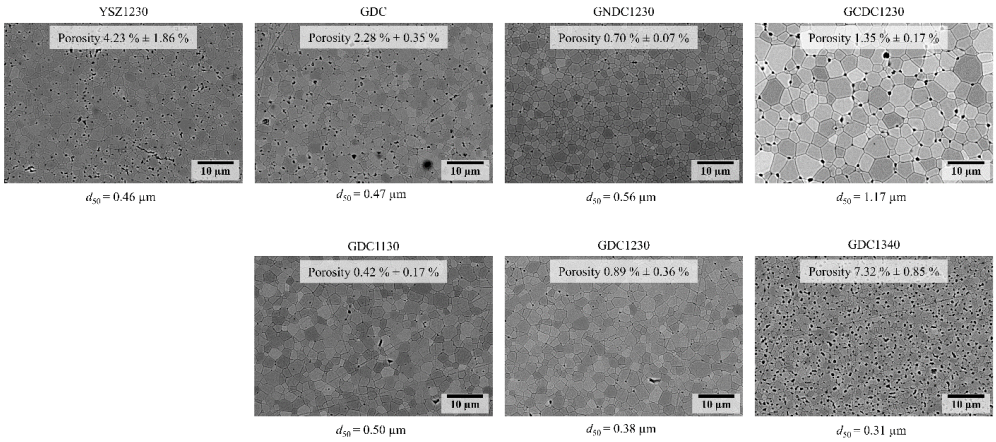


**Figure 4.5:** Polished and thermally etched surface microstructures of the investigated electrolyte pellets used for dilatometry measurements, including YSZ, as-received GDC, GDC powders calcined at 1130 °C, 1230 °C and 1340 °C, as well as co-doped GDC powders with 0.5 mol% NiO (GNDC1230) and 0.5 mol% $Co_2O_3$ (GCDC1230). All images were taken at the same magnification for direct comparison.

In addition to qualitative comparison of grain morphologies, quantitative analysis of the particle size distributions and $d_{50}$ values as the mean particle size obtained from these images was performed to assess

grain growth behavior. Porosity values for each pellet were also determined, enabling a direct comparison with the observed densification characteristics.

This quantitative image analysis shows that porosity is lowest for GDC1130 (0.42 %) and GNDC1230 (0.70 %), followed by GDC1230 (0.89 %) and GCDC1230 (1.35 %). The as-received GDC and the standard YSZ pellet exhibit more moderate porosity levels with values of 2.28 % and 4.23 % respectively. Notably, GDC1340 demonstrates the highest porosity at 7.32 %, correlating with its significantly reduced total shrinkage and low shrinkage rates at 1400 °C observed in the dilatometry measurements. Quantitative grain size analysis shows $d_{50}$ values ranging from 0.31 µm (GDC1340) to 1.17 µm (GCDC1230), with the co-doped GCDC1230 exhibiting the largest grain size among the investigated samples, suggesting pronounced grain growth most likely facilitated by the additional $Co_2O_3$ doping. GNDC1230 also shows a relatively large $d_{50}$ of 0.56 µm, while the remaining samples remain within a narrow range between 0.38 µm – 0.50 µm. In terms of pore morphology, porosity predominantly localizes at grain boundaries and triple grain junctions for all samples. However, YSZ, as-received GDC and particularly GCDC1230 show also isolated intergranular pores, indicating potential pore entrapment during grain growth. In general, all co-doped samples, as well as GDC1130 and GDC1230 show uniformly roundly shaped pore shapes, while YSZ, as-received GDC and GDC1340 exhibit more elongated pore shapes. Here, GDC1340 is displaying the highest extent of pore elongation, consistent with incomplete densification observed in dilatometry measurements and the elevated porosity values. Overall, these microstructural observations correlate well with the previously discussed dilatometry data, confirming that the reduced porosity in calcined and co-doped powders are proof of their enhanced sintering behaviors. The significant observable grain growth in GCDC1230 and GNDC1230, paired with low porosity values, suggests accelerated mass transport and grain boundary mobility induced by the dopants. This is consistent with the high shrinkage rates and low sintering onset temperatures observed. Conversely, the high porosity and elongated pores in GDC1340 indicate insufficient densification, aligning with its limited shrinkage, low maximum shrinkage rates and high sintering onset temperatures.

In addition to microstructural investigations, the influence of co-doping on the lattice parameter of GDC was examined to gain insight into the dopant incorporation behavior and its potential correlation with the enhanced sintering kinetics observed. As previously described in Chapter 3.1.1, nitrate precursors were used for introducing Co and Ni ions to the GDC powder, followed by calcination at 400 °C to transform the nitrates into their respective oxides. However, the precise processing step at which the dopant ions incorporate into the GDC lattice remains unclear in literature reports, warranting further investigation. To address this, XRD measurements combined with Rietveld refinements were performed on pure GDC, GCDC1230 after calcination at 400 °C, GCDC1230 and GNDC1230 after sintering at 1400 °C for 5 h. The diffractograms presented in Figure 4.6 revealed clear differences in peak positions and lattice parameters. Pure GDC exhibited a lattice parameter of 5.4199 Å, whereas the co-doped samples showed slightly reduced lattice parameters after sintering of 5.4175 Å for GCDC1230 and

5.4149 Å for GNDC1230. The sample subjected only to the calcination step at 400 °C showed a slight peak broadening, possibly indicating lower crystallinity or the formation of a very thin and diffuse CoO or $Co_2O_3$ layer around the GDC grains, although no distinct Co peaks could be detected.

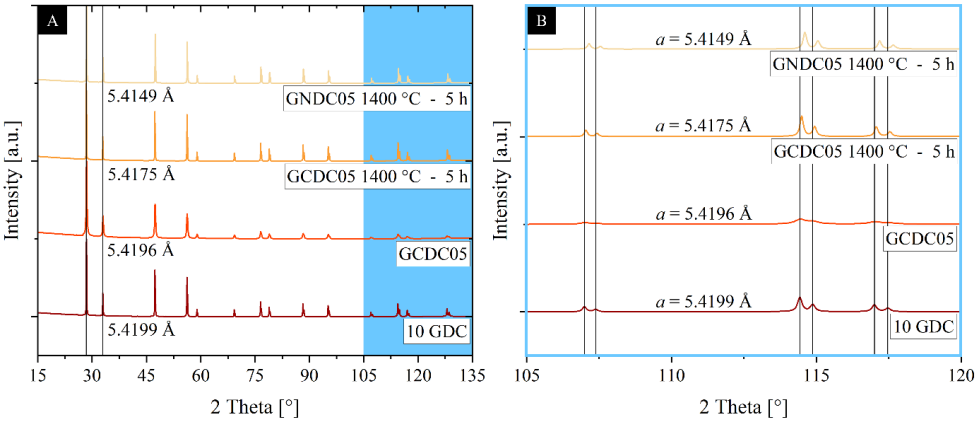


**Figure 4.6: A** X-ray diffraction patterns of pure GDC, GCDC130 after calcination at 400 °C and GCDC1230 and GNDC1230 after sintering at 1400 °C for 5 h. All samples exhibit pure compositions without detectable secondary phases. **B** Magnified view of the 2θ range 105° - 120°, highlighting the shift in peak positions among these samples. Lattice parameters are indicated.

The observations suggest that the incorporation of Co and Ni dopants into the GDC lattice predominantly occurs during high-temperature sintering rather than the initial low-temperature calcination step. The clear shift in diffraction peaks and the reduction in lattice parameters observed after sintering indicate that the dopant ions are effectively incorporated into the fluorite structure of GDC. Considering the ionic sizes, $Ce^{4+}$ (101 pm) is substantially larger than both $Ni^{2+}$ (83 pm) and $Co^{3+}$ (68.5 pm) or $Co^{2+}$ (79 pm), suggesting that substitutional incorporation on the $Ce^{4+}$ sites is the most plausible mechanism [171]. Interstitial incorporation is unlikely as the fluorite structure of GDC offers only limited interstitial sites and would also typically result in lattice expansion, which is not the case here.

Interestingly, the lattice parameter of GNDC1230 is slightly smaller than that of GCDC1230 despite $Ni^{2+}$ having a larger ionic radius than $Co^{3+}$ in sixfold coordination. This apparent contradiction can be explained by differences in oxidation state and coordination environment within the GDC lattice, as well as differences in defect chemistry. Ni incorporation may promote additional oxygen vacancy formation or local lattice distortions that contribute to an overall contraction of the lattice parameter. Moreover, the valence state of Co can vary between $Co^{2+}$ and $Co^{3+}$ and its actual state in the lattice is potentially influenced by the local oxygen partial pressure during sintering. When compared with the dilatometry results, the enhanced sintering kinetics and lower sintering onset temperatures observed for the co-doped samples are consistent with the dopants being present within the lattice, facilitating mass transport during sintering through increased defect concentrations and enhanced diffusion pathways. Additionally,

the potential for liquid phase formation at grain boundaries during sintering may further accelerate densification, although no signs of a liquid phase were observed in SEM analysis.

## 4.3 Dispersant selection and concentration determination

The choice and concentration of the dispersant is important when regarding stability, homogeneity and processability of ceramic suspensions. In the case of screen-printing pastes, improper selection or concentration of the dispersant can lead to issues such as particle re-agglomeration, poor print quality and formation of secondary phases during sintering caused by chemical incompatibility. During post-stack test analysis of the prototype cell, such impurities were observed in the screen-printed GDC containing layers (fuel electrode and electrolyte) as shown in Figure 4.7. Here, secondary phases containing gadolinium and phosphorus ($GdPO_4$ and $GdP_5O_{14}$) could be identified. After ruling out other sources of contamination, ICP-OES analysis of the dispersant used (Nuosperse FX9086) indicated it as the only potential source of phosphorus.

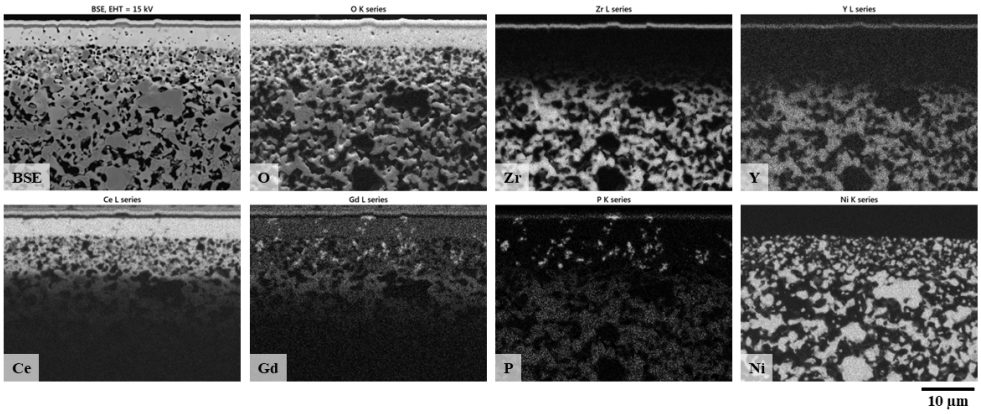


**Figure 4.7:** Backscattered electron (BSE) image of a cross-section through a prototype full cell after stack testing. Accompanied by EDS elemental maps for O, Zr, Y, Ce, Gd, P and Ni. A distinct co-localization of Gd and P is visible in specific regions oft the GDC containing screen-printed layers, indicating potential formation of secondary Gd-P-rich phases. Distribution of other elements corresponds to the expected compositions. Analysis was carried out by Luzie Wehner (IMD-1).

Due to the contamination most likely stemming from the dispersant and the switch in powder supplier as mentioned earlier, a new dispersant system had to be selected. This was done to ensure stable dispersion of GDC in the terpineol-based paste system, while avoiding the formation of a secondary phase. Because terpineol is a non-polar solvent, electro kinetic measurements such as zeta potential analysis were not applicable, as they rely on the presence of a polar solvent to form a strong enough electric double layer. Instead, a screening approach was adopted based on rheological characterizations. As already explained in Chapter 3.2.8, zero shear viscosity measurements were performed to identify a suitable dispersant and its concentration. Here, lower viscosities imply a higher dispersion quality. For

this, suspensions containing 75 wt% of GDC and varying dispersants at two initial concentrations of 1 wt% and 3 wt% were prepared. The dispersant system resulting in the lowest viscosities was selected for further optimization. In this optimization, more suspensions with dispersant concentrations between 1 wt% and 9 wt% were prepared and tested.

For the initial screening, 9 different dispersants were tested. However, the following results only include dispersants that were soluble in terpineol. Figure 4.8 A shows the result of that screening experiment. Here, the dispersant Hypermer KD2 was selected for more detailed investigations, as it resulted in the lowest viscosities with both tested concentrations. In the subsequent optimization step, dispersant concentrations ranging from 1 wt% to 9 wt% were tested again using zero shear viscosity measurements. As shown in Figure 4.8 B, the lowest viscosity was achieved at a concentration of 5 wt%. However, this value is specific to the particular powder batch used and does not necessarily translate across powders with differing specific surface areas. To ensure a more transferable formulation, the dispersant concentration was recalculated based on the powder's measured specific surface area. This resulted in an optimal Hypermer KD2 concentration of 13 mg/m² ceramic surface area. This is aimed to offer a more robust and reproducible basis for paste recipes, especially when working with powders of varying particle sizes.

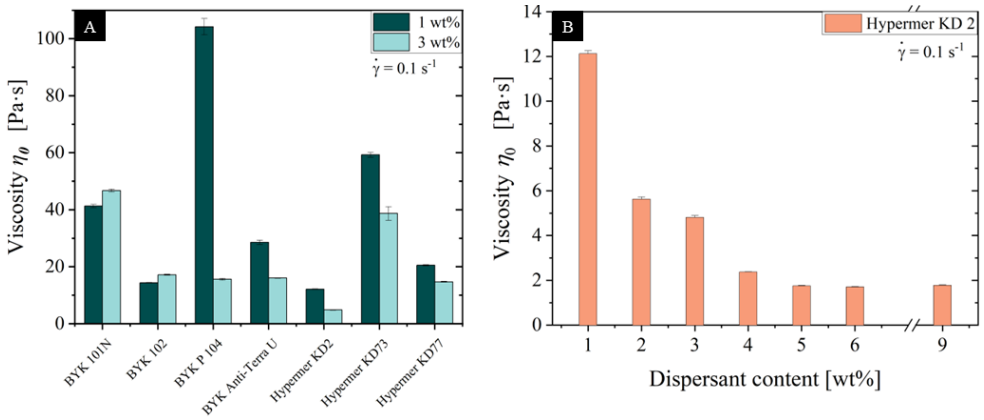


**Figure 4.8:** Zero shear viscosity measurements of suspensions containing 75 wt% GDC with varying dispersants and concentrations. **A** Initial screening results for different dispersants at concentration of 1 wt% and 3 wt%, showing Hypermer KD2 as the most effective dispersant. **B** Concentration-dependent viscosity of suspensions with Hypermer KD2, tested between 1 wt% and 9 wt%. Lowest viscosity was achieved at 5 wt%.

## 4.4 Influence of rheological behavior on dried layer properties

In this work, layers of five different pastes were evaluated based on their dry layer thickness $d_{dry}$ and geometric accuracy via the fidelity factor $F_{PE}$. Values for these parameters were obtained by conducting differential scanning measurements of printed and dried layers using the CT 300T optical inspection system as described in Chapter 3.2.7. For this, the layers were printed onto stainless-steel substrates using a polyester screen with a screen opening of 40 mm x 40 mm, a mesh with 48 threads/cm and a thread thickness of 55 µm. Print settings were kept constant with a squeegee speed of 110 mm/s, squeegee pressure of 1.5 bar (0.15 MPa) and a snap-off distance of 1.6 mm. All layers were dried at 60 °C for at least 24 h before measuring. Table 4.3 summarizes the solids and binder content of each paste, alongside their rheological parameters damping factor $\tan\delta$, yield point $\gamma_y$ and flow point $\gamma_f$ when applicable. Furthermore, the aforementioned layer evaluation characteristics are also listed. While rheological properties such as viscosity $\eta$, storage modulus $G'$ and loss modulus $G''$ are typically used for paste characterization in literature, their correlation with the evaluation criteria was unexpectedly weak. Values for storage and loss modulus were taken as averages from within the linear viscoelastic region during an amplitude sweep test. This lack of statistical significance is illustrated in Figure 4.9 through Figure 4.11 respectively, where no clear trends could be identified using regression analysis. Therefore, the following in-depth discussion focuses solely on the yield point and damping factor.

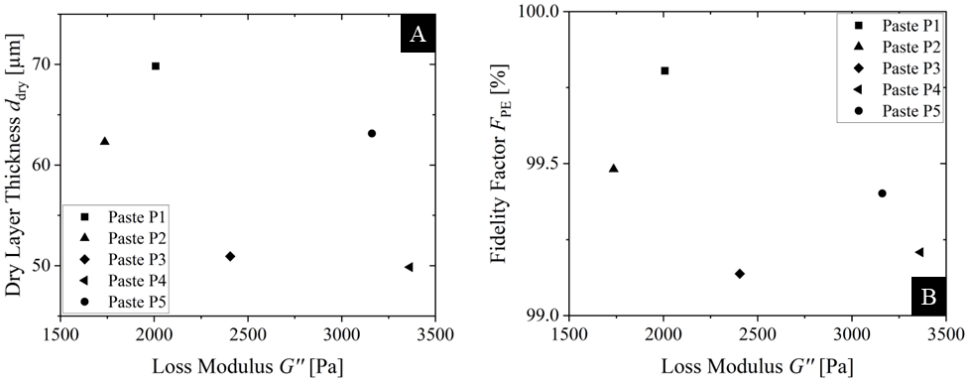


**Figure 4.9: A** Loss modulus $G''$ taken as an average value from the linear viscoelastic region of 5 pastes vs dry layer thickness $d_{dry}$ ($R^2 = 0.26$) and **B** fidelity factor $F_{PE}$ ($R^2 = 0.29$). There is no significant correlation between the loss modulus $G''$ and the evaluation parameters as indicated by the $R^2$ values.

**Table 4.3:** Solids and binder content of 5 different pastes and their rheological parameters loss factor, yield point and flow point, if applicable. Indication of an average layer thickness and an average dimensional accuracy of printed and dried layers. Layers were produced under identical conditions.

| # | Solids [wt.%] | Binder [wt.%] | Grain Size $d_{10}$/ $d_{50}$/ $d_{90}$ [µm] | Damping Factor tan δ [1] | Yield Point $\gamma_y$ [%] | Flow Point $\gamma_f$ [%] | Layer Thickness $d_{dry}$ [µm] | Fidelity Factor $F_{PE}$ [%] |
|---|---|---|---|---|---|---|---|---|
| P1 | 68 | 2 | 0.07 / 0.10 / 0.17$^{P}$ | 0.79 | 58 | 87 | 70 ± 2 | 99.8 ± 0.0 |
| P2 | 64 | 3 | 0.07 / 0.10 / 0.16$^{P}$ | 0.97 | 52 | 58 | 62 ± 3 | 99.5 ± 0.0 |
| P3 | 64 | 3 | 0.07 / 0.12 / 0.24$^{T}$ | 1.10 | 43 | - | 51 ± 1 | 99.1 ± 0.1 |
| P4 | 56 | 5 | 0.12 / 0.20 / 0.32$^{T}$ | 1.14 | 42 | - | 50 ± 2 | 99.2 ± 0.0 |
| P5 | 63 | 3 | 0.07 / 0.10 / 0.17$^{P}$ | 0.93 | 52 | 53 | 63 ± 2 | 99.4 ± 0.0 |

P: Planetary Ball Mill PM-MPS Route
T: Tumbling Mixer TM-DPS Route

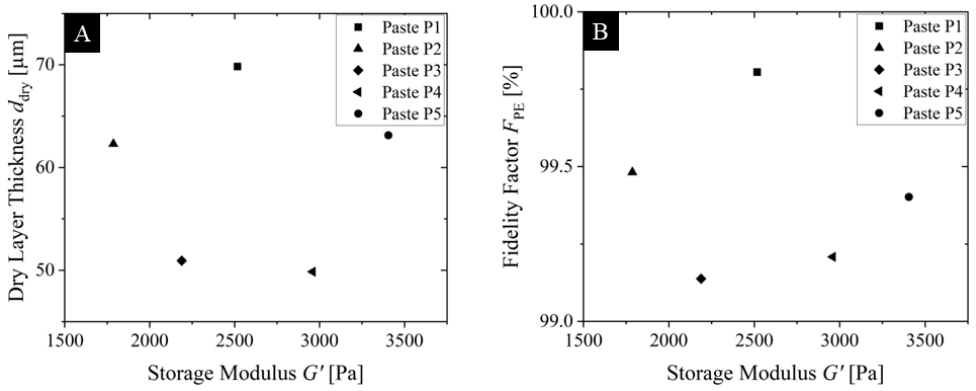


**Figure 4.10: A** Storage modulus $G'$ taken as an average value from the linear viscoelastic region of 5 pastes vs dry layer thickness $d_{dry}$ ($R^2 = 0.00$) and **B** fidelity factor $F_{PE}$ ($R^2 = 0.01$). There is no significant correlation between the storage modulus $G'$ and the evaluation parameters as indicated by the $R^2$ values.

Although one might expect a direct relationship between solid content and layer thickness, the data presented here suggests that relying solely on the description of solid and binder contents in wt% is insufficient for fully describing a paste and predicting its print outcome. For example, paste P4 which has the lowest solid content, produces the thinnest layer at 50 µm. However, this apparent correlation between solid content and layer thickness breaks down when comparing pastes P2 and P3, which have the same composition but differ in layer thickness of about 10 µm. Moreover, paste P3 yields a layer thickness comparable to that of P4, despite containing 8 wt% more solids. These observations indicate that other factors significantly influence the deposition outcome that must be considered alongside basic compositional values.

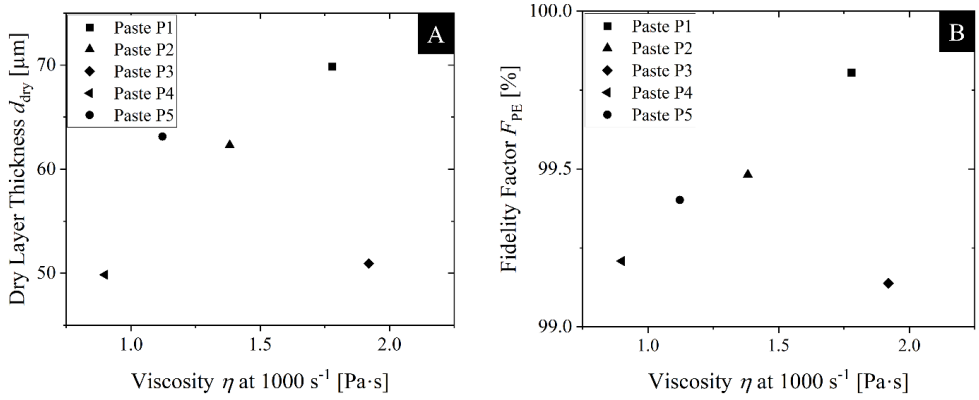


**Figure 4.11: A** Viscosity $\eta$ measured at shear rates of 1000 $s^{-1}$ of 5 pastes vs dry layer thickness $d_{dry}$ ($R^2 = 0.05$) and **B** fidelity factor $F_{PE}$ ($R^2 = 0.06$). There is no significant correlation between the viscosity and the evaluation parameters as indicated by the $R^2$ values. Viscosities were measured at 20 °C.

### 4.4.1 Damping factor tan $\delta$

A clearer and more meaningful correlation emerges when focusing on the aforementioned rheological properties of the pastes damping factor tan $\delta$ and yield point $\gamma_y$ first, rather than on the composition of the pastes. As shown in Figure 4.12, the damping factor exhibits a strong relationship with both the measured dry layer thickness and the fidelity factor. The corresponding $R^2$ and Pearson $r$ values exceed 0.9 in all cases, indicating a high degree of linear correlation. This already hints towards rheological behavior being a more direct predictor of print outcome. Regarding layer thickness depicted in Figure 4.12 A, an increase in the damping factor is associated with thinner dried layers. This trend can be attributed to the increase in dominating viscous behavior, which in turn reduces the elastic solid-like behavior of the paste and enhances the ability to flow. This increased flowability may lead to more efficient particle packing or increased paste bleeding, both of which can result in thinner printed layers. Another possible explanation involves the screen flooding process prior to printing. In pastes with higher damping factors, potentially a reduced quantity of paste is filled into the screen mesh openings. The volume of paste retained in each mesh opening is influenced by surface tension and adhesion effects, which are affected by rheological behavior. A lower damping factor may promote the formation of more concave menisci within the mesh opening, reducing the paste volume and resulting in thinner printed layers.

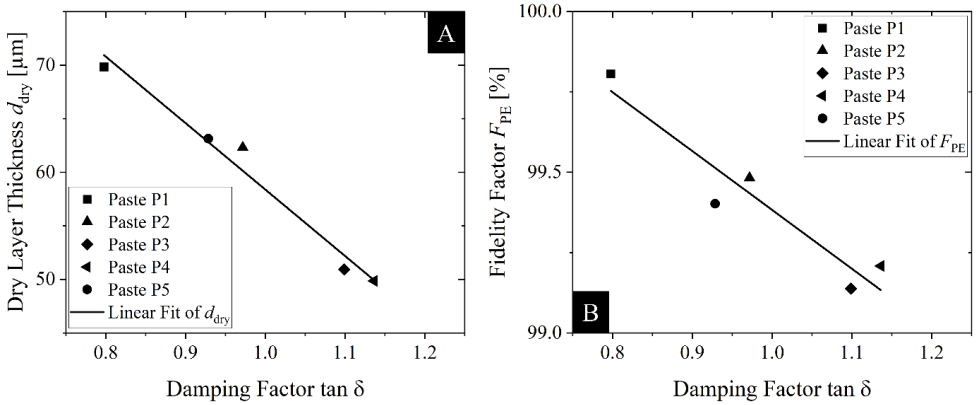


**Figure 4.12: A** Influence of the damping factor $tan\,\delta$ on the dry layer thickness $d_{dry}$ ($R^2$ = 0.97) and **B** on the fidelity factor $F_{PE}$ ($R^2$ = 0.90) with regression lines using 5 different screen-printing pastes. Damping factor were calculated from $G'$ and $G''$ values obtained from the linear viscoelastic region during amplitude sweep tests.

A similar trend is observed when correlating the damping factor with the fidelity factor as shown in Figure 4.12 B. Here for example, paste P1, which has the lowest damping factor produces layers with the highest dimensional accuracy. Interestingly, paste P4 does not result in the lowest fidelity, despite producing the thinnest layers. This suggests that with this paste a denser packing without significant bleeding might be possible.

### 4.4.2 Yield point $\gamma_y$ and yielding behavior

When analyzing the relationship between yield point and the layer evaluation criteria, Figure 4.13 A and B demonstrates a clear correlation that pastes yielding at higher deformation values tend to produce both thicker dry layers and layers with higher dimensional accuracy. In general, a higher yield point corresponds to a stronger particle-binder network, which is able to resist plastic deformation more effectively under applied stress [172]. Here, a more robust internal structure implies stronger interparticle and binder interactions at rest, making the paste more resistant to structural breakdown induced by the printing process. Furthermore, a stronger network may undergo less irreversible deformation during the printing process and may be able to recover more of its initial structure afterwards. This structural resilience appears to contribute favorably to improved fidelity and increase layer thickness, as indicated by the data presented.

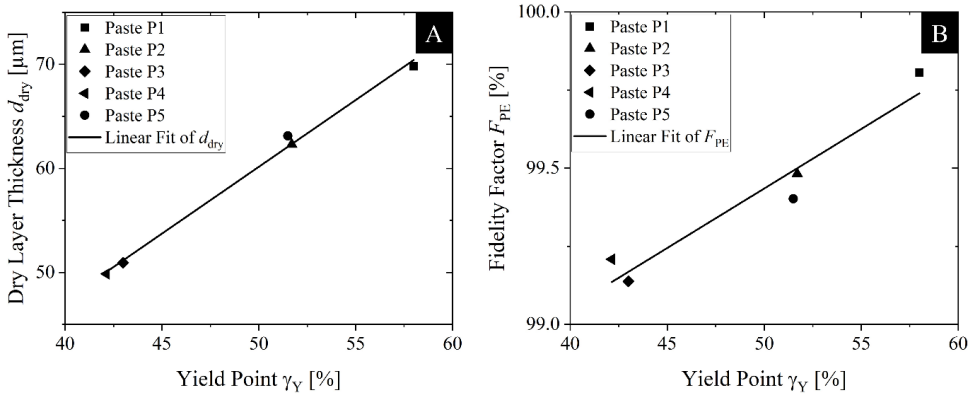


**Figure 4.13: A** Influence of the yield point$\gamma_y$ on the dry layer thickness $d_{dry}$ ($R^2$ = 0.99) and **B** on the fidelity factor $F_{PE}$ ($R^2$ = 0.93) with regression lines using 5 different pastes. Yield points were obtained at the end of the linear viscoelastic region during amplitude sweep tests.

However, it is important to note that yielding does not occur instantaneously but rather as a process that evolves more or less gradually over a deformation range. This transitional behavior is better captured by examining the flow transition index (*FTI*), which reflects the extent of deformation between yield point and flow point, as already outlined in Chapter 3.2.8. For pastes that exhibit both a yield and a flow point, the FTI may provide additional insights into how gradually or abruptly the paste transitions from more solid-like behavior to liquid-like behavior. As shown in Figure 4.14, pastes with a high FTI, that transition more gradually into flow, tend to produce thicker dry layers that simultaneously exhibit higher fidelity.

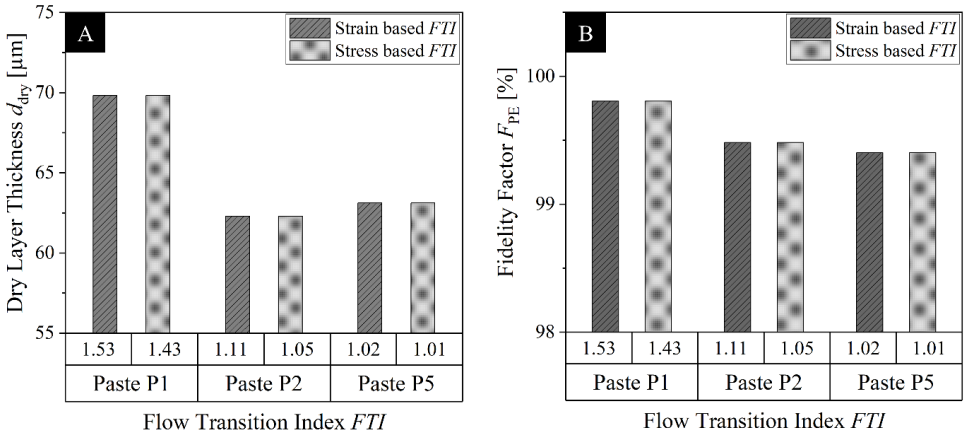


**Figure 4.14: A** Strain-based and stress-based *FTI* vs dry layer thickness $d_{dry}$ and **B** fidelity factor $F_{PE}$ of 3 testes pastes, that had a showed a transition behavior into flowing. *FTI* were calculated from yield and flow points that were obtained during amplitude sweep tests.

These results can be better understood by considering the thixotropic nature of these pastes, which was investigated using the 3-interval-thixotropy-test (3ITT). Thixotropy refers to a material's ability to undergo structural breakdown under shear and then gradually rebuild its internal structure once the external stress is removed. The 3ITT specifically examines the paste's quasi-undisturbed structural recovery following a controlled deformation phase which is aimed to mimic conditions experienced during the printing process. Particularly interesting here is that the observed flow transition behavior appears to act in opposition to the thixotropic recovery behavior. When comparing the 3ITT results shown in Figure 4.15 with the *FTI* values, a clear relationship emerges. Here, vertical lines and $\Delta t$ indicate the time within the 3rd interval where structural recovery defined by $G' = G''$ occurs. Pastes that exhibit a more gradual transition into flow, indicated by a higher *FTI*, tend to recover significantly faster after printing. For example, paste P1 shows the most gradual behavior into flow but regains its elastic-dominant behavior in just 5 seconds after the shear period ends. Conversely, paste P5 with the most abrupt yielding behavior fails to recover into its elastic-dominant structure even after 386 s. From a printability standpoint, this means that pastes capable of quickly regaining a more solid-like structure after printing are more likely to produce layers with greater thickness and higher dimensional accuracy. Their more rapid transition back to a rigid state seems to facilitate the stabilization of the printed features and prevent excessive deformation after deposition.

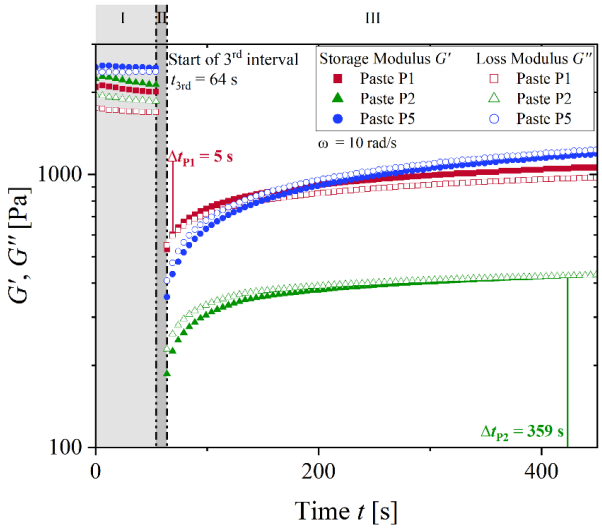


**Figure 4.15:** Results of the 3ITT for Paste P1 (red), Paste P2 (green) and Paste P5 (blue). Recording of the measured values in the first and third interval using oscillation. Simulation of the printing process in the second interval using rotation (no measured values for storage and loss modulus). Vertical lines and $\Delta t$ indicate the time within the 3rd interval where structural recovery ($G'' = G'$) occurs. Measured at 20 °C with a serrated plate-plate system (25 mm).

## 4.5 Influence of powder characteristics and paste composition on rheological properties

Having established how the rheological properties damping factor and yielding behavior correlate with printing outcomes such as layer thickness and fidelity, the next logical step is to explore what governs these key rheological behaviors. Therefore, this subsection shifts focus on the paste composition itself, examining how variations in formulation influence rheology. Understanding these compositional dependencies was essential for tailoring paste formulations that achieve the desired rheological properties and print performance.

### 4.5.1 The ceramic powder

As already stated in Chapter 4.1, the initial layers developed by Jun Zhang for the tri-layer electrolyte prototype cell, while showing excellent performance, ultimately could not be reproduced in this work. Through the course of this work, it was discovered that the change in powder manufacturer was the decisive factor responsible for this. However, this critical insight was only able to come to light and be quantified through a more detailed analysis of the powder characteristics, going beyond the more traditional metrics. By applying the bimodality coefficient as a more refined measure (see Chapter

3.2.1), it was possible to identify subtler aspects of the particle size distribution, that would have otherwise been overlooked.

To investigate this, a total of nine screen-printing pastes were analyzed. This list comprises the five pastes previously discussed (see Table 4.3), along with four additional pastes which compositions can be found in Table 4.4.

**Table 4.4:** Solids and binder content of 4 additional pastes and their rheological parameters loss factor and yield point used to assess the influence of powder characteristics on rheological parameters.

| # | Solids [wt.%] | Binder [wt.%] | Grain Size $d_{10}$/ $d_{50}$/ $d_{90}$ [µm] | Damping Factor tan δ [1] | Yield Point $\gamma_y$ [%] | Flow Point $\gamma_f$ [%] |
|---|---|---|---|---|---|---|
| P6 | 64 | 3 | 0.07 / 0.12 / 0.24$^{T}$ | 1.55 | 40 | - |
| P7 | 56 | 5 | 0.11/ 0.19 / 0.29$^{P}$ | 1.12 | 44 | - |
| P8 | 64 | 3 | 0.07 / 0.11 / 0.27$^{T}$ | 1.16 | 53 | - |
| P9 | 64 | 3 | 0.06 / 0.10 / 0.27$^{T}$ | 1.77 | 37 | - |

P: Planetary Ball Mill PM-MPS Route
T: Tumbling Mixer TM-DPS Route

Traditionally, powder characterization relies heavily on summary metrics like $d_{10}$, $d_{50}$ and $d_{90}$ of a particle size distribution, with the $d_{50}$ value as the mean particle diameter being the most commonly reported parameter in studies relating to rheology in suspension-based processes. However, as shown in Figure 4.16 A and B, correlating this $d_{50}$ value with the two previously determined most influential rheological properties damping factor and yield point reveals no meaningful trend. This suggests that in

these cases, the median particle size itself has no distinguishable influence on these rheological properties. Similarly, no clear relationship is observed when trying to correlate solid content as another traditionally used metric with yield point and damping factor as shown in Figure 4.16 C and D, within the investigated range.

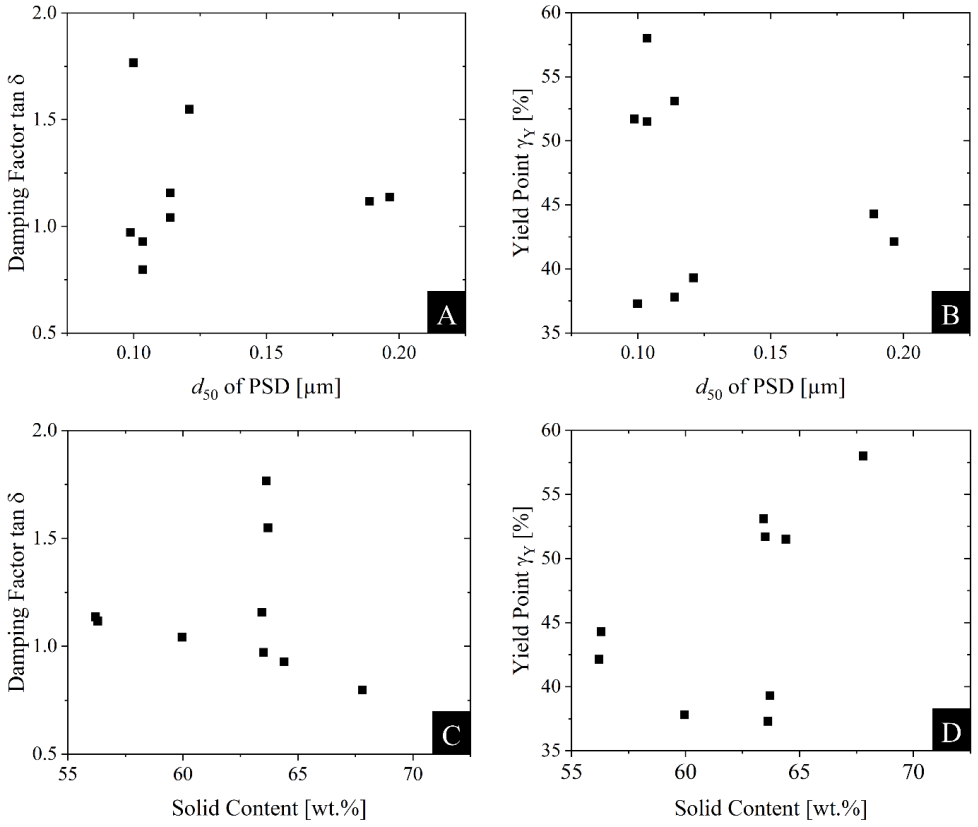


**Figure 4.16:** $d_{50}$ of PSD vs damping factor tan δ **A** and yield point $\gamma_y$ **B**. Solid content in wt% vs damping factor $tan\,\delta$ **C** and yield point $\gamma_y$ **B** of 9 different pastes. There is no clear correlation observable.

These results emphasize the limitations of relying solely on conventional particle size or paste metrics and reinforce the need for more advanced descriptors. For example, when the powders are analyzed in more detail using the bimodality coefficient, skewness and kurtosis, clear linear correlations emerge. As shown in Figure 4.17 A-C, these parameters exhibit strong linear correlations with the damping factor ($R^2$ = 0.75, 0.87 and 0.89 respectively). As the asymmetry of the PSD increases, the damping factor also increases, which results in progressively more dominating viscous behavior of the paste. Although these correlations are weaker than those seen in the previous chapter between rheological properties and print outcomes, this is expected. Rheological behavior is influenced by a combination of interacting factors

and here only one of such factors is being isolated. This effect becomes especially evident in pastes or data points that lie directly above each other in Figure 4.17. In these cases, multiple pastes with different compositions were produced from the same powder, also resulting in slightly different rheological properties although the overarching trend stays the same. Interestingly, while the shape of the particle size distribution appears to significantly affect the damping factor, it does not show a meaningful correlation with the yield point as illustrated in Figure 4.17 D-F. This suggests that the damping factor is more sensitive to PSD asymmetry, while the yield point seems to be more influenced by other structural or compositional elements.

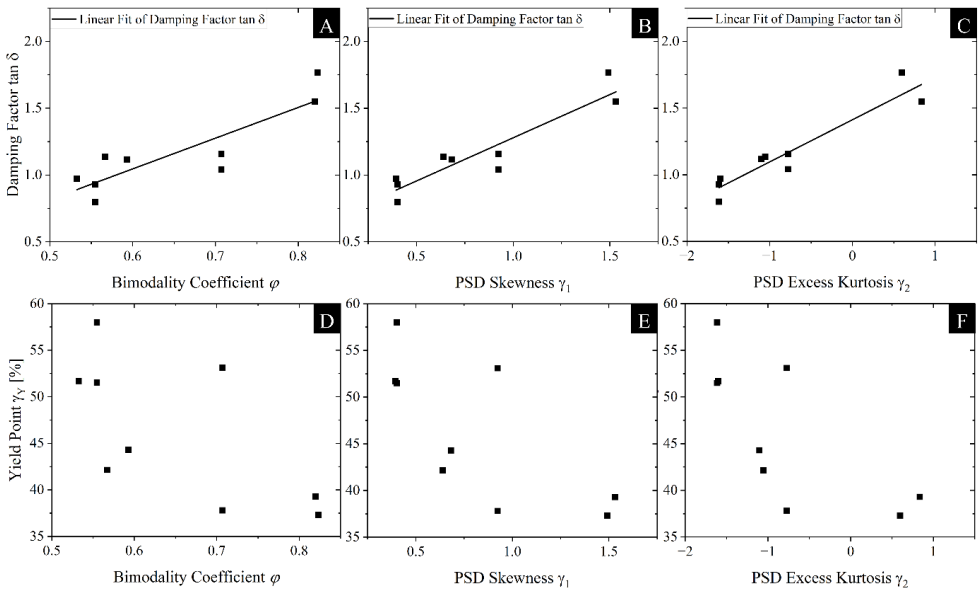


**Figure 4.17: A-C** Damping factor $tan\,\delta$ vs. powder characteristics bimodality coefficient $\varphi$ ($R^2$ = 0.75), skewness $\gamma_1$ ($R^2$ = 0.87) and excess kurtosis $\gamma_2$ ($R^2$ = 0.89), showing a linear regression. **D-F** Yield point $\gamma_y$ vs. powder characteristics bimodality coefficient, skewness and excess kurtosis without a linear regression. Values of the rheological parameters were obtained from the amplitude sweep test.

The influence of PSD asymmetry becomes even more apparent when examining amplitude sweep tests of three pastes with identical compositions (64 wt% solids and 3 wt% binder), but different PSD profiles. As shown in Figure 4.18, the green and blue curves represent pastes formulated with monomodal powders (bimodality coefficients $\varphi$ = 0.53 and 0.55), while the red curve corresponds to a paste made from a bimodal powder with $\varphi$ = 0.82. Despite having the same composition, the pastes behave very differently. The monomodal powders produce pastes with dominant elastic behavior ($G' > G''$) within the linear viscoelastic region, whereas the paste with the bimodal powder exhibits dominant viscous behavior ($G' < G''$). Since the asymmetry of the bimodal PSD is most likely stemming from residual agglomerates, it is hypothesized that these agglomerates cause this destabilization of the three-dimensional network. This destabilization would then lead to the paste behaving more like a suspension

with untangled polymer chains that shows dominant viscous behavior. PSD analysis revealed that the agglomerates are typically 10 to 100 times larger than the average particle.

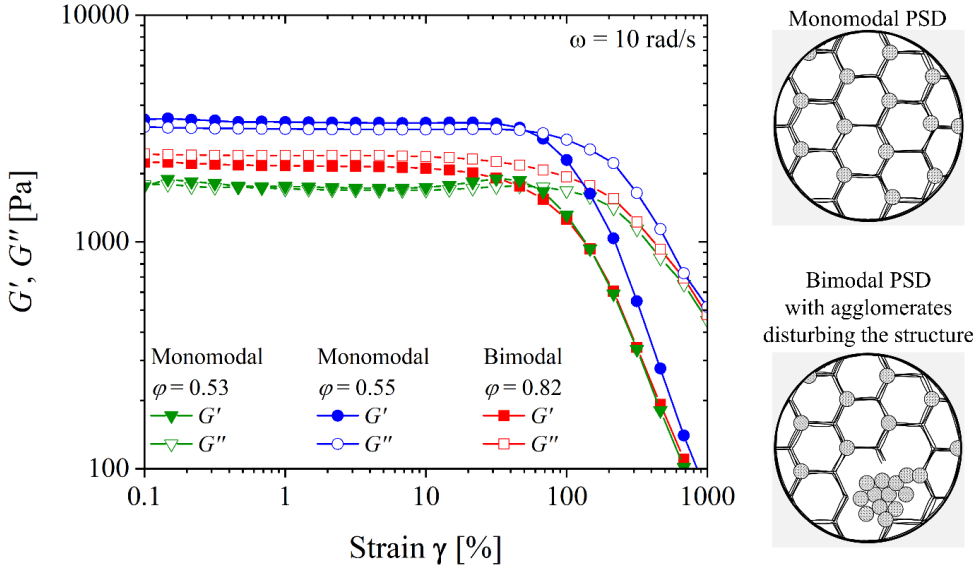


**Figure 4.18:** Results of amplitude sweep tests for pastes with monomodal powder (green and blue) and a paste with a similar composition but bimodal powder (red). Measured at 20 °C with a serrated plate-plate system (25 mm) and an angular frequency of 10 rad/s. All three pastes contained 64 wt.% of ceramic particles and 3 wt.% of binder.

This trend is further supported by specific surface area measurements. As shown in Figure 4.19 A, a clear linear correlation exists between specific surface area and the damping factor. Here, low surface areas, as a sign of insufficient deagglomeration during powder processing, lead to higher damping factors.

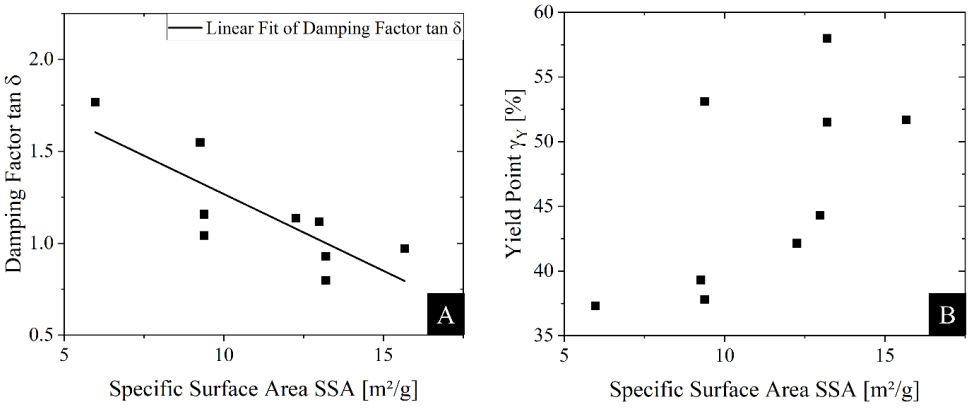


**Figure 4.19: A** Specific surface area SSA vs. damping factor $tan\,\delta$ with a linear fit ($R^2 = 0.66$). **B** Specific surface area SSA vs. yield point $\gamma_y$ without a linear fit. Values of the rheological parameters were obtained from the amplitude sweep test.

This correlation reinforces the hypothesis that residual agglomerates contribute to more pronounced viscous behavior. However, analogous to the PSD metrics, specific surface area shows no meaningful correlation with the yield point as shown in Figure 4.19 B. This re-establishes that the factors influencing yield stress are distinct from those affecting the damping factor.

### 4.5.2 The polymer binder

Since no meaningful correlation between the powder PSD and the yield point could be observed, it becomes evident that other factors must be responsible for governing the structural strength of the paste. Therefore, the influence of the polymer binder, as the second major component in screen-printing pastes and responsible for network formation, was investigated.

When assessing the binder's influence, particularly when trying to compare pastes produced with different powders, it is more insightful to consider the binder-to-ceramic surface area ratio rather than a simple weight-based binder content. This approach accounts for the actual interaction sites between polymer chains and the ceramic particle surface, which are necessary to form a cohesive three-dimensional network. Figure 4.20 A illustrates the relationship between this ratio and the damping factor. Although a regression is indicated, the relatively low $R^2$ value of 0.39 suggests only a weak correlation. Still, the observed trend shows that an increase in binder per ceramic surface area may promote a shift to more viscous dominating behavior.

This trend becomes clearer in direct comparison of two pastes with similar particle size distributions but differing binder contents, as shown in Figure 4.20 B. Here, the paste with less binder exhibits elastic-dominated behavior in the linear viscoelastic region ($G' > G''$). The paste with the higher binder content shows dominant viscous behavior ($G' < G''$). This supports a hypothesis that once the binder content exceeds critical concentrations relative to the available ceramic surface, the particle network loses

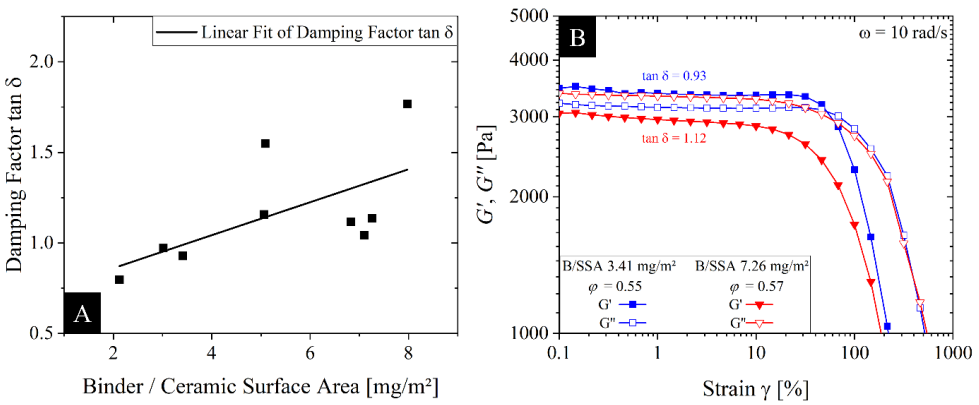


**Figure 4.20**: **A** Binder content per ceramic surface area vs. damping factor $tan\,\delta$ with a linear fit ($R^2$ = 0.39). **B** Results of amplitude sweep tests for two pastes with monomodal powder and low binder content (blue) and significantly higher binder content (red). Measured at 20 °C with a serrated plate-plate system (25 mm) and an angular frequency of 10 rad/s.

structural strength. The system begins to behave more like an unstructured polymer solution or melt, where insufficient anchoring points result in reduced elastic character [173].

In contrast to the relatively weak influence on the damping factor, the binder-to-surface area ratio shows a much stronger and clearer correlation with the yield point. As shown in Figure 4.21 A, the $R^2$ value of 0.81 points to a strong relationship in which an increase in binder content relative to ceramic surface area leads to a shift of the yield point towards lower deformation values. This suggests that the strength of the network diminishes as binder content increases, potentially due to reduced particle-particle connectivity

This relationship is reinforced by a comparison of two pastes made with the same powder, but different binder contents, shown in Figure 4.21 B. The paste with the lower binder content (green curve) yields at higher strains, indicating a more flexible network structure. However, its yielding behavior is also different. Both storage and loss moduli initially increase, which is hypothesized to indicate microcracks forming within the structure, that only completely penetrate the measuring gap at higher deformations, characterized by the kinking of the curves after passing through their respective maximum [157]. Interestingly, while this paste yields at a higher strain, its critical yield stress (2300 Pa) is actually lower than that of the paste with more binder (2600 Pa). This apparent contradiction underscores the distinction between resistance to deformation (strain) and resistance to applied force (stress) in evaluation yielding behavior. A higher critical strain, as shown by the paste with less binder, indicates greater tolerance to deformation, which implies a more ductile and flexible network.

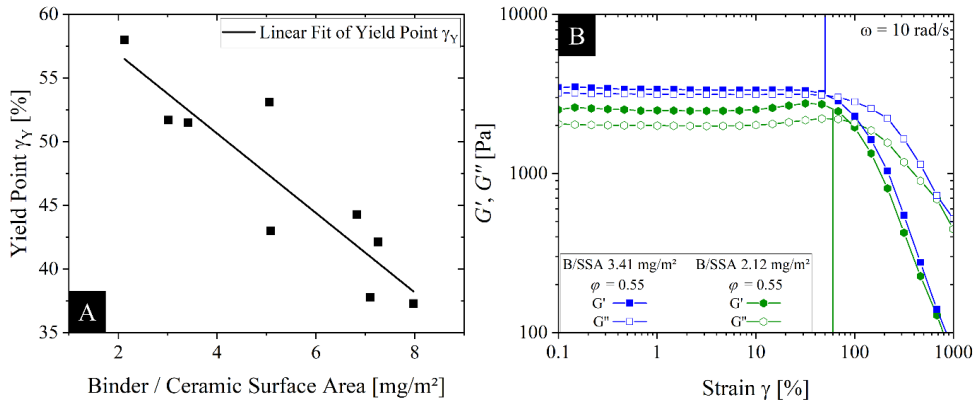


**Figure 4.21: A** Binder content per ceramic surface area vs. yield point $\gamma_y$ with a linear fit ($R^2$ = 0.81). **B** Results of amplitude sweep tests for pastes made from the same powder and a higher binder content per ceramic surface area (blue) and a lower binder content per ceramic surface area (green). Here, vertical lines indicate the position of the respective yield points. Measured at 20 °C with a serrated plate-plate system (25 mm) and an angular frequency of 10 rad/s.

However, its lower critical stress implies that less force is needed to initiate flow. Conversely, the paste with higher binder content yields at lower strains but withstands greater stress, suggesting a stiffer and more brittle network. While both critical stress and strain are informative, it is argued that critical strain

is more practically relevant in the context of screen printing. Here the paste is subjected to rapid and substantial deformations, well beyond the linear viscoelastic range. The applied stresses typically far exceed the measured yield stresses. This means that the ability of the paste to resist large strains without structural breakdown seems to play a decisive role in print quality. As demonstrated through this work, this tolerance to deformation is closely tied to print fidelity and structural integrity before and after printing.

## 4.6 Microstructure development of single GDC layers co-sintered on fuel electrode supports

In this chapter, the microstructure evolution of single screen-printed GDC electrolyte layers during co-sintering on NiO-8YSZ supports for half-cell fabrication is investigated. Building upon dilatometric analysis and microstructure characterization of pellets (see Chapter 4.2), this chapter aims to determine whether the observed sintering behavior and microstructural trends of the different GDC powders can be directly translated to screen-printed layers under realistic co-sintering conditions. All half-cells investigated in this section were fabricated by screen-printing single GDC electrolyte layers onto NiO-8YSZ substrates that were calcined at 1230 °C, followed by co-sintering at 1400 °C for 5 h under conditions relevant for standard half-cell processing. Figure 4.22 displays representative polished cross-sections of the investigated half-cells alongside quantified porosity values of the respective GDC electrolyte layers. Overall, a clear variation in final porosity was observed, depending on the GDC powder used for paste preparation. The results indicate that, when compared to pellet sintering, porosity in the co-sintered screen-printed layers remains significantly higher across all compositions. This can be attributed to lower green densities typically achievable in screen-printed layers compared to uniaxially pressed pellets. Furthermore, the potential constrained sintering imposed by the more rigid NiO-8YSZ support can inhibit densification within the GDC layer. However, porosity trends versus calcination temperature show that for both calcined and co-doped samples, an increase in pre-calcination temperature of the GDC powder generally correlates with increased final porosity in the co-sintered layers. This aligns with the dilatometry trends previously discussed in Chapter 4.2. Here, higher calcination temperatures lead to reduced sintering activity, higher sintering onset temperatures and lower total shrinkage. Although direct dilatometry data for all powders used for the presented screen-printed layers are not available, reasonable interpretation of the observed trends still suggest consistency between the lower sintering activity and higher porosity observed in the co-sintered layers. However, notable unexpected deviations could be observed. GNDC1340 for example exhibits an exceptionally high porosity of 27.0 %, which is considerably higher than the undoped GDC1340 layer (12.6 %), despite the expectations of enhanced sintering kinetics due to co-doping with NiO. Moreover, the porosity in GNDC1340 appears predominantly elongated and potentially interconnected, indicating the formation of open porosity networks rather than isolated pores. This suggests that factors beyond

intrinsic powder sintering behavior, such as interactions with the support or printing setup may play a dominant role under co-sintering conditions. Similarly, GCDC1340 also exhibits higher porosity values with 17.6 % than its undoped GDC1340 counterpart. Although here, porosity seems to be less elongated and more roundly shaped and closed off.

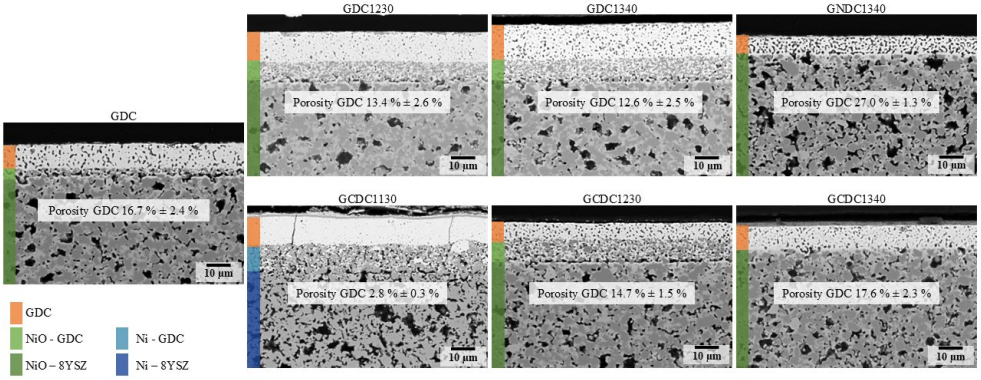


**Figure 4.22:** Polished cross-sections of screen-printed GDC electrolyte layers co-sintered on NiO-8YSZ supports at 1400 °C for 5 h. Meausred porosity from image analysis is shown for each composition. Differences in microstructure and porosity demonstrate the influence of powder pre-treatment and co-doping on densification during differential sintering.

Furthermore, GDC1340 exhibited a slightly lower porosity than GDC1230 (13.4 %), despite its lower observed sintering activity analyzed in the dilatometry measurements. Although when taking the standard deviation into account, both porosities are virtually identical. However, this counterintuitive result further highlights the dominant influence of co-sintering with the NiO-8YSZ support [174]. It could be hypothesized that the slower sintering kinetics of GDC12340 might align more closely with the later stage shrinkage of the support. Contrary to this hypothesis, GCDC1130 with presumably the highest sintering activity at the lowest temperatures exhibits by far the lowest porosity with only 2.8 %. This could indicate that the early-stage sintering behavior of the electrolyte might be more critical for densification than alignment with substrate sintering behavior. Here, the high sintering activity already starting at lower temperatures might facilitate almost complete pore removal before substantial substrate shrinkage even begins.

Nonetheless, these observations suggest that the interactions of support and electrolyte might be crucial for the evolution of final microstructure after co-sintering. Furthermore, it should be considered that differences in paste formulation, driven by varying specific surface areas and particle size distributions of the employed powders may also contribute to the observed porosity differences and some of these counterintuitive results. For example, paste with higher binder contents could potentially result in lower densities after debindering. This may affect pore structure formation and densification during early stages of sintering. This further emphasizes that sintering behavior trends derived from dilatometry measurements might not always be directly translatable to screen-printed layers, especially when the

sintering behavior of the support and its interplay with the electrolyte layer is not considered. Therefore, a more detailed analysis of these interactions, including their dependence on calcination and sintering temperatures and dwell time will be provided in Chapters 5.3 to 5.5. Here, tri-layer electrolyte half-cell sintering behavior, shrinkage and microstructure evolution under various sintering conditions will be systematically discussed.

While the precise mechanisms driving the observed microstructure evolution remain complex and not fully resolved, it is evident that compared to the GDC layer with the untreated as-received GDC powder, significant improvements in layer density were achieved through powder modifications. Overall, nearly all co-sintered GDC layers exhibited satisfactory microstructures with only a few exceptions showing notably higher porosity. Importantly, no delamination was detected in any sample, indicating that despite inherent shrinkage mismatches between electrolyte layers and supports, adhesion was maintained under the used sintering conditions. These results emphasize that although co-sintering is challenging, careful optimization of powder characteristics and sintering behavior can enable the production of sufficiently dense layers, suitable for solid oxide cells.

## 4.7 Potential defects in screen-printed layers

### 4.7.1 Insufficient paste leveling

A common phenomenon that can occur in screen printing is insufficient paste leveling immediately after the printing process. This can result in a range of defects, each with its own unique appearance and potential underlying causes. Three of these defects linked to abnormal leveling behavior were investigated in this thesis and will be discussed in the following.

**Paste bleeding**

Paste bleeding describes the undesirable spreading of a paste beyond the intended area or the seeping into structures located beneath the printed layer (e.g., open pores within the substrate) [175, 176]. This occurred during the initial phases of paste optimization in this thesis and when trying to replicate the layers of the prototype cell, using information from the publications of Jun Zhang. The most severe consequence occurring during this work regarding paste bleeding was the seepage of electrolyte paste into the porous fuel electrode, which prevented the formation of a clearly defined electrolyte layer. It was assumed that the capillary forces of the fuel electrode surface may cause the paste to partially penetrate that structure. A possible cause for this could be identified in the damping factor $\tan\delta$ of the pastes. Pastes with a damping factor of $\tan\delta \gg 1$ (highly dominant viscous behavior) within the linear viscoelastic region appeared to bleed more readily into the fuel electrode structure. In pastes with dominant elastic behavior ($\tan\delta < 1$) paste bleeding did not occur. To illustrate this phenomenon, Figure 4.23 compares two half-cells produced with different electrolyte pastes. The electrolyte shown

in Figure 4.23 A was printed with an electrolyte paste that had a damping factor of $\tan\delta = 3$. Here, the electrolyte can barely be distinguished from the NiO – GDC fuel electrode and the formation of the electrolyte layer appears uneven. The resulting average layer thickness after sintering was $2.3\ \mu m \pm 0.5\ \mu m$. When comparing this to the electrolyte of the half cell in Figure 4.23 B, the effect of the damping factor becomes clear. The electrolyte in B was printed with a paste that had a damping factor $\tan\delta < 1$, indicating dominant elastic behavior. Here, the average resulting layer thickness after sintering is $10.3\ \mu m \pm 0.2\ \mu m$. The layer has a higher thickness, is easy to distinguish from the fuel electrode and appears more uniform. This is also evident in the standard deviation of the layer thicknesses. Although the electrolyte showcased in Figure 4.23 B is significantly thicker, the standard deviation of the thickness is lower, indicating a more even application.

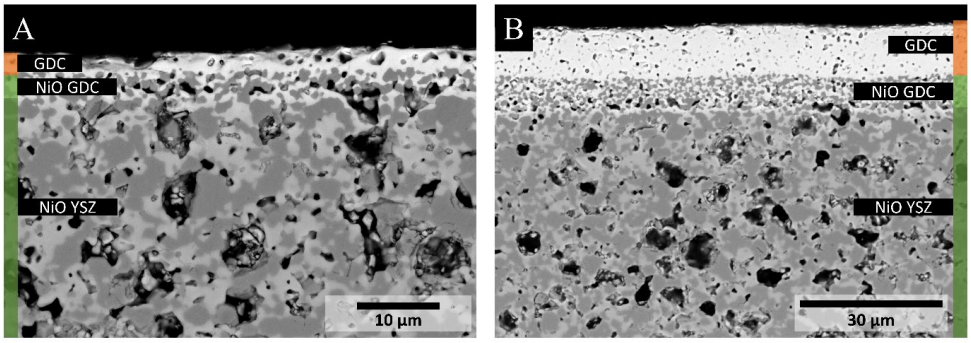


**Figure 4.23:** BSE-SEM images of half-cell cross-sections. Printed GDC electrolyte layers of two different pastes are showcased that were sintered at 1400 °C. **A**: GDC paste with a damping factor $tan\,\delta = 3$, resulting in an average layer thickness of $2.3\ \mu m \pm 0.5\ \mu m$. **B**: GDC paste with a damping factor of $tan\,\delta < 1$, resulting in a layer thickness of $10.3\ \mu m \pm 0.2\ \mu m$.

The connection between paste bleeding and the damping factor has already been statistically demonstrated in Figure 4.12. In that case, printing was conducted on dense metal substrates and the effects were mainly evident in the layer thickness and fidelity factor. It was shown that a higher damping factor results in thinner layers and lower geometric accuracy of the print image. However, as shown here, this correlation also appears to exist for printing on porous substrates, although it manifests itself differently, namely in the form of the printed layer penetrating into the porous substrate structure.

**Screen imprints**

Another defect that appeared throughout this work is visible indentations or imprints of the screen mesh into printed layers, which remain even after the sintering process. Figure 4.24 shows an SEM image of such a screen imprint in the electrolyte surface of a sintered half-cell. Here, the negative impact becomes apparent. The imprint seems to tear open the electrolyte, exposing the underlying layer. Laser microscope analysis revealed that the depth of such a tear can be a multiple of the actual layer thickness. This hints towards the possibility of the screen-printing process being able to damage underlying layers

as well. Therefore, it can be assumed that screen imprints cause the electrolyte to not be gas tight. However, it is unclear how many of these defects have to occur to cause a significant amount of gas leakage to diminish the cell performance or to render the cell unusable.

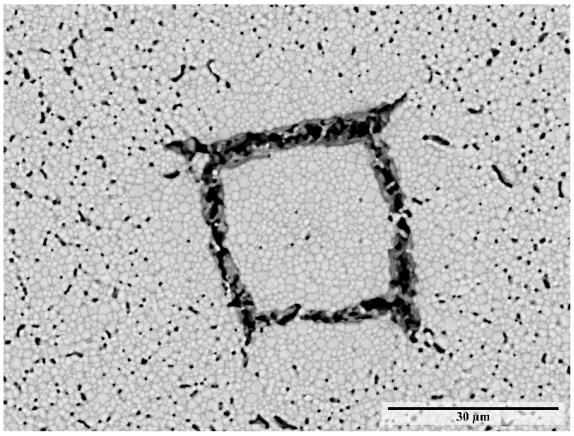


**Figure 4.24:** BSE-SEM image of a porous GDC electrolyte surface, showing a screen imprint. The torn electrolyte layer exposes the underlying NiO-GDC fuel electrode.

There are two possible causes for the appearance of screen imprints, which can also have a combined effect. One origin of this defect lies in the use of screens made with unsuitable mesh materials. In this work, screens with polymer meshes and metal wire meshes were used. Generally, the use of polymer screens resulted in screen imprints. This is most likely due to the larger thread thickness used in polyester screens compared to stainless-steel screens. The latter also allow for larger mesh openings to be achieved due to their higher stiffness and smaller thread thickness. Furthermore, the thread junctions in these screens are more point-shaped rather than oval or square, so that less surface area has to be closed again by paste flowing after the printing. Therefore, the use of stainless-steel screens is particularly recommended for printing electrolyte layers, especially as they also allow for thinner layers to be printed.

Another potential cause for the formation of screen imprints can also be found in the rheological properties of the pastes. Here, the yield point could be identified as the critical parameter [177]. Figure 4.25 shows laser microscope images of GDC electrolyte surfaces made from two different pastes. The electrolyte surface in Figure 4.25 A clearly shows repetitive and deep imprints. In contrast, the electrolyte surface in Figure 4.25 B is free of such defects. The difference between these two GDC pastes is the height of the yield point. From the rheological investigations it is indicated, that imprints are probably a result of a paste that is too stiff and does not yield enough during the printing process. The paste that was used in A only begins to yield at a deformation of 60 %, whereas the paste in B already begins to yield at a deformation of 43 %. As explained before, these differences in yielding are

due to the different binder-to-ceramic surface area ratios, which was higher for the paste that exhibited screen imprints, subsequently shifting the yield point to higher deformation values.

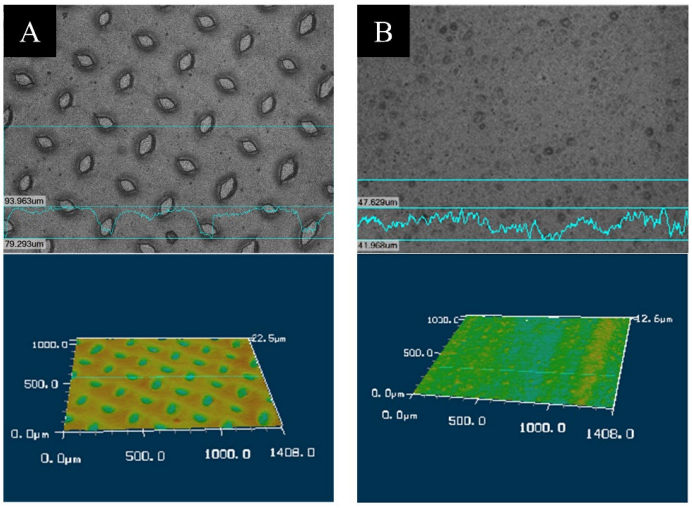


**Figure 4.25:** Laser microscope images with depth profile scans of screen-printed GDC electrolyte surfaces on fuel electrode supports, sintered at 1400 °C. **A:** Layer shows prominent screen imprints due to a yield point at a high deformation of approx. 60 %. **B:** Paste has a yield point at lower deformations due to a lower binder-to-ceramic surface ratio and the resulting layer shows no screen imprints.

**Texturing**

Textures or insufficient leveling is a phenomenon that, in principle, does not have immediate negative consequences for the functionality of the final solid oxide cell. However, layers with greatly varying thicknesses can lead to inhomogeneous sintering behavior and thus to undesirable deformations during sintering. Applying further layers to a significantly uneven layer can also be challenging, as the distance between screen and the cell is no longer consistent across the entire surface [178]. In this work, a link between the squeegee speed and the occurrence of textures could be observed. Therefore, a parameter study was carried out using a stainless-steel screen. Here, the squeegee speed was varied between 20 mm/s and 220 mm/s. All the other printer settings were not changed. To investigate the influence of paste rheology, two different GDC electrolyte pastes were printed directly onto NiO – YSZ supports. One of these pastes had a damping factor $\tan\delta < 1$, meaning that it exhibited predominantly elastic behavior within the linear viscoelastic range and therefore also shows a transition into flow. The other paste had a damping factor $\tan\delta > 1$ and did not have a flow point. Figure 4.26 displays the topography of the sintered GDC electrolyte layers, produced for this investigation, in respect to the squeegee speed during printing. At speeds of 20 mm/s and 55 mm/s both pastes show signs of textures. For electrolytes produced with a squeegee speed of 20 mm/s some screen imprints can be observed. They also seem to appear more frequent when using a paste that has no transition behavior into flow. At squeegee speeds of 75 mm/s and higher, none of these pastes show imprints. Other texturing effects also

seem to be reduced and layers appear more even. This indicates that regardless of paste rheology, a high enough velocity is needed, inducing a certain amount of shear stress, to apply layers without excessive texturing effects.

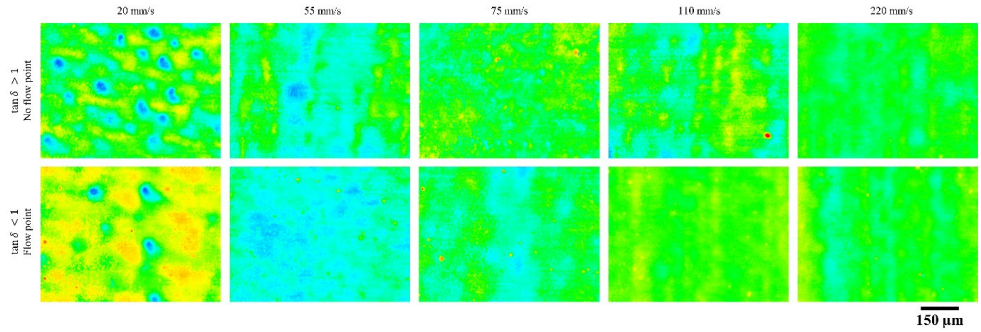


**Figure 4.26:** Topography of GDC electrolytes, printed on NiO – YSZ substrates and subsequently sintered at 1400 °C. The influence of squeegee speed on the formation of textures using two different GDC pastes is displayed. Top row: Paste without a flow point. Bottom row: Paste with a flow point.

### 4.7.2 Drying cracks

Drying cracks are macroscopical cracks that appear on the cell surface during drying of screen-printed layers, as shown in Figure 4.27. During this work, this defect did not appear frequently. However, investigations indicate that it can be potentially linked to pastes recovering too quickly after the printing process. Pastes with very fast recovery times of lower than 10 s, as measured in the 3ITT, exhibited cracks after drying at 60 °C. Therefore, it is proposed that these cracks appear due to the internal structure of the paste already rebuilding very quickly during the initial stages of drying, leading to the formation of strong bonds between particles, binder and solvent. If then the solvent begins to evaporate, it presumably pulls on the already rigid binder and ceramic network. This would result in relatively strong forces that could lead to these drying cracks. Altering the drying temperature had no influence on the formation of this defect. However, as these cracks were not a prominent issue during this work, further investigations were not carried out. To gain a clearer understanding of the mechanisms at play, rheological characterizations at elevated temperatures, for example 60 °C should be conducted [177].

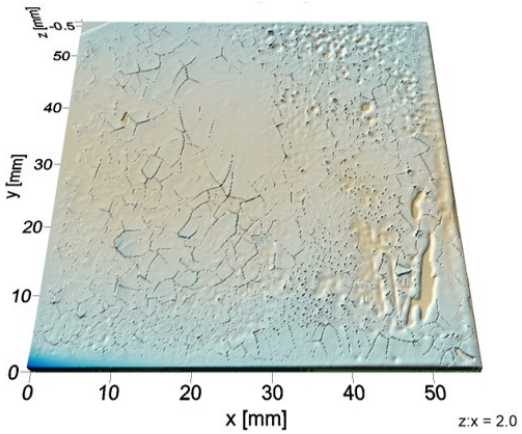


**Figure 4.27:** Topography image taken with the optical inspection system CT300 T of a dry GDC electrolyte layer. Layer shows visible drying cracks and insufficient paste application, as well as pinholes.

### 4.7.3 Silicon contamination during the manufacturing process

During manufacturing, defects manifesting as macroscopical “dark spots” firstly appear after half-cell co-sintering at 1400 °C. The distribution and size of these spots is irregular and seems to follow no pattern. Furthermore, cells that were printed and sintered identically on the same day show differences in defect frequency and appearance. For example, Figure 4.28 displays three different half cells consisting of the green NiO-YSZ substrate, the green NiO-GDC fuel electrode layer and the opaque, translucent GDC electrolyte, that were manufactured under the same conditions but exhibiting different degrees of defect frequency.

Microscopic examinations using an SEM in Figure 4.29 and Figure 4.30 show that these dark spots are holes with a surrounding halo, that exhibits an altered microstructure compared to the ordinary microstructure. The microstructure between the halo and the large open pore in the center appears significantly denser than the regular GDC microstructure, with only a few accumulated pores in certain areas. Porosity appears to be increased just outside of the halo. Topography measurements revealed that these holes can exceed the thickness of the electrolyte layer thickness, reaching depths of 4 to 20 µm. EDS analyses also identified the presence of silicon in the immediate vicinity of these defects.

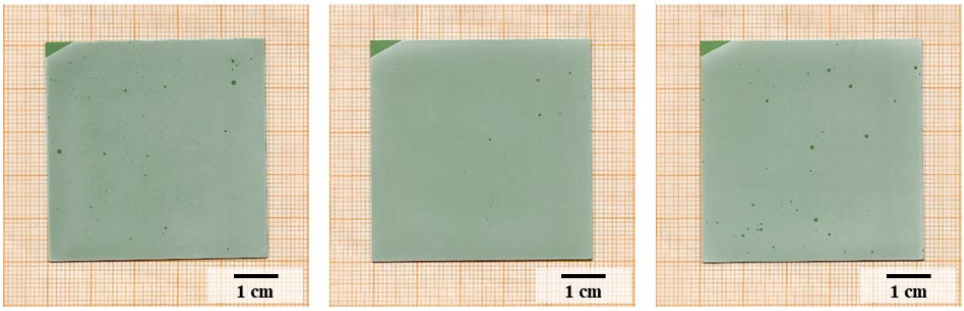


**Figure 4.28:** Photographs of three similar half-cells with one GDC electrolyte layer manufactured on the same day. The cells show varying degrees of defect frequency. Defects appearing as dark spots on the cell surface

The aforementioned halo contains silicon and gadolinium rich acicular grains. This presents two significant concerns for electrolyte layers in SOCs. First, if this defect occurs frequently enough, it can be assumed that the electrolyte is not gas-tight, potentially allowing reaction gases to mix during operation. This would significantly decrease cell performance and, in the worst case, render the cell unusable. However, it is unclear how frequently this defect must occur to significantly impact cell performance.

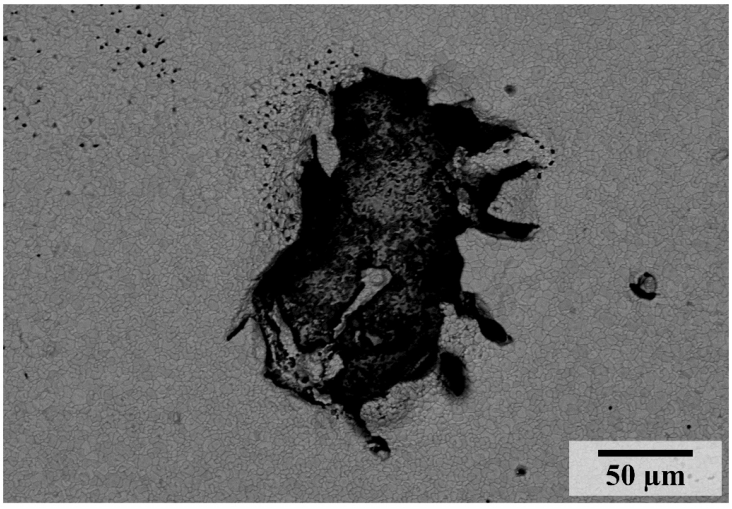


**Figure 4.29:** BSE-SEM micrograph of the open pore at the center of defect caused by external silicon contamination during the manufacturing process. Microstructure surrounding the pore is almost completely densified.

Secondly, Si contamination could reduce the oxygen ion conductivity when forming secondary phases with GDC or other cell components, which is already a well-established phenomenon in solid oxide cells [179]. Depending on their origin, Si contaminants can be grouped into different categories, which also has an influence on appearance and effects of subsequent defects or degradation symptoms. For

instance, Si can already enter the cell via impurities contained in the raw materials. Additionally, Si can also enter the cell during operation. For example, biogas or natural gas used as fuel may contain Si impurities, as well as ambient air when used on the air side. Furthermore, Si can also enter the gas stream as organic siloxanes, which are components of sealants, lubricants, piping and fittings of the gas delivery systems. In addition, the glass sealant used for sealing the cell to the interconnector can release silicon to the cell or gas stream. On the fuel side, silicon has been observed to form silica or other silicate phases on the surface of nickel particles, a phenomenon known as catalyst poisoning. This typically results in a decrease in electrochemical activity and an increase in polarization resistance, caused by a reduction of accessible triple-phase-boundaries and pores getting clogged, restricting reaction gases from entering the porous electrode structure.

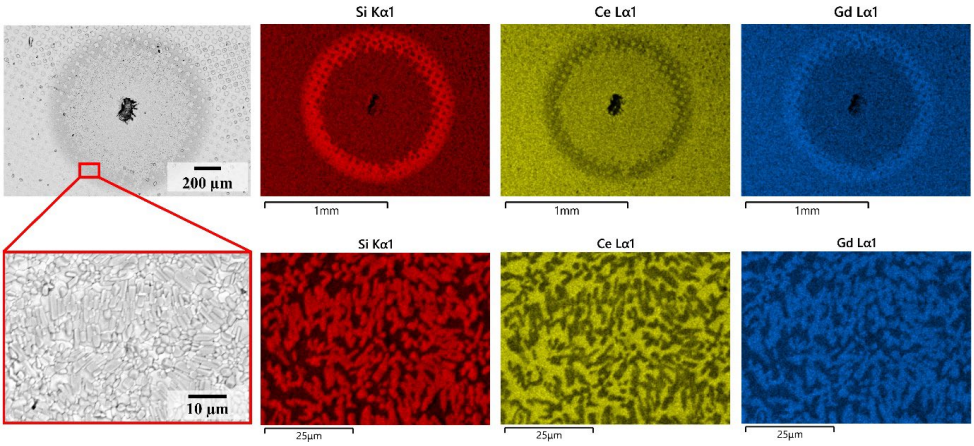


**Figure 4.30:** SE-SEM images with corresponding EDS maps for Si, Ce and Gd. Micrographs show an open pore surrounded by an Si-rich halo. The microstructure within the ring shows Si- and Gd-rich grains. Between the halo and the center pore, the microstructure exhibits significantly more dense area.

With these contamination pathways, silicon is usually found on the surface of particles or at grain boundaries in larger parts of the cell. In contrast, the Si contamination presented here is much more localized and confined to individual, clearly separable, almost pinpoint areas. This is already a strong indicator that the silicon does not originate from the raw material in this case, but rather from an external source in the manufacturing process. Additionally, the presence of silicon impurities in the raw materials could be ruled out using ICP-OES analysis. No significant amount of silicon was found in any of the paste components (GDC powder, dispersant, terpineol and ethyl cellulose). Furthermore, the irregular distribution of defects suggests that they are unlikely to originate from a homogeneous paste. It is much more likely that these silicon contaminants enter the cell during cleaning before and after printing or sintering. The following three potential sources could be identified and subsequently eliminated in this work:

- Debris from a passivating $SiO_2$ layer forming around $MoSi_2$ heating coils used in furnaces for conventional sintering.

- Silicon carbide or silica particles adhering to the NiO-YSZ support during the debindering and pre-sintering step when using SiC setter plates.
- Silicon containing dust particles or siloxanes if compressed air is used to clean the cells prior to screen printing.

Regarding sintering, the position of the cell within the furnace and the furnace's volume would influence the defects' distribution and thus cause quasi-irregularities when comparing different cells. Contamination caused by $MoSi_2$ heating elements during ceramic sintering in conventional furnaces is a well-known phenomenon [100]. With this type of heating element, a $SiO_2$ layer forms around the coils and grows over time. Once a critical thickness is reached, the layer can spall off and fall onto unprotected samples during sintering [180]. Footage acquired during this work by a thermo-optical measuring device (TOMMIplus furnace), which was equipped with $MoSi_2$ heating elements, indicates that this spalling occurs at temperatures around 90 °C. At this temperature, particles appear on the cell surface and disappear at around 1170 °C, probably due to them reacting with GDC. Completely covering the cells during every sintering step is crucial for eliminating the risk of Si contaminants falling onto the sample. It is therefore recommended that completely closed alumina or YSZ crucibles are used to cover and protect the cells from all sides. To prevent SiC or $SiO_2$ from adhering to the electrolyte side of the cell during calcination of the support, it is advised to substitute the SiC plates with YSZ plates, that additionally show an advanced stability in air at high temperatures. Furthermore, to avoid contamination during cell cleaning, impure compressed air was substituted with technical grade canned air to remove dust particles from the cell surface prior to and following the printing process.

To understand why this type of defect has a strong impact predominantly in GDC based SOCs rather than in YSZ state-of-the-art cells, one has to consider the reactivity of silicon with GDC. As indicated by the EDS analysis in Figure 4.30, it seems that mainly the gadolinium reacts with silicon to form the aforementioned Gd-Si rich grains. According to FactSage™ calculations by Zhi et al. [181] alongside of experimental data found in [182 - 184], $Gd_2O_3$ and $SiO_2$ are capable of forming solid solutions at any ratio. Here, depending on the amount of silica, solid solutions of $Gd_2O_3$ + $Gd_2SiO_5$, $Gd_2Si_2O_7$ + $Gd_2SiO_5$ or $SiO_2$ + $Gd_2Si_2O_7$ would form at equilibrium and are stable at processing temperatures of 1400 °C. In contrast, literature shows that in the ternary system $Y_2O_3$-$ZrO_2$-$SiO_2$, especially at low $SiO_2$ concentrations, the tetragonal phase of YSZ is largely stable at processing conditions. Furthermore, experiments presented in literature showed that $SiO_2$ is most likely to accumulate at the YSZ grain boundaries instead of forming solid solutions. However, prolonged exposure to high temperatures, for example during SOC operation, silica at the grain boundaries might cause yttria to leach out of the YSZ crystal structure. Nevertheless, literature suggests that YSZ is relatively inert towards silica at processing conditions [179]. GDC on the other hand tends to have much more rapid and extensive interactions with silica, probably induced by the generally higher cation mobility in GDC when compared to YSZ. However, since these contamination pathways during the manufacturing process also hold true for the production of the Jülich YSZ-based cells, it might be beneficial to apply the proposed mitigation

strategies here too. Even if the contamination is not impacting the cell directly after manufacturing, silica will inevitably cause a loss in performance later on during cell operation.

## 4.8 Conclusion

The sintering behavior of Gd-doped ceria (GDC) and yttria-stabilized zirconia (YSZ) powders was systematically investigated to understand their densification kinetics and shrinkage behavior relevant for solid oxide cell fabrication. Dilatometry measurements revealed that GDC powders generally exhibit lower sintering onset temperatures compared to the more refractory YSZ powder, which shows higher onset temperatures. Powder modifications, such as higher pre-calcination temperatures resulted in reduced sintering activity of GDC, leading to higher sintering onset temperatures and lower total shrinkage, aligning it more with the sintering behavior of the YSZ. Additional co-doping of GDC with NiO or CoO resulted in increased sintering kinetics while shifting the GDC lattice parameter to lower values.

Building upon these insights, the microstructure evolution of single screen-printed GDC electrolyte layers during co-sintering on NiO-8YSZ supports was investigated to determine whether sintering trends observed in pellets could translate to realistic screen-printed layers. Results showed that porosity in co-sintered screen-printed layers remains significantly higher across all compositions compared to pellet sintering, primarily due to lower green densities achievable in screen-printed layers and constrained sintering imposed by the more rigid NiO-8YSZ support. Nevertheless, porosity trends versus calcination temperature remained consistent with dilatometry findings, as higher pre-calcination temperatures generally resulted in increased final porosity due to reduced sintering activity.

However, notable deviations were observed, indicating that factors beyond intrinsic powder behavior, such as support interactions and the screen-printing process itself, play a significant role in shaping the final microstructure. For instance, co-doped samples like GNDC1340 exhibited unexpectedly high porosity, while the early-stage sintering behavior of the electrolyte appeared critical for densification, as shown by the low porosity of GCDC1130 due to its high sintering activity at lower temperatures, facilitating pore removal before substantial substrate shrinkage began.

Importantly, this study also highlighted that the paste composition and rheological properties have a substantial impact on the dried layer thickness and geometric accuracy in screen-printing processes. Among the rheological parameters investigated, the damping factor showed a negative correlation with layer thickness and accuracy, while the yield point displayed a positive correlation. Interestingly, viscosity and values for loss and storage moduli did not exhibit significant correlations with printing outcomes. Further investigation revealed that particle size distribution asymmetry strongly affects the damping factor, likely due to agglomerates disrupting the paste's 3D network structure. Traditional metrics like $d_{10}$, $d_{50}$ and $d_{90}$ values were insufficient to capture these relationships, whereas a bimodality

coefficient derived from skewness and excess kurtosis proved to be a more meaningful characterization tool for predicting paste behavior.

Binder content, when assessed relative to the ceramic particle surface area rather than as a weight percentage alone, also demonstrated robust correlations with the yield point, indicating that excessive binder can weaken the paste's network structure and shift the yield point to lower deformation values. These findings emphasize the necessity of precise powder characterization and tailored paste formulations to optimize screen-printing outcomes, as rheological properties directly influence green layer uniformity and densification during sintering. Notably, while solid content within the tested range did not significantly impact the damping factor or yield behavior, the combined effects of particle size distribution, surface area and binder-particle interactions are critical in defining the paste's performance.

These results collectively demonstrate that while trends in sintering behavior derived from dilatometry provide a foundational understanding, they may not always directly translate to screen-printed layers under co-sintering conditions due to the additional complexity introduced by paste rheology and substrate interactions. The interplay between sintering kinetics, powder characteristics, paste composition and the sintering constraints of the substrate defines the final microstructure and functional performance of electrolyte layers in solid oxide cells.
Importantly, despite inherent challenges, nearly all co-sintered GDC layers in this study exhibited satisfactory microstructures without delamination. Moving forward, further rheological studies, including frequency-dependent measurements and temperature-adapted rheology, will be essential to deepen the understanding of paste behavior during drying.

In summary, this integrated investigation demonstrates that achieving high-quality electrolyte layers for solid oxide cells requires a holistic approach that considers powder-specific sintering behavior, rheological properties of pastes and substrate interactions during co-sintering.

# 5 Fabrication of solid oxide cells with a tri-layer electrolyte

## 5.1 Motivation

Fuel electrode-supported solid oxide cells (FESCs) present notable advantages in terms of reduced ohmic losses and mechanical robustness. However, the fabrication of such fuel electrode-supported cells is considerably more challenging than electrolyte-supported configuration due to the complexity of achieving and maintaining electrolyte integrity and functionality on a porous substrate [174, 185]. The incorporation of a tri-layer electrolyte architecture further amplifies these challenges. The layered structure introduces additional interfaces, each susceptible to interdiffusion phenomena and differential sintering during thermal treatment. These factors can potentially induce microstructural defects, interfacial porosity and residual stresses, compromising the mechanical stability and electrochemical performance of the cells.

In this chapter, the motivation is to address these fabrication challenges systematically by investigating feasible processing routes for manufacturing tri-layer electrolyte FESCs. Different printing and sintering sequences are explored to evaluate their impact on microstructural evolution and overall integrity of the tri-layer electrolyte. Special emphasis is placed on the sintering behavior of fully co-sintered tri-layer electrolyte half-cells, the most cost-effective processing route, employing thermo-optical analysis to monitor shrinkage behavior and understand its correlation with observed warping of sintered cells. From this, residual stresses that are linked to different thermal expansions of the layered structure are also examined in bi-layer and tri-layer electrolyte samples. By connecting these processing parameters with microstructural features of the half-cells, this chapter aims to provide a comprehensive understanding of the critical factors influencing the successful fabrication of tri-layer electrolyte FESCs.

## 5.2 Overview of the processing route

This chapter aims to provide a brief overview of the fuel electrode-supported cell manufacturing strategy employed in this work, focusing on the layer deposition sequence and the key thermal processing steps applied to the half-cell structure and support. As paste formulation and screen-printing methodology are described and discussed in detail throughout Chapter 4, this chapter will only focus on the sequence of fabrication and the variations introduced in substrate calcination and electrolyte processing. A visual summary is provided in Figure 5.1.

In this work, all cells were fabricated using the in-house tape-cast fuel electrode support composed of NiO-8YSZ. This support is also used in the production of the Jülich Type III cell where it is calcined at 1230 °C prior to fuel electrode deposition. Initially, the substrates used in this work were also calcined at this temperature. However, due to insufficient densification of the electrolyte, the influence of different substrate calcination temperatures on electrolyte densification was investigated. For this,

supports were calcined at 1050 °C, 1100 °C, 1150 °C and 1200 °C, alongside the standard 1230 °C for 3 h. Furthermore, the influence of residual stress development of the electrolyte and overall sintering behavior of the half-cell during co-sintering was analyzed and will be discussed in the subsequent chapters. Ultimately, a calcination temperature of 1100 °C is recommended for tri-layer electrolyte cells using this specific type of substrate, as it provided the best compromise between mechanical stability for subsequent screen printing and handling, as well as sufficient shrinkage during co-sintering to promote densification of the electrolyte layers.

After substrate calcination, one layer of NiO-GDC fuel electrode is printed onto the support and calcined at 1000 °C for 1 h. Following fuel electrode deposition and calcination, the tri-layer electrolyte was applied. Here, six variations were produced, which will be introduced in the following. All approaches maintained the same general layer sequence of GDC-YSZ-GDC but differed in terms of layer thickness, thermal treatment and deposition techniques.

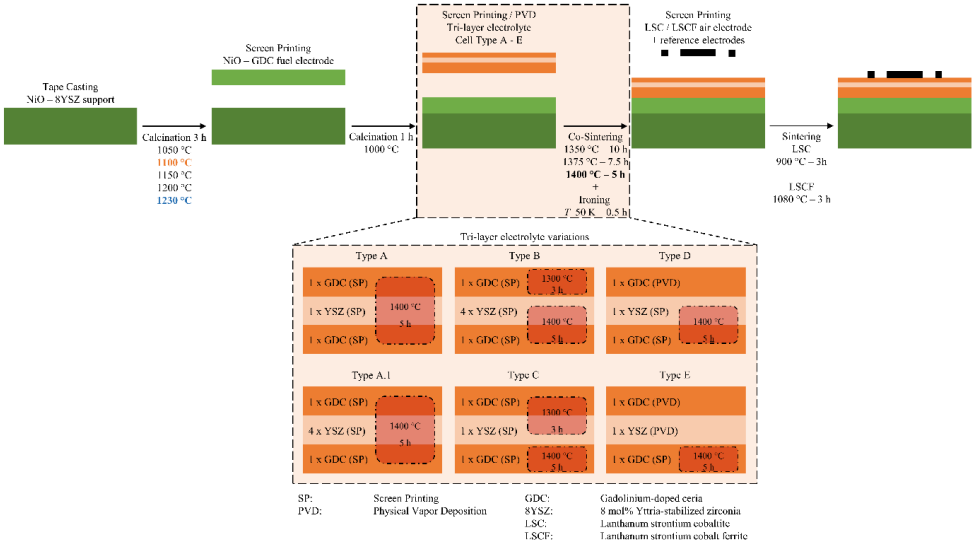


**Figure 5.1:** Overviev of the general processing route for the fuel electrode-supported tri-layer electrolyte cells investigated in this work. The different tri-layer electrolyte configurations are shown with detailed information on the respective fabriaction methods and sintering sequences.

### Type A (fully screen-printed and co-sintered)

Here, the entire tri-layer electrolyte was deposited by sequential screen printing with in-between drying. A single layer of GDC was printed onto the fuel electrode, followed by one YSZ layer and a final GDC layer. The entire half-cell was then co-sintered at 1400 °C for 5 h, followed by a flattening step. This so-called 'ironing' includes heating the sample to temperatures 50 K below the co-sintering temperature and applying a load of 1.5 – 2 kg per 50 mm × 50 mm cell for 30 min. During cooling down, the load is still applied to the cells and is only removed afterwards. In the fabrication of the Jülich Type III cell,

this ironing step is included within the co-sintering step. However, this ironing step must be conducted separately when dealing with the tri-layer configuration, as SiC plates are used to apply the load and are chemically not compatible with GDC. Therefore, after co-sintering, lightweight YSZ plates are placed on top of the already sintered cells as a barrier between GDC and the SiC ironing plates. This is electrolyte configuration serves as the standard electrolyte configuration throughout this work and is usually referred to unless stated otherwise.

**Type A.1 (fully screen-printed with increased YSZ thickness)**

This variant is identical to Type A, except that the YSZ layer is printed four times instead of once to increase its thickness. Each layer is dried before the next layer is applied. The entire tri-layer electrolyte is co-sintered at 1400 °C for 5 h, followed by ironing.

**Type B (fully screen-printed with separate GDC barrier layer sintering)**

In this case, the bottom GDC layer is screen-printed, followed by four consecutive YSZ layers. Here, this bi-layer configuration is then co-sintered at 1400 °C for 5 h, followed by ironing. Only after this, the final GDC barrier layer is printed onto the already sintered YSZ layer and sintered at 1300 °C for 3 h.

**Type C (fully screen-printed with separate YSZ and GDC barrier layer sintering)**

Here, a single GDC layer is screen-printed and sintered at 1400 °C for 5 h and ironed. Subsequently, one YSZ and one GDC layer are printed as barrier layers and sintered at 1300 °C for 3 h. However, this approach proved unsuccessful. None of the fabricated cells survived this manufacturing process. Despite attempts to optimize the sintering strategy in terms of increasing holding times, reducing heating rates or adjusting the sintering temperature, adhesion between YSZ and the pre-sintered GDC layer was insufficient. It is suspected that the lack of substrate shrinkage introduced too much mechanical constraint that prevented effective sintering of the YSZ and GDC layer.

**Type D (hybrid electrolyte with sputtered GDC barrier layer)**

This variant involves screen printing the first GDC layer and one YSZ barrier layer, followed by co-sintering at 1400 °C for 5 h and subsequent ironing. The top GDC barrier layer was not screen-printed but instead deposited as an approximately 500 nm thin layer via sputtering.

**Type E (hybrid electrolyte with sputtered GDC and YSZ barrier layers)**

In this final configuration, only a single GDC layer is screen-printed and co-sintered at 1400 °C for 5 h. After the subsequent ironing step, both the YSZ and the GDC barrier layers are deposited by magnetron sputtering. This configuration replicates the electrolyte structure that was initially developed by Jun

Zhang in IMD-2 as the tri-layer electrolyte prototype cell which serves as one of the technological benchmark for this work.
After successful electrolyte deposition and sintering, the final step in cell production is the deposition of the air electrode. In this work, both LSC and LSCF electrodes were used. Both types of air electrodes are screen printed identically to the processing protocol of the Jülich Type III cell. LSC electrodes are sintered at 900 °C for 3 h, whereas LSCF electrodes are sintered at 1080 °C for 3 h.

This chapter provides the processing context for the experimental results discussed in the following chapters, where the impact of these fabrication variations on microstructure, sintering behavior, densification and residual stress development is evaluated.

## 5.3 Co-sintering behavior of tri-layer electrolyte half-cells

Half-cell co-sintering is a critical step in the production of fuel electrode-supported solid oxide cells. It is during this consolidation step that the final microstructures of the electrolyte and its interfaces are formed, which greatly influence the cell performance. Especially for tri-layer electrolyte cells, co-sintering of multi-layer ceramics poses significant challenges due to the necessity of simultaneously densifying layers with different sintering kinetics, shrinkage rates and coefficients of thermal expansion (CTE). Insufficient alignment of these factors can lead to layer delamination, warpage and bending, as well as incomplete densification, which negatively affects mechanical stability and electrochemical performance. Therefore, this chapter aims to investigate the co-sintering behavior of the newly developed tri-layer electrolyte half-cell Type A, to gain insights into how this process can potentially be optimized and to identify limiting factors. Additionally, it was aimed to lower co-sintering temperatures to reduce overall energy consumption and cost, as well as to mitigate interdiffusion between YSZ and GDC electrolyte layers which was later identified to be the main challenge of this cell architecture and processing strategy.
To investigate the sintering behavior of the half-cell, thermo-optical analyses were carried out under various conditions. While this method is unfortunately not able to provide quantitative shrinkage data due to software issues related to the recognition of bended shapes, it enables real-time observation of the cell bending and movements during thermal treatment. With this, it was attempted to identify at which temperatures the electrolyte and support begin to sinter, depending on the conditions and how the behavior of individual layers might influence the sintering of adjacent layers during co-sintering.
For this, first the NiO-8YSZ fuel electrode support (calcined at 1230 °C) was examined separately to build a baseline. Then, a systematic study was conducted with a sample matrix containing half-cells manufactured using different support calcination temperatures of 1050 °C, 1100 °C, 1150 °C and 1200 °C, combined with varying co-sintering conditions of sintering at 1350 °C for 10 h, 1375 °C for 7 h and 1400 °C for 5 h. Preliminary experiments already identified 1350 °C to be the lowest possible

co-sintering temperature with this cell architecture. Attempts to sinter at 1300 °C, using different heating rates and dwell times, always led to electrolyte delamination. For each thermo-optical examination, two half-cells are placed inside the furnace, to increase comparability. Half-cells with substrates calcined at 1050 °C and 1100 °C were always analyzed together, as well as half-cells with substrates calcined at 1150 °C and 1200 °C. Additional shrinkage measurements and analysis of residual cell camber after sintering completed the evaluation of the co-sintering behavior of these half-cells. All investigated cells were prepared on the same day, using the same pastes and screen-printing parameters for the individual layers.

When examining the sintering behavior of the already calcined (1230 °C) NiO-8YSZ support on its own at 1400 °C for 5 h, substantial shrinkage was observed to start at approximately 1350 °C. This is congruent with observations by Wolfgang Schafbauer, who developed the NiO-8YSZ support, as reported in his thesis [51]. However, it should be noted that in his work, the 8YSZ is supplied from a different manufacturer to that used for the substrate currently. Furthermore, throughout the entire sintering process, the substrate exhibited no warpage and remained flat, indicating a uniform shrinkage which suggests a homogeneous tape microstructure and consistent green density. As this serves as the baseline for evaluating the half-cell co-sintering experiments, it can be assumed that any warpage or bending occurring is assumed to be linked to differential sintering phenomena. These phenomena originate from sintering behavior mismatches between the support and the electrolyte layers or fuel electrode.

When comparing the sintering behavior of the substrate with that of the half-cells, distinct differences emerge. First, the co-sintering of half-cells at 1400 °C for 5 h will be discussed. Figure 5.2 summarizes the observations during this experiment.

The first noticeable movement manifests as a concave bending of the half-cells during the heating stage. This is attributed to the sintering of the tri-layer electrolyte. As the electrolyte shrinks and starts to densify, the top of the half-cells pulls together which would result in this observed concave warping, where the edges lift off while the center stays on the ground. Interestingly, this warpage starts to develop at temperatures just below or slightly above the temperature at which the respective support was calcined. This already hints toward a substantial impact of substrate calcination temperature. As this movement is attributed to electrolyte sintering, it is hypothesized that it already begins to shrink at even lower temperatures. However, considering the temperature at which this warping occurs, electrolyte shrinkage seems to be impeded by the stiffness of the significantly thicker substrate.

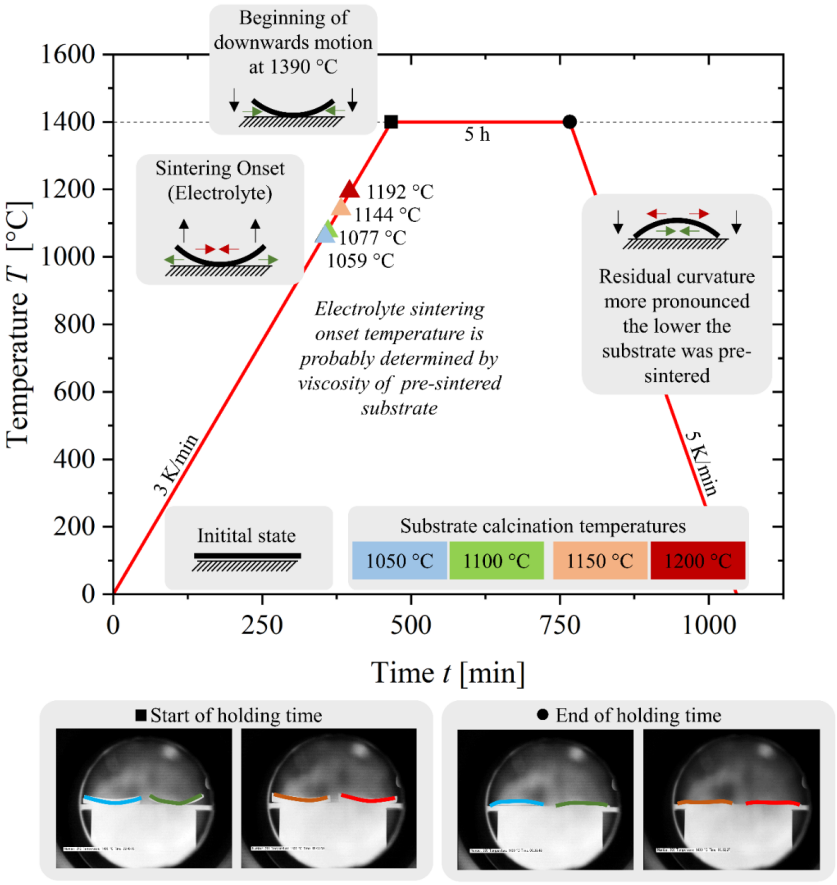


**Figure 5.2:** Overview of the sintering behavior of tri-layer electrolyte half-cells when co-sintered at 1400 °C for 5 h. Investigated half-cells were fabricated using substrates that were calcined at either 1050 °C, 1100 °C, 1150 °C or 1200 °C to analyze its influence on the overall sintering behavior and subsequent properties.

Therefore, it is assumed that only when the initial substrate calcination temperature is reached, the viscosity of the substrate is low enough for significant and observable electrolyte shrinkage to occur. This bending increases until it reaches its maximum at 1390 °C, after which the edges start to bend down again towards an overall flat shape of the half-cell. Although a bit higher than the previously reported sintering onset at 1350 °C of the calcined support, this movement is hypothesized to originate from substrate shrinkage. The slightly higher temperature at which this occurs can be explained by the superimposed electrolyte shrinkage, that counteracts this downward motion. Only when the sintering kinetics of the substrate are fast enough does the substrate shrinkage appear to dominate and initiate this downward motion. Interestingly, substantial substrate shrinkage appears to occur at the same temperature for all half-cells, regardless of substrate calcination temperature. At the beginning of the

dwelling time at 1400 °C, the half-cells are still bent concavely. However, during dwelling at 1400 °C, the shape transitions from being concave to convex. This would indicate that the support has an overall higher shrinkage potential than the electrolyte and that this mismatch results in the half-cells not being flat after sintering. During cooling, no changes in warpage occur and the shape observable at the end of the dwelling time remains as residual curvature. This curvature appears to be more pronounced if the substrate was calcined at lower temperatures.

Partially similar observations can be made when investigating the sintering behavior of half-cells when co-sintering at 1350 °C for 10 h, which is the lowest tested temperature. Again, the concave warping, attributed to electrolyte shrinkage, begins to manifest at temperatures around the respective substrate calcination temperatures, as summarized in Figure 5.3.

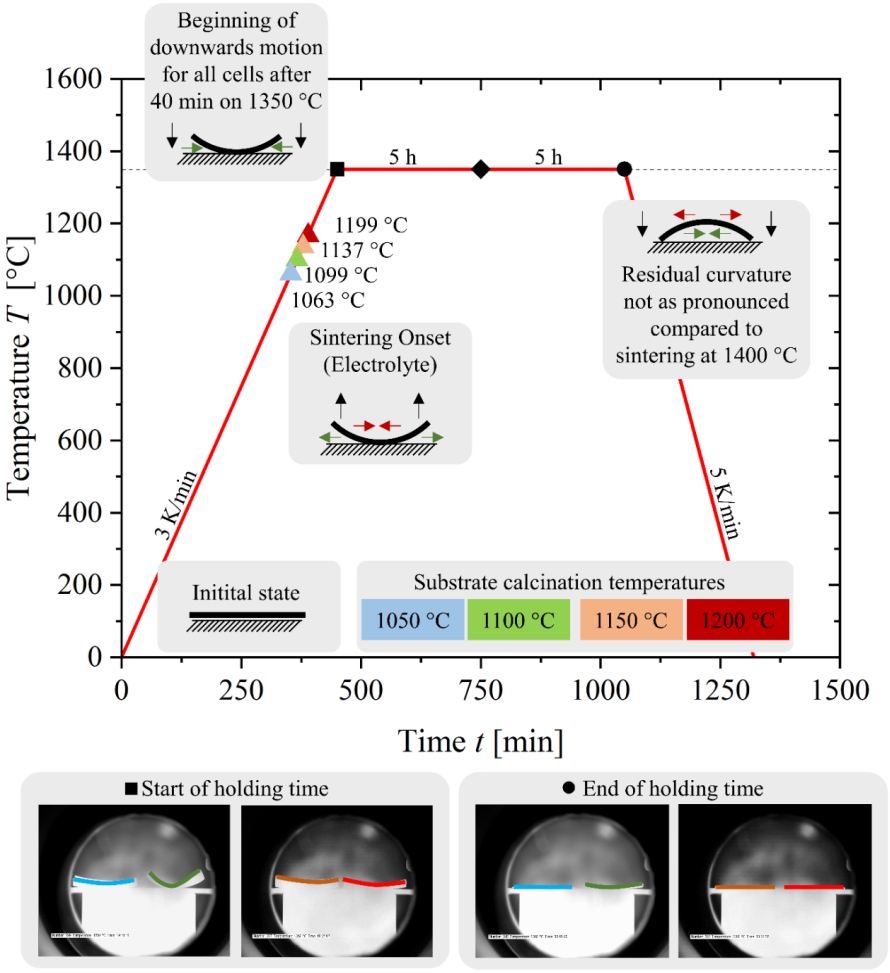


**Figure 5.3:** Overview of the sintering behavior of tri-layer electrolyte half-cells when co-sintered at 1350°C for 10 h. Investigated half-cells were fabricated using substrates that were calcined at either 1050 °C, 1100 °C, 1150 °C or 1200 °C to analyze its influence on the overall sintering behavior and subsequent properties.

However, since temperatures of 1390 °C for the onset of substrate shrinkage are never reached during this co-sintering process, the associated downwards motion only starts to occur after roughly 40 minutes at 1350 °C during the dwelling time. This can be explained by substantially slower sintering kinetics caused by the lower temperature. Further evidence for this can be found in the residual curvature at the end of the dwelling time. Although the dwelling time was twice as long when compared to the previously discussed co-sintering at 1400 °C for 5 h, the residual convex curvature is not as pronounced. Here it is assumed that due to the lower co-sintering temperature, the maximum possible shrinkage of the substrate is never reached. Nevertheless, half-cells with lower calcined substrates again appear to contain a more pronounced residual curvature.

Table 5.1 summarizes the discussed characteristics of electrolyte and substrate sintering behavior for all co-sintering and substrate calcination temperature combination investigated in this work. Also, during co-sintering at 1375 °C for 7.5 h, the 1390 °C necessary for substrate shrinkage is not reached. Here, the substrate only appears to shrink significantly and visibly after around 10 min at 1375 °C. Another indication for slower sintering kinetics can be found when analyzing the time it takes for the half-cells to reach a flat position again. The values in Table 5.1, clearly show that at low co-sintering temperatures, generally a longer time is required until the substrate has shrunk to such an extent that the half-cells are flat. Additionally, it appears that for the same co-sintering temperature, this duration until flatness is reached is longer if the substrate was calcined at higher temperatures. This can potentially be attributed to less overall shrinkage potential of the substrate when already calcined at higher temperatures.

**Table 5.1:** Summary of the sintering behavior of tri-layer electrolyte half-cells as a function of support calcination temperature and co-sintering conditions, showing electrolyte sintering onset, substrate sintering onset and time until cells appear flat during dwelling.

| Co-sintering | Support calcination temperature [°C] | Sintering onset electrolyte [°C] | Sintering onset substrate | Time until flat during dwelling [min] |
|---|---|---|---|---|
| 1350 °C 10 h | 1050 | 1063 | After 40 min on 1350 °C | 298 |
| | 1100 | 1099 | | 395 |
| | 1150 | 1137 | | 322 |
| | 1200 | 1199 | | 328 |
| 1375 °C 7.5 h | 1050 | 1064 | After 10 min on 1375 °C | 95 |
| | 1100 | 1107 | | 171 |
| | 1150 | 1145 | | 177 |
| | 1200 | 1187 | | 237 |
| 1400 °C 5h | 1050 | 1059 | 1390 °C | 54 |
| | 1100 | 1077 | | 70 |
| | 1150 | 1144 | | 68 |
| | 1200 | 1192 | | 85 |

To further evaluate and quantify the impact of substrate calcination and half-cell co-sintering conditions on the sintering outcome, the residual curvature after sintering was assessed using the optical white light inspection system (see Chapter 3.2.7). The results for this are presented in Figure 5.4. Here it was observed that cells produced with a combination of a substrate calcination temperature of 1050 °C and co-sintering conditions of 1400 °C for 5 h, exhibited the most pronounced convex bending. In general, lower substrate calcination temperatures consistently resulted in higher residual curvature. In contrast, cells with supports calcined at 1200 °C and co-sintered at 1350 °C for 10 h appeared nearly flat, suggesting a better sintering match between electrolyte and substrate under these conditions. Additionally, most cells displayed a characteristic localized dip near the center, although the exact position of this feature varied between the samples. Furthermore, cells marked with a red "X" in this figure indicate samples where the electrolyte chipped off prior to the curvature assessment, while green checkmarks denote intact samples. Interestingly, none of the electrolyte delamination occurred during the cooling phase of sintering. Instead, the electrolytes chipped into fine flakes seemingly spontaneous after several days at room temperature. This indicates that meaningful residual stresses may be present in the electrolyte after sintering which are potentially influenced by the combination of sintering conditions and substrate calcination temperatures. Residual stresses within the electrolyte layers are investigated in more detail in Chapter 5.4.

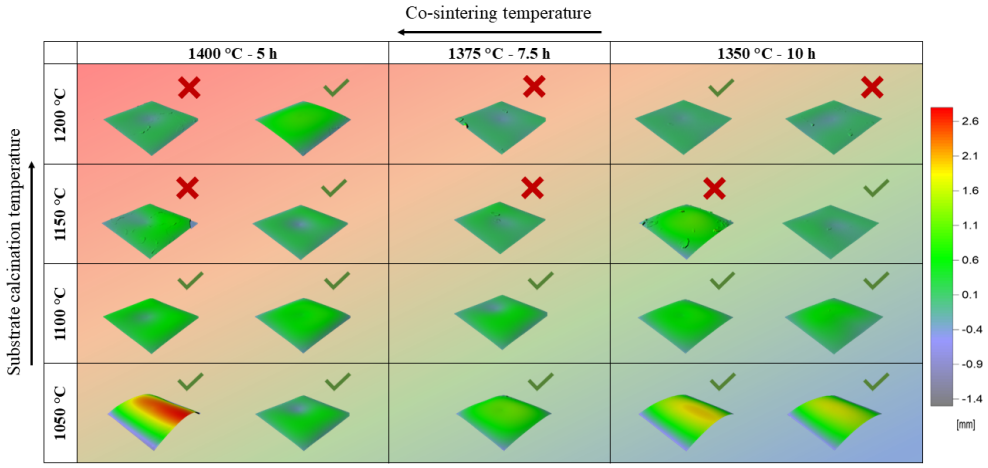


**Figure 5.4:** Residual curvature of fuel electrode supported tri-layer electrolyte half-cells after co-sintering at different temperatures and dwell times, in combination with varying substrate calcination temperatures. Each image represents a 3D scan of a sintered half-cell, with curvature indicated by the color scale on the right. Green checkmarks denote successful sintering; red crosses indicate electrolyte chipping post sintering. Measurements were conducted using the white light optical inspection system CT 300T equipped with an DHS 10000 sensor head.

Following the evaluation of residual curvature, the total shrinkage after sintering was assessed to further understand the sintering behavior. The cells were flattened via ironing prior to shrinkage measurements to ensure consistent geometry for comparison. The results, presented in Figure 5.5, show the longitudinal shrinkage as a function of substrate calcination temperature for each co-sintering procedure. The highest

linear shrinkage (~ 15 %) was achieved using a combination of a substrate calcination temperature of 1050 °C with co-sintering at 1400 °C for 5 h. Notably, this combination also resulted in the most pronounced convex cell bending, indicating a link between cell curvature during sintering and shrinkage. In comparison, the standard manufacturing procedure (support calcination at 1200 °C and co-sintering at 1400 °C for 5 h) resulted in a shrinkage of only approximately 12 %. This is consistent with observations by Schafbauer. Interestingly, they obtained similar shrinkage values when only the substrate was sintered under these conditions after calcination at 1230 °C. This indicates that the overall shrinkage of the half-cell is most likely predominantly governed by the substrate's shrinkage behavior [174]. The data further shows that comparable or even higher shrinkage can be achieved at lower co-sintering temperatures (1350 °C) if substrates are calcined at lower temperatures. For example, co-sintering at 1350 °C using a support calcined at 1050 °C resulted in a shrinkage of roughly 14 %, surpassing the shrinkage achieved under standard processing conditions. These results highlight that sufficient shrinkage, which is critical for achieving dense electrolyte layers, can be maintained even at reduced co-sintering temperatures when appropriately adjusted substrate calcination conditions are utilized. Therefore, from these results it is recommended to use substrate calcination temperatures of 1100 °C for tri-layer electrolyte cells using this specific type of substrate, as it provides the best compromise between mechanical stability for subsequent screen printing and handling, as well as sufficient shrinkage during co-sintering and resulting in an acceptable amount of cell curvature.

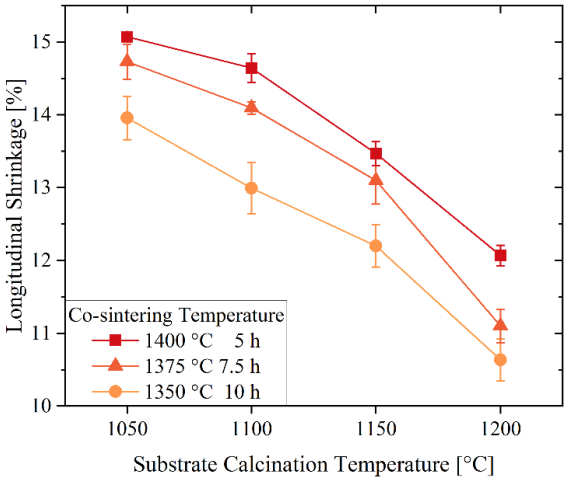


**Figure 5.5:** Longitudinal shrinkage of co-sintered fuel electrode-supported tri-layer electrolyte half-cells as a function of substrate calcination temperature for different co-sintering procedures. Half-cells were flattened prior to shrinkage assessment to ensure consistent geometry.

## 5.4 Residual stresses in bi- and tri-layer electrolytes

In multilayer ceramic systems, such as sintered solid oxide cells, residual stresses inevitably develop during processing due to thermal gradients, differential sintering behavior and mismatches in thermal expansion between layers [186, 187]. While these stresses are not necessarily directly responsible for failure modes such as delamination, spalling or cracking, they establish the initial mechanical state of the electrolyte and can significantly impact its response to subsequent chemical or thermal stimuli. In particular, reducing ceria-based electrolytes, which is accompanied by chemical expansion, can lead to cracking or structural degradation. Therefore, in this work the residual stress state of the electrolyte in as-sintered half cells manufactured using various processing conditions was investigated. By establishing this baseline stress state through ex situ room-temperature measurements, it was aimed to gather information about the influence of sintering parameters and processing sequence on the mechanical preconditioning of the electrolyte and its potential impact on structural integrity.

For this, two sets of experiments were performed. The first set focused on medium-format 5 cm x 5 cm sintered half-cells, some of which exhibited partial delamination of the electrolyte layers. In these cells, the electrolyte barrier layers did not cover the entire cell area and were rotated 45° which resulted in a diamond shaped area. Cells investigated include both bi-layer electrolyte samples (GDC-YSZ) and tri-layer (GDC-YSZ-GDC) electrolyte architectures. In the bi-layer samples, residual stress measurements targeted the YSZ barrier layer and the exposed bottom GDC layer in areas where the YSZ layer delaminated. In the tri-layer electrolyte samples, only the GDC layers were evaluated. This includes the top GDC barrier layer and the bottom GDC electrolyte layer in regions where the YSZ and top GDC layers chipped off. Additionally, the bottom GDC layer was also investigated in areas that had never been covered by the upper layers. Figure 5.6 provides an overview of these samples indicating the areas that were investigated for analysis. All measurements were conducted using the $\sin^2\Psi$ method. Here, the cells were co-sintered at 1400 °C for 5 h on a support that was calcined at 1230 °C for 3 h. This set of experiments was conducted in order to investigate the influence of processing sequence on the residual stress state. Since these cells were already fairly flat after sintering, they were not flattened (ironed) before the stress measurements to not alter their stress state.

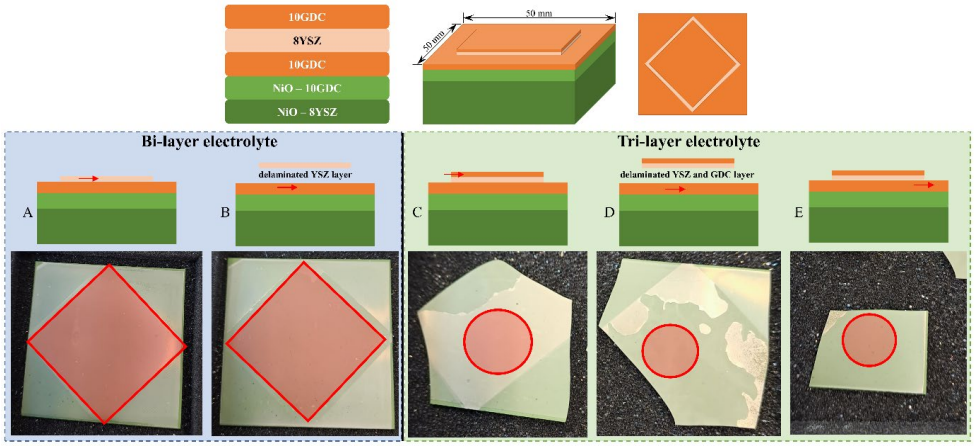


**Figure 5.6:** Overview of the samples investigated in the first set of residual stress measurements. Bi-layer (GDC-YSZ) and tri-layer (GDC-YSZ-GDC) electrolyte 5 cm x 5 cm half-cells were examined. The investigated layer and specific area are indicated by red frames and arrows. Electrolyte layers were partially delaminated.

A second set of experiments was carried out on smaller 2.5 cm x 2.5 cm tri-layer electrolyte half-cells in order to systematically study the effect of sintering conditions on the residual stress state. For this, a matrix of processing conditions was explored by varying the calcination temperature of the support (1050 °C, 1100 °C, 1150 °C and 1200 °C for 3 h each) and the co-sintering temperature of the half-cell (1350 °C – 10 h, 1375 °C – 7.5 h and 1400 °C – 5 h). Residual stress in the electrolyte layers was measured using the omega stress method after the samples had been ironed to simulate real application conditions. Figure 5.7 presents an overview of the cells investigated in this second set of residual stress analysis. Here, it can be seen that some electrolytes are delaminated or chipped off after sintering. Especially cells that were prepared with a combination of high calcination temperatures of the support and low co-sintering temperatures are affected by this.

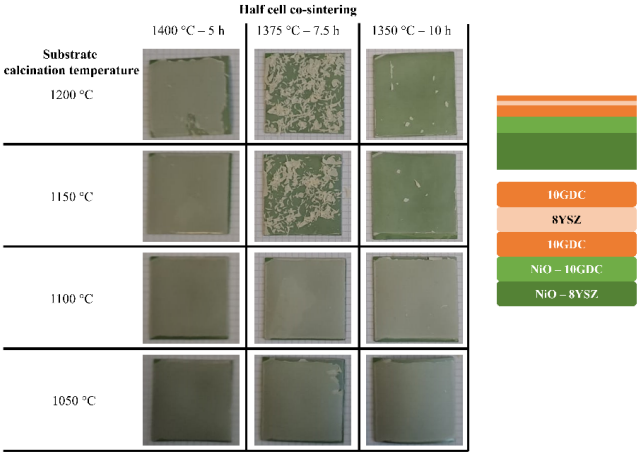


**Figure 5.7:** Overview of samples for residual stress measurements on 2.5 cm x 2.5 cm tri-layer electrolyte half-cells manufactured using varying sintering conditions. Different support calcination temperatures were combined with varying co-sintering temperatures to investigate the effect of sintering on residual stresses.

Table 5.2 provides the results of the first set of residual stress measurements performed on the bi- and tri-layer electrolyte samples. All measured layers exclusively exhibit compressive stresses. In the sintered bi-layer electrolyte, the intact YSZ layer (A) contains the highest compressive stress of – 674.4 MPa ± 20.7 MPa. The underlying GDC layer (B), when measured on the chipped sample, shows significantly lower compressive stresses of only - 278.6 MPa ± 24.5 MPa. For samples with the tri-layer electrolyte, the highest residual compressive stresses were measured in the center of the bottom GDC electrolyte layer (D) (- 942.7 MPa ± 73.0 MPa). However, within the same layer but outside the area of barrier layers (E), compressive stresses were only – 88.3 MPa ± 9.2 MPa. The top GDC barrier layer (C) exhibits compressive stresses of – 150.4 MPa ± 25.6 MPa.

**Table 5.2:** Results of residual stress measurements via XRD $\sin^2\Psi$ method, carried out by Dr. Sohn (IMD-2) using the Empyrean diffractometer with Bragg-Brentano geometry.

| Electrolyte architecture | Measured layer | | Residual stress [MPa] |
|---|---|---|---|
| Bi-layer | A | YSZ | - 674.4 ± 20.7 |
| Bi-layer | B | Bottom GDC | - 278.6 ± 24.5 |
| Tri-layer | C | Top GDC | - 150.4 ± 25.6 |
| Tri-layer | D | Bottom GDC (within barrier area) | - 942.7 ± 73.0 |
| Tri-layer | E | Bottom GDC (outside barrier area) | - 88.3 ± 9.2 |

One likely explanation for the significantly higher compressive residual stress observed in the YSZ of the bi-layer electrolyte is the difference in thermal expansion coefficients (CTE) between the materials. GDC generally has a slightly higher CTE (12.7 µm $m^{-1}$ $°C^{-1}$ in air between 30 °C and 800 °C) compared

to 8YSZ (10.2 µm $m^{-1}$ $°C^{-1}$ in air between 30 °C and 800 °C) [104]. Upon cooling down from the sintering temperature, the GDC layer contracts more than the YSZ layer. Since those electrolyte layers are already mechanically bonded at that time, this differential contraction places the YSZ layer most likely under in-plane compressive stresses. For the same reason, GDC would exhibit lower compressive stresses. Compensating tensile stresses are likely to be found in the NiO-YSZ substrate because of its comparatively large thickness (~ 200 – 300 µm) or the fuel electrode as it is the layer with the highest CTE (13.2 µm $m^{-1}$ $°C^{-1}$). A summary of reported CTE values for all layer compositions can be found in Table 5.3. The neutral axis is therefore suspected to be either located close to the fuel electrode but within the support, or at both of the fuel electrode interfaces.

**Table 5.3:** Summary of CTE values for all investigated layer compositions. Values were taken from literature.

| Composition | CTE [µm $m^{-1}$ $°C^{-1}$] | Source |
|---|---|---|
| 8YSZ | 10.2 | [104] |
| NiO-8YSZ | 12.2 | [104] |
| 10GDC | 12.7 | [104][188][189] |
| NiO-10GDC (50:50) | 13.5 | [188][190] |
| NiO | 14.5 | [188] |

In addition to the thermal expansion mismatch, differential and constrained sintering can also generate residual stresses within the electrolyte layers. As already discussed in Chapter 5.3, the cells transform from early stage convex bending to concave bending in later sintering stages. This is a clear indication that sintering onset and shrinkage rate mismatches are present in the system. At early stages, the electrolyte already starts to densify while the support lags behind, creating mismatch strains that can lead to internal stress buildup. As sintering progresses and the support densifies, the electrolyte is potentially already close to its shrinkage maximum and not able to fully compensate the support shrinkage. This would lead to additional compressive stresses within the electrolyte layers. While the potential to bend allows for partial stress relaxation, a full stress release is unlikely. This is supported when further investigating the influence of constrained or differential sintering in regard to the stress state of the bottom GDC layer in the tri-layer electrolyte more closely. The significant difference in compressive residual stress observed within that layer between covered and uncovered regions is most likely attributed to differences in mechanical constraint during sintering. In the covered region, the bottom GDC layer is confined between the fuel electrode and the support below and the additional electrolyte layers above (YSZ and top GDC). This constraint potentially inhibits stress relaxation during sintering and cooling, resulting in high biaxial compressive stress. Due to this constraint, these stresses are even higher than the compressive stresses in the YSZ of the bi-layer electrolyte cell. Conversely, in the uncovered region, the same bottom GDC layer has an exposed surface which is relatively free to deform. This allows for some of the stress to relax either by surface bending or creep and explains the

lower stress state in the uncovered area of the bottom GDC electrolyte layer [191, 192]. Unfortunately, the YSZ layer of the tri-layer electrolyte could not be measured in $\sin^2\Psi$ due to the thickness of the top GDC layer. However, because of the additional constraints induced by the top GDC layer, it is hypothesized that the stress state of the sandwiched YSZ layer in the tri-layer electrolyte is higher than that of the bi-layer electrolyte.

Further information on this can be obtained when analyzing the results of the second set of experiments. In contrast to the first set of experiments, the omega stress method was employed here to measure a stress gradient through the uppermost micrometers of the tri-layer electrolyte. Figure 5.8 A presents the residual stresses of the YSZ and Figure 5.8 B the stresses of the top GDC layer, co-sintered at 1350 °C and 1400 °C, as a function of substrate calcination temperature. When examining the results for the YSZ layer, there appears to be a correlation between the residual stresses and substrate calcination temperature, as well as co-sintering temperature. Co-sintering at higher temperatures appears to result in higher compressive stresses. At the same time, the residual stress also appears to increase with increased substrate calcination temperature. The observed trend of lower residual compressive stresses in the YSZ layer for cells co-sintered at lower temperatures can be attributed to the reduced overall shrinkage occurring during sintering. Lower co-sintering temperatures are synonymous to slower densification kinetics and less shrinkage of both the electrolyte layers and the support, thereby diminishing the dimensional mismatch caused by differential shrinkage between layers. Since shrinkage mismatches were already identified as one potential cause for residual stress buildup, the reduced differential strain at lower temperatures leading to smaller residual compressive stresses in the YSZ layer further supports this hypothesis.

This shrinkage mismatch between electrolyte and support can be partially alleviated by lowering the substrate calcination temperature prior to co-sintering. Substrates calcined at lower temperatures remain more porous and retain greater shrinkage potential during co-sintering. This allows the support to densify more concurrently with the electrolyte layers, promoting more synchronized shrinkage behavior and reducing mechanical constraint. As a result, the differential shrinkage is reduced. In contrast, supports calcined at higher temperatures are already more densified and shrink less during co-sintering, acting as a more rigid constraint and intensifying the mismatch between support and electrolyte. This constraint subsequently promotes greater residual compressive stress in the YSZ. Therefore, both higher substrate calcination temperature and higher co-sintering temperatures lead to increased overall differential strain and consequently higher residual compressive stresses in the YSZ layer.

Interestingly, one cell co-sintered at 1400 °C with a substrate calcination temperature of 1200 °C deviates from this trend. As this combination of processing conditions is very close to the standard manufacturing procedure used in the first set of experiments, it is possible to compare this data point with the results from the measurement of the bi-layer electrolyte. Contrary to the previously stated expectation that a sandwiched architecture would lead to higher residual stresses, the stress state of the YSZ layers when comparing bi-layer and tri-layer architectures are virtually the same with 674.4 MPa ±

20.7 and 672.5 MPa ± 30.7 respectively. However, there are multiple factors to consider when trying to interpret the data. The tri-layer electrolyte samples were flattened prior to the stress measurement. This is typically done by heating the already sintered and bent cells up to a temperature of 50 K below the co-sintering temperature and subsequently applying a load of 1.5 – 2 kg per cell for 0.5 h (see Chapter 5.2). This combination of an applied load at elevated temperatures most likely induces creep within the materials, potentially resulting in some stress relaxation. Especially the GDC layers are most likely to undergo stress relaxation through creep. In particular, the top GDC barrier layer appears to have relaxed almost entirely, as evidenced by its near zero residual stress after ironing as depicted in Figure 5.8 B. This suggests that surrounding GDC layers may absorb and redistribute part of the mechanical constraint, thereby preventing and reducing compressive stress buildup in the sandwiched YSZ layer. As YSZ itself has a much lower capability to creep, it retains more of its sintering-induced stress. However, the additional confinement in the tri-layer structure did not lead to higher compressive stress due to the stress-relieving effect of the more deformable GDC layers.

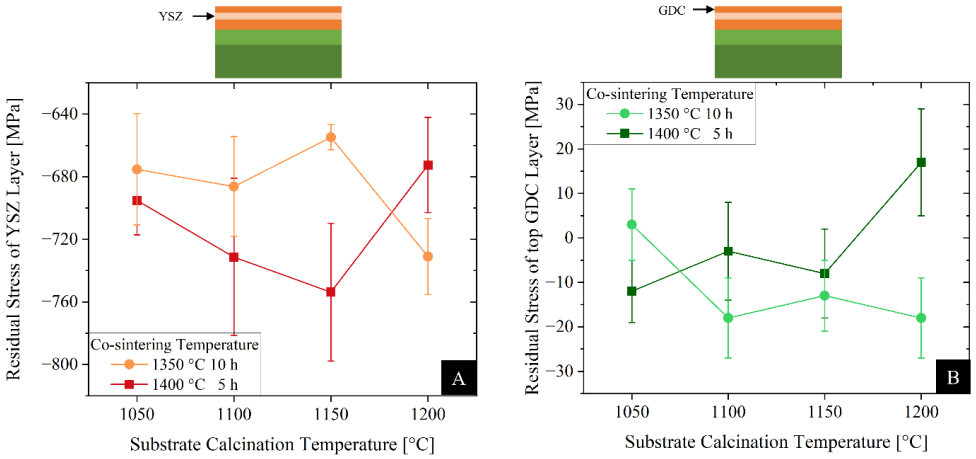


**Figure 5.8:** Residual stress in the tri-layer electrolyte as a function of substrate calcination temperature for two co-sintering temperatures (1350 °C and 1400 °C), measured by Mirco Ziegner (IMD-1) using the omega stress method**. A** Residual stress in YSZ layer. **B** Residual stress in the top GDC layer.

In addition to the potential creep related stress relaxation of the GDC layers, another factor that may contribute to the apparent similarity in residual stress between the sandwiched YSZ and the YSZ in the bi-layer electrolyte is interdiffusion between GDC and YSZ during co-sintering. At high sintering temperatures, significant interdiffusion between adjacent GDC and YSZ layers was observed in the tri-layer electrolyte. This was evidenced by asymmetries in the recorded X-ray diffraction reflexes. As showcased in Figure 5.9 A, YSZ reflexes consistently showed a broadening at the left peak flank, while GDC peaks exhibited a broadening at the right peak flank toward higher angles. Such peak asymmetries indicate intermixing of those two phases across the interface, which alters the local lattice parameters of

these materials. For YSZ, this interdiffusion appears to shift the lattice parameter towards larger values, which opposes the lattice contraction typically caused by compressive stresses. As a result, the true compressive stress in the YSZ layer may be underestimated in these XRD stress measurements due to this superimposed chemical strain. Since data fitting assumes that the peak shifts solely originate from mechanical strain, the overlapping effects of interdiffusion complicate the accurate identification of peak positions and subsequent quantification of residual stress. Although it is not possible to precisely deconvolute the chemical and mechanical contributions to the observed peak positions, acknowledging this possible interference provides further context for the seemingly unchanged stress levels in the tri-layer architecture and suggests that the true mechanical stress state in the YSZ may in fact be higher than measured. Additionally, this effect of interdiffusion is assumed to be more pronounced in the tri-layer electrolyte, as YSZ is sandwiched between GDC on both sides, as opposed to being positioned next to only one layer of GDC, as is the case in the bi-layer architecture.

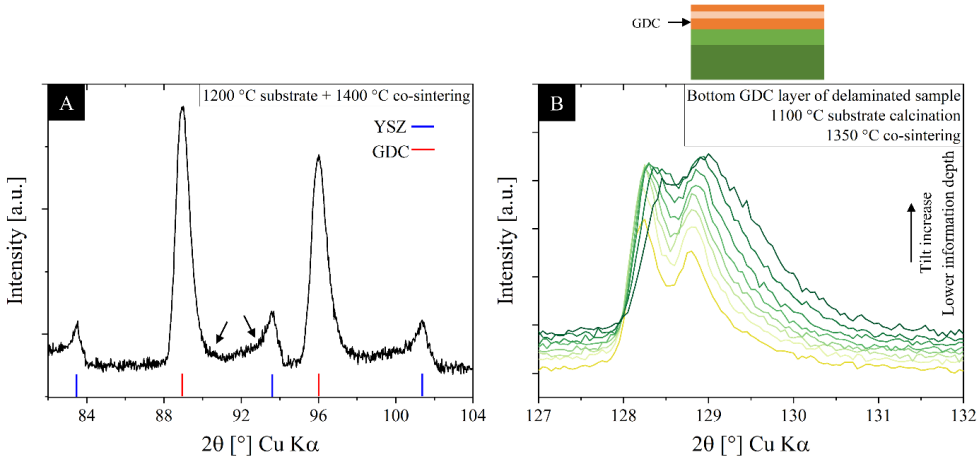


**Figure 5.9:** Implications of interdiffusion between GDC and YSZ in tri-layer electrolyte samples. Diffraction patterns generated by Mirko Ziegner (IMD-1) using a parallel beam geometry. **A** Diffraction pattern showing asymmetric broadening of YSZ and GDC peaks. YSZ peaks show a broadening at the left peak flank, GDC peaks show a broadening at right peak flanks as indicated by the arrows. **B** Tilt-angle-dependent diffraction patterns of the bottom GDC electrolyte layer. With increasing tilt, peak asymmetry becomes more pronounced and peak positions shift significantly towards higher diffraction angles.

The tilt-dependent diffraction patterns of the bottom GDC layer shown in Figure 5.9 B offer further evidence for interdiffusion between GDC and YSZ in the tri-layer electrolyte architecture. As the tilt angle increases, corresponding to a lower information depth and thus probing regions closer to the GDC/YSZ interface, both the asymmetry and the shift in peak positions of the GDC reflexes become more pronounced. This hints toward a composition gradient across the GDC layer, which is most likely attributed to interdiffusion happening during manufacturing. Such an interdiffusion gradient results in a variation of the lattice parameters, which complicates the interpretation of peak positions and renders accurate residual stress determination highly uncertain. Consequently, all stress values presented here

must be regarded with caution. The large error indicated in Figure 5.8 reflects this uncertainty and the limitations caused by the superimposed effects of mechanical strain and compositional changes. Therefore, the precise magnitude and distribution of the electrolyte stress state remains largely unresolved due to the influence of interdiffusion.

Nevertheless, Table 5.4 aims to summarize all the discussed potential mechanisms at play and their hypothesized effect on the residual stress state in YSZ and GDC electrolyte layers.

**Table 5.4:** Summary of the mechanisms potentially influencing the residual stress development in YSZ and GDC layers within the bi- or tri-layer electrolyte.

| Mechanism | Effect on residual stress in YSZ | Effect on residual stress in GDC |
|---|---|---|
| Thermal expansion mismatch GDC > YSZ | • Compressive stress in YSZ due to constrained cooling | • Lower in plane compressive stress (if tensile stress in support) |
| Electrolyte densifying earlier than support during sintering | • Increased compressive stress from support shrinkage in later stages of sintering | |
| Lower calcination temperature of support / higher shrinkage potential during co-sintering | • Lower compressive stress due to more synchronized shrinkage between support and electrolyte | |
| Higher co-sintering temperature | • Increased constraint and compressive stress due to higher shrinkage mismatch between individual electrolyte layers and the support | |
| Tri-layer electrolyte architecture | • Expected higher compressive stress due to increased constraint | • Potential lower stress in top GDC layer due to stress redistribution but increased stress in bottom GDC layer due to increased constraint |
| Ironing post sintering at elevated temperatures | • Some stress relief through stress distribution facilitated by creep of GDC layers | • Significant stress relaxation, especially in top GDC layer due to creep |
| Interdiffusion between GDC and YSZ | • Measured peak shifts towards lower angles partially masking compressive stress (underestimation) | • Measured peak shifts towards higher angles partially amplifying compressive stress (overestimation) |

## 5.5 Half-cell and full cell microstructures

The microstructure of the tri-layer electrolyte in the investigated fuel electrode-supported SOCs is a decisive factor for cell performance, as it directly influences ionic conductivity, gas tightness and interfacial resistances. Therefore, this chapter investigates factors such as substrate calcination temperature and co-sintering conditions on the microstructure of the electrolyte, with particular focus on porosity formation within the YSZ and GDC electrolyte layers, as well as the YSZ/GDC interface using 3D-reconstruction techniques. Furthermore, the cell structures of the different cell types introduced in Chapter 5.2 are discussed. Additionally, the formation of interdiffusion zones at the GDC/YSZ interface during these different cell manufacturing processes is discussed as well as their implications for densification and interface integrity.

SEM cross-sections of oxidized Type A half-cells are presented in Figure 5.10 and were analyzed to evaluate the tri-layer electrolyte microstructure and interface quality when produced using different substrate calcination temperature and co-sintering temperature combinations. Across all investigated samples, a dense and well-adhered interface between the NiO-GDC fuel electrode and the bottom GDC electrolyte layer is observed. No pore fringes or delamination are visible at this electrochemically highly active area.

However, a notable observation is that for samples co-sintered at lower temperatures (1350 °C – 10 h and 1375 °C – 7.5 h) in combination with high substrate calcination temperatures (1150 °C and 1200 °C), the YSZ barrier and GDC barrier layers are no longer present. These layers spalled off during cooling to room temperature, likely in the temperature range between 100 °C and 20 °C after removal from the furnace. This spallation is most likely attributed to insufficient densification of these layers under these sintering conditions, in combination with the potentially pronounced interface porosity between GDC and YSZ. This interfacial porosity likely critically lowers the effective fracture toughness of the interface, causing it to fail mechanically and not be able to withstand the stresses arising during cooling. For all other samples processed under the remaining sintering conditions, the tri-layer electrolyte structure remained intact after co-sintering. Variations in porosity within the electrolyte layers, particularly in the GDC layers are observed depending on the substrate calcination temperature and co-sintering temperature. However, due to mechanical damage during polishing of these cross-sections, the porosity of the top GDC barrier layer could not be reliably quantified and is therefore not reported and discussed further. Porosity values for the YSZ barrier layer and bottom GDC layer are presented separately in Figure 5.11 A and B respectively. Here porosity is shown as a function of substrate calcination temperature for each co-sintering temperature.

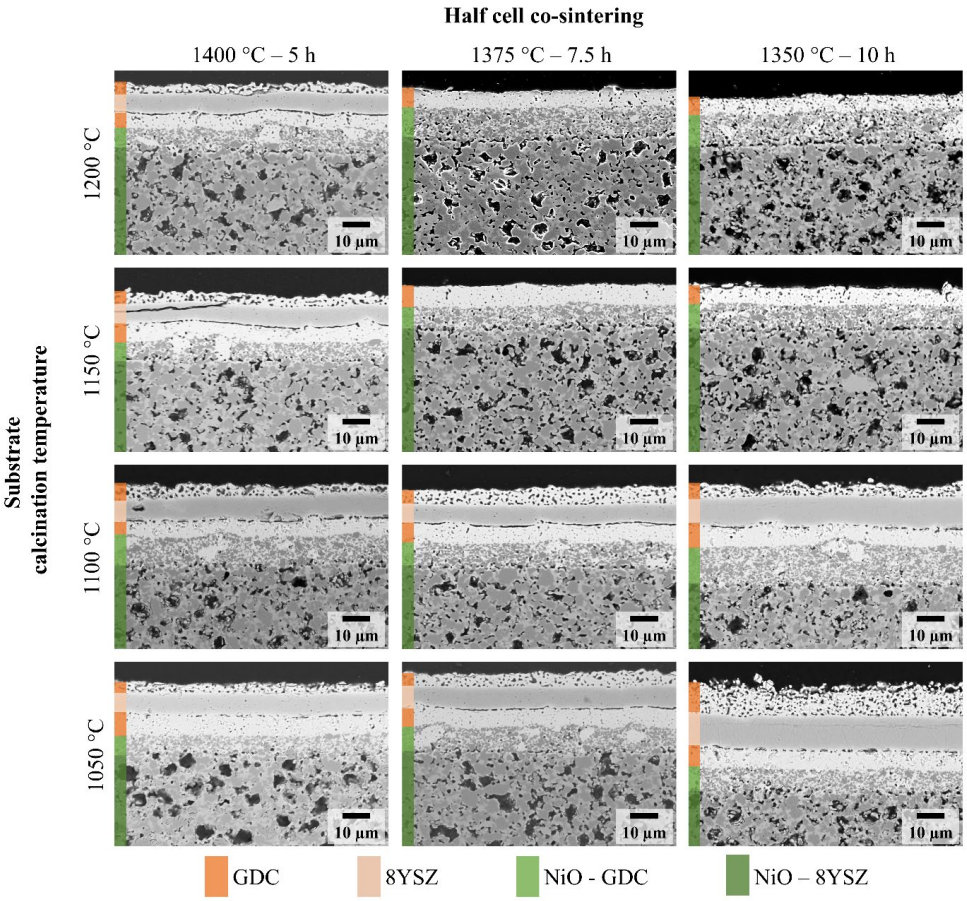


**Figure 5.10:** BSE-SEM images of Type A half-cell cross-sections. Cells were sintered on substrates calcined at varying temperatures (1050 °C, 1100 °C, 1150 °C and 1200 °C) using different co-sintering conditions (1350 °C – 10 h; 1375 °C – 7.5 h and 1400 °C – 5 h). A dense and well-adhered interface is observed between the fuel electrode and the bottom GDC layer across all samples.

The quantified porosity analysis reveals that the YSZ layer is consistently more dense than the bottom GDC layer across all processing conditions. Due to the electrolyte spallation observed for cells using substrates calcined at 1150 °C and 1200 °C and co-sintering temperatures below 1400 °C, no porosity values could be obtained for these combinations. In general, the bulk porosity of the YSZ layer remains low, ranging from < 1% to 3 % across all investigated sintering conditions. A clear trend is observed where higher co-sintering temperatures lead to lower bulk porosity within the YSZ layer. However, for cells using substrates calcined at 1050 °C, this trend is less pronounced due to the overall low porosity (< 1 %), making differences difficult to resolve in image analysis.

Similar trends are observed for the bottom GDC electrolyte layer, though the porosity values here are generally higher, with average values ranging between 3 % and 11 %. The lowest porosities (~ 3 %) are achieved when co-sintering at 1400 °C while using substrates that were calcined at 1050 °C. These

values are substantially lower than those achieved under standard processing conditions (substrate calcination at 1230 °C with co-sintering at 1400 °C), where the bottom GDC layer typically exhibits bulk porosities around 8 %. This demonstrates that reducing substrate calcination temperatures can support GDC densification even at reduced co-sintering temperatures, indicating a potential pathway for lowering co-sintering temperatures while maintaining dense electrolyte microstructures. These findings are in line with the observed shrinkage behavior that was previously reported in Chapter 5.3.

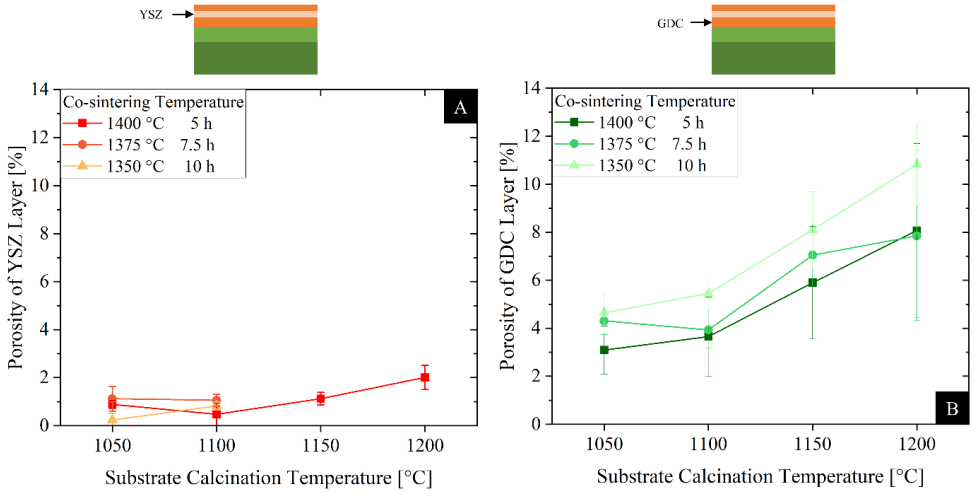


**Figure 5.11:** Porosity in the tri-layer electrolyte layers as a function of substrate calcination temperature for all investigated co-sintering temperatures (1350 °C, 1375 °C and 1400 °C) analyzed from SEM cross-sections using the image analysis software Fiji (ImageJ). **A** Porosity in YSZ layer. **B** Porosity in bottom GDC layer.

While the bulk porosity of both YSZ and bottom GDC electrolyte layers appears reasonable under all investigated sintering conditions, the porosity at the GDC/YSZ interface within the tri-layer electrolyte is more concerning. Due to limitations in image analysis in these regions, a quantitative analysis of this interface porosity was not feasible for the various substrate calcination and co-sintering temperature combinations investigated, making the formulation of clear trends difficult. Nonetheless, pronounced porosity at the GDC/YSZ interface was observed across all cells. It could be cautiously argued that, for a given co-sintering temperature, this interface porosity appears less pronounced when lower substrate calcination temperatures are used. This observation suggests that if the substrate exhibits higher shrinkage potential during co-sintering (due to lower calcination temperatures and thus lower initial densification), it may constrain the electrolyte layers less during co-sintering. As a result, the differential sintering between the GDC and YSZ layers becomes less pronounced, potentially leading to reduced interface porosity. However, it is hypothesized that interdiffusion phenomena between GDC and YSZ are the main reason for this interface porosity formation. As from interdiffusion studies previously conducted by Alexander Schwiers at IMD-2 and corresponding literature for this material system, it is known that this pronounced porosity can result from such interdiffusion processes [120]. Specifically,

since the diffusion of ceria into YSZ is slower than the counter-diffusion of zirconia into GDC, Kirkendall porosity can form at the interface during co-sintering. Given that solid-state diffusion is predominantly thermally activated, one would expect that lower co-sintering temperatures would limit interdiffusion-driven porosity formation at the interface. However, this trend is not clearly observable in the presented SEM images of Figure 5.10. A possible reason for this could be that although the variations in co-sintering temperatures employed in this study (maximum of 50 K) should produce a discernable difference in interdiffusion magnitude and therefore porosity, this effect is superimposed with the previously discussed influences of substrate calcination temperature and the associated substrate shrinkage and constraint behavior during co-sintering, making it difficult to discern the contributions of temperature dependent interdiffusion.

Further insight into the evolution of interface porosity is gained by comparing 3D reconstructions (compiled by Luzie Wehner, IMD-1) of a Type A cell with a fully screen-printed and co-sintered tri-layer electrolyte and a Type E cell that was tested at KIT (only bottom GDC layer is screen-printed, while YSZ and GDC barrier layers are subsequently sputtered). These reconstructions, presented in Figure 5.12 alongside pore structure reconstructions of the bottom screen-printed GDC layer, clearly show that the pronounced interface porosity is only present in Type A cells indicating that it develops during high-temperature co-sintering of fully screen-printed electrolytes rather than during cell operation. In Type E cells, no interface porosity is visible, reinforcing the hypothesis that the observed interface porosity in Type A cells is primarily Kirkendall porosity driven by interdiffusion. Interestingly, while the extensive and interconnecting interface porosity is present in Type A cells, the pores within the screen-printed layer itself would be isolated when not connected to the interface porosity. This implies that although Type A cells would not be gas-tight without the dense YSZ layer, it is the presence of this YSZ layer during co-sintering that contributes to the extensive pore formation within the GDC layer and at the interface due to interdiffusion. This is also evident when comparing pore tortuosity of this GDC layer between Type A ($\tau = 7$) and Type E cell ($\tau = 17$), alongside of bulk and interface porosity which are summarized in Table 5.5. Here, the evaluated porosity of the bottom GDC layer of the Type A cell well agrees with the porosity showcased in Figure 5.11 for the same sintering conditions.

**Table 5.5:** Summary of pore characteristics in the bottom GDC layer of Type A and Type E half-cells. Presented are bulk porosity, interface porosity at the GDC/YSZ interface and pore tortuosity gathered from 3D reconstructions compiled by Luzie Wehner (IMD-1).

| Microstructural Parameter | Type A Cell | Type E Cell |
|---|---|---|
| Porosity of GDC Electrolyte Layer | 8 % | 4 % |
| Pore Tortuosity of GDC Electrolyte Layer | 7 | 17 |
| Interface Porosity GDC/YSZ | 10 % | < 1 % |

Furthermore, the data in Table 5.5 shows that the interface porosity at the GDC/YSZ interface in the Type A cell is significantly higher (~ 10 %) compared to the Type E cell, where it remains below 1 %. This stark difference underscores that the interface porosity observed in co-sintered fully screen-printed electrolytes (Type A) is not an inevitable feature of the material system itself but rather the result of processing at high co-sintering temperatures. Given its magnitude and location, it is assumed that this interface porosity will contribute substantially to the overall cell resistance, acting as a bottleneck for ionic transport across the electrolyte layers. Consequently, this finding highlights the critical need to address interface porosity formation during co-sintering if further reductions in cell resistance and improvements in overall performance are to be achieved.

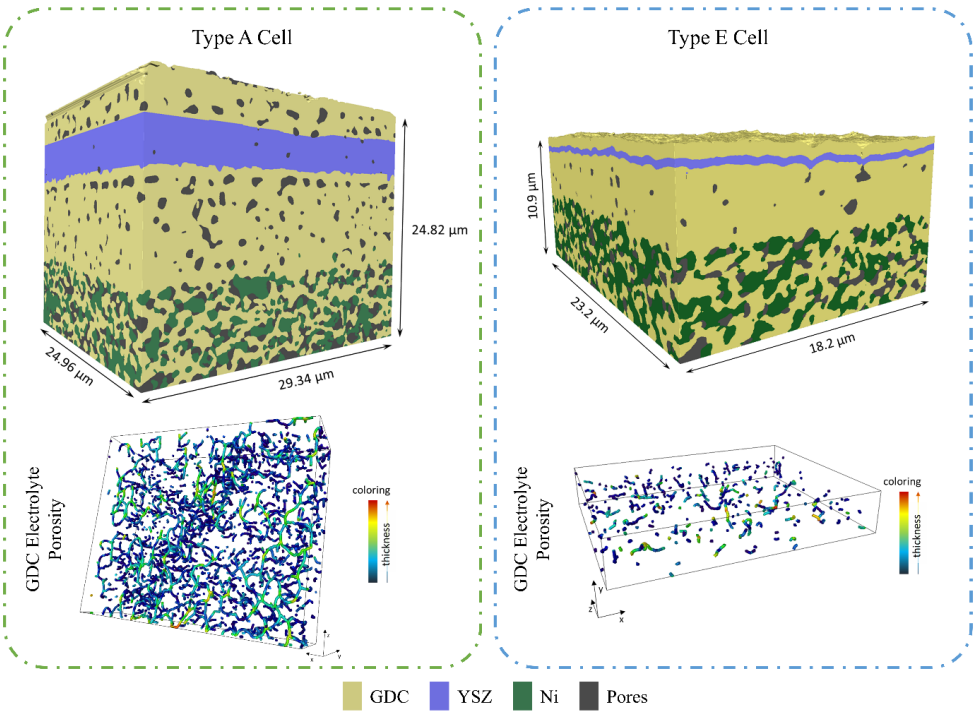


**Figure 5.12:** 3D reconstructions of the tri-layer electrolyte microstructure in Type A cells (fully screen-printed and co-sintered) and a Type E cell (screen-printed bottom GDC layer with subsequently sputtered GDC and YSZ barrier layers. Reconstruction of the pore structure within the bottom GDC layer are shown underneath the respective half-cell reconstruction. Pronounced interface porosity is visible in Type A cells, while missing in Type E cells. 3D reconstruction and analysis provided by Luzie Wehner (IMD-1).

It is further noticeable that in Type A cells, the interface porosity is more pronounced at the fuel-side GDC/YSZ interface than at the air-side GDC/YSZ interface. While the precise mechanism behind this asymmetry is not yet fully understood, it is plausible that differences in mechanical constraints during co-sintering play a role. The top GDC layer (air side) remains exposed to the atmosphere during sintering, allowing it to move and deform more freely, which could reduce pore formation at the

interface. In contrast, the bottom GDC/YSZ interface on the fuel side is tightly constrained between the densifying substrate and the other electrolyte layers, potentially leading to higher local stresses and a stronger driving force for interface porosity formation during interdiffusion. These observations hint towards interface porosity not only being a function of interdiffusion and co-sintering temperature but also of the mechanical boundary conditions during processing.

This pronounced interface porosity on the fuel side is also clearly visible in Type A.1 and Type B cells, which feature very thick YSZ layers (~ 22 µm), as showcased in Figure 5.13. A thicker YSZ layer may lead to higher internal stresses during co-sintering, promoting the formation of pores at the GDC/YSZ interface due to constrained sintering and interdiffusion effects. Interestingly, this interface porosity is less evident in Type D cells, where only the bottom GDC and YSZ layers are co-sintered, analogous to Type B cells. This may be attributed to the GDC layer in the Type D cell being generally more porous, making localized interface porosity less distinguishable, or it may result from the thinner YSZ layer, which, being exposed to the atmosphere during sintering, can deform more freely and thus reduce stress concentrations at the fuel-side interface, mitigating pore formation. In these cells, the top GDC layer is sputtered, with no interface porosity visible. The same absence of interface porosity is observed in both Type E cell cross-sections, which utilize only sputtered barrier layers.

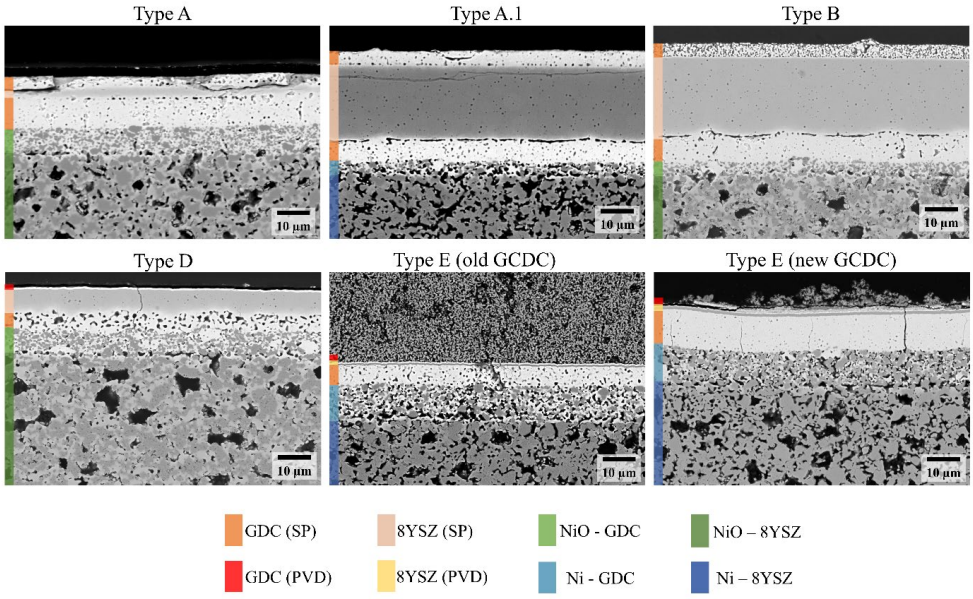


**Figure 5.13:** BSE-SEM cross-section images of the various cell types manufactured and investigated in this work, illustrating the presence or absence of GDC/YSZ interface porosity depending on the electrolyte architecture and processing routes. Layers deposited by screen-printing (SP) and sputtering (PVD) are indicated for clarity.

To gain a deeper understanding of the extent of interdiffusion at the GDC/YSZ interfaces, quantitative analyses were attempted using EDS line scans at low acceleration voltages (6 kV) on various Type A cells and a Type A.1 cell. The focus was on determining both the interdiffusion zone length and the residual cerium content within the YSZ layer after co-sintering. It became evident that only in Type A.1 cells, featuring a significantly thicker YSZ layer (~ 22 µm), the true interdiffusion zone length could be reliably measured. Here, a zone of approximately 5 µm at each interface was identified, within which a clear cerium concentration gradient was observed, decreasing to ~ 0.5 at% in the remaining bulk of the YSZ layer, effectively indicating negligible cerium incorporation beyond this interfacial region. In contrast, for Type A cells with thinner YSZ layers (4 – 10 µm), interdiffusion zones originating from both the fuel and air side interfaces overlapped within the YSZ layer. This led to substantially higher residual cerium contents throughout the YSZ, with values measured at ~ 5 at% for GDC Type A cells with thin YSZ layers, ~ 3 at% for GDC Type A cells with slightly thicker YSZ layers and ~ 7 at% for GCDC Type A cells with thin YSZ layers. EDS line scan profiles illustrating the element gradients are provided in the Appendix. Table 5.6 summarizes the residual cerium contents and interdiffusion zone lengths for each cell type investigated. Here, 'interdiffusion zone length' is defined as the distance from the interface to the point of the lowest measured cerium concentration within the YSZ layer, which is shortest in the GCDC Type A cell and is characterized by shallower cerium gradients compared to cells using regular GDC. This suggests that additional co-doping of GDC with $Co_2O_3$ (GCDC) further enhances cation mobility, thereby accelerating interdiffusion during co-sintering. Interestingly, no clear differences between air side or fuel side interfaces were observable.

**Table 5.6:** Residual cerium content within the YSZ electrolyte layer and estimated interdiffusion zone lengths for Type A and Type A.1 cells after co-sintering. Residual cerium content is measured as the average at% of cerium in the YSZ layer, while the interdiffusion zone length is defined as the distance from the GDC/YSZ interface to the point of minimum cerium concentration within the YSZ. Data were obtained from EDS line scans at 6 kV conducted by Luzie Wehner (IMD-1).

| Cell Type | Interdiffusion Zone Length [µm] | Residual Cerium Content within YSZ Layer [at%] |
|---|---|---|
| Type A (GDC) YSZ ~ 4 µm | 2.6 | 5 |
| Type A (GDC) YSZ ~ 10 µm | 2.4 | 3 |
| Type A (GCDC) YSZ ~ 4 µm | 1.9 | 7 |
| Type A.1 YSZ ~ 22 µm | 5.0 | < 1 |

## 5.6 Conclusion

In this thesis, the sintering behavior and microstructural evolution of different types of fuel electrode-supported solid oxide cells was investigated, with particular focus on the formation of fully screen-printed and co-sintered tri-layer electrolytes.

Here, the sintering behavior of such half-cells was found to be heavily dependent on the interplay between the individual sintering behaviors of the electrolyte layers and the preconditioning of the substrate. The substrate calcination temperature was proven to critically affect the entire half-cell's shrinkage behavior during co-sintering, which in turn influences the densification of the electrolyte layers and the evolution of residual stresses within the cell. While sufficient substrate shrinkage can support electrolyte densification during co-sintering at lower temperatures, substrates calcined at already relatively high temperatures constrain and impede electrolyte densification leading to increased residual electrolyte porosity.

Additionally, residual bending of the half-cells after co-sintering was observed to correlate with mismatches in shrinkage and densification kinetics between the substrate and the electrolyte layers, underscoring the importance of sintering behavior alignment to minimize mechanical stresses during processing. These stresses, together with stresses due to thermal gradients during cooling and thermal expansion mismatches, influence the mechanical stability of the tri-layer electrolyte, critically impacting interface integrity.

Furthermore, the microstructure of the tri-layer electrolyte, particularly the porosity within the GDC and YSZ layers and at their interfaces, was shown to be highly sensitive to processing conditions. Pronounced interface porosity, primarily attributed to interdiffusion-driven Kirkendall porosity, was identified as a critical feature formed during high-temperature co-sintering, with its extent strongly dependent on the manufacturing route, as electrolytes processed via PVD techniques exhibited no interface porosity. Additionally, the length of these interdiffusion zones and the residual ceria content within the YSZ barrier layer were found to be highly dependent on YSZ layer thicknesses, additional doping of GDC and the applied sintering conditions.

Overall, these investigations emphasize the complex interdependence between substrate pre-treatment, shrinkage behavior, electrolyte layer densification and the evolution of residual stresses and porosity in the final microstructure of tri-layer electrolyte fuel electrode-supported SOCs. Therefore, it is proposed that for successfully producing fully screen-printed and co-sintered tri-layer electrolyte half-cells with thin electrolyte layers, it is likely that a new substrate needs to be developed. The current Type III substrate requires too high co-sintering temperatures for densification, as at lower temperatures it heavily impedes electrolyte densification. However, these high temperatures promote interdiffusion and extensive interface porosity within the electrolyte, potentially decreasing the functionality and performance of the cell. Although applying thicker YSZ layers can mitigate critical interdiffusion, this approach compromises the benefits of thin electrolytes as the key advantage of FESCs. To fully unlock

the potential of these screen-printed tri-layer electrolyte cells, the development of a substrate that allows sufficient electrolyte densification at significantly lower co-sintering temperatures will be essential, enabling the use of thin, high-performance electrolyte layers while maintaining interface integrity and mechanical stability. One possible solution to this could be the utilization of sequential tape casting, which enables co-sintering of the entire half-cell without the need for prior substrate pre-sintering.

# 6 Electrochemical characterization and performance of full cells

## 6.1 Motivation

Throughout the development of the cells presented in this thesis, achieving sufficiently high open-circuit voltages (OCV) has been a persistent challenge. Low OCV values were identified early on as a prominent issue affecting overall reliability of the cells. Consequently, OCV has been the electrochemical parameter investigated most extensively within this work. The focus on OCV measurements was driven not only by its importance as an indicator for structural integrity but also by the need to identify the underlying causes of the observed low OCV values. In particular, it was unclear whether these limitations originated from microstructural factors, interdiffusion between GDC and YSZ, cracking of the electrolyte during the reduction of the cell prior to measurements or a combination of all of these factors. Additionally, potential sealing issues within the test benches could not be excluded as contributing factors. OCV investigations were therefore essential to disentangle these possible causes and to guide targeted improvements in cell design and especially processing.
In addition to OCV measurements, complementary electrochemical characterizations, including current-voltage (I-V) curves and preliminary degradation studies were conducted to provide a broader understanding of the electrochemical behavior and stability of the fabricated cells under operation conditions.

## 6.2 Open circuit voltage (OCV)

Figure 6.1 shows the OCV values measured at 800 °C under dry hydrogen conditions for the various cell types discussed in Chapter 5. The values are also presented in Table 6.1.
Although Type A cells exhibit significantly lower OCV values compared to the other cell types, averaging between 0.4 V and 0.7 V, cross-section SEM images confirmed that all electrolyte layers, including those of Type A cells appear dense and gas tight. Especially the screen-printed YSZ layers show almost no residual porosity and therefore act as a sufficient gas separation layer. This observation indicates that the low OCV in Type A cells is not due to gas leakage caused by extensive electrolyte porosity or open pathways. Given the dense microstructure, cation interdiffusion during high-temperature co-sintering emerges as the more likely cause of the low OCV. In Type A cells, the thin YSZ electron-blocking layer (~ 3 µm) seems to be completely penetrated by cerium and gadolinium from the adjacent GDC layers during co-sintering at 1400 °C, leading to partial electronic conduction across the entire YSZ layer. Separate SEM-EDS and TEM-EDS analyses confirmed extensive diffusion, with minimum cerium concentrations measured at ~ 9 at% (TEM) and 5 at% (SEM) within the YSZ layer, indicating the partial electronic conductivity potential through the entire YSZ layer (see Chapter 5.5). This electronic leakage effectively short-circuits the electrolyte, reducing the achievable OCV far

below the theoretical Nernst Voltage of 1.2 V for these conditions. In Type A.1 cells, which utilize a significantly thicker screen-printed YSZ layer (~ 20 µm), OCV values increase to approximately 1.09 V, approaching the theoretical value under these test conditions. Previous interdiffusion investigations presented in Chapter 5.5 showed that the interdiffusion length of cerium into YSZ is ~ 5 µm from each interface under the applied co-sintering conditions. Consequently, in Type A.1 cells, a central electronically insulating region within the YSZ layer is preserved, restoring the electron-blocking function of the electrolyte and enabling higher OCV values.

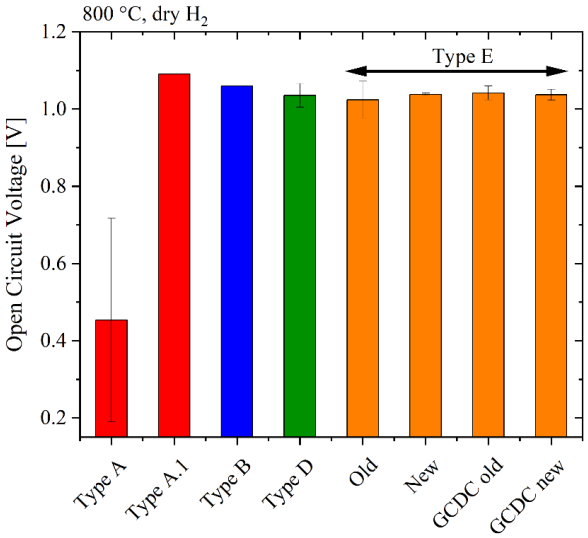


**Figure 6.1:** Open circuit voltage (OCV) values measured at 800 °C under dry $H_2$ for the different cell types manufactured and investigated in this work. OCV measurements for Type A to Type D cells were conducted at the single cell test bench at IMD-2 and Type E cell OCV measurements were conducted by IAM-ET at KIT by Dr Iurii Kogut. Type A to Type B cells are fully screen-printed while Type D contains one sputtered GDC barrier layer and Type E contains sputtered GDC and YSZ barrier layers.

A similar high OCV is observed in Type B (1.06 V) and Type D (1.04 V) cells. Type B cells also employ a thick (~ 20 µm) YSZ layer, while Type D cells utilize a thinner YSZ layer (~ 5 – 7 µm). Both cell types feature asymmetrical electrolyte structures (GDC-YSZ) during high-temperature co-sintering, limiting the potential cation interdiffusion observed in Type A cells. In Type B cells, the thick YSZ layer fully prevents cerium diffusion from crossing the electrolyte, similar to Type A.1 cells, preserving electronic insulation. In Type D cells, although the YSZ layer is thinner, the asymmetry during co-sintering and reduced cerium incorporation (~ 2 at% or even lower) appear insufficient to induce electronic leakage, allowing for the high OCV values.

Additionally, a slight trend of Type B cells exhibiting marginally higher OCV than Type D cells was observed. It is hypothesized that the post-sintering application of an additional ~ 5 µm screen-printed GDC layer sintered at 1300 °C in Type B may help some potential surface defects or microcracks arising

from warping during the asymmetric co-sintering. The thinner 500 nm PVD GDC layer in Type D cells on the other hand may be insufficient to fully cover such defects. Generally, cells with thicker electrolyte structure typically exhibit higher OCVs as the probability of defects pores fully penetrating the entirety of the electrolyte decreases with increasing layer thickness. However, the observed difference in OCV is small and remains within the typical variability of SOCs.

Although Type E cells exhibit slightly lower OCV values (~ 1.02 V – 1.04 V) than the fully screen-printed Type A.1 and Type B cells (~ 1.06 V and 1.09 V), these values remain sufficiently high for further electrochemical characterization and reliable operation. Within the Type E series, the transition from "old" to "new" cells and the use of Co-doped GDC (GCDC) electrolyte layers led to improvements in consistency across multiple tested twin cells. While the difference in average OCV values between old and new variants is not substantial, the scatter and variability between cells were notably reduced in the new, optimized variants. These improvements in consistency indicate that the reduction of local defects such as screen imprints or silicon contamination leading to holes during electrolyte optimization positively impacts overall gas tightness and structural reproducibility and reliability. However, the initial hypothesis during this thesis, that these defects would significantly reduce OCV values and were responsible for the low OCV of Type A cells, could not be confirmed in the measured data, suggesting that such defects were either too few or too small.

Nonetheless, while not directly reflected in OCV values, these defects had a potential practical impact on cell handling. A higher number of new and optimized Type E cells passed ethanol leakage tests, survived the mounting in the test bench and the reduction protocol without cracking compared to older Type E variants. Thus, the improvements made in the new Type E cells primarily enhanced the robustness and testing yield of the cells, indirectly contributing to reliable OCV measurement and stable operation, even if the direct OCV improvements were minor.

However, it should be noted that the measured OCV values may be underestimated for all cell types except Type A due to sealing challenges during testing. The fully screen-printed cells often exhibited slight residual bending after sintering and mechanical flattening, leading to imperfect contact with the gold gasket and potential minor gas leakage during measurement. This is most likely the reason for Type A.1 and Type B cells not achieving the optimal OCV of 1.2 V. Similarly, for cells with PVD deposited electrolyte layers (Type D and E), insufficient adhesion between the gold gasket and the dense GDC PVD surface occasionally limited sealing quality, which may have contributed to small gas leakage currents and slightly reduced measured OCV values in these cell types. Complementary photographs of these sealing issues are presented in the Appendix.

In summary, OCV measurements across the investigated cell types demonstrated that while all electrolytes were sufficiently dense, YSZ layer thickness and control of cation interdiffusion during co-sintering were decisive for achieving high OCV values. Type E cells, despite showing slightly lower OCV than fully screen-printed cells, maintained sufficiently high OCV for testing, with electrolyte optimization reducing variability and increasing reproducibility and robustness of the cells during

mounting and reduction, ensuring reliable performance without significant changes in the average OCV itself.

**Table 6.1:** Average open circuit voltage (OCV) values for the different cell types manufactured and investigated in this work, including standard deviations where multiple cells were measured. Cells were measured at 800 °C under dry $H_2$. OCV measurements for Type A to Type D cells were conducted at the single cell test bench at IMD-2 and Type E cell OCV measurements were conducted by IAM-ET at KIT by Dr Iurii Kogut.

| Cell Type | OCV [V] | Standard Deviation [V] |
|---|---|---|
| A | 0.600 | 0.263 |
| A.1 | 1.09 | - |
| B | 1.06 | - |
| D | 1.035 | 0.031 |
| E old | 1.024 | 0.048 |
| E new | 1.038 | 0.003 |
| E GCDC old | 1.042 | 0.018 |
| E GCDC new | 1.037 | 0.014 |

## 6.3 I-V Characteristics

Figure 6.2 shows the current-voltage (I-V) characteristics measured for the different cell types discussed in this work. The measurements were performed under ambient pressure conditions with dry hydrogen supplied at 60 NL/h on the fuel electrode and air supplied at 60 NL/h on the air electrode. Cells were heated to 800 °C and reduced under hydrogen prior to the I-V measurements. The observed downward slope in voltage at higher current densities for Type D cells can be most likely attributed to a measurement artifact related to the air supply of the test bench setup rather than actual cell performance. As a result, only the measured values at lower current densities were used for fitting and calculating the area-specific resistance (ASR) of these cells. Furthermore, for calculation, the active area was assumed to be 1 cm². However, as depicted in Chapter 3.2.11, the true active area is slightly larger than 1 cm² due to the additional reference air electrodes. In the setup used for these I-V measurements, the reference electrodes are not contacted separately and therefore only increase the active area without any distinction between air electrode and reference electrodes being possible. This means that the ASR values presented here are slightly underestimated. Since this is a systematic error for each measurement, the observable trends however, still hold true.

Type A.1 cells exhibit very high ASR of 604 mΩ·cm². Even if the entire electrolyte with a thickness of approximately 30 µm is considered to be entirely composed of YSZ, as the worse ionic conductor in this system, the ASR of 604 mΩ·cm² is not accounted for. It is estimated that a 30 µm thick YSZ electrolyte would rather result in an ASR of 60 mΩ·cm² under the investigated conditions. Therefore, it

can be assumed that likely even more critically seems to be the influence of the large GDC/YSZ interface porosity within the electrolyte which was analyzed to be roughly 12 % at the interface located at the fuel side. This porosity likely reduces the effective cross-sectional area for oxygen ion conduction within the electrolyte structure. Additionally, interdiffusion between YSZ and GDC at this interface during high-temperature co-sintering at 1400 °C leads to the formation of mixed-phase, which typically exhibits lower ionic conductivity, further contributing to the high ASR in Type A.1 cells. Similar observations were made by the Technical University of Denmark, as reported in Chapter 2.2.1, where the high ASR of their cell design (0.6 Ω·cm²), was also attributed to interface porosity and mixed-phase formation at the fuel electrode/electrolyte interface.

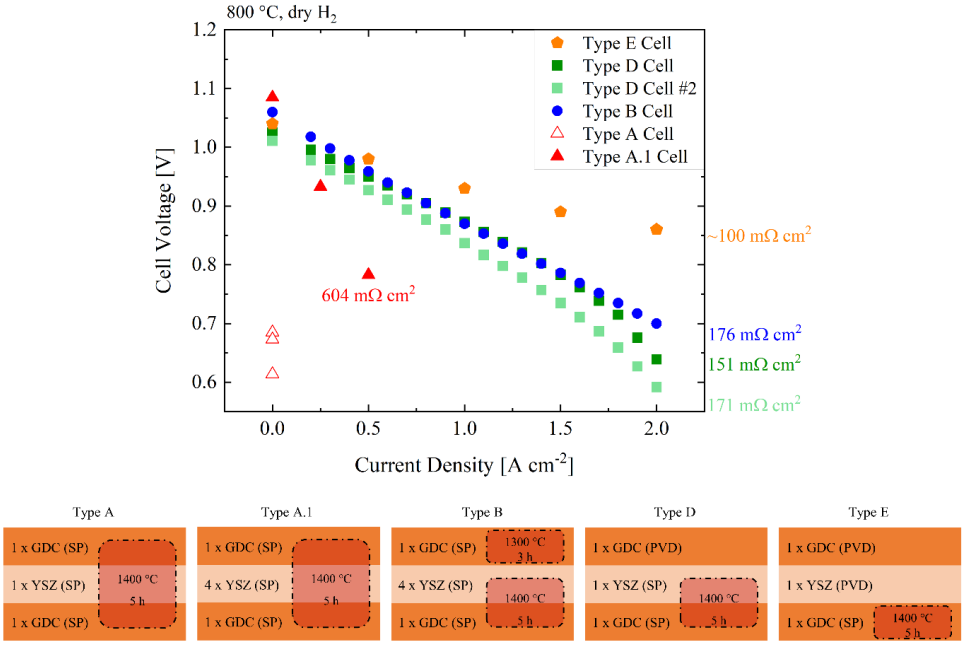


**Figure 6.2:** Current-voltage (I-V) characteristics of SOCs with different electrolyte architectures (Type A.1, B, D, D #2, E) measured at 800 °C under dry hydrogen (60 NL/h) and air (60 NL/h) at ambient pressure. Values for area-specific resistance is provided and calculated from fits at low current densities of the I-V curves.

Although Type B cells exhibit a very similar total electrolyte thickness and architecture compared to Type A.1 cells, the calculated ASR in Type B cells is significantly lower with approximately 176 mΩ·cm². In this cell type, the first two electrolyte layers (GDC and YSZ) are co-sintered at 1400 °C, resulting in a comparable interdiffusion zone on the fuel side as in Type A.1 cells. However, the upper GDC barrier layer on the air side is subsequently applied and sintered at only 1300 °C onto the already densified YSZ. Since YSZ is fully sintered at this stage, it is less prone to interdiffusion and the lower sintering temperature further limits cation mobility, resulting in a significantly shorter interdiffusion length and reduced interface porosity on the air side. As a result, a larger proportion of the tri- electrolyte

structure retains higher ionic conductivity in undisturbed GDC and YSZ regions, lowering the overall ASR. This suggests that asymmetric interdiffusion within the electrolyte architecture, driven by incremental sintering, is a major factor for reduced ASR in Type B cells, even with similar total electrolyte thickness.

For Type D and E cells, the introduction of PVD layers leads to further ASR reduction. In Type D cells, the upper GDC barrier layer is sputtered, while in Type E cells, both YSZ and GDC barrier layers are applied via PVD. Using PVD for layer application prevents interdiffusion and the formation of interface porosity within the electrolyte structure. This results in an overall cleaner structure with less or no interdiffusion zones and therefore lower local resistance contributions as evident from the further decreased ASR values measured in these cells. Consequently, the lowest ASR of ~ 100 mΩ·cm² is observed in Type E cells, where both barrier layers of the electrolyte were sputtered and no interface porosity or interdiffusion zone is formed.

Furthermore, the comparison between Type D and Type B cells, despite their difference in total electrolyte thickness, supports the interpretation that interdiffusion zone length and interface porosity are the dominant factors, influencing ASR at this level, while the impact of total electrolyte thickness is secondary in this case.

To enable direct performance comparison between the investigated cells, current densities at 0.7 V and 800 °C under dry hydrogen and air were evaluated for each cell type. Current densities are summarized alongside ASR values in Table 6.2.

For Type D cells, due to the aforementioned measurement artifact at higher current densities, current densities at 0.7 V were interpolated using linear fits from the low-current density region, resulting in 2.15 $Acm^{-2}$ for Type D #1 cell and 1.83 $Acm^{-2}$ for Type D #2 cell at 0.7 V. For Type B cells, the voltage at 2 $Acm^{-2}$ was directly measured as 0.7 V, providing a reliable, measured current density at this voltage under test conditions. During the measurement of the Type E cell, voltages never dropped as low as 0.7 V in the tested current density range. However, based on the low ASR and the slope of the I-V curve, it is reasonable to assume current densities exceeding 2 $Acm^{-2}$, likely approaching or exceeding 3 $Acm^{-2}$ at 0.7 V for this cell type.

**Table 6.2:** Overview of measured area-specific resistance (ASR) and corresponding current densities at 0.7 V for each investigated cell type in SOFC operation at 800 °C under dry $H_2$ and air. For Type D cells, values were interpolated using linear fits due to measurement artifacts at higher current densities. For Type E cells, values are estimated based on the I-V curve slope and low ASR.

| Cell Type | ASR [mΩ·cm²] | Current Density (0.7 V; 800 °C, dry $H_2$) [$Acm^{-2}$] |
|---|---|---|
| B | 176 | 2.00 |
| D #1 | 151 | 2.15 |
| D #2 | 171 | 1.83 |
| E | ~ 100 | > 2 - 3 |

To further contextualize the findings, a comparison can be made with the state-of-the-art Jülich Type III YSZ-based SOCs. When testing under similar conditions at 820 °C and dry hydrogen, they achieve current densities of approximately 2 $Acm^{-2}$ at 0.7 V. A comparison of the cells investigated here with the reference Type III cells reveals that the GDC based cells achieve comparable or even higher current densities (Type B, Type D #1 and Type E cells), despite the apparent penalty caused by interdiffusion. This is primarily attributed to the utilization of Ni-GDC fuel electrodes in the present thesis, as opposed to the conventional Ni-YSZ fuel electrodes used in Type III cells. The Ni-GDC fuel electrode offers superior electrode kinetics and improved interface compatibility with the GDC-containing electrolyte architectures, effectively reducing fuel-side polarization and enabling higher current densities at a given voltage. Interestingly, when a Ni-GDC fuel electrode is incorporated into the Type III cell architecture without utilizing the tri-layer electrolyte design, the interdiffusion penalty appears much more pronounced. As investigated by Lenser et al. in 2017, such Ni-GDC cells only exhibited current densities of ~ 1.05 $Acm^{-2}$ at 0.7 V, which is again attributed to interdiffusion of GDC and YSZ, here at the fuel electrode/electrolyte interface [193]. This suggests that the penalty caused by interdiffusion is higher if the interdiffusion zone is located at the fuel electrode/electrolyte interface than if it is located within the electrolyte, as is the case for the tri-layer electrolyte architecture.

Encouragingly, this high-performance operation was not achieved at the expense of stability. A preliminary degradation study conducted at KIT on a Type E cell demonstrated excellent stability with negligible performance degradation over 1000 hours of operation. Figure 6.3 A presents the I-V curves for this Type E cell tested under 50 % $H_2O$/50 % $H_2$ mixture at temperatures between 800 °C and 600 °C. Current density sweeps were conducted between -2 $Acm^{-2}$ and 2 $Acm^{-2}$. Here, for the measurement performed at 800 °C the initial total polarization resistance of 70.5 $m\Omega \cdot cm^2$ gathered from complementary distribution of relaxation times (DRT) analysis is indicated and compared to a second I-V curve measured at the same temperature after 540 h of total operation with an analyzed total polarization resistance of 75.7 $m\Omega \cdot cm^2$, indicating excellent stability under continuous high-current operation. A more detailed presentation of resistance evolution over time at 800 °C is provide in Figure 6.3 B from 560 h up to 1080 h of operation at -1.5 $Acm^{-2}$. Here, total resistance $R_{tot}$ in green, polarization resistance $R_{pol}$ of the Ni-GDC electrode in red and ohmic resistance $R_{Ohm}$ in blue are presented. While ohmic resistance remained stable around 5 $m\Omega \cdot cm^2$, polarization resistance also remained stable or even slightly decreased from 67.7 $m\Omega \cdot cm^2$ to about 67.5 $m\Omega \cdot cm^2$.
Furthermore, this Type E cell demonstrated a current density of 2 $Acm^{-2}$ at 0.77 V, confirming its high power density capability even in humidified fuel gas. Under SOEC conditions at -2 $Acm^{-2}$ the cell operated at a voltage of 1.06 V, indicating low overpotentials and efficient electrolysis performance in direct comparison to the relatively low OCV of 0.92 V at these conditions.

These results demonstrate that the high performance of Type E cells is durable and not only observable in fresh cells. The low degradation rates under elevated steam concentrations and high current densities highlight the advantages of using Ni-GDC fuel electrodes, which enable higher performance when compared to the state-of-the-art Type III Ni-YSZ based Jülich cell under similar conditions, while maintaining stability during extended operation.

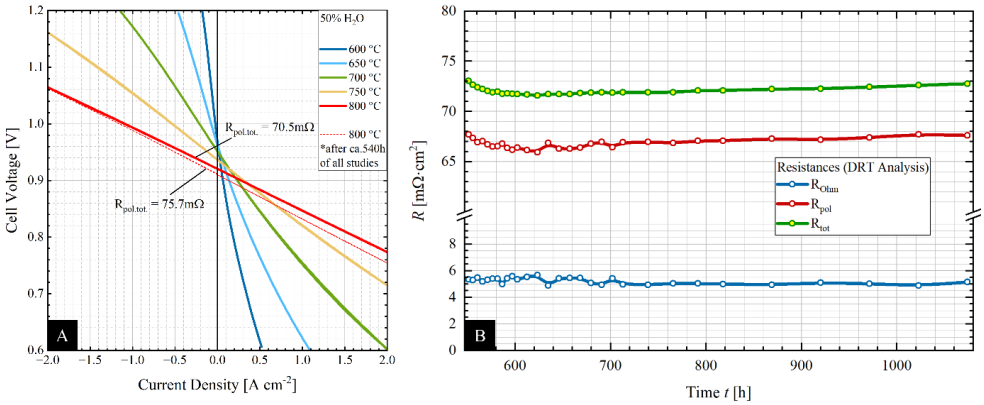


**Figure 6.3: A** I-V curves measured at current densities between – 2 Acm$^{-2}$ and 2 Acm$^{-2}$ at various temperatures in fuel side gas mixtures of 50 % $H_2O$/50 % $H_2$ and air. **B** Time evolution of ohmic deconvoluted cell resistance extracted from periodically performed DRT analysis between 560 h and 1080 h of operation at 800 °C under SOEC conditions at -1.5 Acm$^{-2}$. Both ohmic resistance and Ni-GDC polarization resistance remained stable over the investigated time period.

## 6.4 Conclusion

In this study, fuel electrode-supported solid oxide cells with systematically varied electrolyte architectures were evaluated to assess their electrochemical performance and stability. OCV measurements confirmed sufficient gas-tightness of the cell structure with only minor gas leakages stemming from the test bench. Additionally, employing thicker YSZ electron blocking layers in the fully screen-printed electrolyte architecture could successfully prevent detrimental electronic leakage caused by GDC/YSZ interdiffusion during manufacturing.

I-V characterization at 800 °C demonstrated that replacing conventional Ni-YSZ fuel electrodes with Ni-GDC electrodes in this fully screen-printed tri-layer configuration enables comparable current densities at 0.7 V (up to ~2 Acm$^{-2}$) in reference to Jülich Type III cells (~ 2 Acm$^{-2}$). When employing PVD techniques to manufacture the tri-layer electrolyte with clean interfaces, current densities are even higher (close to 3 Acm$^{-2}$ at 0.7 V), highlighting the effectiveness of the GDC-based approach. Although Type E cells with PVD-deposited barrier layers exhibited the lowest ASR and best overall electrochemical performance, it is notable that fully screen-printed architectures can closely compete.

The observed differences in ASR were primarily linked to the presence or elimination of interfacial porosity and interdiffusion layers within the electrolyte architecture rather than total electrolyte thickness alone, with PVD-applied barrier layers successfully minimizing these detrimental effects. Mid-term testing of a Type E cell demonstrated excellent stability under SOEC operating conditions, with negligible degradation over 1000 h, indicating robust microstructural and electrochemical resilience.

In summary, these findings demonstrate that targeted electrolyte architecture tailoring, in addition to the use of Ni-GDC electrodes and advanced barrier layer processing, can significantly enhance SOEC stability while maintaining high performance. Future studies should evaluate the degradation behavior of fully screen-printed cells, which show promising initial performance, to assess their long-term viability for practical SOC applications. Additionally, testing under more realistic fuel compositions, including steam variations and reversible operation will further advance these cells towards application readiness. Finally, a data-driven optimization of the Ni-GDC fuel electrode may yield further improvements.

# 7 Summary and outlook

This dissertation investigated the manufacturing, microstructural evolution and electrochemical performance of fuel electrode-supported solid oxide cells (SOCs), with a focus on developing fully screen-printed and co-sintered tri-layer electrolyte architectures. The work addressed critical challenges in paste formulation, sintering compatibility and cell design to support the advancement of cost-effective, high-performance SOC technologies.

A systematic study of the sintering behavior of Gd-doped ceria and yttria-stabilized zirconia powders provided foundational insights into the densification kinetics of these materials. GDC powders exhibited earlier sintering onset and higher shrinkage than YSZ, although pre-calcination and co-doping strategies effectively modified their sintering behavior. These findings were essential in aligning the sintering properties of electrolyte layers for co-processing with fuel electrode supports. Translating pellet-based sintering insights into screen-printed films revealed additional complexities due to lower green densities and mechanical constraints imposed by the pre-sintered or calcined NiO-8YSZ substrates. Notably, early sintering behavior proved crucial for successful densification of screen-printed layers. Furthermore, strong correlations were observed between paste rheology, particularly damping factor, yield point, and particle distribution asymmetry and print quality. These relationships emphasize the importance of powder engineering and rheological tuning in achieving high-quality, defect-free electrolyte layers.

Building on this foundation, the manufacturing and co-sintering of tri-layer electrolytes on fuel electrode supports was explored. The shrinkage behavior of the substrate was shown to critically influence electrolyte densification and the development of residual stresses during co-sintering. Substrates pre-calcined at high temperatures impeded densification of the electrolyte, leading to higher residual porosity and warping of the half-cells, which is detrimental to structural integrity. Moreover, microstructural examination of the electrolyte revealed that porosity formation at the GDC/YSZ interfaces, driven by interdiffusion and Kirkendall porosity, is highly dependent on the sintering temperature and manufacturing route. This interface porosity was absent in barrier layers deposited by PVD, reinforcing the influence of processing on the microstructural outcome.

The final part of the thesis evaluated the electrochemical performance of SOCs with systematically varied electrolyte architectures. SOE cells with Ni-GDC fuel electrodes demonstrated significantly higher current stability than conventional Ni-YSZ-based cells, validating the advantage of GDC for enhanced performance. While cells with PVD-applied barrier layers achieved the best area-specific resistance and electrochemical stability, fully screen-printed cells exhibited competitive performance and comparable initial current densities as the state-of-the-art Jülich Type III reference, confirming the

potential of cost-effective screen-printed architectures. The performance differences were primarily attributed to the presence or mitigation of interfacial porosity and interdiffusion zones rather than total electrolyte thickness. Importantly, mid-term stability testing confirmed the robustness of carefully designed tri-layer cells under solid oxide electrolysis conditions.

Taken together, this work demonstrates that the successful realization of fully screen-printed fuel electrode-supported SOCs with tri-layer electrolytes hinges on a delicate balance between powder properties, paste formulation, sintering compatibility and architectural design. While high co-sintering temperatures facilitate electrolyte densification, they also promote undesirable interdiffusion and porosity, that was shown to significantly compromise performance. Thus, the development of a novel substrate that allows for sufficient densification at lower sintering temperatures emerges as a key future requirement. Such a substrate would enable the benefits of thin electrolytes to be fully utilized while maintaining microstructural integrity and minimizing residual stress.

Additionally, future studies should focus on the long-term durability of fully screen-printed architectures under realistic operating conditions, including reversible operation and varying steam concentrations, preferably in a stack-test environment. Further exploration of temperature-dependent paste rheology, advanced powder preparation methods, and new co-sintering strategies would also be beneficial for the development of next-generation SOCs that are not only efficient and stable but also economically viable for hydrogen production and energy conversion technologies.

# Appendix

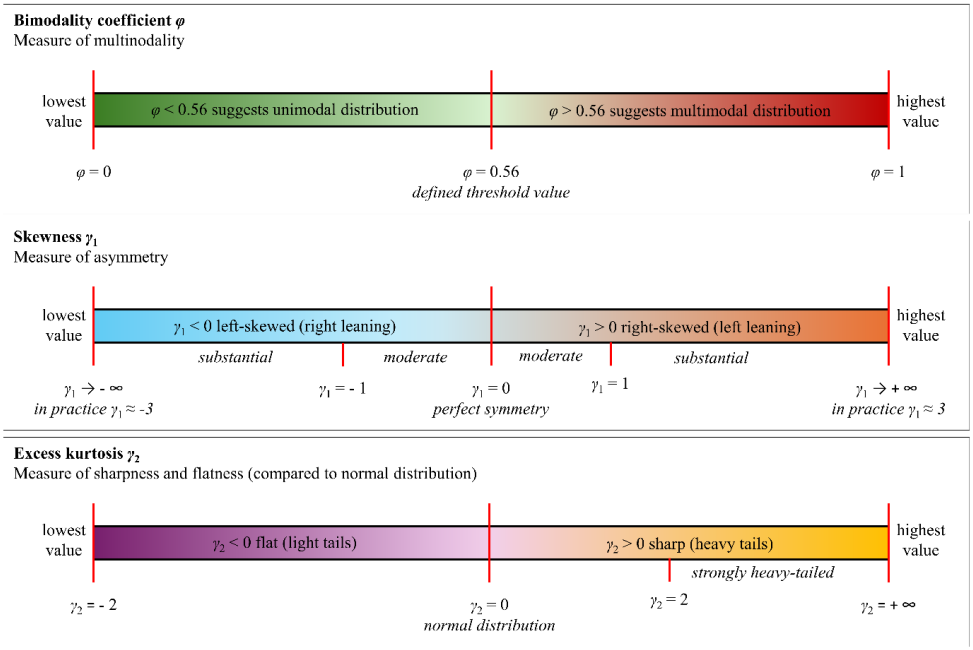


**Figure A- 1:** Visualized ranges of distribution descriptors such as bimodality coefficient, skewness and excess kurtosis.

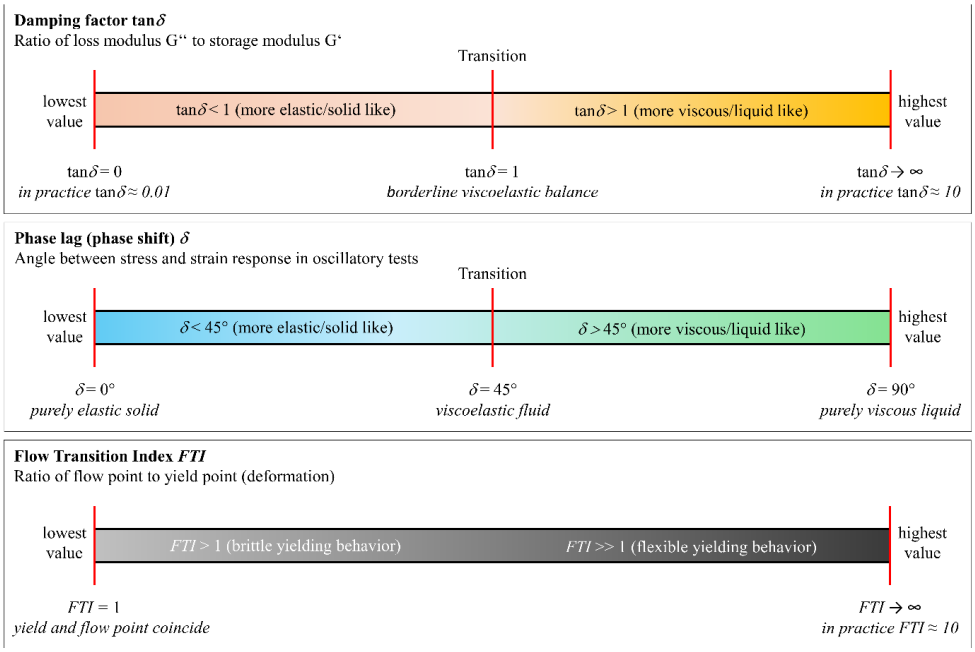


**Figure A- 2:** Visualized ranges of rheological properties such as damping factor, phase lag and flow transition index.

**Table A- 1:** ICP-OES analysis of all investigated dispersants. Two parallel extractions of approx. 200 µl mg per sample were weighed, placed in closed vessels in a microwave system (Mars5: org unpolar3) with 2 ml $HNO_3$ / 1 ml $H_2O_2$. Each extraction solution was transferred, mixed with 0.5 ml HF, and brought to a total volume of 50 mL. The extraction solutions were analyzed undiluted, and 3 parallel dilutions of each extraction solution (100-fold) were prepared and analyzed. Analyses conducted by former ZEA-3.

| Dispersant | P [%] | Si [%] |
|---|---|---|
| BYK 104 | < 0.0008 | < 0.0008 |
| Hypermer KD2 | < 0.0008 | < 0.0008 |
| Hypermer KD73 | < 0.0006 | 0.00072 |
| Hypermer KD77 | < 0.0006 | 0.00074 |
| BYK 101N | < 0.0009 | 0.0019 |
| BYK 102 | 3.2 | < 0.0008 |
| BYK AntiTerra U | < 0.0008 | 0.0026 |
| Nuosperse FX9086 | 0.84 | < 0.0008 |

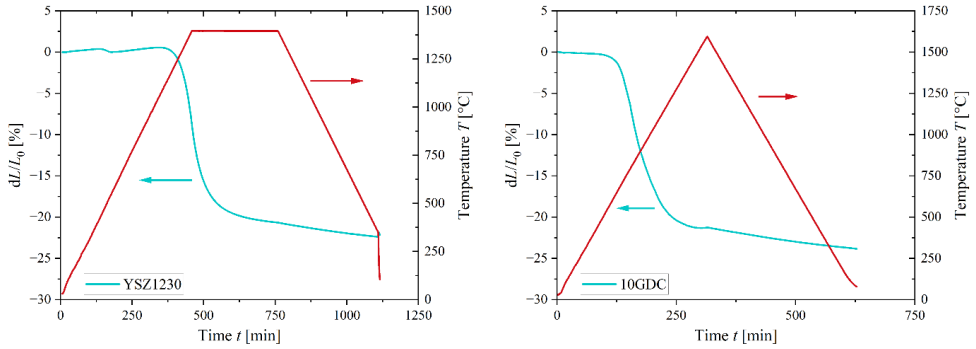


**Figure A- 3**: Dilatometry measurement results for a YSZ1230 and a 10GDC sample with the respective temperature profiles.

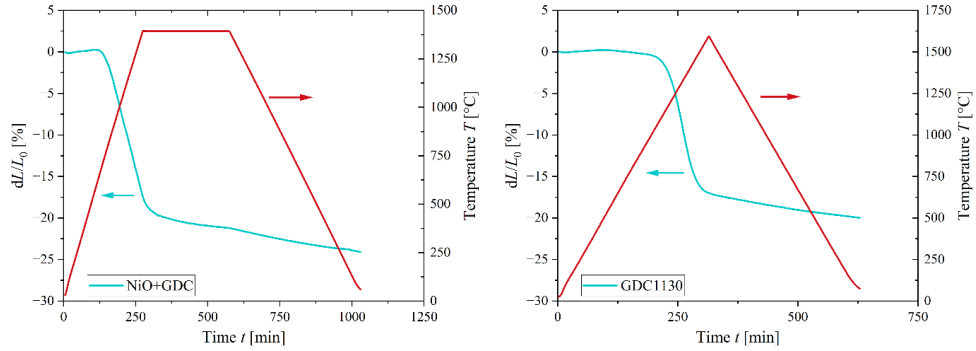


**Figure A- 4:** Dilatometry measurement results for a NiO-GDc and a GDC1130 sample with the respective temperature profiles.

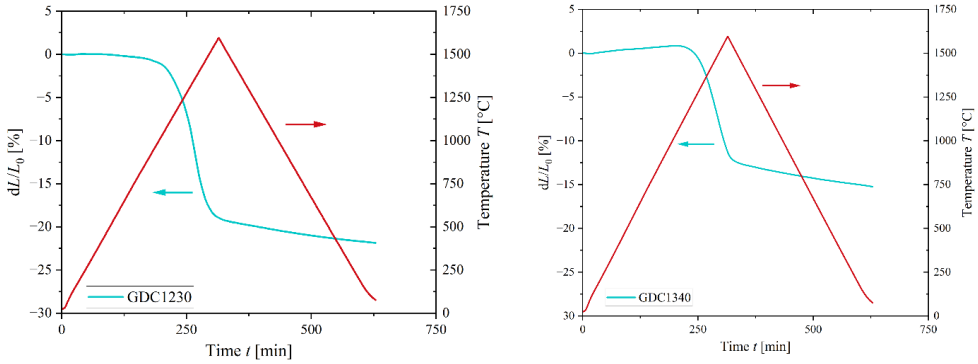


**Figure A- 7:** Dilatometry measurement results for a GDC1230 and a GDC1340 sample with the respective temperature profiles.

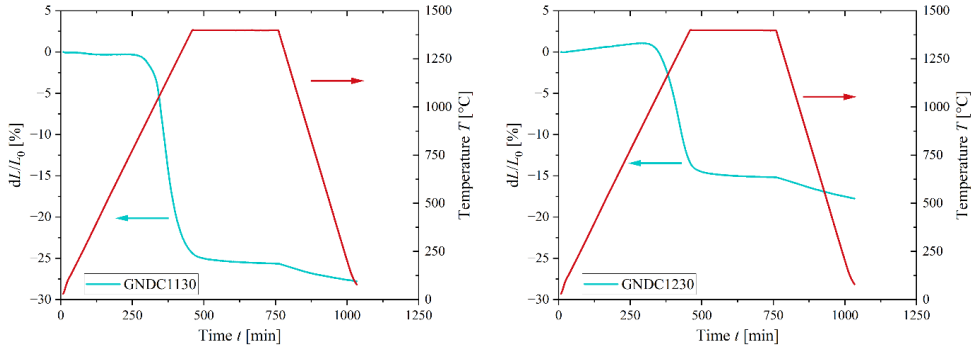


**Figure A- 6:** Dilatometry measurement results for a GNDC1130 and a GNDC1230 sample with the respective temperature profiles.

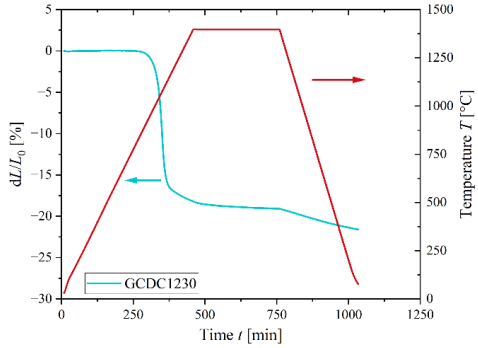


**Figure A- 5:** Dilatometry measurement result for a GCDC1230 sample.

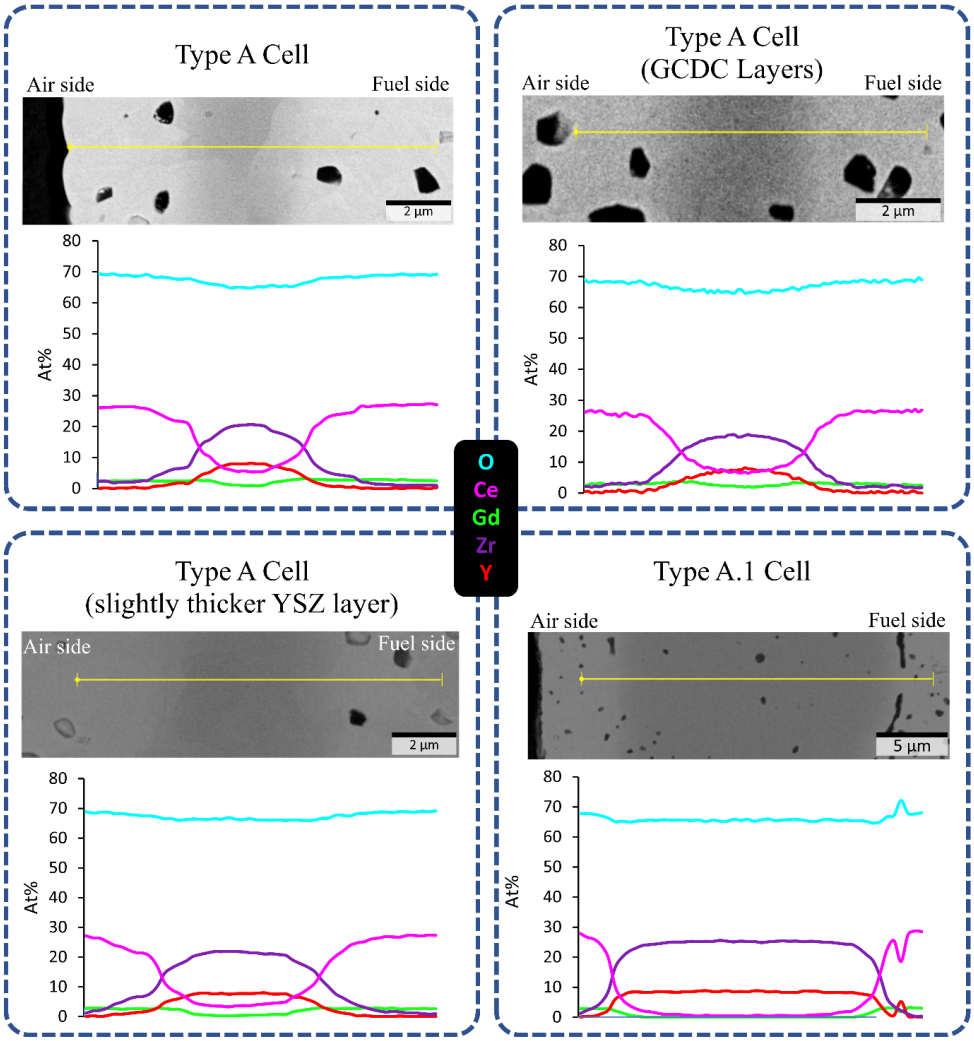


**Figure A- 8:** EDS line scan profiles on polished cross-sections, illustrating the element gradient at the GDC/YSZ electrolyte interface for different Type A cells. Analysis was conducted by Luzie Wehner (IMD-1).

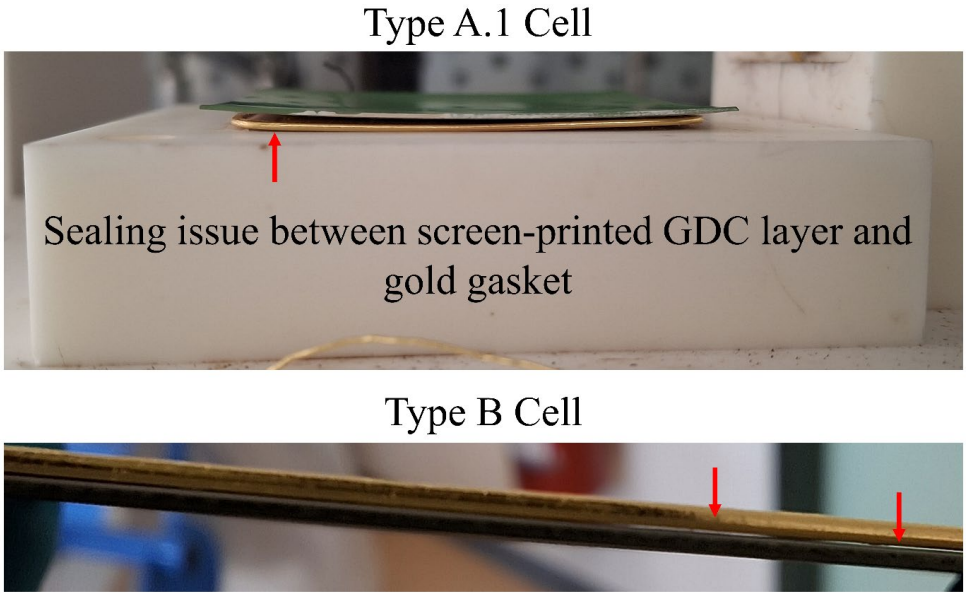


**Figure A- 9:** Photographs of a Type A.1 and a Type B cell post electrochemical characterization testing.

## References

[1] United Nations, “The Sustainable Development Goals Report 2024,” 2024. [Online]. Available: https://unstats.un.org/sdgs/report/2024/The-Sustainable-Development-Goals-Report-2024.pdf

[2] UNEP and UNEP, Eds., *The hydrogen economy: a non-technical review*. Nairobi, Kenya: United Nations Environment Programme, 2006.

[3] International Energy Agency, “Hydrogen and hydrogen-based fuels,” *Energy Technology Perspectives*, p. 400, 2020.

[4] O. Schmidt, A. Gambhir, I. Staffell, A. Hawkes, J. Nelson, and S. Few, “Future cost and performance of water electrolysis: An expert elicitation study,” *International Journal of Hydrogen Energy*, vol. 42, no. 52, pp. 30470–30492, Dec. 2017, doi: 10.1016/j.ijhydene.2017.10.045.

[5] Y. Li, R. Lin, R. O’Shea, V. Thaore, D. Wall, and J. D. Murphy, “A perspective on three sustainable hydrogen production technologies with a focus on technology readiness level, cost of production and life cycle environmental impacts,” *Heliyon*, vol. 10, no. 5, p. e26637, Mar. 2024, doi: 10.1016/j.heliyon.2024.e26637.

[6] A. Gailani, S. Cooper, S. Allen, A. Pimm, P. Taylor, and R. Gross, “Assessing the potential of decarbonization options for industrial sectors,” *Joule*, vol. 8, no. 3, pp. 576–603, Mar. 2024, doi: 10.1016/j.joule.2024.01.007.

[7] L. A. Jolaoso, I. T. Bello, O. A. Ojelade, A. Yousuf, C. Duan, and P. Kazempoor, “Operational and scaling-up barriers of SOEC and mitigation strategies to boost H2 production- a comprehensive review,” *International Journal of Hydrogen Energy*, vol. 48, no. 85, pp. 33017–33041, Oct. 2023, doi: 10.1016/j.ijhydene.2023.05.077.

[8] L. Mathur, Y. Namgung, H. Kim, and S.-J. Song, “Recent progress in electrolyte-supported solid oxide fuel cells: a review,” *J. Korean Ceram. Soc.*, vol. 60, no. 4, pp. 614–636, Jul. 2023, doi: 10.1007/s43207-023-00296-3.

[9] D. Udomsilp *et al.*, “Metal-Supported Solid Oxide Fuel Cells with Exceptionally High Power Density for Range Extender Systems,” *Cell Reports Physical Science*, vol. 1, no. 6, p. 100072, Jun. 2020, doi: 10.1016/j.xcrp.2020.100072.

[10] H. Xu, Y. Han, J. Zhu, M. Ni, and Z. Yao, “Status and progress of metal-supported solid oxide fuel cell: Towards large-scale manufactory and practical applications,” *Energy Reviews*, vol. 3, no. 1, p. 100051, Mar. 2024, doi: 10.1016/j.enrev.2023.100051.

[11] J. Zhang, C. Lenser, N. Russner, A. Weber, N. H. Menzler, and O. Guillon, “Boosting intermediate temperature performance of solid oxide fuel cells via a tri-layer ceria–zirconia–ceria electrolyte,” *J Am Ceram Soc.*, vol. 106, no. 1, pp. 93–99, Jan. 2023, doi: 10.1111/jace.18482.

[12] C. Lenser, J. Zhang, N. Russner, A. Weber, O. Guillon, and N. H. Menzler, “Electro-chemo-mechanical analysis of a solid oxide cell based on doped ceria,” *Journal of Power Sources*, 2022, doi: https://doi.org/10.1016/j.jpowsour.2022.231505.

[13] A. Atkinson, “Chemically-induced stresses in gadolinium-doped ceria solid oxide fuel cell electrolytes,” *Solid State Ionics*, vol. 95, no. 3–4, pp. 249–258, Mar. 1997, doi: 10.1016/S0167-2738(96)00588-7.

[14] B. Charlas *et al.*, “Residual stresses in a co-sintered SOC half-cell during post-sintering cooling,” 2014.

[15] B. Charlas, H. L. Frandsen, K. Brodersen, P. V. Henriksen, and M. Chen, “Residual stresses and strength of multilayer tape cast solid oxide fuel and electrolysis half-cells,” *Journal of Power Sources*, vol. 288, pp. 243–252, Aug. 2015, doi: 10.1016/j.jpowsour.2015.04.105.

[16] R. Clague, A. J. Marquis, and N. P. Brandon, “Finite element and analytical stress analysis of a solid oxide fuel cell,” *Journal of Power Sources*, vol. 210, pp. 224–232, Jul. 2012, doi: 10.1016/j.jpowsour.2012.03.027.

[17] B. F. SØrensen, S. Sarraute, O. JØrgensen, and A. Horsewell, “Thermally induced delamination of multilayers,” *Acta Materialia*, vol. 46, no. 8, pp. 2603–2615, May 1998, doi: 10.1016/S1359-6454(97)00472-2.

[18] J. R. Wilson and S. A. Barnett, “Solid Oxide Fuel Cell Ni–YSZ Anodes: Effect of Composition on Microstructure and Performance,” *Electrochem. Solid-State Lett.*, vol. 11, no. 10, p. B181, 2008, doi: 10.1149/1.2960528.

[19] M. Hubert, J. Laurencin, P. Cloetens, B. Morel, D. Montinaro, and F. Lefebvre-Joud, “Impact of Nickel agglomeration on Solid Oxide Cell operated in fuel cell and electrolysis modes,” *Journal of Power Sources*, vol. 397, pp. 240–251, Sep. 2018, doi: 10.1016/j.jpowsour.2018.06.097.

[20] J. Lee, “The impact of anode microstructure on the power generating characteristics of SOFC,” *Solid State Ionics*, vol. 158, no. 3–4, pp. 225–232, Mar. 2003, doi: 10.1016/S0167-2738(02)00915-3.

[21] T. Suzuki, Z. Hasan, Y. Funahashi, T. Yamaguchi, Y. Fujishiro, and M. Awano, “Impact of Anode Microstructure on Solid Oxide Fuel Cells,” *Science*, vol. 325, no. 5942, pp. 852–855, Aug. 2009, doi: 10.1126/science.1176404.

[22] J. W. Phair, “Rheological Analysis of Concentrated Zirconia Pastes with Ethyl Cellulose for Screen Printing SOFC Electrolyte Films,” *Journal of the American Ceramic Society*, vol. 91, no. 7, pp. 2130–2137, Jul. 2008, doi: 10.1111/j.1551-2916.2008.02443.x.

[23] N. Q. Minh and M. B. Mogensen, “Reversible Solid Oxide Fuel Cell Technology for Green Fuel and Power Production,” *Interface magazine*, vol. 22, no. 4, pp. 55–62, Jan. 2013, doi: 10.1149/2.F05134if.

[24] M. B. Mogensen *et al.*, “Reversible solid-oxide cells for clean and sustainable energy,” *Clean Energy*, vol. 3, no. 3, pp. 175–201, Nov. 2019, doi: 10.1093/ce/zkz023.

[25] M. Mogensen, K. V. Jensen, M. J. Jørgensen, and S. Primdahl, “Progress in understanding SOFC electrodes,” *Solid State Ionics*, p. 7, 2002.

[26] O. Guillon, Ed., *Advanced ceramics for energy conversion and storage*. in Elsevier series in advanced ceramic materials. Amsterdam, Netherlands ; Cambridge, MA: Elsevier, 2020.

[27] A. Hauch, “Solid Oxide Electrolysis Cells”.

[28] S. D. Ebbesen, S. H. Jensen, A. Hauch, and M. B. Mogensen, “High Temperature Electrolysis in Alkaline Cells, Solid Proton Conducting Cells, and Solid Oxide Cells,” *Chem. Rev.*, vol. 114, no. 21, pp. 10697–10734, Nov. 2014, doi: 10.1021/cr5000865.

[29] A. Coralli, B. J. M. Sarruf, L. Osimeri, S. Specchia, and N. Q. Minh, “Chapter 2 - Fuel Cells,” in *Science and Engineering of Hydrogen-Based Energy Technologies : Hydrogen Production and Practical Applications in Energy Generation*, P. E. de Miranda., Ed., Academic Press, 2019, pp. 39–122. [Online]. Available: https://doi.org/10.1016/B978-0-12-814251-6.00002-2.

[30] A. Weber, “Entwicklung von Kathodenstrukturen für die Hochtemperatur-Brennstoffzelle SOFC [online],” 2002, doi: 10.5445/IR/13662002.

[31] U.S. Department of Energy, “Fuel Cell Handbook (Seventh Edition),” Office of Fossil Energy - National Energy Technology Laboratory, 2004.

[32] T. L. Skafte *et al.*, “Electrothermally balanced operation of solid oxide electrolysis cells,” *Journal of Power Sources*, vol. 523, p. 231040, Mar. 2022, doi: 10.1016/j.jpowsour.2022.231040.

[33] M. Chen, X. Sun, C. Chatzichristodoulou, S. Koch, P. V. Hendriksen, and M. B. Mogensen, “Thermoneutral Operation of Solid Oxide Electrolysis Cells in Potentiostatic Mode,” *ECS Trans.*, vol. 78, no. 1, pp. 3077–3088, May 2017, doi: 10.1149/07801.3077ecst.

[34] C. Mendonça, A. Ferreira, and D. M. F. Santos, “Towards the Commercialization of Solid Oxide Fuel Cells: Recent Advances in Materials and Integration Strategies,” *Fuels*, vol. 2, no. 4, pp. 393–419, Oct. 2021, doi: 10.3390/fuels2040023.

[35] F. Han, M. Lang, P. Szabo, C. Geipel, C. Walter, and R. Costa, “Performance and Degradation of Electrolyte Supported SOECs with Advanced Thin-Film Gadolinium Doped Ceria Barrier Layers in Long-Term Stack Test,” *J. Electrochem. Soc.*, vol. 171, no. 5, p. 054515, May 2024, doi: 10.1149/1945-7111/ad4781.

[36] N. H. Menzler, D. Schäfer, N. Kruse, R. Peters, and F. Kunz, “Solid Oxide Cells for Hydrogen Generation and Usage: From Materials to Systems”.

[37] D. Roehrens *et al.*, “Advances beyond traditional SOFC cell designs,” *International Journal of Hydrogen Energy*, vol. 40, no. 35, pp. 11538–11542, Sep. 2015, doi: 10.1016/j.ijhydene.2015.01.155.

[38] M. C. Tucker, “Progress in metal-supported solid oxide fuel cells: A review,” *Journal of Power Sources*, vol. 195, no. 15, pp. 4570–4582, Aug. 2010, doi: 10.1016/j.jpowsour.2010.02.035.

[39] D. E. Riemer, “The Theoretical Fundamentals of the Screen Printing Process,” *Microelectronics International*, vol. 6, no. 1, pp. 8–17, Jan. 1989, doi: 10.1108/eb044350.

[40] C. Chen *et al.*, “Screen-Printing Technology for Scale Manufacturing of Perovskite Solar Cells,” *Advanced Science*, vol. 10, no. 28, p. 2303992, Oct. 2023, doi: 10.1002/advs.202303992.

[41] M. A. Belal *et al.*, “Advances in gas sensors using screen printing,” *J. Mater. Chem. A*, vol. 13, no. 8, pp. 5447–5497, 2025, doi: 10.1039/D4TA06632D.

[42] Y. D. Kim and J. Hone, “Screen printing of 2D semiconductors,” *Nature*, vol. 544, no. 7649, pp. 167–168, Apr. 2017, doi: 10.1038/nature21908.

[43] J. Suikkola *et al.*, “Screen-Printing Fabrication and Characterization of Stretchable Electronics,” *Sci Rep*, vol. 6, no. 1, p. 25784, May 2016, doi: 10.1038/srep25784.

[44] B. R. Sankapal, A. Ennaoui, R. B. Gupta, and C. D. Lokhande, Eds., *Simple Chemical Methods for Thin Film Deposition: Synthesis and Applications*. Singapore: Springer Nature Singapore, 2023. doi: 10.1007/978-981-99-0961-2.

[45] N. Kapur, S. J. Abbott, E. D. Dolden, and P. H. Gaskell, “Predicting the Behavior of Screen Printing,” *IEEE Trans. Compon., Packag. Manufact. Technol.*, vol. 3, no. 3, pp. 508–515, Mar. 2013, doi: 10.1109/TCPMT.2012.2228743.

[46] N. Zavanelli and W.-H. Yeo, “Advances in Screen Printing of Conductive Nanomaterials for Stretchable Electronics,” *ACS Omega*, vol. 6, no. 14, pp. 9344–9351, Apr. 2021, doi: 10.1021/acsomega.1c00638.

[47] R. A. Terpstra, P. P. A. C. Pex, and A. H. De Vries, Eds., *Ceramic Processing*. Dordrecht: Springer Netherlands, 1995. doi: 10.1007/978-94-011-0531-6.

[48] N. H. Menzler, F. Tietz, S. Uhlenbruck, H. P. Buchkremer, and D. Stöver, “Materials and manufacturing technologies for solid oxide fuel cells,” *J Mater Sci*, vol. 45, no. 12, pp. 3109–3135, Jun. 2010, doi: 10.1007/s10853-010-4279-9.

[49] R. K. Nishihora, P. L. Rachadel, M. G. N. Quadri, and D. Hotza, “Manufacturing porous ceramic materials by tape casting—A review,” *Journal of the European Ceramic Society*, vol. 38, no. 4, pp. 988–1001, Apr. 2018, doi: 10.1016/j.jeurceramsoc.2017.11.047.

[50] M. Cassidy, “Trends in the processing and manufacture of solid oxide fuel cells,” *WIREs Energy & Environment*, vol. 6, no. 5, p. e248, Sep. 2017, doi: 10.1002/wene.248.

[51] W. Schafbauer, *Entwicklung und Herstellung von foliengegossenen, anodengestützten Festoxidbrennstoffzellen*. in Schriften des Forschungszentrums Jülich Reihe Energie & Umwelt, no. Bd. 66. Jülich: Forschungszentrum Jülich, 2010.

[52] F. D. Minatto, P. Milak, A. De Noni, D. Hotza, and O. R. K. Montedo, “Multilayered ceramic composites – a review,” *Advances in Applied Ceramics*, vol. 114, no. 3, pp. 127–138, Apr. 2015, doi: 10.1179/1743676114Y.0000000215.

[53] Z. Lan *et al.*, “Simulation and analysis of sintering stress and warpage displacement in anode supported planar solid oxide fuel cells,” *International Journal of Hydrogen Energy*, vol. 47, no. 60, pp. 25378–25390, Jul. 2022, doi: 10.1016/j.ijhydene.2022.05.290.

[54] L. D. Jadhav, S. H. Pawar, and M. G. Chourashiya, “Effect of sintering temperature on structural and electrical properties of gadolinium doped ceria (Ce0·9Gd0·1O1·95),” *Bull Mater Sci*, vol. 30, no. 2, pp. 97–100, Apr. 2007, doi: 10.1007/s12034-007-0017-6.

[55] D. W. Ni *et al.*, “Densification and grain growth during sintering of porous Ce0.9Gd0.1O1.95 tape cast layers: A comprehensive study on heuristic methods,” *Journal of the European Ceramic Society*, vol. 33, no. 13–14, pp. 2529–2537, Nov. 2013, doi: 10.1016/j.jeurceramsoc.2013.03.025.

[56] H.-W. Lee *et al.*, “Constrained Sintering in Fabrication of Solid Oxide Fuel Cells,” *Materials*, vol. 9, no. 8, p. 675, Aug. 2016, doi: 10.3390/ma9080675.

[57] E. A. Olevsky, V. Tikare, and T. Garino, “Multi-Scale Study of Sintering: A Review,” *Journal of the American Ceramic Society*, vol. 89, no. 6, pp. 1914–1922, Jun. 2006, doi: 10.1111/j.1551-2916.2006.01054.x.

[58] T. Deng *et al.*, “Modeling of solid oxide fuel cell sintering stress and deformation,” *International Journal of Mechanical Sciences*, vol. 265, p. 108895, Mar. 2024, doi: 10.1016/j.ijmecsci.2023.108895.

[59] D. J. Green, O. Guillon, and J. Rödel, “Constrained sintering: A delicate balance of scales,” *Journal of the European Ceramic Society*, vol. 28, no. 7, pp. 1451–1466, Jan. 2008, doi: 10.1016/j.jeurceramsoc.2007.12.012.

[60] P. Z. Cai, D. J. Green, and G. L. Messing, “Constrained Densification of Alumina/Zirconia Hybrid Laminates, II: Viscoelastic Stress Computation,” *Journal of the American Ceramic Society*, vol. 80, no. 8, pp. 1940–1948, Jan. 2005, doi: 10.1111/j.1151-2916.1997.tb03076.x.

[61] D. Bouvard and T. Meister, “Modelling bulk viscosity of powder aggregate during sintering,” *Modelling Simul. Mater. Sci. Eng.*, vol. 8, no. 3, pp. 377–388, May 2000, doi: 10.1088/0965-0393/8/3/316.

[62] C. H. Hsueh, A. G. Evans, R. M. Cannon, and R. J. Brook, “Viscoelastic stresses and sintering damage in heterogeneous powder compacts,” *Acta Metallurgica*, vol. 34, no. 5, pp. 927–936, May 1986, doi: 10.1016/0001-6160(86)90066-0.

[63] S. E. Schoenberg, D. J. Green, A. E. Segall, G. L. Messing, A. S. Grader, and P. M. Halleck, “Stresses and Distortion Due to Green Density Gradients During Densification,” *Journal of the American Ceramic Society*, vol. 89, no. 10, pp. 3027–3033, Oct. 2006, doi: 10.1111/j.1551-2916.2006.01182.x.

[64] S. E. Schoenberg, D. J. Green, and G. L. Messing, “Effect of Green Density on the Thermomechanical Properties of a Ceramic During Sintering,” *Journal of the American Ceramic Society*, vol. 89, no. 8, pp. 2448–2452, Aug. 2006, doi: 10.1111/j.1551-2916.2006.01097.x.

[65] C. Bischof *et al.*, “Microstructure optimization of nickel/gadolinium-doped ceria anodes as key to significantly increasing power density of metal-supported solid oxide fuel cells,” *International Journal of Hydrogen Energy*, vol. 44, no. 59, pp. 31475–31487, Nov. 2019, doi: 10.1016/j.ijhydene.2019.10.010.

[66] S. Golani, F. Wankmüller, W. Herzhof, C. Dellen, N. H. Menzler, and A. Weber, “Impact of GDC Interlayer Microstructure on Strontium Zirconate Interphase Formation and Cell Performance,” *J. Electrochem. Soc.*, vol. 170, no. 10, p. 104501, Oct. 2023, doi: 10.1149/1945-7111/acfc2c.

[67] S. E. Wolf *et al.*, “Solid oxide electrolysis cells – current material development and industrial application,” *J. Mater. Chem. A*, vol. 11, no. 34, pp. 17977–18028, 2023, doi: 10.1039/D3TA02161K.

[68] F. Monaco *et al.*, “Oxygen electrode degradation in solid oxide cells operating in electrolysis and fuel cell modes: LSCF destabilization and interdiffusion at the electrode/electrolyte interface,” *International Journal of Hydrogen Energy*, vol. 46, no. 62, pp. 31533–31549, Sep. 2021, doi: 10.1016/j.ijhydene.2021.07.054.

[69] L. Balice *et al.*, “Constrained flash sintering of gadolinium-doped ceria thin layers,” *J Am Ceram Soc.*, p. e70033, Jun. 2025, doi: 10.1111/jace.70033.

[70] K. A. Khor, L.-G. Yu, S. H. Chan, and X. J. Chen, “Densification of plasma sprayed YSZ electrolytes by spark plasma sintering (SPS),” *Journal of the European Ceramic Society*, vol. 23, no. 11, pp. 1855–1863, Oct. 2003, doi: 10.1016/S0955-2219(02)00421-1.

[71] S. Wang, Y. Liu, J. He, F. Chen, and K. S. Brinkman, “Spark-plasma-sintered barium zirconate based proton conductors for solid oxide fuel cell and hydrogen separation applications,” *International Journal of Hydrogen Energy*, vol. 40, no. 16, pp. 5707–5714, May 2015, doi: 10.1016/j.ijhydene.2015.02.116.

[72] R. Mundra, T. P. Mishra, M. Bram, O. Guillon, and D. Yadav, “Sintering behavior of 8YSZ-Ni cermet: Comparison between conventional, FST/SPS, and flash sintering,” *Int J Applied Ceramic Tech*, vol. 20, no. 4, pp. 2271–2280, Jul. 2023, doi: 10.1111/ijac.14368.

[73] M. A. Janney, C. L. Calhoun, and H. D. Kimrey, “Microwave Sintering of Solid Oxide Fuel Cell Materials: I, Zirconia-8 mol% Yttria,” *Journal of the American Ceramic Society*, vol. 75, no. 2, pp. 341–346, Feb. 1992, doi: 10.1111/j.1151-2916.1992.tb08184.x.

[74] J. Wu, X. Wu, Y. Gao, and Z. Yan, “Innovations in Electric Current-Assisted Sintering for SOFC: A Review of Advances in Flash Sintering and Ultrafast High-Temperature Sintering,” *Applied Sciences*, vol. 14, no. 10, p. 3953, May 2024, doi: 10.3390/app14103953.

[75] J. A. Cebollero, R. Lahoz, M. A. Laguna-Bercero, and A. Larrea, “Tailoring the electrode-electrolyte interface of Solid Oxide Fuel Cells (SOFC) by laser micro-patterning to improve their electrochemical performance,” *Journal of Power Sources*, vol. 360, pp. 336–344, Aug. 2017, doi: 10.1016/j.jpowsour.2017.05.106.

[76] J. A. Cebollero, R. Lahoz, M. A. Laguna-Bercero, J. I. Peña, A. Larrea, and V. M. Orera, “Characterization of laser-processed thin ceramic membranes for electrolyte-supported solid oxide fuel cells,” *International Journal of Hydrogen Energy*, vol. 42, no. 19, pp. 13939–13948, May 2017, doi: 10.1016/j.ijhydene.2016.12.112.

[77] J. Zhang, “Electrolyte development for a SOFC operating at low temperature,” 2020.

[78] J. Zhang, C. Lenser, N. Russner, A. Weber, N. H. Menzler, and O. Guillon, “Boosting intermediate temperature performance of solid oxide fuel cells via a tri-layer ceria–zirconia–ceria electrolyte,” *J Am Ceram Soc.*, vol. 106, no. 1, pp. 93–99, Jan. 2023, doi: 10.1111/jace.18482.

[79] J. Zhang, C. Lenser, N. H. Menzler, and O. Guillon, “Comparison of solid oxide fuel cell (SOFC) electrolyte materials for operation at 500 °C,” *Solid State Ionics*, vol. 344, p. 115138, Jan. 2020, doi: 10.1016/j.ssi.2019.115138.

[80] D. Udomsilp, C. Lenser, O. Guillon, and N. H. Menzler, “Performance Benchmark of Planar Solid Oxide Cells Based on Material Development and Designs,” *Energy Tech*, vol. 9, no. 4, p. 2001062, Apr. 2021, doi: 10.1002/ente.202001062.

[81] J. A. Kilner and B. C. H. Steele, “Mass Transport in Anion-Deficient Fluorite Oxides,” in *Nonstoichiometric Oxides*, Elsevier, 1981, pp. 233–269. doi: 10.1016/B978-0-12-655280-5.50010-9.

[82] S. J. Skinner and J. A. Kilner, “Oxygen ion conductors,” *Materials Today*, vol. 6, no. 3, pp. 30–37, 2003.

[83] S. Scirè and L. Palmisano, “Cerium and cerium oxide: A brief introduction,” in *Cerium Oxide ($CeO_2$): Synthesis, Properties and Applications*, Elsevier, 2020, pp. 1–12. doi: 10.1016/B978-0-12-815661-2.00001-3.

[84] S. Wang, T. Kobayashi, M. Dokiya, and T. Hashimoto, “Electrical and Ionic Conductivity of Gd-Doped Ceria”.

[85] W. J. Bowman, J. Zhu, R. Sharma, and P. A. Crozier, “Electrical conductivity and grain boundary composition of Gd-doped and Gd/Pr co-doped ceria,” *Solid State Ionics*, vol. 272, pp. 9–17, Apr. 2015, doi: 10.1016/j.ssi.2014.12.006.

[86] C. Ahamer, A. K. Opitz, G. M. Rupp, and J. Fleig, “Revisiting the Temperature Dependent Ionic Conductivity of Yttria Stabilized Zirconia (YSZ),” *J. Electrochem. Soc.*, vol. 164, no. 7, pp. F790–F803, 2017, doi: 10.1149/2.0641707jes.

[87] E. Ivers-Tiffée, A. Weber, and D. Herbstritt, “Materials and technologies for SOFC-components,” *Journal of the European Ceramic Society*, vol. 21, no. 10–11, pp. 1805–1811, Jan. 2001, doi: 10.1016/S0955-2219(01)00120-0.

[88] M. J. Escudero, C. A. Maffiotte, and J. L. Serrano, “Long-term operation of a solid oxide fuel cell with MoNi–CeO2 as anode directly fed by biogas containing simultaneously sulphur and siloxane,” *Journal of Power Sources*, vol. 481, p. 229048, Jan. 2021, doi: 10.1016/j.jpowsour.2020.229048.

[89] J. F. B. Rasmussen and A. Hagen, “The effect of H2S on the performance of Ni–YSZ anodes in solid oxide fuel cells,” *Journal of Power Sources*, vol. 191, no. 2, pp. 534–541, Jun. 2009, doi: 10.1016/j.jpowsour.2009.02.001.

[90] M. S. Khan, S.-B. Lee, R.-H. Song, J.-W. Lee, T.-H. Lim, and S.-J. Park, “Fundamental mechanisms involved in the degradation of nickel–yttria stabilized zirconia (Ni–YSZ) anode during solid oxide fuel cells operation: A review,” *Ceramics International*, vol. 42, no. 1, pp. 35–48, Jan. 2016, doi: 10.1016/j.ceramint.2015.09.006.

[91] Q. Fang, L. Blum, N. H. Menzler, and D. Stolten, “Solid Oxide Electrolyzer Stack with 20,000 h of Operation,” *ECS Trans.*, vol. 78, no. 1, pp. 2885–2893, May 2017, doi: 10.1149/07801.2885ecst.

[92] J. Kim *et al.*, "Degradation mechanism of electrolyte and air electrode in solid oxide electrolysis cells operating at high polarization," *International Journal of Hydrogen Energy*, vol. 38, no. 3, pp. 1225–1235, Feb. 2013, doi: 10.1016/j.ijhydene.2012.10.113.

[93] M. B. Mogensen *et al.*, "Ni migration in solid oxide cell electrodes: Review and revised hypothesis," *Fuel Cells*, vol. 21, no. 5, pp. 415–429, Oct. 2021, doi: 10.1002/fuce.202100072.

[94] M. Trini, A. Hauch, S. De Angelis, X. Tong, P. V. Hendriksen, and M. Chen, "Comparison of microstructural evolution of fuel electrodes in solid oxide fuel cells and electrolysis cells," *Journal of Power Sources*, vol. 450, p. 227599, Feb. 2020, doi: 10.1016/j.jpowsour.2019.227599.

[95] F. Monaco *et al.*, "Degradation of Ni-YSZ Electrodes in Solid Oxide Cells: Impact of Polarization and Initial Microstructure on the Ni Evolution," *J. Electrochem. Soc.*, vol. 166, no. 15, pp. F1229–F1242, 2019, doi: 10.1149/2.1261915jes.

[96] I. D. Unachukwu, V. Vibhu, J. Uecker, I. C. Vinke, R.-A. Eichel, and L. G. J. (Bert) De Haart, "Comparison of the Electrochemical and Degradation Behaviour of Ni-YSZ and Ni-GDC Electrodes Under Steam, Co- and $CO_2$ Electrolysis," *ECS Trans.*, vol. 111, no. 6, pp. 1445–1452, May 2023, doi: 10.1149/11106.1445ecst.

[97] A. Sciazko, Y. Komatsu, T. Shimura, and N. Shikazono, "Multiscale microstructural evolutions of nickel-gadolinium doped ceria in solid oxide fuel cell anode," *Journal of Power Sources*, vol. 478, p. 228710, Dec. 2020, doi: 10.1016/j.jpowsour.2020.228710.

[98] L. Holzer *et al.*, "Microstructure degradation of cermet anodes for solid oxide fuel cells: Quantification of nickel grain growth in dry and in humid atmospheres," *Journal of Power Sources*, vol. 196, no. 3, pp. 1279–1294, Feb. 2011, doi: 10.1016/j.jpowsour.2010.08.017.

[99] L. Holzer, B. Münch, B. Iwanschitz, M. Cantoni, Th. Hocker, and Th. Graule, "Quantitative relationships between composition, particle size, triple phase boundary length and surface area in nickel-cermet anodes for Solid Oxide Fuel Cells," *Journal of Power Sources*, vol. 196, no. 17, pp. 7076–7089, Sep. 2011, doi: 10.1016/j.jpowsour.2010.08.006.

[100] A. Jaiswal and E. D. Wachsman, "Fabrication of anode supported thick film ceria electrolytes for IT-SOFCs," *Ionics*, vol. 11, no. 3–4, pp. 161–170, May 2005, doi: 10.1007/BF02430371.

[101] E. D. Wachsman and K. T. Lee, "Lowering the Temperature of Solid Oxide Fuel Cells," *Science*, vol. 334, no. 6058, pp. 935–939, Nov. 2011, doi: 10.1126/science.1204090.

[102] M. P. Klitkou *et al.*, "Development of Fuel Electrode Supported Solid Oxide Cell with Ni/CGO Active Layer," *ECS Trans.*, vol. 111, no. 6, pp. 1407–1413, May 2023, doi: 10.1149/11106.1407ecst.

[103] M. P. Klitkou *et al.*, "Investigating Viability of Low Temperature Co-Sintering to Produce Ni-Ysz Supported Solid Oxide Electrolysis Cells with a Ni-Gdc Active Layer," 2025, *SSRN*. doi: 10.2139/ssrn.5158312.

[104] S. R. Bishop, K. Duncan, and E. D. Wachsman, "Thermo-Chemical Expansion of SOFC Materials," *ECS Trans.*, vol. 1, no. 7, pp. 13–21, Jun. 2006, doi: 10.1149/1.2215539.

[105] S. R. Bishop, K. L. Duncan, and E. D. Wachsman, “Defect equilibria and chemical expansion in non-stoichiometric undoped and gadolinium-doped cerium oxide,” *Electrochimica Acta*, vol. 54, no. 5, pp. 1436–1443, Feb. 2009, doi: 10.1016/j.electacta.2008.09.026.

[106] D. Marrocchelli, S. R. Bishop, H. L. Tuller, and B. Yildiz, “Understanding Chemical Expansion in Non-Stoichiometric Oxides: Ceria and Zirconia Case Studies,” *Adv. Funct. Mater.*, p. 9, 2012.

[107] T. R. Marrero and E. A. Mason, “TEMPERATURE DEPENDENCE OF GASEOUS DIFFUSION COEFFICIENTS,” *Chemical Engineering Communications*, vol. 7, no. 1–3, pp. 159–168, Jan. 1980, doi: 10.1080/00986448008912555.

[108] “History and Bibliography of Diffusion,” in *Diffusion in Solids*, vol. 155, in Springer Series in Solid-State Sciences, vol. 155. , Berlin, Heidelberg: Springer Berlin Heidelberg, 2007, pp. 1–23. doi: 10.1007/978-3-540-71488-0_1.

[109] S. Gennard, F. Corà, and C. R. A. Catlow, “Comparison of the Bulk and Surface Properties of Ceria and Zirconia by ab Initio Investigations,” *J. Phys. Chem. B*, vol. 103, no. 46, pp. 10158–10170, Nov. 1999, doi: 10.1021/jp9913923.

[110] J. P. Goff, W. Hayes, S. Hull, M. T. Hutchings, and K. N. Clausen, “Defect structure of yttria-stabilized zirconia and its influence on the ionic conductivity at elevated temperatures,” *Phys. Rev. B*, vol. 59, no. 22, pp. 14202–14219, Jun. 1999, doi: 10.1103/PhysRevB.59.14202.

[111] V. Kulyk, Z. Duriagina, A. Kostryzhev, B. Vasyliv, V. Vavrukh, and O. Marenych, “The Effect of Yttria Content on Microstructure, Strength, and Fracture Behavior of Yttria-Stabilized Zirconia,” *Materials*, vol. 15, no. 15, p. 5212, Jul. 2022, doi: 10.3390/ma15155212.

[112] B. Wang, X. Xi, and A. N. Cormack, “Chemical Strain and Point Defect Configurations in Reduced Ceria,” *Chem. Mater.*, vol. 26, no. 12, pp. 3687–3692, Jun. 2014, doi: 10.1021/cm500946s.

[113] N. V. Skorodumova, R. Ahuja, S. I. Simak, I. A. Abrikosov, B. Johansson, and B. I. Lundqvist, “Electronic, bonding, and optical properties of CeO 2 and Ce 2 O 3 from first principles,” *Phys. Rev. B*, vol. 64, no. 11, p. 115108, Aug. 2001, doi: 10.1103/PhysRevB.64.115108.

[114] Q. Zhang, J. Yang, B. An, K. Wang, D. Song, and H. Su, “Enhancement effects of Ga-Gd Co-doping on the structure, conductivity, and interfacial polarization of CeO2-based electrolytes,” *Ceramics International*, vol. 51, no. 4, pp. 5362–5380, Feb. 2025, doi: 10.1016/j.ceramint.2024.11.510.

[115] H. Xu, K. Cheng, M. Chen, L. Zhang, K. Brodersen, and Y. Du, “Interdiffusion between gadolinia doped ceria and yttria stabilized zirconia in solid oxide fuel cells: Experimental investigation and kinetic modeling,” *Journal of Power Sources*, vol. 441, p. 227152, Nov. 2019, doi: 10.1016/j.jpowsour.2019.227152.

[116] A. Varez, E. Garcia-Gonzalez, and J. Sanz, “Cation miscibility in $CeO_2$ –$ZrO_2$ oxides with fluorite structure. A combined TEM, SAED and XRD Rietveld analysis,” *J. Mater. Chem.*, vol. 16, no. 43, pp. 4249–4256, 2006, doi: 10.1039/B607778A.

[117] A. Tsoga, A. Gupta, A. Naoumidis, and P. Nikolopoulos, “Gadolinia-doped ceria and yttria stabilized zirconia interfaces: regarding their application for SOFC technology,” *Acta Materialia*, vol. 48, no. 18–19, pp. 4709–4714, Dec. 2000, doi: 10.1016/s1359-6454(00)00261-5.

[118] K. Eguchi, “Process of solid state reaction between doped ceria and zirconia,” *Solid State Ionics*, vol. 135, no. 1–4, pp. 589–594, Nov. 2000, doi: 10.1016/S0167-2738(00)00416-1.

[119] B. Liang, T. Tao, S. Zhang, Y. Huang, Z. Cai, and S. Lu, “Asymmetric diffusion of Zr, Sc and Ce, Gd at the interface between zirconia electrolyte and ceria interlayer for solid oxide fuel cells,” *Journal of Alloys and Compounds*, vol. 679, pp. 191–195, Sep. 2016, doi: 10.1016/j.jallcom.2016.04.077.

[120] A. Schwiers, C. Lenser, O. Guillon, and N. H. Menzler, “Interdiffusion at electrochemical interfaces between yttria-stabilized zirconia and doped ceria,” *Journal of the European Ceramic Society*, vol. 43, no. 14, pp. 6189–6199, Nov. 2023, doi: 10.1016/j.jeurceramsoc.2023.06.015.

[121] A. Tsoga, “Total electrical conductivity and defect structure of ZrO2–CeO2–Y2O3–Gd2O3 solid solutions,” *Solid State Ionics*, vol. 135, no. 1–4, pp. 403–409, Nov. 2000, doi: 10.1016/S0167-2738(00)00477-X.

[122] J. Luo, R. J. Ball, and R. Stevens, “Gadolinia doped ceria/yttria stabilised zirconia electrolytes for solid oxide fuel cell applications,” *Journal of Materials Science*, vol. 39, no. 1, pp. 235–240, Jan. 2004, doi: 10.1023/B:JMSC.0000007749.72739.bb.

[123] V. Rührup and H.-D. Wiemhöfer, “Ionic Conductivity of Gd- and Y-Doped Ceria-Zirconia Solid Solutions,” *Zeitschrift für Naturforschung B*, vol. 61, no. 7, pp. 916–922, Jul. 2006, doi: 10.1515/znb-2006-0721.

[124] J. Nicholas and L. Dejonghe, “Prediction and evaluation of sintering aids for Cerium Gadolinium Oxide,” *Solid State Ionics*, vol. 178, no. 19–20, pp. 1187–1194, Jul. 2007, doi: 10.1016/j.ssi.2007.05.019.

[125] C. J. Fu, Q. L. Liu, S. H. Chan, X. M. Ge, and G. Pasciak, “Effects of transition metal oxides on the densification of thin-film GDC electrolyte and on the performance of intermediate-temperature SOFC,” *International Journal of Hydrogen Energy*, vol. 35, no. 20, pp. 11200–11207, Oct. 2010, doi: 10.1016/j.ijhydene.2010.07.049.

[126] A. K. Baral, H. P. Dasari, B.-K. Kim, and J.-H. Lee, “Effect of sintering aid (CoO) on transport properties of nanocrystalline Gd doped ceria (GDC) materials prepared by co-precipitation method,” *Journal of Alloys and Compounds*, vol. 575, pp. 455–460, Oct. 2013, doi: 10.1016/j.jallcom.2013.05.191.

[127] V. Gil, C. Moure, P. Duran, and J. Tartaj, “Low-temperature densification and grain growth of Bi2O3-doped-ceria gadolinia ceramics,” *Solid State Ionics*, vol. 178, no. 5–6, pp. 359–365, Mar. 2007, doi: 10.1016/j.ssi.2007.02.002.

[128] V. Gil, J. Tartaj, C. Moure, and P. Duran, “Rapid densification by using Bi2O3 as an aid for sintering of gadolinia-doped ceria ceramics,” *Ceramics International*, vol. 33, no. 3, pp. 471–475, Apr. 2007, doi: 10.1016/j.ceramint.2005.10.012.

[129] L. Guan, S. Le, X. Zhu, S. He, and K. Sun, “Densification and grain growth behavior study of trivalent MO1.5 (M=Gd, Bi) doped ceria systems,” *Journal of the European Ceramic Society*, vol. 35, no. 10, pp. 2815–2821, Sep. 2015, doi: 10.1016/j.jeurceramsoc.2015.03.045.

[130] H. Inaba, “Sintering behaviors of ceria and gadolinia-doped ceria,” *Solid State Ionics*, vol. 106, no. 3–4, pp. 263–268, Feb. 1998, doi: 10.1016/S0167-2738(97)00496-7.

[131] E. Jud, Z. Zhang, W. Sigle, and L. J. Gauckler, “Microstructure of cobalt oxide doped sintered ceria solid solutions,” *J Electroceram*, vol. 16, no. 3, pp. 191–197, May 2006, doi: 10.1007/s10832-006-6258-8.

[132] C. Kleinlogel and L. J. Gauckler, “Sintering of Nanocrystalline CeO2 Ceramics,” *Adv. Mater.*, vol. 13, no. 14, pp. 1081–1085, Jul. 2001, doi: 10.1002/1521-4095(200107)13:14<1081::AID-ADMA1081>3.0.CO;2-D.

[133] G. Lewis, “Effect of Co addition on the lattice parameter, electrical conductivity and sintering of gadolinia-doped ceria,” *Solid State Ionics*, vol. 152–153, pp. 567–573, Dec. 2002, doi: 10.1016/S0167-2738(02)00372-7.

[134] D. M. Mattox, *Handbook of physical vapor deposition (PVD) processing*, 2nd ed. Oxford, UK: William Andrew, 2010.

[135] H. Salmang and H. Scholze, *Keramik: mit 551 Abbildungen und 132 Tabellen*, 7., Vollständig neubearbeitete und erweiterte Auflage. Berlin Heidelberg: Springer, 2007.

[136] R. Oberacker, “Powder Compaction by Dry Pressing,” in *Ceramics Science and Technology*, 1st ed., R. Riedel and I. Chen, Eds., Wiley, 2011, pp. 1–37. doi: 10.1002/9783527631957.ch1.

[137] M. N. Rahaman, *Ceramic processing and sintering*, 2nd ed. in Materials engineering, no. 23. New York: M. Dekker, 2003.

[138] R. M. German, “Thermodynamics of sintering,” in *Sintering of Advanced Materials*, Elsevier, 2010, pp. 3–32. doi: 10.1533/9781845699949.1.3.

[139] D. Lehner, G. Kellner, H. Schnablegger, and O. Glatter, “Static Light Scattering on Dense Colloidal Systems: New Instrumentation and Experimental Results,” *Journal of Colloid and Interface Science*, vol. 201, no. 1, pp. 34–47, May 1998, doi: 10.1006/jcis.1997.5327.

[140] R. Finsy, L. Deriemaeker, E. Geladé, and J. Joosten, “Inversion of static light scattering measurements for particle size distributions,” *Journal of Colloid and Interface Science*, vol. 153, no. 2, pp. 337–354, Oct. 1992, doi: 10.1016/0021-9797(92)90326-H.

[141] N. Tarbă, M.-L. Voncilă, and C.-A. Boiangiu, “On Generalizing Sarle’s Bimodality Coefficient as a Path towards a Newly Composite Bimodality Coefficient,” *Mathematics*, vol. 10, no. 7, p. 1042, Mar. 2022, doi: 10.3390/math10071042.

[142] S. Brunauer, P. H. Emmett, and E. Teller, “Adsorption of Gases in Multimolecular Layers,” *J. Am. Chem. Soc.*, vol. 60, no. 2, pp. 309–319, Feb. 1938, doi: 10.1021/ja01269a023.

[143] M. J. Pomeroy, “Thermal Analysis Techniques for Technical Ceramics and Glasses,” in *Encyclopedia of Materials: Technical Ceramics and Glasses*, Elsevier, 2021, pp. 676–688. doi: 10.1016/B978-0-12-818542-1.00059-X.

[144] M. Hunkel, H. Surm, and M. Steinbacher, “Dilatometry,” in *Handbook of Thermal Analysis and Calorimetry*, vol. 6, Elsevier, 2018, pp. 103–129. doi: 10.1016/B978-0-444-64062-8.00019-X.

[145] A. Sarmast, J. Schubnell, J. Preußner, M. Hinterstein, and E. Carl, “Residual stress analysis in industrial parts: a comprehensive comparison of XRD methods,” *J Mater Sci*, vol. 58, no. 44, pp. 16905–16929, Nov. 2023, doi: 10.1007/s10853-023-09069-z.

[146] J. Epp, “X-ray diffraction (XRD) techniques for materials characterization,” in *Materials Characterization Using Nondestructive Evaluation (NDE) Methods*, Elsevier, 2016, pp. 81–124. doi: 10.1016/B978-0-08-100040-3.00004-3.

[147] U. Welzel, J. Ligot, P. Lamparter, A. C. Vermeulen, and E. J. Mittemeijer, “Stress analysis of polycrystalline thin films and surface regions by X-ray diffraction,” *J Appl Crystallogr*, vol. 38, no. 1, pp. 1–29, Feb. 2005, doi: 10.1107/S0021889804029516.

[148] D. M. Kannan, “Scanning Electron Microscopy: Principle, Components and Applications”.

[149] J. I. Goldstein, D. E. Newbury, J. R. Michael, N. W. M. Ritchie, J. H. J. Scott, and D. C. Joy, *Scanning Electron Microscopy and X-Ray Microanalysis*. New York, NY: Springer New York, 2018. doi: 10.1007/978-1-4939-6676-9.

[150] R. Mücke, O. Büchler, N. H. Menzler, B. Lindl, R. Vaßen, and H. P. Buchkremer, “High-precision green densities of thick films and their correlation with powder, ink, and film properties,” *Journal of the European Ceramic Society*, vol. 34, no. 15, pp. 3897–3916, Dec. 2014, doi: 10.1016/j.jeurceramsoc.2014.04.012.

[151] J. S. Reed and J. S. Reed, *Principles of ceramics processing*, 2nd ed. New York: Wiley, 1995.

[152] A. J. Malkin, Ed., *Rheology fundamentals*. Toronto-Scarborough, Ont: ChemTec Pub, 1994.

[153] J. M. Krishnan, A. P. Deshpande, and P. B. S. Kumar, Eds., *Rheology of Complex Fluids*. New York, NY: Springer New York, 2010. doi: 10.1007/978-1-4419-6494-6.

[154] J. W. Phair and A. F.-J. Kaiser, “Determination and Assessment of the Rheological Properties of Pastes for Screen Printing Ceramics,” p. 5.

[155] K. Reinhardt, N. Hofmann, and M. Eberstein, “The importance of shear thinning, thixotropic and viscoelastic properties of thick film pastes to predict effects on printing performance,” in *2017 21st European Microelectronics and Packaging Conference (EMPC) & Exhibition*, Warsaw, Poland: IEEE, Sep. 2017, pp. 1–7. doi: 10.23919/EMPC.2017.8346831.

[156] M. R. Somalu, A. Muchtar, W. R. W. Daud, and N. P. Brandon, “Screen-printing inks for the fabrication of solid oxide fuel cell films: A review,” *Renewable and Sustainable Energy Reviews*, vol. 75, pp. 426–439, Aug. 2017, doi: 10.1016/j.rser.2016.11.008.

[157] T. G. Mezger, *Das Rheologie Handbuch*, 5th ed. Hannover: Vincentz, 2016.

[158] T.G. Mezger and D. Van Peij, “Modern Rheology Measurements in Today’s Coatings Industry.”

[159] P. Wei, C. Cipriani, C.-M. Hsieh, K. Kamani, S. Rogers, and E. Pentzer, “Go with the flow: Rheological requirements for direct ink write printability,” *Journal of Applied Physics*, vol. 134, no. 10, p. 100701, Sep. 2023, doi: 10.1063/5.0155896.

[160] Malvern Instruments Limited, “Understanding Yield Stress Measurements,” Worcestershire, UK, White Paper, 2015.

[161] D. Klotz, A. Weber, and E. Ivers-Tiffée, “Practical Guidelines for Reliable Electrochemical Characterization of Solid Oxide Fuel Cells,” *Electrochimica Acta*, vol. 227, pp. 110–126, Feb. 2017, doi: 10.1016/j.electacta.2016.12.148.

[162] M. R. Somalu, V. Yufit, and N. P. Brandon, “The effect of solids loading on the screen-printing and properties of nickel/scandia-stabilized-zirconia anodes for solid oxide fuel cells,” *International Journal of Hydrogen Energy*, vol. 38, no. 22, pp. 9500–9510, Jul. 2013, doi: 10.1016/j.ijhydene.2012.06.061.

[163] P. Ried *et al.*, “Processing of YSZ screen printing pastes and the characterization of the electrolyte layers for anode supported SOFC,” *Journal of the European Ceramic Society*, vol. 28, no. 9, pp. 1801–1808, Jan. 2008, doi: 10.1016/j.jeurceramsoc.2007.11.018.

[164] P. Von Dollen and S. Barnett, “A Study of Screen Printed Yttria-Stabilized Zirconia Layers for Solid Oxide Fuel Cells,” *Journal of the American Ceramic Society*, vol. 88, no. 12, pp. 3361–3368, Dec. 2005, doi: 10.1111/j.1551-2916.2005.00625.x.

[165] D. Marani, C. Gadea, J. Hjelm, P. Hjalmarsson, M. Wandel, and R. Kiebach, “Influence of hydroxyl content of binders on rheological properties of cerium–gadolinium oxide (CGO) screen printing inks,” *Journal of the European Ceramic Society*, vol. 35, no. 5, pp. 1495–1504, May 2015, doi: 10.1016/j.jeurceramsoc.2014.11.025.

[166] C. P. Hsu, R. H. Guo, C. C. Hua, C.-L. Shih, W.-T. Chen, and T.-I. Chang, “Effect of polymer binders in screen printing technique of silver pastes,” *J Polym Res*, vol. 20, no. 10, p. 277, Oct. 2013, doi: 10.1007/s10965-013-0277-3.

[167] M. R. Somalu, V. Yufit, I. P. Shapiro, P. Xiao, and N. P. Brandon, “The impact of ink rheology on the properties of screen-printed solid oxide fuel cell anodes,” *International Journal of Hydrogen Energy*, vol. 38, no. 16, pp. 6789–6801, May 2013, doi: 10.1016/j.ijhydene.2013.03.108.

[168] S. Murakami *et al.*, “Effects of ethyl cellulose polymers on rheological properties of (La,Sr)(Ti,Fe)O3-terpineol pastes for screen printing,” *Ceramics International*, vol. 40, no. 1, pp. 1661–1666, Jan. 2014, doi: 10.1016/j.ceramint.2013.07.057.

[169] D. Marani, J. Hjelm, and M. Wandel, “Rheological analysis of stabilized cerium-gadolinium oxide (CGO) dispersions,” *Journal of the European Ceramic Society*, vol. 34, no. 3, pp. 695–702, Mar. 2014, doi: 10.1016/j.jeurceramsoc.2013.09.022.

[170] D. J. Ramler, R. Mücke, C. Lenser, O. Guillon, and N. H. Menzler, “Influence of powder characteristics on the rheology of ceria-based screen-printing pastes for solid oxide cell applications,” *Journal of the European Ceramic Society*, vol. 45, no. 15, p. 117570, Dec. 2025, doi: 10.1016/j.jeurceramsoc.2025.117570.

[171] M. Winter, “Ionic Radii.” The University of Sheffield. [Online]. Available: https://www.webelements.com

[172] G. J. Donley, W. W. Hyde, S. A. Rogers, and F. Nettesheim, “Yielding and recovery of conductive pastes for screen printing,” *Rheol Acta*, vol. 58, no. 6–7, pp. 361–382, Jul. 2019, doi: 10.1007/s00397-019-01148-w.

[173] T. K. Goh, K. D. Coventry, A. Blencowe, and G. G. Qiao, “Rheology of core cross-linked star polymers,” *Polymer*, vol. 49, no. 23, pp. 5095–5104, Oct. 2008, doi: 10.1016/j.polymer.2008.09.030.

[174] R. Mücke, N. H. Menzler, H. P. Buchkremer, and D. Stöver, “Cofiring of Thin Zirconia Films During SOFC Manufacturing,” *Journal of the American Ceramic Society*, vol. 92, pp. S95–S102, Jan. 2009, doi: 10.1111/j.1551-2916.2008.02707.x.

[175] M. R. Somalu and N. P. Brandon, “Rheological Studies of Nickel/Scandia-Stabilized-Zirconia Screen Printing Inks for Solid Oxide Fuel Cell Anode Fabrication,” *J. Am. Ceram. Soc.*, vol. 95, no. 4, pp. 1220–1228, Apr. 2012, doi: 10.1111/j.1551-2916.2011.05014.x.

[176] C. Xu and N. Willenbacher, “How rheological properties affect fine-line screen printing of pastes: a combined rheological and high-speed video imaging study,” *J Coat Technol Res*, vol. 15, no. 6, pp. 1401–1412, Nov. 2018, doi: 10.1007/s11998-018-0091-2.

[177] R. Rudež, J. Pavlič, and S. Bernik, “Preparation and influence of highly concentrated screen-printing inks on the development and characteristics of thick-film varistors,” *Journal of the European Ceramic Society*, vol. 35, no. 11, pp. 3013–3023, Oct. 2015, doi: 10.1016/j.jeurceramsoc.2015.04.035.

[178] J. W. Phair, M. Lundberg, and A. Kaiser, “Leveling and thixotropic characteristics of concentrated zirconia inks for screen-printing,” *Rheol Acta*, vol. 48, no. 2, pp. 121–133, Mar. 2009, doi: 10.1007/s00397-008-0301-4.

[179] M. Lankin, Y. Du, and C. Finnerty, “A Review of the Implications of Silica in Solid Oxide Fuel Cells,” *Journal of Fuel Cell Science and Technology*, vol. 8, no. 5, p. 054001, Oct. 2011, doi: 10.1115/1.4003980.

[180] L. Zhang *et al.*, “Key issues of MoSi2-UHTC ceramics for ultra high temperature heating element applications: Mechanical, electrical, oxidation and thermal shock behaviors,” *Journal of Alloys and Compounds*, vol. 780, pp. 156–163, Apr. 2019, doi: 10.1016/j.jallcom.2018.11.384.

[181] W. Zhi *et al.*, “Thermodynamic assessment of the CaO-Gd2O3–SiO2 system,” *Calphad*, vol. 75, p. 102348, Dec. 2021, doi: 10.1016/j.calphad.2021.102348.

[182] F. Zhang, M. Chen, S. Zhang, P. Zhou, and Y. Du, “Thermodynamic modeling of ZrO2–Y2O3–SiO2 and ZrO2-Gd2O3–SiO2 systems,” *Calphad*, vol. 72, p. 102248, Mar. 2021, doi: 10.1016/j.calphad.2020.102248.

[183] N. A. Toropov, F. Ya. Galakhov, and S. F. Konovalova, “Silicates of the rare earth elements: Communication 2. Phase diagram of the binary system gadolinium oxide-silica,” *Russ Chem Bull*, vol. 10, no. 4, pp. 497–501, Apr. 1961, doi: 10.1007/BF00909108.

[184] J. Felsche, “Polymorphism and crystal data of the rare-earth disilicates of type R.E.2Si2O7,” *Journal of the Less Common Metals*, vol. 21, no. 1, pp. 1–14, May 1970, doi: 10.1016/0022-5088(70)90159-1.

[185] C. Seok *et al.*, “Low-temperature co-sintering technique for the fabrication of multi-layer functional ceramics for solid oxide fuel cells,” *Journal of the European Ceramic Society*, vol. 36, no. 6, pp. 1417–1425, May 2016, doi: 10.1016/j.jeurceramsoc.2015.12.029.

[186] W. Fischer, J. Malzbender, G. Blass, and R. W. Steinbrech, “Residual stresses in planar solid oxide fuel cells,” *Journal of Power Sources*, vol. 150, pp. 73–77, Oct. 2005, doi: 10.1016/j.jpowsour.2005.02.014.

[187] J. Malzbender, W. Fischer, and R. W. Steinbrech, “Studies of residual stresses in planar solid oxide fuel cells,” *Journal of Power Sources*, vol. 182, no. 2, pp. 594–598, Aug. 2008, doi: 10.1016/j.jpowsour.2008.04.035.

[188] V. Gil, J. Tartaj, and C. Moure, “Chemical and thermomechanical compatibility between Ni–GDC anode and electrolytes based on ceria,” *Ceramics International*, vol. 35, no. 2, pp. 839–846, Mar. 2009, doi: 10.1016/j.ceramint.2008.03.004.

[189] P. Bance, N. P. Brandon, B. Girvan, P. Holbeche, S. O’Dea, and B. C. H. Steele, “Spinning-out a fuel cell company from a UK University—2 years of progress at Ceres Power,” *Journal of Power Sources*, vol. 131, no. 1–2, pp. 86–90, May 2004, doi: 10.1016/j.jpowsour.2003.11.077.

[190] T. Ishihara, T. Shibayama, H. Nishiguchi, and Y. Takita, “Nickel–Gd-doped CeO2 cermet anode for intermediate temperature operating solid oxide fuel cells using LaGaO3-based perovskite electrolyte,” *Solid State Ionics*, vol. 132, no. 3–4, pp. 209–216, Jul. 2000, doi: 10.1016/S0167-2738(00)00660-3.

[191] M. P. Klitkou, “Development of Novel Durable Solid Oxide Electrolysis Cells - Integration of Ni-GDC Fuel Electrodes into Fuel Electrode Supported Cells,” Technical University of Denmark, Lyngby, 2024.

[192] A. Kabir, J. Kyu Han, B. Merle, and V. Esposito, “The role of oxygen defects on the electro-chemo-mechanical properties of highly defective gadolinium doped ceria,” *Materials Letters*, vol. 266, p. 127490, May 2020, doi: 10.1016/j.matlet.2020.127490.

[193] C. Lenser, H. Jeong, Y. J. Sohn, N. Russner, O. Guillon, and N. H. Menzler, “Interaction of a ceria-based anode functional layer with a stabilized zirconia electrolyte: Considerations from a materials perspective,” *J Am Ceram Soc*, vol. 101, no. 2, pp. 739–748, Feb. 2018, doi: 10.1111/jace.15214.

**Acknowledgements**

I am deeply grateful to Hon. Prof. Norbert H. Menzler, Dr. Christian Lenser and Prof. Olivier Guillon for giving me the opportunity to pursue my doctorate at the Institute of Energy Materials and Devices – Material Synthesis and Processing (IMD-2). My thanks also go to Prof. Spatschek for kindly serving as the second reviewer of this thesis.

A special thank you goes to my doctoral supervisor, Hon. Prof. Norbert H. Menzler, for his constant support, scientific expertise, and open-door policy. His approachability and encouragement made a lasting impact on my work and experience as a doctoral student.

I am especially thankful to my daily supervisor, Dr. Christian Lenser, especially for his trust, his constant words of encouragement, his immense expertise, and the creative exchange of "silly ideas and questions." Although ElChFest may not have had the ending we had hoped for, my time on this project was still a "Fest" for me.

With this I also want to extend my sincere thanks to the project partners from IMD-1 and Karlsruhe. I have fond memories of our collaboration and monthly meetings, which played a significant role in shaping this thesis into what it is today.

To all my colleagues at IMD-2, past and present, thank you for making the lab and office feel like a place I genuinely enjoyed coming to each day. A special shout-out to Monica and Martin. It was a privilege to start my journey together with you in Cosy. And thank you for staying an integral part in my life ever since. Look how far we've come! I'm also incredibly thankful to the amazing people in Office 154, with whom I had the privilege of sharing an office: Franziska, Artur, and Andrea. Thank you for the in-depth discussions about just everything, for reading reviewer comments and emails when I was too scared to do it, and for simply being there through the ups and downs. And to Laura, I learned so much from you, even beyond science, and couldn't have asked for a better tandem partner. A big thank you also to Luca, who always made sure that I had enough food and motivation, especially in the final stages. I couldn't have done it without you.

To my friends, thank you for the beers, the open ears and the laughter, especially when things got rough. Your presence made the tough moments manageable and the good ones even better.

Last but certainly not least, I would like to thank my family. Your support during every phase of my life has always enabled me to pursue my dreams. Without you, I would certainly not be where I am today. Thank you for always believing in me. Und jetzt auf Deutsch, damit du es auch lesen kannst: Danke für alles, Papa! Du hattest doch wie immer recht gehabt. Ich hab's geschafft! Den Rest erzähle ich dir später.

**List of tables**

## List of figures

Band / Volume 677
**First principles simulations of high-entropy materials for energy storage**
Y. Ting (2025), xviii, 169 pp
ISBN: 978-3-95806-858-2

Band / Volume 678
**Deployment of Fuel Cell Vehicles in Road Transport and the Expansion of the Hydrogen Refueling Station Network**
T. Grube, M. Sander (2025), iv, 61 pp
ISBN: 978-3-95806-859-9

Band / Volume 679
**Entwicklung von nickelbasierten katalysatorbeschichteten Diaphragmen für die alkalische Wasserelektrolyse**
C. B. Karacan (2025), 146 pp
ISBN: 978-3-95806-860-5

Band / Volume 680
**Bewertung lokaler Eigenspannungsverteilungen bei der lokalen Bauteilreparatur durch Kaltgasspritzen**
J.-C. Schmitt (2025), 154, xxvii pp
ISBN: 978-3-95806-861-2

Band / Volume 681
**First principles study of the effect of substitution\doping on the performance of layered oxide cathode materials for secondary batteries**
N. Yaqoob (2025), iii, 126 pp
ISBN: 978-3-95806-864-3

Band / Volume 682
**Field assisted sintering technology/spark plasma sintering in the direct recycling of hot-deformed Nd-Fe-B scrap and PM T15 steel swarf**
M. T. M. Keszler (2025), viii, 173 pp
ISBN: 978-3-95806-866-7

Band / Volume 683
**Assessment of erosion in recessed areas of fusion devices using multi-scale computer simulations**
S. W. Rode (2025), viii, 196 pp
ISBN: 978-3-95806-867-4

Band / Volume 684
**Europäische Energiewende – Deutschland im Herzen Europas**
T. Klütz, P. Dunkel, T. Busch, J. Linssen, D. Stolten (2025), IV, 56 pp
ISBN: 978-3-95806-870-4

Band / Volume 685
**Performance and stability of solar cells and modules: From laboratory characterization to field data analysis**
T. S. Vaas (2025), xvii, 146 pp
ISBN: 978-3-95806-871-1

Band / Volume 686
**From Soil Legacy to Wheat Yield Decline: Studying the Plant-Soil Feedback Mechanisms in Wheat Rotations**
N. Kaloterakis (2025), XXIX, 188 pp
ISBN: 978-3-95806-874-2

Band / Volume 687
**Entwicklung von Beschichtungsverfahren für die Herstellung von Wärmedämmschichten auf additiv gefertigten Komponenten**
M. Rüßmann (2026), ix, 188 pp
ISBN: 978-3-95806-877-3

Band / Volume 688
**Model Perovskite Oxide Electrocatalysts for the Oxygen Evolution Reaction and their Material Sustainability Evaluation**
L. Heymann (2026), vi, 174 pp
ISBN: 978-3-95806-878-0

Band / Volume 689
**Development of an oxygen ion conducting solid oxide electrolysis cell based on gadolinium-doped cerium oxide as fuel electrode and electrolyte material**
D. Ramler (2026), ix, 162 pp
ISBN: 978-3-95806-879-7

Energie & Umwelt / Energy & Environment
Band / Volume 689
ISBN 978-3-95806-879-7

Mitglied der Helmholtz-Gemeinschaft

JÜLICH
Forschungszentrum